Modeling the Flow and Isotope Transport of a Low Speed Countercurrent Gas Centrifuge

A Dissertation

Presented to

the faculty of the School of Engineering and Applied Science

University of Virginia

in partial fulfillment
of the requirements for the degree

Doctor of Philosophy

by

Benjamin Rogers Thomas

May 2019

APPROVAL SHEET

This Dissertation
is submitted in partial fulfillment of the requirements
for the degree of
Doctor of Philosophy

Author Signature: ______________________

This Dissertation has been read and approved by the examining committee:

Advisor: Houston G. Wood

Committee Member: Haibo Dong

Committee Member: Christopher P. Goyne

Committee Member: Sean R. Agnew

Committee Member: Steven L. Creighton

Committee Member: ______________________

Accepted for the School of Engineering and Applied Science:

Craig H. Benson, School of Engineering and Applied Science

May 2019

Abstract

Based on the Onsager Equation with Carrier-Maslen end conditions, a linearized sixth-order partial differential equation describing the flow in the interior volume of the rotor of a gas centrifuge is solved using a finite element algorithm employed by the *CurvSOL* hydrodynamics code. The results are compared to results from the *Pancake* code, an existing code employing an eigenfunction expansion solution technique to solve the Onsager equation. Comparison of the axial mass flux, streamfunction, upflow ratio, and flow profile efficiency demonstrates excellent agreement between the *CurvSOL* and *Pancake* solutions for both the wall temperature gradient and scoop drive mechanisms, as well as the overall mass flux profile for both the Rome and Iguaçu centrifuge designs. The radius of the rotor plays a key role in influence of wall curvature on the flow solution.

The axial mass flux profile derived from the hydrodynamic solution is used in a finite differencing scheme to obtain a numerical solution of the diffusion equation to predict the steady-state transport of uranium hexafluoride molecules in the *xPort* code. The generally accepted method of approximation describes the axial variation of the radially averaged concentration. The newly developed two dimensional concentration field approximation allows for separative performance calculation at all points along the radial direction. Comparison of the two dimensional solution averaged at each axial plane and the one dimensional radial averaging solution shows that while the results from both methods differed by an atomic fraction of 6% at select axial plane near the middle of the rotor, the averages at the end-caps agree to within 2%.

The separative performance values and separation factors are mapped over ranging process gas feed rates and desired ratios of product to feed, and theses performance maps are subsequently employed in cascade analysis software packages. Using the *FixedCascBin* code, the stage flow rates and enrichment levels are calculated for cascades utilizing the Rome and Iguaçu machines. Comparison of the results from

performance maps derived from the one dimensional radial averaging separation calculations and those from the *xPort* code show that while the magnitude of the flow in the stripping section is higher in the one dimensional case, both the upflow and downflow in the enriching section is higher in the two dimensional case. Overall, the two dimensional case upflow enrichment is lower at every stage until the top of the cascade, while the downflow enrichment is lower at every stage until the bottom of the cascade.

Two additional potential applications for the centrifuge performance maps are introduced. The *CascSCAN* code uses a modified version of the *FixedCascBin* to scan over the possible arrangement of centrifuges in cascades designed to enrich from natural uranium to weapons grade uranium in three or four step batch processes. A breakout study is performed using the Iguaçu centrifuge, and a performance map based on the *xPort* results predicts a lower breakout time as additional inventory of enriched material is added to the feed stream. The results differ by as much as four months in the case of the four step batch process with 1500 kg of additional inventory enriched to 3.5% uranium-235. Finally, a recently proposed method for enrichment plant monitoring and characterization offers a potential application for usage of the newly developed performance maps. The potential utility of the *xPort* based performance maps is demonstrated by results of several scenarios simulated with *TransCasc* mapped on a surface that describes all commercial cascades and compared to results from *MSTAR*, a mixed abundance ratio cascade code. The codes *CurveSOL*, *xPort*, and *CascSCAN* were developed by the author to achieve the research objectives presented in this paper.

Acknowledgments

I am forever grateful for the love and support of my family, particularly my wife, Courtney, my kids Caroline, Allison, and Wade, as well as my parents, Bob and Sue Thomas, and my in-laws, Henry and Janice McLeroy.

I would like to extend my sincere appreciation to Dr. Houston Wood. His knowledge and experience certainly inspired me, and without his invitation and direction, I'm not sure where this would have begun or ended.

I would also like to thank the other members of my committee: Dr. Haibo Dong, Dr. Chris Goyne, Dr. Steve Creighton, and Dr. Sean Agnew. Additinally. I thank the Faculty of the Mechanical and Aerospace Engineering Department, with particular thanks to Dr. Rita Schnipke, Dr. Jason Kerrigan, Dr. Harsha Chelliah, and Dr. Roger Fittro.

Financial support for this research was provided primarily by the United States Army's Advanced Civil Schooling Program, which provided me the opportunity to advance my education without putting my career on hold. I would also like to thank the Rotating Machinery and Controls (ROMAC) research consortium, including Dr. Brian Weaver and Mrs. Lori Pederson, for providing me a vehicle to present my research and also for the opportunity to participate in diverse and interesting projects.

Finally, I'd like to thank my fellow graduate students. In no particular order I thank Day, Neal, Micheal, Cori, Thomas, Benny, Xin, Mallory, Brendan, Brian, Carlos, Wisher, and Harrison.

Table of Contents

List of Figures

List of Tables

Nomenclature

α_n	Stage Heads Separation Factor
β_n	Stage Tails Separation Factor
χ	Master Potential
ϵ_f	Flow Profile Efficiency
ϵ_s	Transfer Coefficient
η	General Coordinate
γ	Separation Factor
$\hat{K}$	Brinkman Number
$\mathscr{M}$	Mass source/sink
$\mathscr{T}$	Energy source/sink
$\mathscr{U}$	Radial Momentum source/sink
$\mathscr{V}$	Axial Momentum source/sink
$\mathscr{W}$	Azimuthal Momentum source/sink
μ	Viscosity

Ω	Rotational Velocity
ϕ_r	Net Radial Transport
ϕ_z	Net Axial Transport
ψ	Streamfunction
ρ	Density
ρ_w	Wall Density
D	Diffusion Coefficient
K	Transfer Unit Height
L	Rotor Height
L	Upflow
L_0	Total Upflow
N	Shape Function
N_f	Feed Stream
N_p	Product Stream, "Heads"
N_w	Waste Stream, "Tails"
Pr	Prandtl Number
Re	Reynolds Number
R	Abundance Ratio
UF_6	Uranium Hexafluoride
Z	Aspect Ratio
θ	Cut
$\vec{\phi}^B$	Back Diffusion
$\vec{\phi}^C$	Convection
$\vec{\phi}^P$	Pressure Diffusion
ξ	General Coordinate
A	Stratification Parameter
a	Radius

C_p	Specific Heat
k	Thermal Conductivity
k_B	Boltzman Constant
m	Cohen's Ratio
m	Molecular Weight
p_0	Initial Pressure
p_w	Wall Pressure
T_0	Initial Temperature
x	Scaled Radial Component
AEC	Atomic Energy Commission
DSMC	Direct Simulation Monte Carlo
GCEP	Gas Centrifuge Enrichment Plant
HEU	Highly Enriched Uranium
IAEA	International Atomic Energy Agency
JCPOA	Joint Comprehensive Plan of Action
LEU	Low Enriched Uranium
MIST	Minor Isotope Safeguards Techniques
NDA	Nondestructive Assay
NPT	Nonproliferation Treaty
SQ	Significant Quantity
SWU	Separative Work Unit
UN	United Nations
WGU	Weapons Grade Uranium

1 Introduction

The history of the development of nuclear technologies serves as a chronology of proliferation. The team at Los Alamos that developed the first nuclear weapons consisted primarily of US scientists, but also had a number of representatives from the Allied Nations including Bertrand Goldschmidt, the "father" of the French nuclear weapons program [1]. The Soviet program benefited significantly from spies such as the Rosenbergs [2]. The Soviets greatly assisted the Chinese by sharing technology until relations became strained in 1959 [3].

While the information and technology to build a crude nuclear weapon has proliferated widely over the course of the decades since the first nuclear test at the Trinity Test Site in New Mexico, the universally accepted roadblock to the acquisition of nuclear weapons remains special nuclear material (SNM). Weapons-grade nuclear material is uranium that is enriched to approximately 90% of the isotope uranium-235, or plutonium containing less than approximately 20% of the isotope plutonium-240. A significant quantity (SQ) of weapons-grade material is the amount of material required to construct a nuclear weapon, which the International Atomic Energy Agency (IAEA) estimates to be either 25 kg of uranium-235 or 9 kg of plutonium-239 [4]. In addition to production and handling requirements, the technical acumen required to design, build, and successfully test an implosion type device without detection and international response makes plutonium a slightly smaller proliferation concern for emerging states of concern.

Fissionable material will undergo fission after capturing either a fast or thermal neutron, while a fissile material will fission only after capturing a thermal neutron. The neutrons released from a fissioned uranium-238 nucleus are not of sufficient energy to cause a subsequent fission. Thus, uranium-238, while fissionable, cannot sustain a fission chain reaction. Natural uranium consists primarily of uranium-238 and contains just 0.72% uranium-235. Over the decades since the discovery of the radioactive properties of uranium, a number of different methods have been developed to separate the fissile 235 isotope from the fissionable 238. Gaseous diffusion, electromagnetic isotope separation, and centrifuge separation were all tested as possible means of enrichment for the Manhattan Project in the early 1940s. Gaseous diffusion was eventually selected as the method that would allow the fastest route to attain the greateset amount of weapons grade uranium (WGU). Though not the most efficient technique because of the enormous amount of energy required to maintain pressure gradients across thousands of required stages of diffusion cells, the plants constructed for the war effort remained in operation until 2013 [5].

In the decades after the Second World War, the gas centrifuge emerged as one of the most efficient methods to enrich uranium. It served as a primary method by which the Soviet program attained enriched uranium for its weapons program. In addition to defense applications, there is a large commercial market for uranium enrichment. Numerous corporations have constructed plants to enrich uranium to serve as fuel for reactors. Abdul Qadeer Khan, a nuclear scientist and metallurgical engineer, infamously stole proprietary and sensitive centrifuge and cascade design information from his Dutch employer, Physical Dynamics Research Laboratory (FDO), a subsidiary of the enrichment conglomerate URENCO, before returning to his native Pakistan to lead their weapons program. In the years since his return to Pakistan, evidence of continued proliferation of this critical information to countries with nuclear ambitions continues to mount.

The current geopolitical landscape includes several small nuclear-power-equipped states with declared or suspected nuclear weapon ambitions. The IAEA is responsible for monitoring these emerging capabilities and preventing the spread of weapons while encouraging the peaceful proliferation of energy technology. The toolkit for limiting and monitoring the usage of peaceful or dual-use technologies is relatively limited and often requires the collaboration of the state under scrutiny [6]. While actual physical monitoring of enrichment capability is the responsibility of the IAEA, the international community at large must make every possible effort to police each other. This includes developing computational tools to model and predict the enrichment capability of those emerging states to ensure the IAEA and the UN have ample time to react in the event that the state should "break out" of their IAEA sponsored agreement framework and make an effort to acquire a nuclear weapon.

Dissertation Outline

The over-arching goal of this research effort is to gain a better understanding of the performance of gas centrifuges operated at low speeds by the development and application of various computational models. The scope of this dissertation is limited to the use of data in the literature from previously established modeling techniques and accepted machine designs. Thus, the primary motivations and objectives of this project are:

Motivation: Proprietary and proliferation sensitivity concerns preclude the sharing of machine design information, limiting the ability of the interested community to develop efficient tools to analyze the separative capacity of different centrifuges.

Objective: Create a more efficient flow and separation model for comparison with existing techniques based on limited proliferation-risk-free design parameters.

Motivation: Current proliferation risk material monitoring techniques and "break-out scenario" enrichment timeline estimate calculations are based on simplified performance models or figures of merit derived from long term steady state operation of commercial enrichment plants.

Objective: Develop an improved model for machine separative performance based on the isotope transport in the entire volume of the machine for incorporation into existing cascade performance simulators.

The remainder of this dissertation is arranged to step through the processes necessary to analyze the performance of an individual machine and the potential performance of that machine arranged in a cascade, and finally, the potential applications of that analysis in breakout scenario modeling and safeguards development. This is accomplished through the following chapters:

Chapter 2 - The Gas Centrifuge

The dissertation begins with a brief history of the development of the gas centrifuge and the historical efforts conducted to model its performance.

Chapter 3 - Hydrodynamics

The mathematics governing the hydrodynamics of the centrifuge are discussed, particularly the Onsager model with and without the pancake approximation and including Carrier-Maslen boundary conditions.

Chapter 4 - Numerical Modeling of the Flow Field

A Galerkin finite element method is presented, motivated by the Onsager Equation, to model the axial mass flux profile of a two dimensional cross-section of the rotor volume and compared to accepted solutions.

Chapter 5 - Isotope Transport

The diffusion of the primary isotopes throughout the flow field is discussed and a method for simplifying the equation governing isotope transport is presented.

Chapter 6 - Finite Difference Approximation

A finite differencing scheme is developed to model the isotope transport in the two dimensional cross section of the rotor volume and that solution is compared to the results of the previously presented solution method.

Chapter 7 - Separation

The Separation Factor and the concept of Separative Work are introduced. The separative performance is estimated for two machine designs and mapped over a range of operating conditions, and a comparison is performed of the separative performance derived from the previously presented solution methods.

Chapter 8 - Applications

Potential applications for these newly developed performance models are presented, including cascade modeling, "breakout" scenario timeline estimates, and a newly proposed Minor Isotope Safeguard Technologies (MIST) technique of cascade usage characterization.

Chapter 9 - Conclusions & Recommendations

The results of the major efforts of the dissertation are summarized, the significance of the findings and applications are discussed, and recommendations for future focused effort are proposed.

2 The Gas Centrifuge

The Manhattan Project explored several methods of uranium enrichment and significantly accelerated the pace of existing atomic energy research efforts. The concept of centrifugal separation of isotopes was first proposed in the literature by Lindemann and Astin in 1919. The first successful demonstration of isotopic separation by centrifuge was conducted by Jesse Beams at the University of Virginia in 1934 when he and his team successfully separated chlorine isotopes [7]. Though gaseous diffusion was ultimately selected as the primary method of enrichment for the US program, much effort was devoted to the exploration of centrifuge enrichment. Cohen (1951) authored a comprehensive study of isotope separation for large-scale enrichment programs [7]. This served as a collection of the research done for the US Atomic Energy Commission (AEC) as part of the Manhattan Project Technical series to record the work done in support of the Nation's wartime effort.

At the end of the war, Gernot Zippe, an Austrian scientist and former Luftwaffe instructor pilot, was interned as a prisoner of war and forced into service developing centrifuges in Russia. After his release, a number of chance encounters led to a series of US intelligence debriefings and, ultimately, two years of research at the University of Virginia, where Zippe recreated the work he performed in Russia. The findings were published in a series of unclassified technical reports, the last of which was titled ORO 315 [8]. Upon completion of this work in the US, Zippe was faced with the choice of either accepting US citizenship and classifying all of his research or returning to his native Austria. Zippe elected to return to Austria. Due to security and proliferation concerns, much of the research conducted in the US in the years between the release of ORO 315 and the official end of the US centrifuge program in 1985 remains classified.

A number of comprehensive compilations of the history and achievements of centrifuge technology development have appeared in the literature over the years since the publication of the work of Beams, Cohen, and Zippe. Olander (1972) published a detailed survey of the centrifuge and then (in 1981) a summary of theory of its application to uranium enrichment [9][10]. Soubbaramayer (1979) provided a complete study of the centrifuge in Villani's enrichment reference volume [11]. Benedict, Pigford, and Levi (1981) published *Nuclear Chemical Engineering*, an excellent resource for the entire nuclear fuel cycle for both the nuclear energy and nuclear weapons communities [12]. Other efforts include Krass et al. (1983), Whitley (1984), and Heriot (1988)[13][14][15].

In an address to the audience of the sixth International Workshop on the Separation Phenomena in Liquids and Gases at Nagoya, Japan, Gernot Zippe (1998) delivered an excellent overview of centrifuge development from his perspective as a key contributor to the modern design [8]. Borisevich and Wood (2000) gave a summary of the centrifuge's role in uranium enrichment and future potential [16]. Wood (2008) discussed the difference of the effects of uranium enrichment by gaseous diffusion and centrifugation on the concentration of the minor isotopes, suggesting applications in the nuclear safeguards and nuclear forensics communities [17]. Kemp (2009) gave a complete overview of the US gas centrifuge program [18]. Delbeke et al. (2010) provided a good overview of centrifuge separation and cascade theory. They present a method and models to simulate cascade performance and provide reasonable productivity predictions based on open source information [19].

2.1 Brief Chronology of Centrifuge Research

The sensitive nature of centrifuge enrichment applications has led to the classification or proprietary "close-hold" secret status of state and corporate research programs. However, peaceful uses of nuclear technologies still require responsible enrichment of uranium. Beams, Linke, and Skarstrom (1937) detailed a concurrent flow centrifuge separation method developed to separate isotope of gas and applied to material separation in liquids [20]. Bramley (1939) discussed the impact of axial

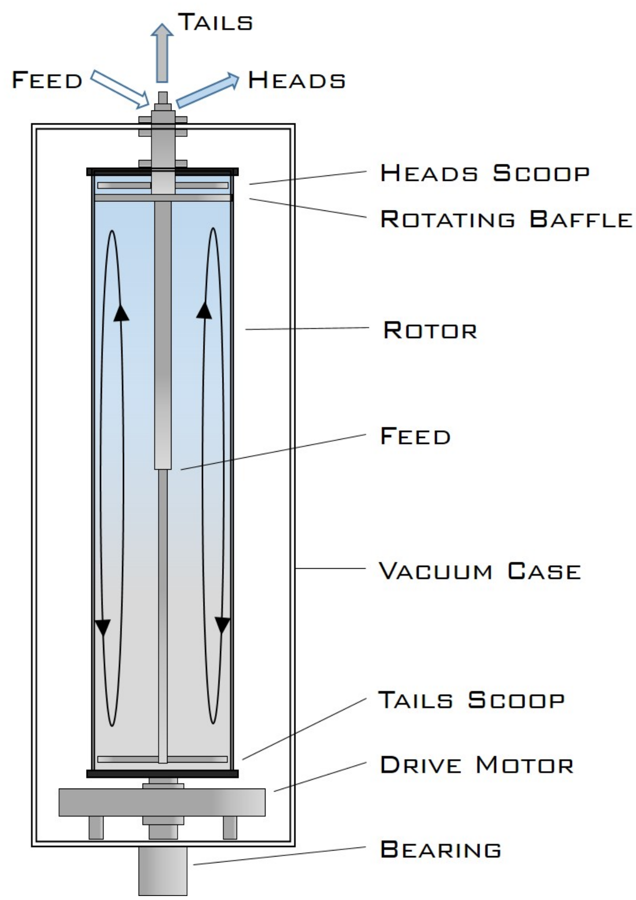

Figure 1: Cross-section of a typical uranium enrichment centrifuge. The rotor is balanced on a bearing inside a vacuum casing. Feed gas enters the rotor volume at the center via a series of concentric tubes along the axis. The product gas, or heads, is removed from near the top of the rotor while the waste, or tails, is removed through a scoop near the bottom. A baffle shields the product scoop from the countercurrent flow. The axial difference in temperature of the process gas and the interaction of the rotating gas with the feed gas and the waste scoop all contribute to the countercurrent flow [23][24]. Although the area of interest in this figure regarding enriched uranium appears to be at rotor's top, the rotor's side walls are also important due to the boundary-layer-type arguments describing compressed high-density phenomena there – discussed below in Section 3.2 "The Pancake Approximation".

motion of mass in thermal diffusion columns and centrifugal fields. He showed that the relative concentrations of two constituents in a process gas changed by varying the axial motion of the mass. He achieved greater differences in concentrations with smaller diameter columns or centrifuges through optimization of the axial mass flux [21]. Cohen (1951) presented a derivation of a partial differential equation describing centrifugal separation and provides an overview of the physics behind evaporative, concurrent and countercurrent centrifuges [7].

Stewartson (1957) examined the flow in a closed circular cylinder and derived the thickness of the layers in which a secondary circulation drifts between end caps. The countercurrent flow is axial in this "Stewartson" layer along the wall of the centrifuge and radial in the "Ekman" layers at the end caps [22][25]. Beams, Snoddy, and Kuhlthau (1958) describe tests made on various centrifuge designs including evaporative, concurrent flow, and countercurrent flow centrifuges. By comparison of the three methods, they showed that the separation achieved by the countercurrent centrifuge was many times that achieved by elementary centrifugal separation processes [26]. Carrier and Maslen (1962) studied the Ekman layers at the ends of a rapidly rotating cylinder and developed a boundary condition to match the flow in the Ekman layers with the main flow field in the center, including the effects of mass and momenta sources, rotating baffles, and temperature gradients [27]. Carrier (1964) later gave a detailed account of several phenomena occurring in rotating fluids including the effects of friction from a cylindrical surface [28]. In the now declassified manuscript, Onsager (1965) describes the linearization of the flow equations, presents the pancake approximation and describes his solution method [29].

Avery and Davies (1973) provided a comprehensive overview of the development and employment of the gas centrifuge for isotope separation [30]. Matsuda (1975) explored thermal drive for a countercurrent centrifuge using the separation theory of Olander as well as Sakurai and Matsuda's hydrodynamics model of a short-bowl countercurrent centrifuge [31]. Bark and Bark (1976) studied the effects of compressibility on the Stewartson layer in an isothermal rotating gas. They found that compressibility thickens the layer at the rotor wall while decreasing the layer thickness at an inner wall [32]. Brouwers (1976) modeled the flow characteristics of a compressible gas in a gas centrifuge [33]. Matsuda and Hashimoto (1976) studied the compressible flow in a gas centrifuge driven thermally, mechanically, or externally by differential rotation of the end caps. They found that insulating the end caps results in suppression of axial flow in the inner inviscid core [34].

Following Olander, May (1977) related the long-bowl countercurrent centrifuge to a distillation column to better represent the physics to the chemical engineering community [35]. Kai (1977) employed a modified Newton's method and a finite difference scheme to approximate the solution of the hydrodynamic flow in a conutercurrent centrifuge. Boundary conidtions allowed for mass addition and removal at the axis and end caps [36]. Brouwers (1978) extended his previous compressibility study to determine the effects on the centrifuge's separative performance and found a difference from the figure Dirac proposed in 1941. He found that the difference from the Dirac prediction increased with rotation speed and rotor length and decreased with radius and gas pressure, which he attributed to the diffusion-controlled core of rarefied gas at the axis of the rotor [37]. Hanel and Humpert (1979) used a finite difference method with successive over-relaxation to solve the diffusion equation of a binary mixture in 4-pole centrifuges. The results showed the influence of radial convective remixing on the separative performance of the centrifuge [38]. Maslen (1979) presented a comparison of computer codes based on Onsager's linearized flow equations, the full linear set of governing equations, and a nonlinear collection of equations [39].

Harada (1980) modeled the hydrodynamics in a countercurrent centrifuge using an DuFort-Frankel/upwind finite differencing scheme. Results of simulations with mechanical and thermomechanical sources indicated that as compressibility is increased, the thermal gradient drive mechanism weakens [40][41]. Cloutman and Gentry (1983) presented the results of a partially implicit finite difference scheme to numerically solve the linearized Navier-Stokes equations and to simulate the flow in a gas centrifuge [42]. Aoki, Suzuki, and Yamamoto (1985) conducted 3D finite difference analysis of the flow field inside and outside of the scoop of the 'Rome' centrifuge [43]. Conlisk (1985) showed that the separative power of the gas centrifuge increased with increasing aspect ratio or decreasing feed flow and may be optimized through control of the countercurrent drive mechanism [44]. Berger (1987) treated the centrifuge as an annulus and used a finite element model to study variation of velocity slip and linear temperature distributions on the inner and outer rotor walls [45].

Ying, Guo, and Wood (1996) established a set of diffusion equations for a multi-component mixture. They used Cohen's radial averaging method and a simplified diffusion transport vector for the multi-component mixture to transform the governing set of nonlinear partial differential equations to a set of nonlinear ordinary differential equations, which they solved iteratively [46]. Andrade and Bastos (1998) developed a finite volume model of the gas flow to determine separative capacity in order to analyze the importance of the rotor wall temperature distribution on the separative capacity [47]. Borisevich, et. al., (2000) presented a numerical model to study the effects of the bellows on separative performance of a super-critical centrifuge. Their results showed that a 40% increase of rotor length resulted in a 20% increase in separative capacity [48]. Omnes (2007) compared two scoop models employed in a finite volume code of the Iguaçu centrifuge. Omnes found that modeling the scoop as a momentum sink required a finer computational mesh than modeling the scoop as a mass source/sink [49].

Migliorini et al. (2013), developed a semi-empirical method to map the separative performance of a centrifuge over a range of operating parameters with only limited historical information derived from published cascade performance data. They specified separative performance and employed a Newton-Raphson iterative approach to characterize various factors, including feed range and cut for that particular design point. They conducted a case-study on the fictitious Iguaçu centrifuge and compared the results to those obtained from a simulation code developed by Oak Ridge National Laboratory. The results showed excellent agreement with previously published results (an average of less than 2% difference for overall separation factor and approximately 15% for separative power) with only minimal information about the actual design variables of the centrifuge itself [50]. Bogovalov et al. (2013), presented a new verification method for numerical solutions where the solution of the linearized Navier-Stokes equations for a rotor of infinite length is matched with a periodic boundary condition to represent the end caps and produce a semi-analytical solution [51].

2.2 The Onsager Model

Formed by the US AEC in the 1960s with the goal of obtaining a better understanding of the flow field in gas centrifuges, a research team of notable scholars led by Dr. Lars Onsager of Yale University (1965) developed a theory for a master potential of the countercurrent flow. The Onsager group used their master potential to simplify the governing hydrodynamic equations into a single partial differential equation of sixth order in the radial variable and second order in the axial variable, henceforth referred to as the Onsager model. This derivation included the "pancake approximation," so named because the strong rotation forces all of the gas to the rotor wall in, effectively, a pancake [29]. Maslen later (1980) detailed a comparison of computer codes employing the Onsager model and the full set of governing equations. He provided a derivation of the Onsager model both with the pancake approximation and retaining the terms influenced by the curvature of teh rotor [39]. Wood and Morton (1980) provided a comprehensive derivation of Onsager's previously unpublished sixth order partial differential equation. They included in their analysis the effects of sources/sinks of mass, momenta, and energy and then obtained a solution for the homogeneous equation using the method of eigenfunction expansion [52].

Gunzburger and Wood (1982) used cubic-spline basis functions to construct a finite element model to numerically solve Onsager's pancake equation [53]. Viecelli (1983) used exponential difference operator approximation formulas to model Onsager's equation with the pancake approximation [54]. Gunzburger, Wood, and Jordan (1984) extended previous work to relax the pancake approximation and included the effects of curvature in their finite element model [55]. Viecelli (1984) applied a pressure continuity constraint to Onsager's equation to properly account for the doubly connected region necessitated by inclusion of a rotating baffle in a gas centrifuge. He then introduced a two-step method to obtain a solution [56].

Wood and Babarsky (1992) consided a non-axisymmetric volume and used an eigensolution technique to simulate the flow driven by mass sources and sinks and thermal gradients, comparing their computed eigenvalue results to those from a complete cylinder [57][58]. Wood, Mason, and Soubbarramayer (1996) used an optimization routine to solve a set of radially averaged diffusion equations for a multi-component mixture. The velocity field was determined through the solution of Onsager's pancake equation adapted for multi-component mixtures [59]. Babarsky, Herbst, and Wood (2002) developed an alternative formulation to Onsager's equation whereby they utilized a temperature potential that behaved analogously to the master potential [60]. De Stadler and Chand (2007) developed a finite difference scheme based on Onsager's equation with the pancake approximation to obtain a solution for the fluid flow in a gas centrifuge [61].

Pradhan and Kumaran (2011) relaxed the pancake approximation and derived a generalized version of Onsager's equation. Following Wood and Morton, they used the method of eigenfunction expansion to obtain solutions of the flow field and found good agreement comparing results to numerical solutions from Direct Simulation Monte Carlo (DSMC) techniques [62]. Migliorini (2013) detailed the basics of two flow field solution methods for the countercurrent gas centrifuge and developed a software set to create centrifuge specific performance models based on Onsager's equation with the pancake approximation. The resulting performance maps for various centrifuge designs were incorporated into various cascade throughput and nonproliferation studies [24][63]. Witt (2013) formulated a generalized version of the Onsager equation retaining curvature terms and incorporating Carrier-Maslen boundary conditions at the end caps and developed a finite element model to solve the flow [64].

3 Hydrodynamics

Increased separative ability of a countercurrent centrifuge is driven by the gas flow field. Cohen, Von Halle, and others have shown that the hydrodynamics and isotope transport in the rotor can be decoupled, and it is convenient to consider each separately [7][24][65]. The solution of the equations governing the flow provides the necessary velocity profiles to solve the diffusion equation [10]. In this section, the governing equations for the flow are discussed and applied to the Onsager model. The pancake approximation is relaxed to retain the influence of the curvature of the rotor wall. Finally, the boundary conditions are defined, including the Carrier-Maslen condition at the end caps.

Assuming axisymmetric flow, the governing equation of state and the mass, momentum, and energy conservation equations form a set of six two-dimensional, nonlinear, partial differential equations. Based on the assumption that the countercurrent flow is a perturbation to the solid-body rotation of the base state and that, due to high rotational velocity, the fluid is restricted to a narrow region at the wall of the rotor, Onsager introduced a "master potential," χ, to describe the flow and developed a method to simplify the set of governing equations. Building on the work of Onsager, Wood and Morton showed that the governing equations may be linearized and reduced, ultimately, to a single linear partial differential equation [52]. As shown by Pradhan and Kumaran in 2011 and Witt in 2013, the pancake approximation may be relaxed and the terms resulting from the curvature of the rotor are carried through the derivation, yielding a generalized version of the Onsager equation[62][64]. The following derivation closely follows the procedures provided in a number of manuscripts detailing the Onsager model, but is informed primarily by [39][52][62][64].

3.1 The Base Flow State

The rotor of the centrifuge may be accurately modeled with a polar-cylindrical coordinate system and a right circular cylinder with the base centered at the origin. Rotating with a constant velocity, Ω, and assuming the base state flow to be ideal steady-state isometric solid-body rotation, the base state velocity components may be written

$$u_0 = 0, \qquad v_0 = r\Omega, \qquad w_0 = 0. \tag{3.1}$$

Applying these base state variables to the radial momentum equation yields

$$\frac{dp_0}{dr} = \rho_0 r \Omega^2. \tag{3.2}$$

Combining the radial momentum equation with the ideal gas equation of state and solving for the pressure gives

$$p_0 = p_w \mathrm{exp} - A^2[1 - (r/a)^2] \ , \tag{3.3}$$

where p_w is the pressure at the rotating wall in the base state. A is the stratification parameter, the ratio of the peripheral speed to the most probable molecular speed [62], and is defined as

$$A = \sqrt{\frac{m\Omega^2 a^2}{2k_B T_0}}, \tag{3.4}$$

where m is the molecular weight, Ω is the rotational speed, a is the rotor radius, k_B is Boltzmann's constant, and T_0 is the base state temperature.

If the base state is perturbed, the total profile variables are expressed as the sum of the base state and the perturbation as

$$\rho = \rho_0 + \tilde{\rho}, \qquad u = 0 + \tilde{u},$$

$$p = p_0 + \tilde{p}, \qquad v = r\Omega + \tilde{v},$$

$$T = T_0 + \tilde{T}, \qquad w = 0 + \tilde{w},$$

where the perturbation values are denoted by the tilde. These total profile variables may be inserted into the mass, momentum, and energy conservation equations to form the governing equations. Assuming axisymmetry, the base state variables are subtracted out and the product terms of perturbation variables neglected, resulting in a linearized set of six equations to solve for dependent variables:

$$\frac{1}{r}\left(r\hat{\rho}u'\right)_r + \hat{\rho}w'_z = 0, \tag{3.5}$$

$$-2\Omega\hat{\rho}v' - r\Omega^2\rho' = -p'_r + \frac{4\mu}{3}\left[\frac{1}{r}\left(ru'_r\right)_r - \frac{u'}{r^2}\right] + \mu u'_{zz} + \frac{\mu}{3}w'_{zr}, \tag{3.6}$$

$$2\Omega\hat{\rho}u' = \mu\left[\frac{1}{r}\left(rv'_r\right)_r + v'_{zz} - \frac{v'}{r^2}\right], \tag{3.7}$$

$$0 = -p'_z + \frac{\mu}{r}\left(rw'_r\right)_r + \frac{4\mu}{3}w'_{zz} + \frac{\mu}{3r}\left(ru'\right)_{rz}, \tag{3.8}$$

$$0 = r\Omega^2\hat{\rho}u' + k\left[\frac{1}{r}\left(rT'_r\right)_r + T'_{zz}\right], \tag{3.9}$$

$$p' = \hat{\rho}RT' + \rho' RT_0, \tag{3.10}$$

where μ is the viscosity and k is the thermal conductivity. Next, dimensionless quantities are defined including

$$
\begin{aligned}
\eta &= \frac{r}{a}, & y &= \frac{z}{a}, & \theta &= \frac{T'}{T_0}, \\
u &= \frac{u'}{a\Omega}, & \omega &= \frac{v'}{a\Omega}, & w &= \frac{w'}{a\Omega}, \\
\rho_0 &= \frac{\hat{\rho}}{\rho_w}, & \rho &= \frac{\rho'}{\rho_w}, & p &= \frac{p'}{p_w},
\end{aligned}
\tag{3.11}
$$

where L is the length of the rotor and ρ_w and p_w are the density and pressure at the rotor wall. Letting Δ represent the Laplace operator in the new dimensionless coordinates η and y, the system of governing equations can be written as

$$(\eta\rho_0 u)_\eta + \eta\rho_0 w_y = 0, \tag{3.12}$$

$$-2\eta\rho_0\omega - \eta\rho = -\frac{1}{2A^2}p_\eta + \frac{1}{Re}\left[\Delta u - \frac{u}{\eta^2} - \frac{2A^2}{3}(\eta u)_\eta\right], \tag{3.13}$$

$$2\rho_0 u = \frac{1}{Re}\left[\Delta(\eta\omega) - \frac{\omega}{\eta}\right], \tag{3.14}$$

$$p_y = \frac{2A^2}{Re}\left[\Delta w - \frac{2A^2}{3}\eta u_y\right], \tag{3.15}$$

$$0 = 4Re\,(S-1)(\eta\rho_0 u) + \Delta\theta, \tag{3.16}$$

$$p = \rho + \rho_0\theta, \tag{3.17}$$

where

$$S = 1 + PrA^2 (\gamma - 1) / 2\gamma,$$

Re is the Reynolds number, given by

$$Re = \frac{\rho_w a^2 \Omega}{\mu},$$

Pr is the Prandtl number, given by

$$Pr = C_p \mu / k,$$

and C_p is the specific heat at constant pressure [52][66][67].

3.2 The Pancake Approximation

If $A \gg 1$, the fluid is assumed confined to a very narrow region in the vicinity of the rotor wall, essentially forming a thin pancake. Setting $\eta = 1$, equations (3.14) and (3.16) may be combined to form

$$\Delta \left[\theta + 2 (S - 1) \omega\right] = 0 \tag{3.18}$$

and

$$\Delta (\theta - 2\omega) = -4ReS\rho_0 u. \tag{3.19}$$

The dimensionless equation of state (3.17) may now be used to eliminate the density from the dimensionless radial momentum conservation equation (3.13) to get

$$\eta\rho_0 (\theta - 2\omega) = \eta p - \frac{1}{2A^2} p_\eta + \frac{1}{Re} \left[\Delta u - \frac{u}{\eta^2} - \frac{2A^2}{3} (\eta u)_\eta\right]. \tag{3.20}$$

Equations (3.18) to (3.20), along with equations (3.12) and (3.15), form the complete system of linearized, dimensionless governing equations. By letting

$$\phi = \theta - 2\omega, \tag{3.21}$$

and defining a new radial coordinate, x, such that

$$x = A^2 \left(1 - \eta^2\right), \tag{3.22}$$

the set of governing equations may be succinctly expressed as

$$e^{-x} w_y - 2A^2 \left(e^{-x} u\right)_x = \mathscr{M}, \tag{3.23}$$

$$\phi = \left(e^x p\right)_x + e^x \mathscr{U}, \tag{3.24}$$

$$\phi_{xx} = -\frac{ReS}{A^4} e^{-x} u - \left(\mathscr{T} - 2\mathscr{V}\right), \tag{3.25}$$

$$p_y = \frac{8A^6}{Re} w_{xx} + \mathscr{W}, \tag{3.26}$$

$$-4A^4 h_{xx} - h_{yy} = \mathscr{T} + 2\left(S - 1\right)\mathscr{V}, \tag{3.27}$$

where $\mathscr{M}, \mathscr{U}, \mathscr{V}, \mathscr{W}, \mathscr{T}$ are dimensionless sources/sinks of mass, momentum, and energy, respectively, and

$$h = \theta + 2\left(S - 1\right)\omega. \tag{3.28}$$

The pressure term is next eliminated by combining equations (3.24) and (3.26) to yield

$$\phi_y = \frac{8A^6}{Re}\left(e^x w_{xx}\right)_x + \left(e^x \mathscr{W}\right)_x + e^x \mathscr{U}_y. \tag{3.29}$$

To accommodate the inclusion of sink/source terms, a streamfunction, ψ, is defined such that

$$e^{-x} u = -\psi_y - \frac{1}{2A^2}\bar{\psi} \tag{3.30}$$

and

$$e^{-x} w = -2A^2 \psi_x. \tag{3.31}$$

The modified mass conservation equation (3.23) and this streamfunction are now used to show that

$$\bar{\psi}\left(x, y\right) = \int_0^x \mathscr{M}\left(x', y\right) dx'. \tag{3.32}$$

Similarly, this streamfunction is introduced into the combined and modified momentum equations (3.25) and (3.29) to give

$$\phi_{xx} = \frac{ReS}{A^4}\psi_y + \frac{ReS}{2A^6}\int_0^x \mathscr{M}\left(x', y\right) dx' - \left(\mathscr{T} - 2\mathscr{V}\right) \tag{3.33}$$

and

$$\phi_y = -\frac{16A^8}{Re}\left(e^x\left(e^x \psi_x\right)_{xx}\right)_x + \left(e^x \mathscr{W}\right)_x + +e^x \mathscr{U}_y. \tag{3.34}$$

Along with (3.27), equations (3.33) and (3.34) form the complete set of governing equations. From here, equations (3.33) and (3.34) may be combined to eliminate ϕ and give

$$\left(e^{x}\left(e^{x}\psi_{x}\right)_{xx}\right)_{xxx}+\frac{Re^{2}S}{16A^{12}}\psi_{yy}=F_{x}\left(x,y\right), \tag{3.35}$$

where

$$F_{x}\left(x,y\right)=\frac{Re}{16A^{8}}\left(e^{x}\mathscr{W}\right)_{xxx}+\frac{Re}{16A^{8}}\left(e^{x}\mathscr{U}_{y}\right)_{xx}-\frac{Re^{2}S}{32A^{14}}\bar{\psi}_{y}$$
$$+\frac{Re}{16A^{8}}\left(\mathscr{T}-2\mathscr{V}\right)_{y}.$$

A master potential, χ, is now defined such that

$$\psi=-2A^{2}\chi_{x}. \tag{3.36}$$

Equation (3.35) can then be integrated once with respect to the scaled radial coordinate, x, to yield the Onsager Equation with the Pancake Approximation given by

$$\left(e^{x}\left(e^{x}\chi_{xx}\right)_{xx}\right)_{xx}+B^{2}\chi_{yy}=F\left(x,y\right), \tag{3.37}$$

where

$$F\left(x,y\right)=\frac{B^{2}A^{2}}{2ReS}\int_{x}^{\infty}\left(\mathscr{T}_{y}-2\mathscr{V}_{y}\right)dx'-\frac{B^{2}}{4A^{4}}\int_{x}^{\infty}\int_{0}^{x'}\mathscr{M}_{y}dx''dx' \tag{3.38}$$
$$-\frac{B^{2}A^{2}}{2ReS}\left[\left(e^{x}\mathscr{U}_{y}\right)_{x}+\left(e^{x}\mathscr{W}\right)_{xx}\right]$$

and

$$B=\frac{ReS^{\frac{1}{2}}}{4A^{6}}. \tag{3.39}$$

It is important here to note that to fully reconcile the system of equations when sources are present, one must incorporate h from equation (3.28).

3.3 The Generalized Onsager Equation

In order to understand the influence of the rotor wall at different speeds of rotation while retaining the curvature terms but relaxing the Pancake approximation of equation (3.37), an alternate derivation is performed, starting once again with equations (3.5) to (3.10) and slightly modifying the previously defined non-dimensional parameters.

Rather than scaling by the radius, the axial coordinate is divided by the rotor height, L, and the two new dimensionless coordinates are

$$\eta = \frac{r}{a} \qquad \text{and} \qquad y = \frac{z}{L}.$$

Additionally, the dimensionless source terms are given by

$$\mathscr{M} = \frac{f_m}{\rho_w \Omega}, \qquad \mathscr{U} = \frac{f_r}{\rho_w a \Omega^2}, \qquad \mathscr{V} = \frac{f_\theta}{\rho_w a \Omega^2}, \qquad \mathscr{W} = \frac{f_z}{\rho_w a \Omega^2}, \qquad \mathscr{T} = \frac{f_e}{\rho_w a^2 \Omega^3},$$

where, f_m, f_r, f_θ, f_z, and f_e, are the original source terms of mass, radial momentum, azimuthal momentum, axial momentum, and energy, respectively.

Finally, two additional dimensionless parameters are defined: the aspect ratio, Z, and the Brinkman number, $\hat{K}$, which are given, respectively, by

$$Z = \frac{L}{a}, \qquad \hat{K} = \frac{a^2 \Omega^2 Pr}{4 C_p T_0}.$$

Incorporating all of these quantities, the resulting set of linearized, dimensionless governing equations yields

$$\frac{1}{\eta}(\eta\bar{\rho}_0\bar{u})_\eta + \frac{1}{Z}(\bar{\rho}_0\bar{w})_y = \mathscr{M}, \tag{3.40}$$

$$\begin{aligned} -2\bar{\rho}_0\eta\bar{v} - \bar{\rho}\eta = -\frac{1}{2A^2}p_\eta + \frac{4}{3Re}\left(\frac{1}{\eta}\left(\eta u_\eta\right)_\eta - \frac{\bar{u}}{\eta^2}\right) \\ + \frac{1}{Re}\left(\frac{1}{Z^2}u_{yy} + \frac{1}{3Z}w_{y\eta}\right) + \mathscr{U}, \end{aligned} \tag{3.41}$$

$$2\bar{\rho}_0\bar{u} = \frac{1}{Re}\left(\frac{1}{\eta}\left(\eta\left(\eta\bar{v}\right)_\eta\right)_\eta\right) + \frac{Z^2}{Re}\left(\eta\bar{v}\right)_{yy} - \frac{1}{Re}\frac{\bar{v}}{\eta} + \mathscr{V}, \tag{3.42}$$

$$0 = -\frac{1}{2A^2}p_y + \frac{Z}{Re}\frac{1}{\eta}\left(\eta w_\eta\right)_\eta + \frac{4}{3}\frac{1}{ZRe}w_{yy} + \frac{1}{3}\frac{1}{Re}\frac{1}{\eta}\left(\eta\bar{u}\right)_{\eta y} + Z\mathscr{W}, \tag{3.43}$$

$$0 = \eta\bar{\rho}_0\bar{u} + \frac{1}{4\hat{K}Re}\frac{1}{\eta}\left(\eta\theta_\eta\right)_\eta + \frac{1}{4\hat{K}Re}\frac{1}{Z^2}\theta_{yy} + \mathscr{T}, \tag{3.44}$$

$$\bar{p} = \bar{\rho}_0\bar{T} + \bar{\rho}. \tag{3.45}$$

Equations (3.40) through (3.45) represent a complete set of six equations with six unknowns. As before, the set of equations can now be algebraically reduced into a single sixth-order equation that describes the flow in the cylinder. Once again, the reduction begins by using the dimensionless equation of state to eliminate the density in the radial momentum equation. The radial and axial momentum equations are then added to form a single combined momentum equation [52][62].

Next, the velocity is expressed in terms of a streamfunction ψ such that

$$\eta\bar{\rho}_0\bar{u} = -\psi_y - \int_\eta^1 \mathscr{M}\eta\mathrm{d}\eta, \tag{3.46}$$

and

$$\eta\bar{\rho}_0\bar{w} = \frac{Z}{\eta}\psi_\eta, \tag{3.47}$$

where

$$\psi(1,y) - \psi(\eta,y) = \frac{1}{Z}\int_\eta^1 \bar{\rho}_0\bar{w}\eta\mathrm{d}\eta. \tag{3.48}$$

Based on this stream function, a master potential, χ, is once again defined such that [52]

$$\psi = \frac{1}{\eta}\chi_\eta, \tag{3.49}$$

and the velocity components $\bar{u}$ and $\bar{w}$ are written

$$\bar{u} = -\frac{1}{\eta\bar{\rho}_0}\left(\frac{1}{\eta}\chi_\eta\right)_y - \frac{1}{\eta\bar{\rho}_0}\int_\eta^1 \mathscr{M}\eta\mathrm{d}\eta \tag{3.50}$$

and

$$\bar{w} = \frac{Z}{\eta^2\bar{\rho}_0}\left(\frac{1}{\eta}\chi_\eta\right)_\eta . \tag{3.51}$$

Expressing the combined momentum equation in terms of this master potential and inserting the velocity in terms of the master potential into the energy equation and the angular momentum equation, the set of governing equations is reduced to three. The energy and angular momentum equations are then combined into a single function, reducing the set of governing equations to two.

Once again, the scaled radial coordinate, x, is introduced where

$$x = A^2(1-\eta^2), \tag{3.52}$$

and the two governing equations can then be reduced into a single partial differential equation. Further manipulation to accommodate homogeneous boundary conditions ultimately results in the modified Onsager-Maslen equation [64], given by

$$(e^x(\eta^2(e^x\chi_{xx})_x)_x)_{xx} + \frac{Re^2}{16A^{12}Z^2}\frac{1+K\eta^2}{\eta^4}\chi_{yy} = \bar{S} + \bar{H}, \tag{3.53}$$

where the source terms are

$$\begin{aligned}
\bar{S} = &- \frac{Re^2}{64A^{16}Z^2}\frac{1+\bar{K}\eta^2}{\eta^4}\int_x^{x_T}\int_0^{x'} \mathscr{M}_y dx'' dx' - \frac{Re}{32A^{10}Z^2}\left(\frac{e^x}{\eta}\mathscr{U}_y\right)_x \\
&- \frac{Re^2}{64A^{14}z^2}\frac{1}{\eta^4}\int_x^{x_T}\eta'\mathscr{V}_y dx' - \frac{Re}{16A^8Z}(e^x\mathscr{W})_{xx} + \frac{Re^2\bar{K}}{32A^{14}Z^2}\frac{1}{\eta^2}\int_x^{x_T}\mathscr{T}_y dx' \\
&- \frac{1}{48A^8Z^2}\left(e^{2x}\mathscr{M}_y\right)_x + \frac{1}{16A^8Z^2}\left(\frac{e^x}{\eta}\left(\eta^2\left(\frac{e^x}{\eta}\int_0^x \mathscr{M}_y dx'\right)_x\right)_x\right)_x \\
&+ \frac{1}{64A^{12}Z^4}\left(\frac{e^{2x}}{\eta^2}\int_0^x \mathscr{M}_{yyy} dx'\right)_x - \frac{1}{64A^{12}Z^2}\left(\left(1+\frac{4A^4\eta^4}{3}\right)\frac{e^{2x}}{\eta^4}\int_0^x \mathscr{M}_y dx'\right)_x
\end{aligned} \tag{3.54}$$

and

$$\bar{H} = -\frac{2h(y)}{x_T^2}\left(e^x\left(\eta^2\left(xe^x\right)_x\right)_x\right)_{xx} - \frac{Re^2}{48A^{12}Z^2}\frac{1+\bar{K}\eta^2}{\eta^4}\frac{x^3-x_T^3}{x_T^2}h''(y), \tag{3.55}$$

and h is defined as

$$\begin{aligned}
h(y) = &\frac{1}{4A^4Z}\int_0^{x_T}\bar{\rho}\bar{v}_z(x,0)dx' + \frac{1}{2A^2}\eta(x_T,y)\int_0^y f(y')dy' \\
&+ \frac{1}{4A^4}\int_0^{x_T}\int_0^y \mathscr{M} dy' dx'.
\end{aligned} \tag{3.56}$$

The system may be more succinctly written

$$(e^x(\eta^2(e^x\chi_{xx})_x)_x)_{xx} + B\chi_{yy} = \bar{S} + \bar{H}, \tag{3.57}$$

where

$$B = \frac{Re^2}{16A^{12}Z^2}\frac{1+\hat{K}\eta^2}{\eta^4}. \tag{3.58}$$

Note that if the curvature variable, η, is set equal to unity and the source terms are set to zero, equation (3.57) simplifies to Onsager's Equation with the pancake approximation as presented in [52].

3.4 Boundary Conditions

The boundaries can be described in three separate regions: at the rotor wall, high in the atmosphere (toward the center of the rotor), and at the top and bottom end caps. At the rotor wall there is no axial velocity due to the no-slip condition [70]. There is also no radial velocity because there is no mass flux through the rotor wall. Additionally, there is a prescribed temperature gradient at the wall [71]. In the rarefied region nearer to the axis (analogous to high in the local atmosphere), there is no radial velocity, no change in axial velocity with radial position, and no change in azimuthal velocity or temperature with radial position [72]. At the end caps, the flow is radial in the Ekman layers and can be described by the Carrier-Maslen boundary condition [27][52][64][69][68].

These boundary conditions may be expressed in terms of the master potential and the previously defined dimensionless variables. At the rotor wall,

$$\chi_x(0, y) = 0, \tag{3.59}$$

$$\chi_{xx}(0, y) = 0, \tag{3.60}$$

and

$$\left(e^x\left(\eta^2\left(e^x\chi_{xx}\right)_x\right)_x\right)_x(0,y)=0. \tag{3.61}$$

High in the atmosphere toward the axis,

$$\chi(x_T,y)=0, \tag{3.62}$$

$$\chi_x(x_T,y)=0, \tag{3.63}$$

and

$$\left(e^x\chi_{xx}\right)_x(x_T,y)=-\frac{2(x_T+1)}{x_T^2}e^{x_T}h(y). \tag{3.64}$$

The Carrier-Maslen boundary condition for the bottom end cap [52][64] is

$$\frac{Re^2}{16A^{12}Z^2}\frac{1+\hat{K}\eta^2}{\eta^4}\chi_y(x,0)=-\frac{Re^{\frac{3}{2}}}{4A^8Z}\left(\frac{(1+\bar{K}\eta^2)^{\frac{3}{4}}}{\eta^2}e^{\frac{x}{2}}\chi_x(x,0)\right)_x+G^-(x), \tag{3.65}$$

where

$$\begin{aligned}G^-(x)=&-\frac{Re^2}{48A^{12}x_T^2Z^2}\frac{1+\hat{K}\eta^2}{\eta^4}(x^3-x_T^3)h'(0)-\frac{Re^{\frac{3}{2}}}{4A^8x_T^2Z}\left(\frac{(1+\bar{K}\eta^2)^{\frac{3}{4}}}{\eta^2}x^2e^{\frac{x}{2}}\right)_x h(0)\\&+\frac{Re}{16A^{10}Z^2}\left(\frac{\sqrt{1+\bar{K}\eta^2}}{\eta}v_r^-\right)_x-\frac{Re}{32A^{10}Z^2}\phi_x^--\frac{Re^{\frac{3}{2}}}{8A^{10}Z}\left(\frac{(1+\bar{K}\eta^2)^{\frac{3}{4}}}{\eta^2}e^{\frac{x}{2}}\psi^-\right)_x\\&-\frac{Re^2}{64A^{16}Z^2}\frac{1+\bar{K}\eta^2}{\eta^4}\int_x^{x_T}\int_0^{x'}\mathscr{M}(x,0)dx''dx'-\frac{Re^2}{64A^{14}Z^2}\frac{1}{\eta^4}\int_x^{x_T}\eta'\mathscr{V}(x,0)dx'\\&+\frac{Re^2\bar{K}}{32A^{14}Z^2}\frac{1}{\eta^2}\int_x^{x_T}\mathscr{T}(x,0)dx'.\end{aligned} \tag{3.66}$$

Similarly, the Carrier-Maslen boundary condition for the top end cap is

$$\frac{Re^2}{16A^{12}Z^2}\frac{1+\hat{K}\eta^2}{\eta^4}\chi_y(x,1) = \frac{Re^{\frac{3}{2}}}{4A^8 Z}\left(\frac{(1+\bar{K}\eta^2)^{\frac{3}{4}}}{\eta^2}e^{\frac{x}{2}}\chi_x(x,1)\right)_x + G^+(x), \tag{3.67}$$

where

$$\begin{aligned} G^+(x) = &-\frac{Re^2}{48A^{12}x_T^2 Z^2}\frac{1+\hat{K}\eta^2}{\eta^4}(x^3 - x_T^3)h'(1) + \frac{Re^{\frac{3}{2}}}{4A^8 x_T^2 Z}\left(\frac{(1+\bar{K}\eta^2)^{\frac{3}{4}}}{\eta^2}x^2 e^{\frac{x}{2}}\right)_x h(1) \\ &+\frac{Re}{16A^{10}Z^2}\left(\frac{\sqrt{1+\bar{K}\eta^2}}{\eta}v_r^+\right)_x - \frac{Re}{32A^{10}Z^2}\phi_x^+ + \frac{Re^{\frac{3}{2}}}{8A^{10}Z}\left(\frac{(1+\bar{K}\eta^2)^{\frac{3}{4}}}{\eta^2}e^{\frac{x}{2}}\psi^+\right)_x \\ &-\frac{Re^2}{64A^{16}Z^2}\frac{1+\bar{K}\eta^2}{\eta^4}\int_x^{x_T}\int_0^{x'}\mathscr{M}(x,1)dx''dx' - \frac{Re^2}{64A^{14}Z^2}\frac{1}{\eta^4}\int_x^{x_T}\eta'\mathscr{V}(x,1)dx' \\ &+\frac{Re^2\bar{K}}{32A^{14}Z^2}\frac{1}{\eta^2}\int_x^{x_T}\mathscr{T}(x,1)dx'. \end{aligned} \tag{3.68}$$

This chapter has detailed the derivation of the Onsager equation, a single sixth-order partial differential equation, both with and without the Pancake approximation. Along with ordinary and Carrier-Maslen boundary conditions of equations (3.59) through (3.67), equation (3.57) fully describes the fluid flow in a two-dimensional cross-section of the gas centrifuge. The following chapter will describe a finite elements-based solution to this equation that will ultimately provide an approximation of the mass flow in the rotor volume. This mass flow field may then be used in subsequent modeling routines to estimate the separative ability of the centrifuge based on the initial parameters defined in the hydrodynamics model.

4 Numerical Modeling of the Flow Field

The finite element method typically involves employment of a variational formulation, a discretization of the domain, the primary solution algorithm, and post-processing. This chapter touches upon each of these areas, giving a complete picture of the model from construction to results. First, the Galerkin method is used as the variational approach. The discretization of the domain and development of the basis functions are then described. Next the construction of the computer program and the underlying algorithm are explained. Finally, the results are presented and examined to determine the feasibility of the use of the model for accurately describing the flow field in the centrifuges simulated.

The results of numerous techniques to solve the Onsager equation exist in the literature as discussed in the opening chapters. In particular, results from finite element models leveraging cubic spline basis functions in the radial direction and linear "hat" basis functions in the axial direction have been reported by [53][55] and [64]. The Onsager equation with the pancake approximation and without source terms was modeled using this method by [53] and with source terms by [55], while a generalized form of Onsager's equation retaining curvature was modeled with this method by [64].

Similar to the models found in [53][55][64], a Galerkin method of weighted residuals is used to create a finite element model of the flow in the centrifuge. The governing equation is first cast into the weak form. The domain is then discretized and a set of basis functions defined. The weak form is then expressed in terms of the basis functions and the associated coefficients. The sum of the product of these basis functions over the domain represents a system of equations that can be solved in a standard matrix equation.

4.1 The Weak Form

From equation (3.57) we first define a residual, $\xi(x,y)$, for discrete points in the domain such that

$$(e^x(\eta^2(e^x\chi_{xx})_x)_x)_{xx} + B\chi_{yy} - \bar{S} - \bar{H} = \xi(x,y). \tag{4.1}$$

Multiplying equation (4.1) by a smooth "test" function, ϕ, and requiring that the residual vanish when integrating the product over the computational domain gives

$$\int_D \int \phi((e^x(\eta^2(e^x\chi_{xx})_x)_x)_{xx} + B\chi_{yy} - \bar{S} - \bar{H})dydx = 0, \tag{4.2}$$

which can be broken down into several integrals. If the first term is integrated by parts three times, the result is

$$\begin{aligned}
\int_0^{x_T} \int_0^1 \phi \left(e^x \left(\eta^2 \left(e^x \chi_{xx}\right)_x\right)_x\right)_{xx} dydx = \\
- \int_0^{x_T} \int_0^1 \eta^2 \left(e^x \chi_{xx}\right)_x \left(e^x \phi_{xx}\right)_x dydx \\
+ \int_0^1 \phi \left(e^x \left(\eta^2 \left(e^x \chi_{xx}\right)_x\right)_x\right)_x \Big|_{x=0}^{x_T} dy \\
- \int_0^1 e^x \phi_x \left(\eta^2 \left(e^x \chi_{xx}\right)_x\right)_x \Big|_{x=0}^{x_T} dy \\
+ \int_0^1 \eta^2 e^x \phi_{xx} \left(e^x \chi_{xx}\right)_x \Big|_{x=0}^{x_T} dy.
\end{aligned} \tag{4.3}$$

The *essential* boundary conditions are those that are applied to the trial function, χ, as well as the test function. The *natural* boundary conditions are those remaining defined boundary conditions not applied to the test function [73]. Applying radial boundary conditions (3.59), (3.60), (3.62), and (3.63) to ϕ, equation (4.3) can be simplified to

$$
\begin{aligned}
\int_0^{x_T}\int_0^1 \phi\left(e^x\left(\eta^2\left(e^x\chi_{xx}\right)_x\right)_x\right)_{xx} dydx = & \qquad (4.4)\\
& -\int_0^{x_T}\int_0^1 \eta^2\left(e^x\chi_{xx}\right)_x\left(e^x\phi_{xx}\right)_x dydx\\
& -\int_0^1 \phi\left(e^x\left(\eta^2\left(e^x\chi_{xx}\right)_x\right)_x\right)_x |_{x=0}\, dy\\
& +\int_0^1 \eta^2 e^x\phi_{xx}\left(e^x\chi_{xx}\right)_x\Big|_{x=x_T} dy.
\end{aligned}
$$

Imposing the *natural* radial boundary conditions (3.61) and (3.64), equation (4.4) becomes

$$
\begin{aligned}
\int_0^{x_T}\int_0^1 \phi\left(e^x\left(\eta^2\left(e^x\chi_{xx}\right)_x\right)_x\right)_{xx} dydx = & \qquad (4.5)\\
& -\int_0^{x_T}\int_0^1 \eta^2\left(e^x\chi_{xx}\right)_x\left(e^x\phi_{xx}\right)_x dydx\\
& -\frac{Re}{32A^{10}Z^2}\int_0^1 \phi\Big|_{x=0}\theta(y)dy\\
& +\frac{10(1-A^{-2}}{x_T^2}\int_0^1 \phi\Big|_{x=0}h(y)dy\\
& -\frac{2(x_T+1)}{x_T^2}e^{2x_T}\int_0^1 \eta^2\phi_{xx}\Big|_{x=x_T}h(y)dy.
\end{aligned}
$$

Integrating the second term in (4.2) by parts gives

$$
\begin{aligned}
\int_0^{x_T}\int_0^1 \frac{Re^2}{16A^{12}Z^2}\frac{1+\hat{K}\eta^2}{\eta^4}\phi\chi_{yy}dydx = & \qquad (4.6)\\
& -\int_0^{x_T}\int_0^1 \frac{Re^2}{16A^{12}Z^2}\frac{1+\hat{K}\eta^2}{\eta^4}\phi_y\chi_y dydx\\
& +\frac{Re^2}{16A^{12}Z^2}\int_0^{x_T}\frac{1+\hat{K}\eta^2}{\eta^4}\phi\chi_y\Big|_{y=0}^1 dx.
\end{aligned}
$$

Applying axial boundary conditions (3.65) and (3.67), equation (4.6) becomes

$$
\begin{aligned}
\int_0^{x_T}\int_0^1 \frac{Re^2}{16A^{12}Z^2}\frac{1+\hat{K}\eta^2}{\eta^4}\phi\chi_{yy}dydx = & \\
& -\int_0^{x_T}\int_0^1 \frac{Re^2}{16A^{12}Z^2}\frac{1+\hat{K}\eta^2}{\eta^4}\phi_y\chi_y dydx \\
& + \frac{Re^{\frac{3}{2}}}{16A^{12}Z^2}\int_0^{x_T}\phi\Big|_{y=0}\left(\frac{\left(1+\hat{K}\eta^2\right)^{\frac{3}{4}}}{\eta^2}e^{\frac{x}{2}}\chi_x\Big|_{y=0}\right)_x dx \\
& + \frac{Re^{\frac{3}{2}}}{16A^{12}Z^2}\int_0^{x_T}\phi\Big|_{y=1}\left(\frac{\left(1+\hat{K}\eta^2\right)^{\frac{3}{4}}}{\eta^2}e^{\frac{x}{2}}\chi_x\Big|_{y=1}\right)_x dx \\
& + \int_0^{x_T}\left(\phi\Big|_{y=1}G^+(x)-\phi\Big|_{y=0}G^-(x)\right)dx.
\end{aligned} \tag{4.7}
$$

Integrating the second and third terms of the right hand side of equation (4.7) by parts and applying the *essential* boundary conditions (3.59), (3.60), (3.62), and (3.63), equation (4.7) simplifies to

$$
\begin{aligned}
\int_0^{x_T}\int_0^1 \frac{Re^2}{16A^{12}Z^2}\frac{1+\hat{K}\eta^2}{\eta^4}\phi\chi_{yy}dydx = & \\
& -\int_0^{x_T}\int_0^1 \frac{Re^2}{16A^{12}Z^2}\frac{1+\hat{K}\eta^2}{\eta^4}\phi_y\chi_y dydx \\
& - \frac{Re^{\frac{3}{2}}}{16A^{12}Z^2}\int_0^{x_T}\frac{\left(1+\hat{K}\eta^2\right)^{\frac{3}{4}}}{\eta^2}e^{\frac{x}{2}}\left(\chi_x\phi_x\Big|_{y=0}+\chi_x\phi_x\Big|_{y=1}\right)dx \\
& + \int_0^{x_T}\left(\phi\Big|_{y=1}G^+(x)-\phi\Big|_{y=0}G^-(x)\right)dx.
\end{aligned} \tag{4.8}
$$

Incorporating the results of (4.5) and (4.8) into equation (4.2), the weak form of the generalized Onsager equation with boundary conditions may finally be written as

$$
\begin{aligned}
&\int_0^{x_T}\int_0^1 \eta^2 \left(e^x \chi_{xx}\right)_x \left(e^x \phi_{xx}\right)_x dydx + \int_0^{x_T}\int_0^1 \frac{Re^2}{16A^{12}Z^2}\frac{1+\hat{K}\eta^2}{\eta^4}\chi_y\phi_y dydx \qquad (4.9)\\
&\quad + \frac{Re^{\frac{3}{2}}}{4A^8 Z}\int_0^{x_T} \frac{\left(1+\hat{K}\eta^2\right)^{\frac{3}{4}}}{\eta^2} e^{\frac{x}{2}} \left(\chi_x\phi_x\Big|_{y=0} + \chi_x\phi_X\Big|_{y=1}\right) dx\\
&\quad = -\int_0^{x_T}\int_0^1 \phi\bar{S}dydx - \int_0^{x_T}\int_0^1 \phi\bar{H}dydx\\
&\quad - \frac{Re}{32A^{10}Z^2}\int_0^1 \phi\Big|_{x=0}\theta(y)dy + \int_0^{x_T}\left(\phi\Big|_{y=1}G^+(x) - \phi\Big|_{y=0}G^-(x)\right)dx\\
&\quad + \frac{10\left(1-A^{-2}\right)}{x_T^2}\int_0^1 \phi\Big|_{x=0}h(y)dy - \frac{2(x_T+1)}{x_T^2}e^{2x_T}\int_0^1 \eta^2\phi_{xx}\Big|_{x=x_T}h(y)dy.
\end{aligned}
$$

Letting

$$
\begin{aligned}
B\left(\chi,\phi\right) = &\int_0^{x_T}\int_0^1 \eta^2 \left(e^x \chi_{xx}\right)_x \left(e^x \phi_{xx}\right)_x dydx \qquad (4.10)\\
&+ \int_0^{x_T}\int_0^1 \frac{Re^2}{16A^{12}Z^2}\frac{1+\hat{K}\eta^2}{\eta^4}\chi_y\phi_y dydx\\
&+ \frac{Re^{\frac{3}{2}}}{4A^8 Z}\int_0^{x_T} \frac{\left(1+\hat{K}\eta^2\right)^{\frac{3}{4}}}{\eta^2} e^{\frac{x}{2}} \left(\chi_x\phi_x\Big|_{y=0} + \chi_x\phi_x\Big|_{y=1}\right) dx,
\end{aligned}
$$

and

$$
\begin{aligned}
F\left(\phi\right) = &-\int_0^{x_T}\int_0^1 \phi\bar{S}dydx - \int_0^{x_T}\int_0^1 \phi\bar{H}dydx \qquad (4.11)\\
&- \frac{Re}{32A^{10}Z^2}\int_0^1 \phi\Big|_{x=0}\theta(y)dy + \int_0^{x_T}\left(\phi\Big|_{y=1}G^+(x) - \phi\Big|_{y=0}G^-(x)\right)dx\\
&+ \frac{10\left(1-A^{-2}\right)}{x_T^2}\int_0^1 \phi\Big|_{x=0}h(y)dy - \frac{2(x_T+1)}{x_T^2}e^{2x_T}\int_0^1 \eta^2\phi_{xx}\Big|_{x=x_T}h(y)dy,
\end{aligned}
$$

there exists a function, χ, where, for all ϕ

$$B(\chi, \phi) = F(\phi). \tag{4.12}$$

This is the weak form of (3.57) given by equation (4.9). Based on this definition, there exists a collection of approximate solutions, χ^m, where m is related to the size of an element of the discretized domain. Thus, for all ϕ^m,

$$B(\chi^m, \phi^m) = F(\phi^m), \tag{4.13}$$

and, as m approaches zero, χ^m approaches χ. Equation (4.13) is the formulation of the problem that the finite element model described in the next section of this chapter is designed to approximate. It is important to note that the majority of variables of interest may be obtained by differentiating this master potential, χ. In particular, the streamfunction and axial mass flux are expressed in terms of the master potential as [52]

$$\psi = -2A^2\chi_x, \tag{4.14}$$

and

$$\rho_0 w = -2A^2\psi_x = 4A^4\chi_{xx}. \tag{4.15}$$

4.2 Model Development

The continuous solution to (4.13) may be approached by a combination of approximate solutions at discrete points in the discretized domain. The error in the approximate solution is minimized by simultaneously solving for the coefficients of the entire assembled array of approximations in a standard matrix algebra problem [74][75][76].

The generalized Onsager equation is sixth order in the radial coordinate and second order in the axial coordinate. As shown in the previous section, the weak form of the equation requires three derivatives with respect to the radial coordinate and one derivative with respect to the axial coordinate [77][78]. Rectangular Lagrangian elements are a popular choice for similar finite element models [73][79]. Based on the order of the governing equation, transitional linear-cubic Lagrangian elements are used in the below described model. These elements utilize two-dimensional shape functions composed of the products of one-dimensional cubic and linear shape functions [81][80].

These shape functions are splined functions, or linear combinations of appropriately ordered polynomial basis functions. The cubic splines, or B-splines, are piecewise defined by cubic basis polynomials, while the linear splines, or 'hat' functions, each have a linear basis [82][83]. The elements of the model are constructed by dividing the computational domain into M sub-intervals in the radial direction, depicted in the dimensionless scale heights variable x, and N sub-intervals in the axial direction, depicted in the dimensionless variable y, such that

$$0 = x_0 < x_1 < x_2 < \cdots < x_M = x_T,$$

and

$$0 = y_0 < y_1 < y_2 < \cdots < y_N = 1.$$

The cubic B-splines for the constrained domain can then be given by

$$l(x) = \sum_{i=-1}^{M-1} c_i^{(l)} l_i(x), \tag{4.16}$$

and the linear 'hat' functions by

$$s(y) = \sum_{j=0}^{N+1} c_j^{(s)} s_j(y), \tag{4.17}$$

where i and j correspond to a discrete position in the domain in the radial and axial direction, respectively. The two-dimensional shape functions can then be described by the product of these splines as

$$\phi_k(x, y) = \sum_{i=1}^{M-1} \sum_{j=0}^{N} c_k s_i(x) l_j(y), \tag{4.18}$$

where $k = (N + 1)(i - 1) + (j + 1)$ and the total number of degrees of freedom for the constrained problem is $K = (M - 1)(N + 1)$.

With respect to a general coordinate ξ, shape functions of *nth* order from the 'Lagrange' family are given [73]

$$l_k^n = \frac{(\xi - \xi_0)(\xi - \xi_1)...(\xi - \xi_{k-1})(\xi - \xi_{k+1})...(\xi - \xi_n)}{(\xi_k - \xi_0)(\xi_k - \xi_1)...(\xi_k - \xi_{k-1})(\xi_k - \xi_{k+1})...(\xi_k - \xi_n)}.$$

Linear shape functions written in terms of a general coordinate η are

$$\begin{aligned} l_1^1 &= \frac{\eta - \eta_2}{\eta_1 - \eta_2} \\ l_2^1 &= \frac{\eta - \eta_1}{\eta_2 - \eta_1}. \end{aligned}$$

Letting $\eta_1 = -1$ and $\eta_2 = 1$, these shape functions can be written

$$\begin{aligned} l_1^1 &= \frac{1}{2}(1 - \eta) \\ l_2^1 &= \frac{1}{2}(1 + \eta). \end{aligned}$$

Similarly, cubic shape functions in the general coordinate ξ are

$$
\begin{aligned}
l_1^3 &= \frac{(\xi-\xi_2)(\xi-\xi_3)(\xi-\xi_4)}{(\xi_1-\xi_2)(\xi_1-\xi_3)(\xi_1-\xi_4)} \\
l_2^3 &= \frac{(\xi-\xi_1)(\xi-\xi_3)(\xi-\xi_4)}{(\xi_2-\xi_1)(\xi_2-\xi_3)(\xi_2-\xi_4)} \\
l_3^3 &= \frac{(\xi-\xi_1)(\xi-\xi_2)(\xi-\xi_4)}{(\xi_3-\xi_1)(\xi_3-\xi_2)(\xi_3-\xi_4)} \\
l_4^3 &= \frac{(\xi-\xi_1)(\xi-\xi_2)(\xi-\xi_3)}{(\xi_4-\xi_1)(\xi_4-\xi_2)(\xi_4-\xi_3)}.
\end{aligned}
$$

Letting $\xi_1 = -1$, $\xi_2 = -1/3$, $\xi_3 = 1/3$, and $\xi_4 = 1$, the cubic shape functions can be written

$$
\begin{aligned}
l_1^3 &= -\frac{48}{27}(\xi+\frac{1}{3})(\xi-\frac{1}{3})(\xi-1) \\
l_2^3 &= \frac{16}{27}(\xi+1)(\xi-\frac{1}{3})(\xi-1) \\
l_3^3 &= -\frac{16}{27}(\xi+1)(\xi+\frac{1}{3})(\xi-1) \\
l_4^3 &= \frac{48}{27}(\xi+1)(\xi+\frac{1}{3})(\xi-\frac{1}{3}),
\end{aligned}
$$

which simplify to

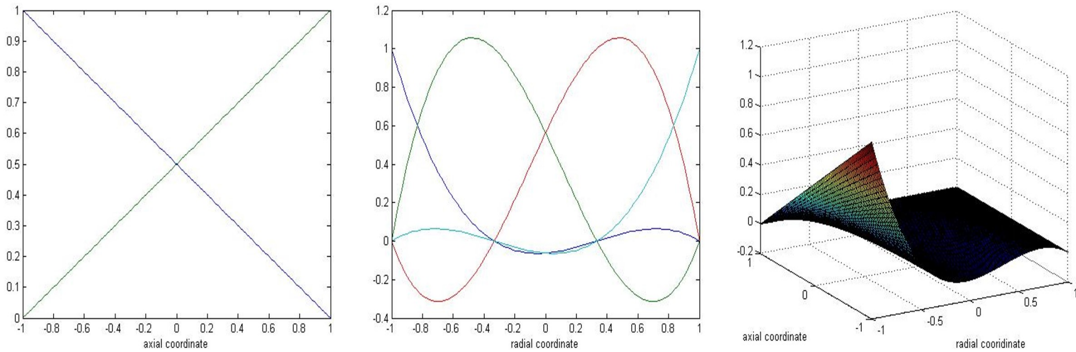

Figure 2: The Lagrange linear-cubic rectangular transitional element (right) is formed by the product of cubic basis functions (center) and linear 'hat' functions (left).

$$\begin{aligned}
l_1^3 &= -\frac{48}{27}(\xi^3 - \xi^2 - \frac{1}{9}\xi + \frac{1}{9}) \\
l_2^3 &= \frac{16}{27}(\xi^3 - \frac{1}{3}\xi^2 - \xi + \frac{1}{3}) \\
l_3^3 &= -\frac{16}{27}(\xi^3 + \frac{1}{3}\xi^2 - \xi - \frac{1}{3}) \\
l_4^3 &= \frac{48}{27}(\xi^3 + \xi^2 - \frac{1}{9}\xi - \frac{1}{9}).
\end{aligned}$$

Figure 2 depicts the construction of the linear hat functions, the cubic splines, and the linear-cubic transitional elements. The two dimensional shape functions that form the Lagrange cubic-linear rectangular elements are products of the 1D shape functions where

$$N_k = N_{ij} = l_i^n l_j^m.$$

In the general coordinate system (ξ, η), the complete set of basis functions can now be written

$$
\begin{aligned}
N_1 &= -\frac{48}{54}(\xi^3 - \xi^2 - \frac{1}{9}\xi + \frac{1}{9})(1-\eta) \\
N_2 &= \frac{16}{54}(\xi^3 - \frac{1}{3}\xi^2 - \xi + \frac{1}{3})(1-\eta) \\
N_3 &= -\frac{16}{54}(\xi^3 + \frac{1}{3}\xi^2 - \xi - \frac{1}{3})(1-\eta) \\
N_4 &= \frac{48}{54}(\xi^3 + \xi^2 - \frac{1}{9}\xi - \frac{1}{9})(1-\eta) \\
N_5 &= -\frac{48}{54}(\xi^3 - \xi^2 - \frac{1}{9}\xi + \frac{1}{9})(1+\eta) \\
N_6 &= \frac{16}{54}(\xi^3 - \frac{1}{3}\xi^2 - \xi + \frac{1}{3})(1+\eta) \\
N_7 &= -\frac{16}{54}(\xi^3 + \frac{1}{3}\xi^2 - \xi - \frac{1}{3})(1+\eta) \\
N_8 &= \frac{48}{54}(\xi^3 + \xi^2 - \frac{1}{9}\xi - \frac{1}{9})(1+\eta).
\end{aligned}
$$

The Galerkin form of the Onsager requires three continuous derivatives in the radial direction and one continuous derivative in the axial direction. The first derivatives with respect to ξ are

$$
\begin{aligned}
\partial N_1/\partial\xi &= -\frac{48}{54}(1-\eta)(3\xi^2-2\xi-\frac{1}{9}) \\
\partial N_2/\partial\xi &= \frac{16}{54}(1-\eta)(3\xi^2-\frac{2}{3}\xi-1) \\
\partial N_3/\partial\xi &= -\frac{16}{54}(1-\eta)(3\xi^2+\frac{2}{3}\xi-1) \\
\partial N_4/\partial\xi &= \frac{48}{54}(1-\eta)(3\xi^2+2\xi-\frac{1}{9}) \\
\partial N_5/\partial\xi &= -\frac{48}{54}(1+\eta)(3\xi^2-2\xi-\frac{1}{9}) \\
\partial N_6/\partial\xi &= \frac{16}{54}(1+\eta)(3\xi^2-\frac{2}{3}\xi-1) \\
\partial N_7/\partial\xi &= -\frac{16}{54}(1+\eta)(3\xi^2+\frac{2}{3}\xi-1) \\
\partial N_8/\partial\xi &= \frac{48}{54}(1+\eta)(3\xi^2+2\xi-\frac{1}{9})
\end{aligned}
$$

and the first derivatives with respect to η are

$$
\begin{aligned}
\partial N_1/\partial\eta &= \frac{48}{54}(\xi^3-\xi^2-\frac{1}{9}\xi-\frac{1}{9}) \\
\partial N_2/\partial\eta &= -\frac{16}{54}(\xi^3-\frac{1}{3}\xi^2-\xi+\frac{1}{3}) \\
\partial N_3/\partial\eta &= \frac{16}{54}(\xi^3+\frac{1}{3}\xi^2-\xi-\frac{1}{3}) \\
\partial N_4/\partial\eta &= -\frac{48}{54}(\xi^3+\xi^2-\frac{1}{9}\xi-\frac{1}{9}) \\
\partial N_5/\partial\eta &= -\frac{48}{54}(\xi^3-\xi^2-\frac{1}{9}\xi+\frac{1}{9}) \\
\partial N_6/\partial\eta &= \frac{16}{54}(\xi^3-\frac{1}{3}\xi^2-\xi+\frac{1}{3}) \\
\partial N_7/\partial\eta &= -\frac{16}{54}(\xi^3+\frac{1}{3}\xi^2-\xi-\frac{1}{3}) \\
\partial N_8/\partial\eta &= \frac{48}{54}(\xi^3+\xi^2-\frac{1}{9}\xi-\frac{1}{9}).
\end{aligned}
$$

The second derivatives with respect to ξ are

$$
\begin{aligned}
\partial^2 N_1/\partial\xi^2 &= -\frac{48}{54}(1-\eta)(6\xi-2) \\
\partial^2 N_2/\partial\xi^2 &= \frac{16}{54}(1-\eta)(6\xi-\frac{2}{3}) \\
\partial^2 N_3/\partial\xi^2 &= -\frac{16}{54}(1-\eta)(6\xi+\frac{2}{3}) \\
\partial^2 N_4/\partial\xi^2 &= \frac{48}{54}(1-\eta)(6\xi+2) \\
\partial^2 N_5/\partial\xi^2 &= -\frac{48}{54}(1+\eta)(6\xi-2) \\
\partial^2 N_6/\partial\xi^2 &= \frac{16}{54}(1+\eta)(6\xi-\frac{2}{3}) \\
\partial^2 N_7/\partial\xi^2 &= -\frac{16}{54}(1+\eta)(6\xi+\frac{2}{3}) \\
\partial^2 N_8/\partial\xi^2 &= \frac{48}{54}(1+\eta)(6\xi+2)
\end{aligned}
$$

and the third derivatives with respect to ξ are

$$\begin{aligned}
\partial^3 N_1/\partial\xi^3 &= -\frac{48}{9}(1-\eta) \\
\partial^3 N_2/\partial\xi^3 &= \frac{16}{9}(1-\eta) \\
\partial^3 N_3/\partial\xi^3 &= -\frac{16}{9}(1-\eta) \\
\partial^3 N_4/\partial\xi^3 &= \frac{48}{9}(1-\eta) \\
\partial^3 N_5/\partial\xi^3 &= -\frac{48}{9}(1+\eta) \\
\partial^3 N_6/\partial\xi^3 &= \frac{16}{9}(1+\eta) \\
\partial^3 N_7/\partial\xi^3 &= -\frac{16}{9}(1+\eta) \\
\partial^3 N_8/\partial\xi^3 &= \frac{48}{9}(1+\eta).
\end{aligned}$$

Returning to the weak formulation, these 2-D basis functions are used to approximate the master potential, χ, and the test function, ϕ, as

$$\chi(x,y) \approx \sum_{k=1}^{K} a_k N_k(x,y), \tag{4.19}$$

and

$$\phi(x,y) \approx \sum_{h=1}^{K} b_h N_k(x,y), \tag{4.20}$$

where like k, $h = 1, 2, 3, \ldots, K$. Equation (4.13) can then be written

$$B\left(\sum_{k=1}^{K} a_k N_k(x,y), \sum_{k=1}^{K} b_k N_k(x,y)\right) = F\left(\sum_{k=1}^{K} b_k N_k(x,y)\right), \tag{4.21}$$

which after pulling out the coefficients and algebraic manipulation, becomes

$$\sum_{h=1}^{K} b_h \sum_{k=1}^{K} a_k B(N_k, N_h) = \sum_{h=1}^{K} b_h F(N_h). \tag{4.22}$$

Therefore, for each h there are

$$\sum_{k=1}^{K} a_k B(N_k, N_h) = F(N_h), \tag{4.23}$$

which are easily represented by the standard matrix equation

$$\mathbf{A}\bar{x} = \bar{b}. \tag{4.24}$$

Here $\mathbf{A}$ is the k x h matrix

$$\mathbf{A} = B(N_k, N_h), \tag{4.25}$$

$\bar{x}$ is the k element vector

$$\bar{x} = a_k, \tag{4.26}$$

and $\bar{b}$ is the h element vector

$$\bar{b} = F(N_h). \tag{4.27}$$

Following Witt in [64], equations (4.10) and (4.11) can be broken into separate integral equations and labeled as

$$I_1 = \int_0^{x_T} \int_0^1 \eta^2 \left(e^x \chi_{xx}\right)_x \left(e^x \phi_{xx}\right)_x dydx \tag{4.28}$$

$$I_2 = \int_0^{x_T} \int_0^1 \frac{Re^2}{16A^{12}Z^2} \frac{1 + \hat{K}\eta^2}{\eta^4} \chi_y \phi_y dydx \tag{4.29}$$

$$I_3 = \frac{Re^{\frac{3}{2}}}{4A^8 Z} \int_0^{x_T} \frac{\left(1+\hat{K}\eta^2\right)^{\frac{3}{4}}}{\eta^2} e^{\frac{x}{2}} \left(\chi_x \phi_x \Big|_{y=0} + \chi_x \phi_x \Big|_{y=1} \right) dx \tag{4.30}$$

$$I_4 = -\int_0^{x_T} \int_0^1 \phi \bar{S} dy dx \tag{4.31}$$

$$I_5 = -\int_0^{x_T} \int_0^1 \phi \bar{H} dy dx \tag{4.32}$$

$$I_6 = -\frac{Re}{32A^{10}Z^2} \int_0^1 \phi \Big|_{x=0} \theta(y) dy \tag{4.33}$$

$$I_7 = \int_0^{x_T} \left(\phi \Big|_{y=1} G^+(x) - \phi \Big|_{y=0} G^-(x) \right) dx \tag{4.34}$$

$$I_8 = \frac{10\left(1-A^{-2}\right)}{x_T^2} \int_0^1 \phi \Big|_{x=0} h(y) dy - \frac{2(x_T+1)}{x_T^2} e^{2x_T} \int_0^1 \eta^2 \phi_{xx} \Big|_{x=x_T} h(y) dy \tag{4.35}$$

Once again, equation (4.23) can be written as the simple matrix equation

$$\mathbf{A}\bar{x} = \bar{b} \tag{4.36}$$

where

$$\mathbf{A} = I_1 + I_2 + I_3, \tag{4.37}$$

$$\bar{b} = I_4 + I_5 + I_6 + I_7 + I_8, \tag{4.38}$$

and $\bar{x}$ represents the vector of coefficients of the spline functions that form the approximation of the solution. Each of these integrals is computed using a standard Gaussian quadrature routine given as

$$\int_{-1}^1 f(x)dx = \sum_{i-1}^{n} w_i f(x_i), \tag{4.39}$$

where n is the number of nodes and w_i, where $i = 1 \ldots n$, are weighting factors.

Gaussian quadrature has been shown to solve exactly polynomials of order $2n - 1$ or less. Therefore, letting $n = 2$ and using the weighting factors $-1/\sqrt{3}$ and $1/\sqrt{3}$, cubic polynomials may be integrated exactly. Figure 3 depicts the intended flow of the computational algorithm. Written in Matlab, the *CurvSOL* code builds the coefficient matrix and force vector and then utilizes built-in algorithms to solve the matrix equation, equation (4.24). Depending on the character of the coefficient matrix, the built-in routine chooses the most appropriate from a number of different solving techniques, including QR decomposition, a triangular solver, a permuted triangular solver, LDL decomposition, LU decomposition, a Hessenberg or Cholesky solver, a diagonal solver, or a banded solver.

4.3 Simulation Results

The sensitive and proprietary nature of specific machine designs effectively stifled information sharing in the early years of centrifuge development. To promote collaborative effort and stimulate innovation within the centrifuge separation community, the completely hypothetical Rome and Iguaçu machine designs are detailed in the literature and have been circulated at biannual gatherings of the International Workshop on Separation Phenomena in Liquids and Gases (SPLG). The *Pancake* code developed by Wood and based on the linearization technique of Onsager is generally considered the standard for comparison of internal flow simulations for countercurrent centrifuges [52][64][84]. The finite element code described previously in this chapter employing the pancake approximation is first compared to the results of the *Pancake* code. The flow solutions obtained with and without application of the pancake approximation are compared to determine the effect of rotor curvature and rotor speed on the internal flow.

A number of different mechanisms drive the countercurrent flow in a gas centrifuge. Three drive mechanisms are modeled in this effort: feed drive, wall temperature gradi-

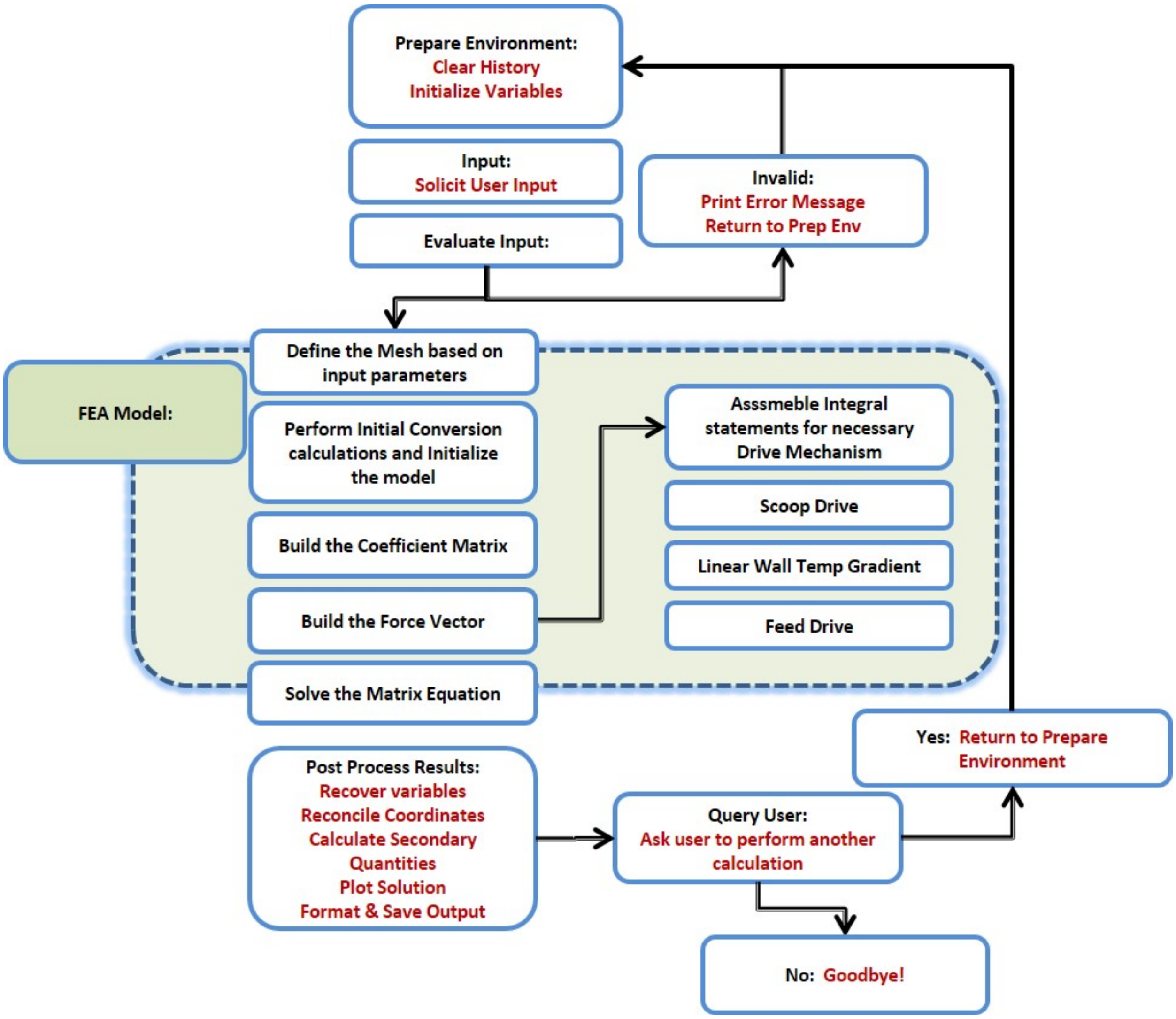

Figure 3: Finite Element model architecture. The user defines the computational mesh, the operating parameters for the centrifuge, and the counter-current drive mechanisms. After performing unit conversions, base calculations and variable initialization, the coefficient matrix and force vector are assembled. The code uses Lagrangian cubic-linear transitional elements and two point Gaussian quadrature. The code then solves the matrix equation using the Matlab matrix inversion built-in routine. The results are then processed and output as results files or graphs, based on user preference.

ent drive, and scoop drive. Applying the principle of superposition, the contributions of each mechanism are summed to generate the approximation of the total countercurrent flow [11]. Using the parameters of the Iguaçu and Rome machines described in Table 1 and a 35 x 25 element mesh, the flow field for each machine was modeled with wall speeds of 500 m/s, 600 m/s, and 700 m/s and compared to the optimized solutions generated by the *Pancake* code [52][64]. A mesh sensitivity was conducted using meshes on the order of 10^3, 10^4, and 10^5 elements. The values obtained at designated key points did not vary significantly between the sampled meshes, though the computing time increased to an unwieldy 8 hours for the finest mesh. Therefore the coarsest mesh was selected.

Table 1: Parameters for each of the machine designs simulated

Parameter	units	Iguaçu	Rome
Height	[cm]	48	500
Radius	[cm]	6	25
Temperature	[K]	300	320
Wall Pressure	[torr]	60	100
Scoop Drag	[dynes]	1000	1000
Radial Scoop Position	[r/a]	0.75	0.75
Axial Scoop Position	[z/L]	0.001	0.001
Axial Feed Region	[cm]	2	20
Axial Feed Point	[z/L]	0.5	0.5

Figures 4 and 5 depict continuous surface plots of the axial mass flux in the Rome and Iguaçu centrifuges simulated with a 700 m/s and 500 m/s wall speed, respectively. These figures offer comparison of the sum of the contributions of each drive mechanism to the total axial mass flux over the entire cross section of the computational domain. These plots demonstrate the complexity of the internal flow, with each presenting key features of the mass flux, including the axial ridge and associated valley along the wall resulting from the wall temperature gradient driven countercurrent flow, the vortex from the mechanical drive generated by the scoop at the bottom end cap, and the effects emanating from the central region towards axis resulting from inclusion of the feed [93]. The figures show the results from both the *CurvSOL* with the pancake approximation and *Pancake* codes. Initial inspection of the shape of each surface suggests excellent agreement between *CurvSOL* and *Pancake*, however, subtle differences are difficult to ascertain at the scale and orientation depicted.

While the plots of the axial mass flux generated by the two codes display similarities in many features including the region around the scoop and along the rotor wall, a comprehensive assessment of the total agreement remains difficult to determine. Comparison of the ratio, m, of the stage upflow and the total upflow provides another effective method of solution comparison [11]. Letting

$$m = \frac{L}{L_0}, \tag{4.40}$$

the stage upflow is given as

$$L_0 = a\rho D \left[2 \int_0^a (\psi/L)^2 \frac{dr}{r} \right]^{-\frac{1}{2}}, \tag{4.41}$$

where the total upflow is

$$L = \frac{1}{2} \int_0^a |\rho V_z| \, 2\pi r dr. \tag{4.42}$$

The flow profile efficiency, as given by

$$\epsilon_f = \frac{4 \left[\int_0^a (\psi/L)\, a^{-2} r dr \right]^2}{\int_0^a (\psi/L)^2 \frac{dr}{r}}, \tag{4.43}$$

provides another tool for comparison. The flow profile efficiency and the upflow ratio, m, together provide an effective picture of model approximation comparison with the accepted standard model solution.

Figures 6 through 17 show the m values and flow profile efficiency for each drive mechanism for the Rome and Iguaçu machines modeled at 700 m/s and 500 m/s wall speeds, respectively, including comparison of results from both the *Pancake* and *CurvSOL* codes with the pancake approximation. All cases display excellent agreement between the results of both codes for the rotor wall temperature gradient and scoop drive mechanisms. Once again, the results for the feed drive match in trend and character, but offer overall poor agreement, suggesting a misapplication of the feed parameters or an error in interpretation during code development.

As described in equation (4.14), the streamfunction, ψ, is easily extracted from the solution for the potential. Figures 18 through 25 show the comparison of the streamfunction for each drive and the sum of all drives. Again, excellent agreement is displayed for the linear wall temperature and scoop drive mechanisms. While the feed drive curves do not match exactly, the general shape of each curve matches with prominent features and similar magnitude. Figures 21 and 25 depict the streamfunction for the sum of all three drive mechanisms for the Rome and Iguaçu machines. Comparison of these figures with the individual drive mechanism streamfunction functions suggests that the impact of the feed drive is minimal in comparison to the influence of the scoop drive.

Considering the agreement between the two models incorporating the pancake approximation, the results from *CurvSOL* incorporating the curvature of the rotor are compared to the those with the pancake approximation. Figures 26 through 28 describe two dimensional representations of the axial mass flux taken at the quarter-plane of the Rome machine with a simulated wall speed of 500 m/s, 600 m/s, and 700 m/s. The linear temperature gradient, feed, and scoop drive mechanisms as well as the sum of drives are shown in comparisons of the solutions from the *CurvSOL* code with the pancake approximation and *CurvSOL* considering the curvature of the rotor. Close agreement is shown between the solutions from the two cases in each graph, once again with the excursion in the feed drive mechanism plot in Figure 27. The scoop drive plots depicted in Figure 28 suggest the effects of the curvature of the rotor become more pronounced as the wall speed slows.

Similarly, Figures 29 through 31 depict the results the Iguaçu cascade run with a simulated wall speed of 500 m/s, 600 m/s, and 700 m/s. Inspection of the *CurvSOL* solutions with and without the pancake approximation for the Iguaçu machine leads to similar results as those for the Rome machine: close agreement is found between the solutions from both codes for the linear wall temperature gradient and scoop drives. However, for the feed drive solutions, the character and shape of the curves is similar but they differ at points by as much as 20% of the maximum feature magnitude. The results in Figures 28 and 31 suggest the radius of each machine as listed in Table 1 also plays a significant role in the effect of curvature on the flow. The smaller radius of the Iguaçu contributes to the difference in the *CurvSOL* solutions at all wall speeds, while the effect of the curvature seems to increase as the speed decreases for the larger Rome machine.

A complete catalog of simulation results for both the Rome and Iguaçu machine models run at all three wall speeds is included in Appendix A. Comparison of the axial mass flux, streamfunction, upflow ratio, and flow profile efficiency for each of three drive mechanisms tends to show that the Iguaçu results agree best at lower wall speeds while the Rome results have excellent agreement at the higher speed. As previously mentioned, the best agreement of code solutions with the pancake approximation is shown between the wall temperature gradient and scoop drive mechanism results, and the feed drive results maintain the same general shape and character with excursions in magnitude. In the next two chapters, comparisons of *CurvSOL* results with and without the pancake approximation continue as these flow solutions are used to model the diffusion equation governing the isotope transport.

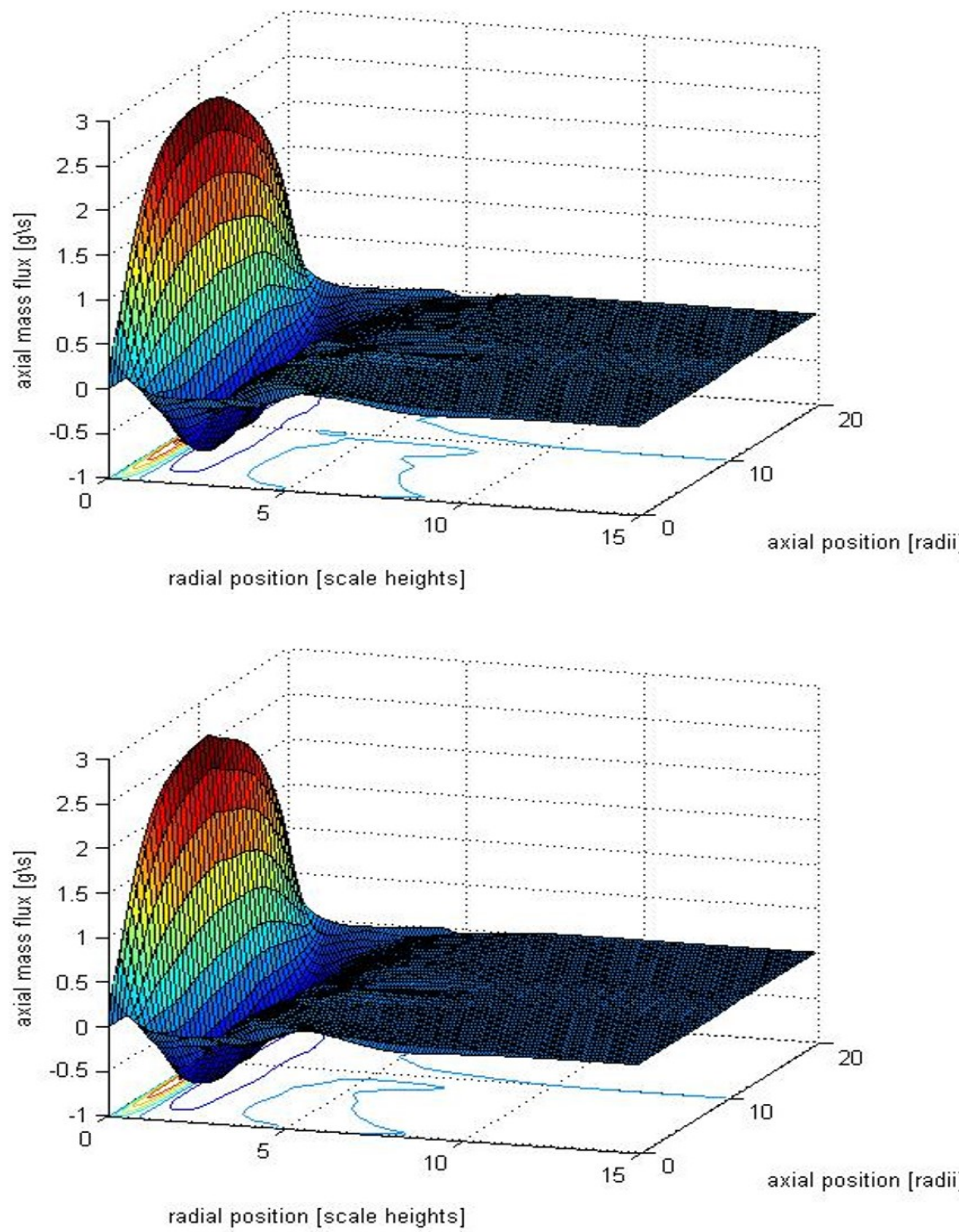

Figure 4: Axial Mass Flux presented as a continuous surface plot of the cross-section of the Rome centrifuge simulated with a wall speed of 700 m/s. The results from the *CurvSOL* code with the pancake approximation are shown (top) as well as those from the *Pancake* Code (bottom).

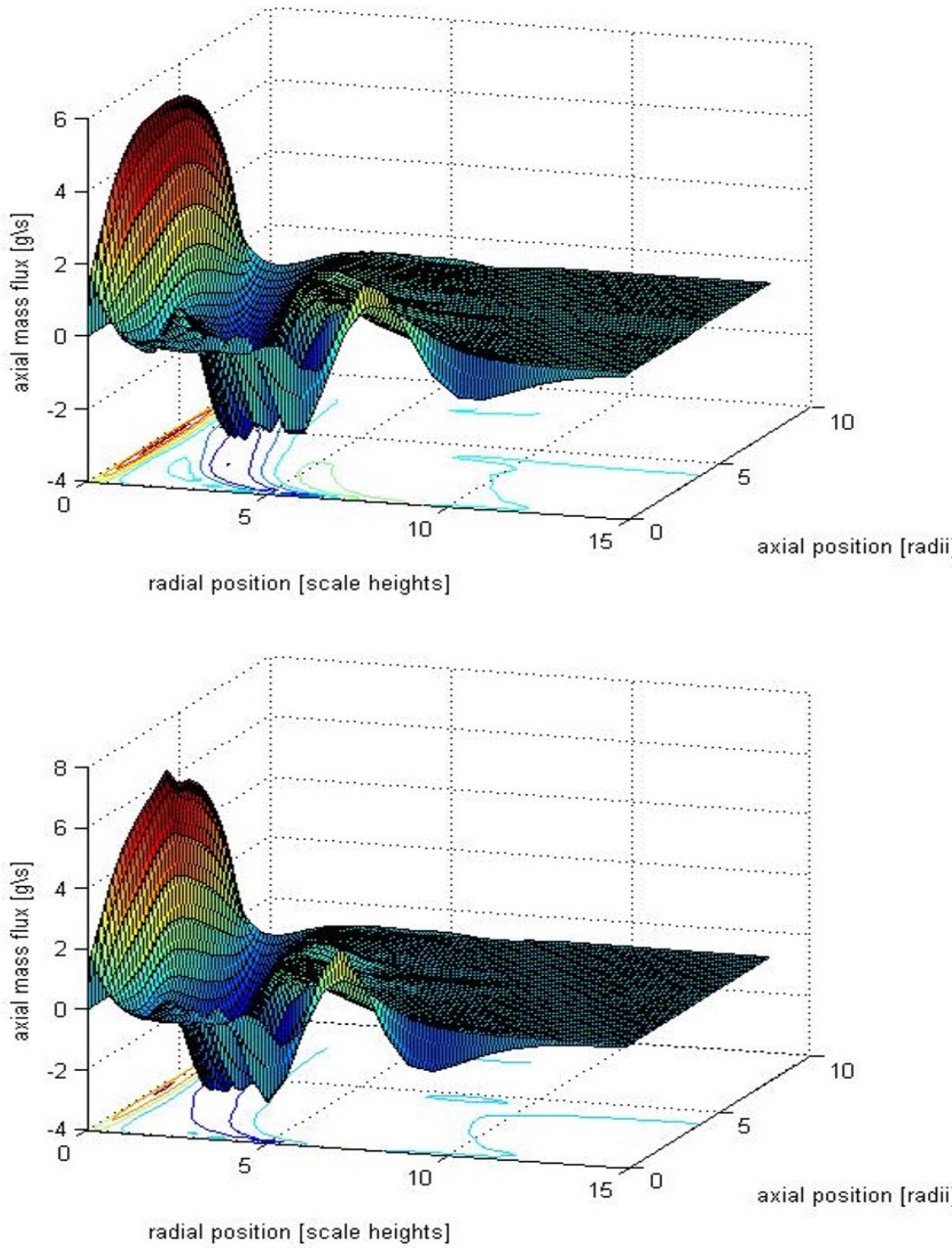

Figure 5: Axial Mass Flux presented as a continuous surface plot of the cross-section of the Iguaçu centrifuge simulated with a wall speed of 500 m/s. The results from the *CurvSOL* code with the pancake approximation are shown (top) as well as those from the *Pancake* Code (bottom).

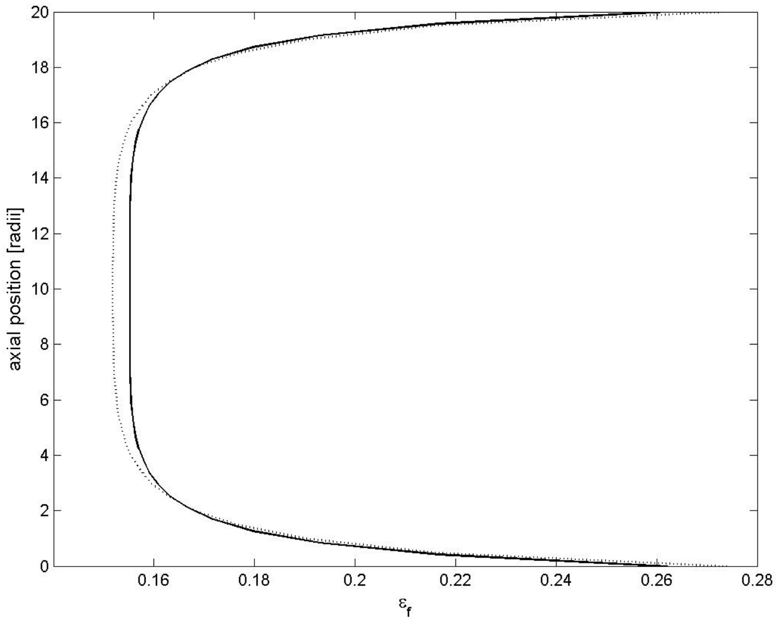

Figure 6: The flow profile efficiency is plotted for the Rome machine with a wall speed of 700 m/s and the countercurrent flow created by a linear wall temperature gradient. The results from the *Pancake* code are shown by the dashed line and the those from the *CurvSOL* code with the pancake approximation are represented by the dotted line.

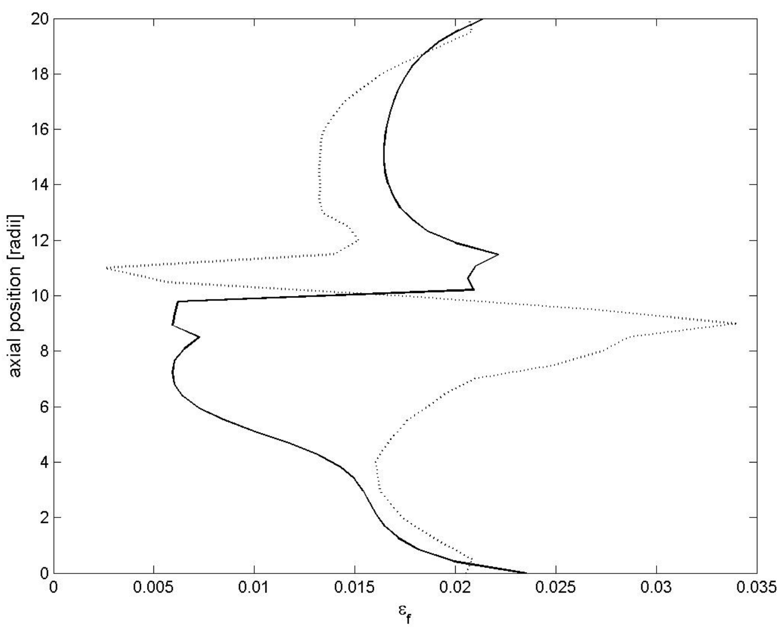

Figure 7: The flow profile efficiency is plotted for the Rome machine with a wall speed of 700 m/s and the countercurrent flow created by a feed source. The results from the *Pancake* code are shown by the dashed line and the those from the *CurvSOL* code with the pancake approximation are represented by the dotted line.

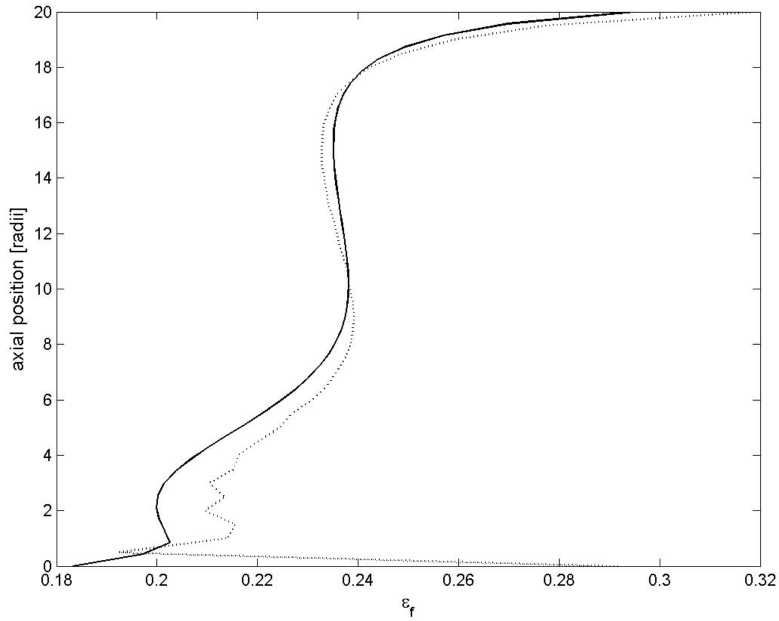

Figure 8: The flow profile efficiency is plotted for the Rome machine with a wall speed of 700 m/s and the countercurrent flow created by a scoop inserted into the flow field. The results from the *Pancake* code are shown by the dashed line and the those from the *CurvSOL* code with the pancake approximation are represented by the dotted line.

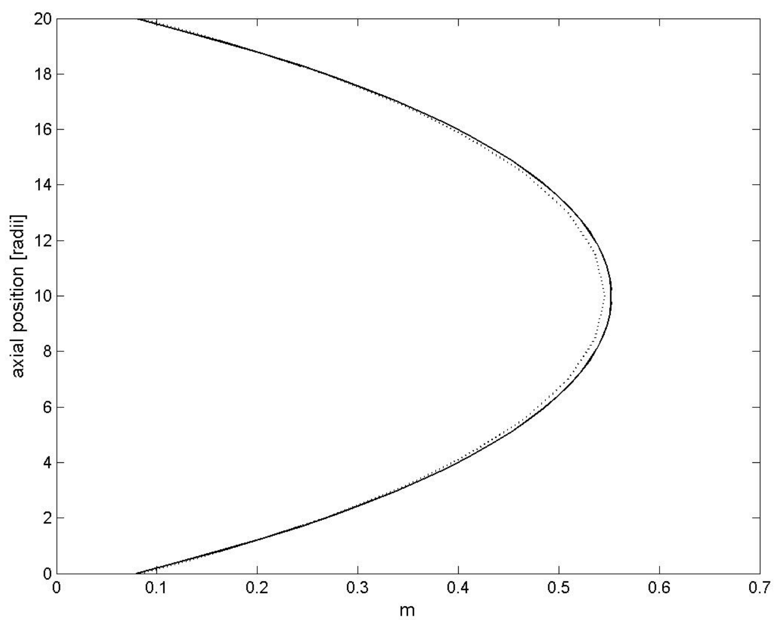

Figure 9: Cohen's 'm' ratio. The ratio of the upflow and total upflow is plotted for the Rome machine with a wall speed of 700 m/s and the countercurrent flow created by a linear wall temperature gradient. The results from the *Pancake* code are shown by the dashed line and the those from the *CurvSOL* code with the pancake approximation are represented by the dotted line.

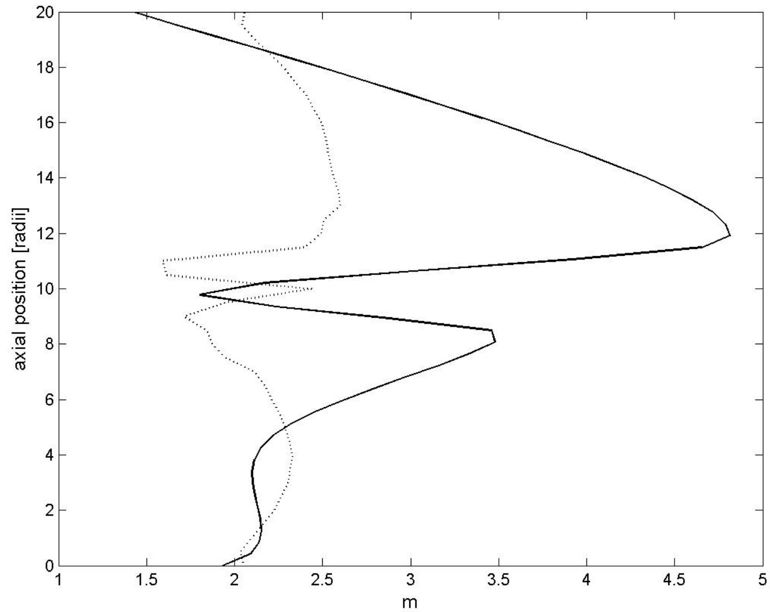

Figure 10: Cohen's 'm' ratio. The ratio of the upflow and total upflow is plotted for the Rome machine with a wall speed of 700 m/s and the countercurrent flow created by a feed drive. The results from the *Pancake* code are shown by the dashed line and the those from the *CurvSOL* code with the pancake approximation are represented by the dotted line.

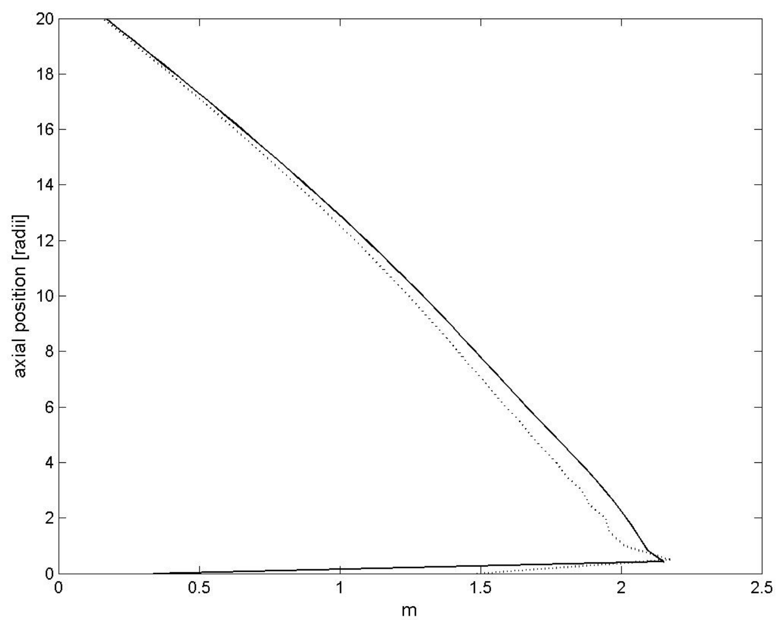

Figure 11: Cohen's 'm' ratio. The ratio of the upflow and total upflow is plotted for the Rome machine with a wall speed of 700 m/s and the countercurrent flow created by a scoop inserted into the flow field. The results from the *Pancake* code are shown by the dashed line and the those from the *CurvSOL* code with the pancake approximation are represented by the dotted line.

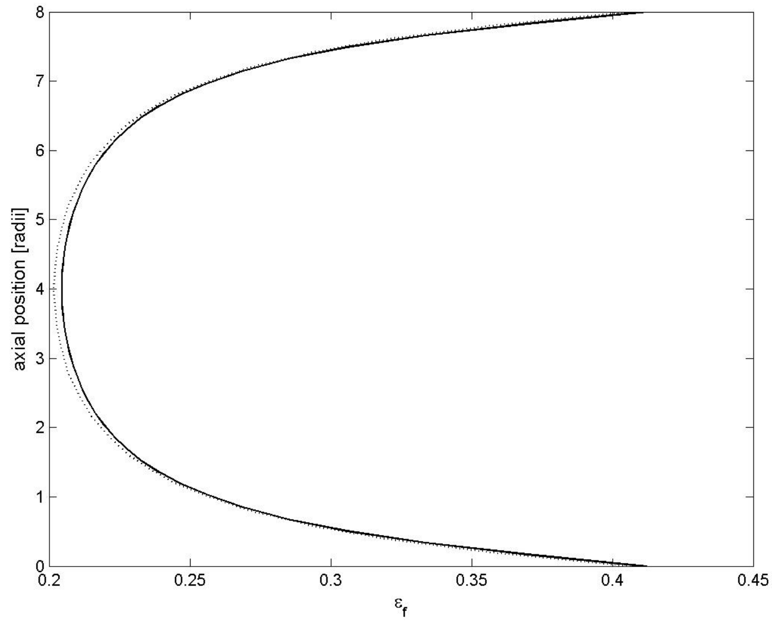

Figure 12: The flow profile efficiency is plotted for the Iguaçu machine with a wall speed of 500 m/s and the countercurrent flow created by a linear wall temperature gradient. The results from the *Pancake* code are shown by the dashed line and the those from the *CurvSOL* code with the pancake approximation are represented by the dotted line.

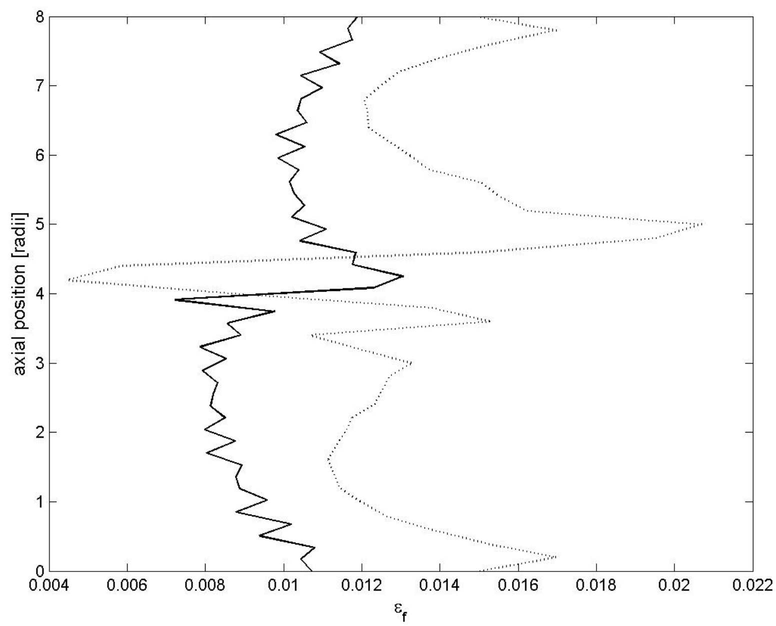

Figure 13: The flow profile efficiency is plotted for the Iguaçu machine with a wall speed of 500 m/s and the countercurrent flow created by a feed drive. The results from the *Pancake* code are shown by the dashed line and the those from the *CurvSOL* code with the pancake approximation are represented by the dotted line.

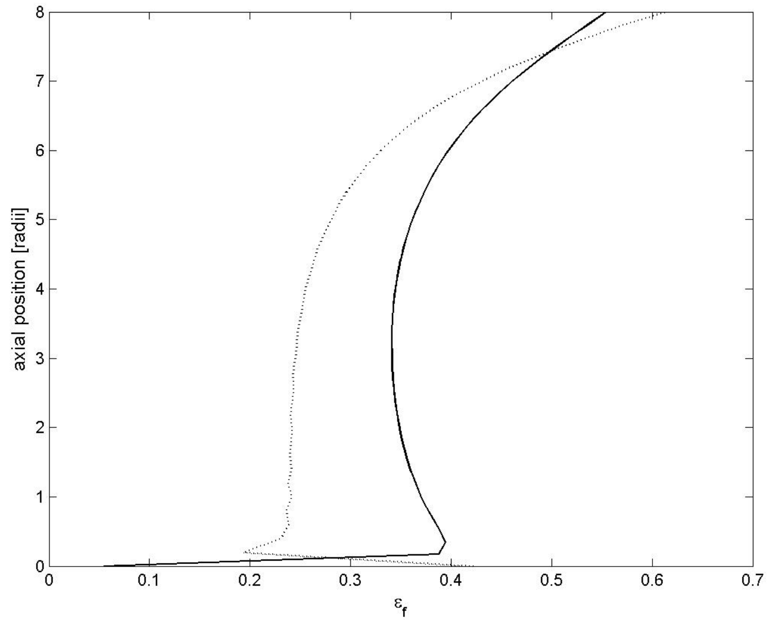

Figure 14: The flow profile efficiency is plotted for the Iguaçu machine with a wall speed of 500 m/s and the countercurrent flow created by a scoop inserted into the flow field. The results from the *Pancake* code are shown by the dashed line and the those from the *CurvSOL* code with the pancake approximation are represented by the dotted line.

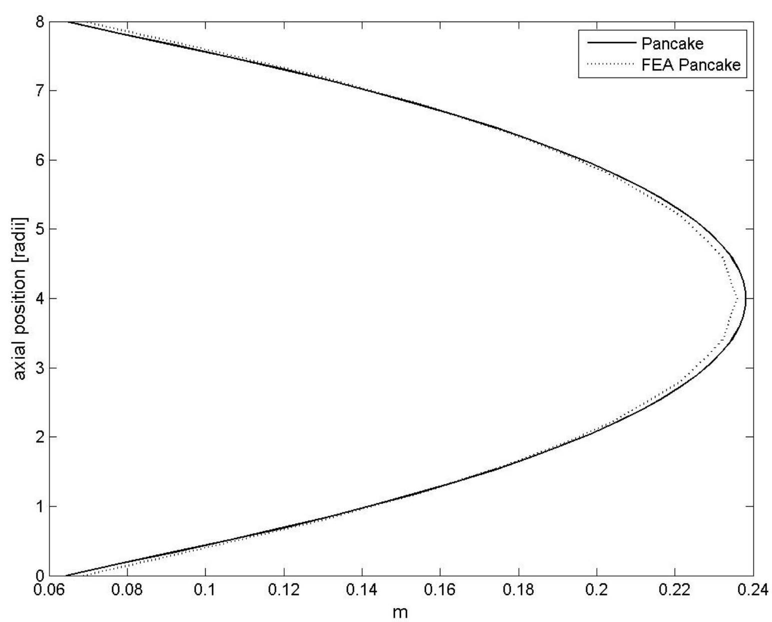

Figure 15: Cohen's 'm' ratio. The ratio of the upflow and total upflow is plotted for the Iguaçu machine with a wall speed of 500 m/s and the countercurrent flow created by a linear wall temperature gradient. The results from the *Pancake* code are shown by the dashed line and the those from the *CurvSOL* code with the pancake approximation are represented by the dotted line.

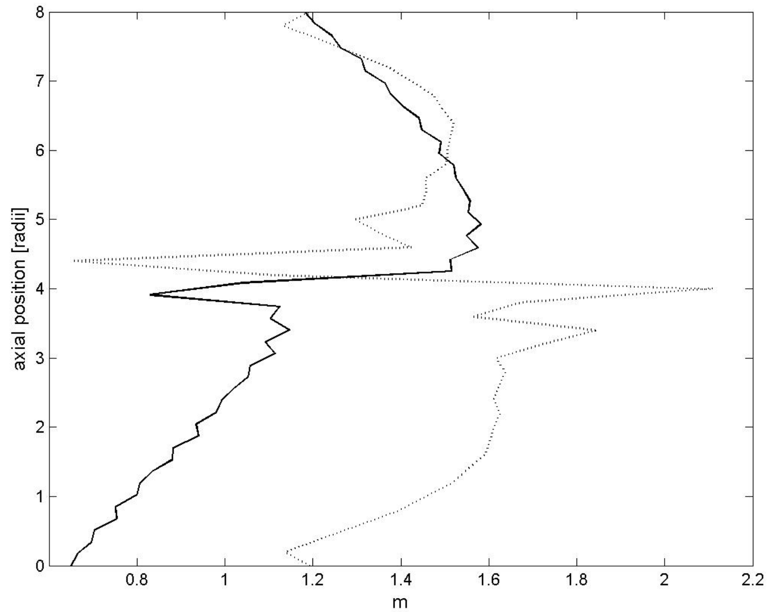

Figure 16: Cohen's 'm' ratio. The ratio of the upflow and total upflow is plotted for the Iguaçu machine with a wall speed of 500 m/s and the countercurrent flow created by a feed drive. The results from the *Pancake* code are shown by the dashed line and the those from the *CurvSOL* code with the pancake approximation are represented by the dotted line.

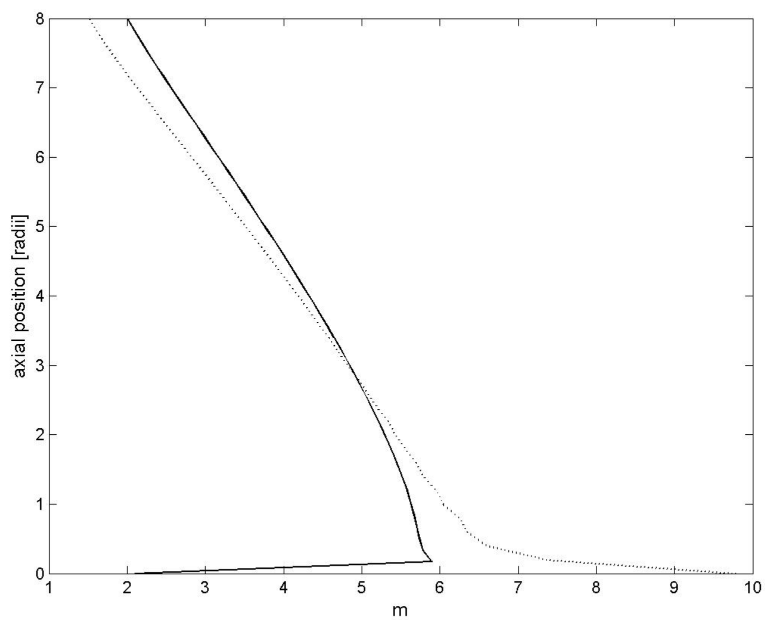

Figure 17: Cohen's 'm' ratio. The ratio of the upflow and total upflow is plotted for the Iguaçu machine with a wall speed of 500 m/s and the countercurrent flow created by a scoop inserted into the flow field. The results from the *Pancake* code are shown by the dashed line and the those from the *CurvSOL* code with the pancake approximation are represented by the dotted line.

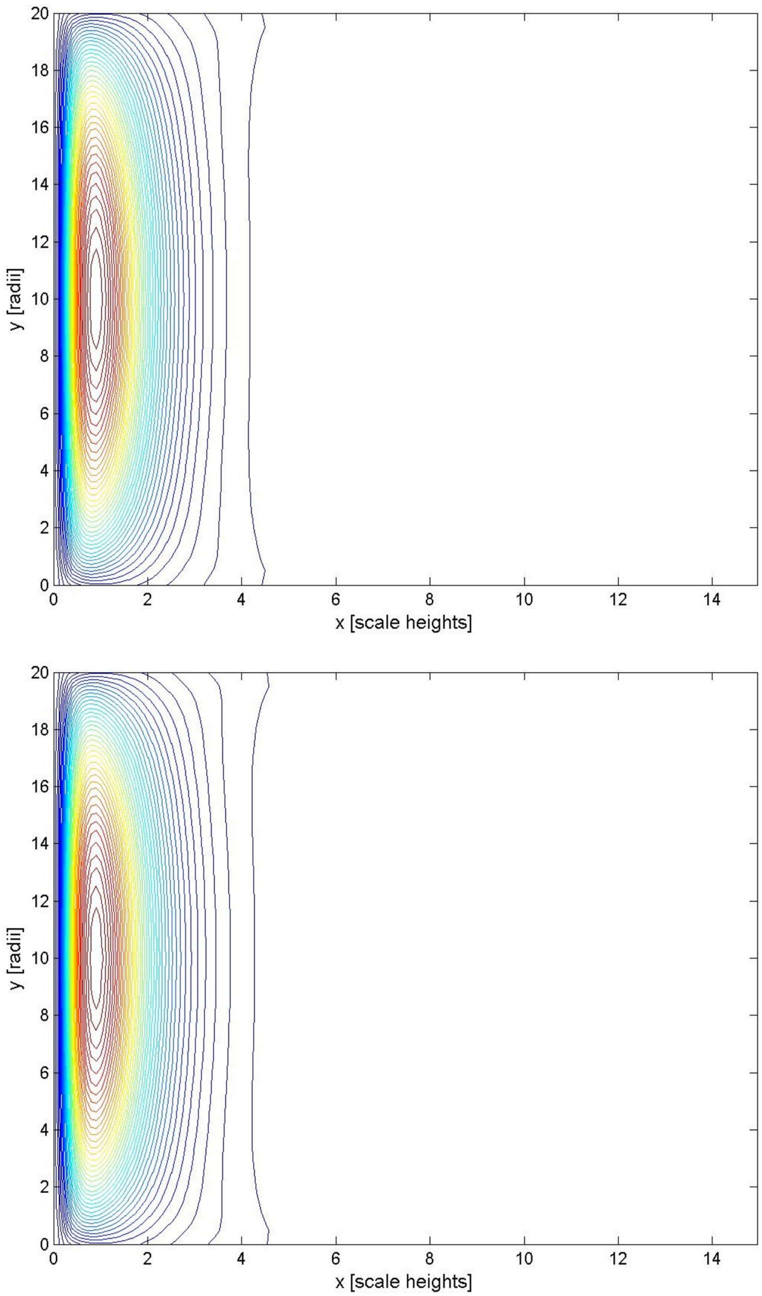

Figure 18: Contour plot of the streamfunction derived from the solution of the *CurvSOL* code with the pancake approximation (top) and the *Pancake* code (bottom) for the Rome machine simulated with a wall speed of 700 m/s and a countercurrent flow created by a linear wall temperature gradient.

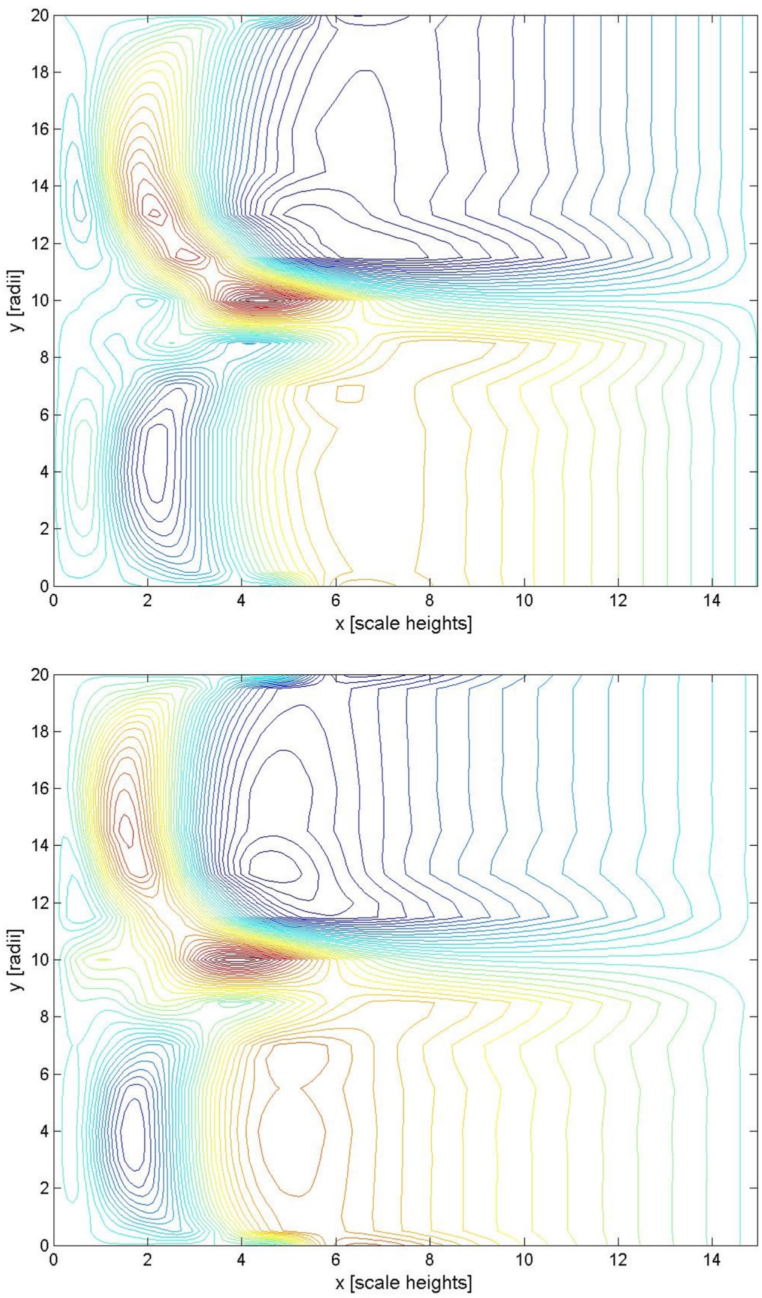

Figure 19: Contour plot of the streamfunction derived from the solution of the *CurvSOL* code with the pancake approximation (top) and the *Pancake* code (bottom) for the Rome machine simulated with a wall speed of 700 m/s and a countercurrent flow created by a feed drive.

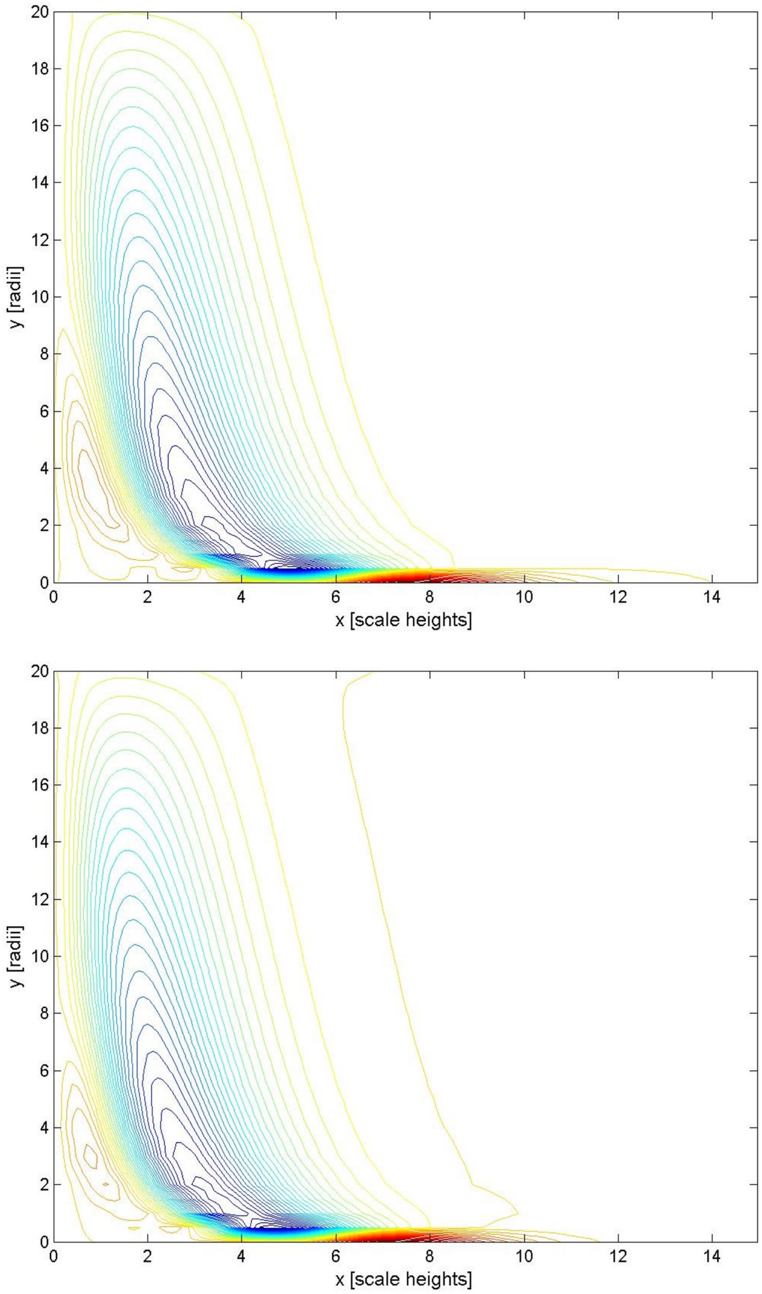

Figure 20: Contour plot of the streamfunction derived from the solution of the *CurvSOL* code with the pancake approximation (top) and the *Pancake* code (bottom) for the Rome machine simulated with a wall speed of 700 m/s and a countercurrent flow created by a scoop inserted into the flow field.

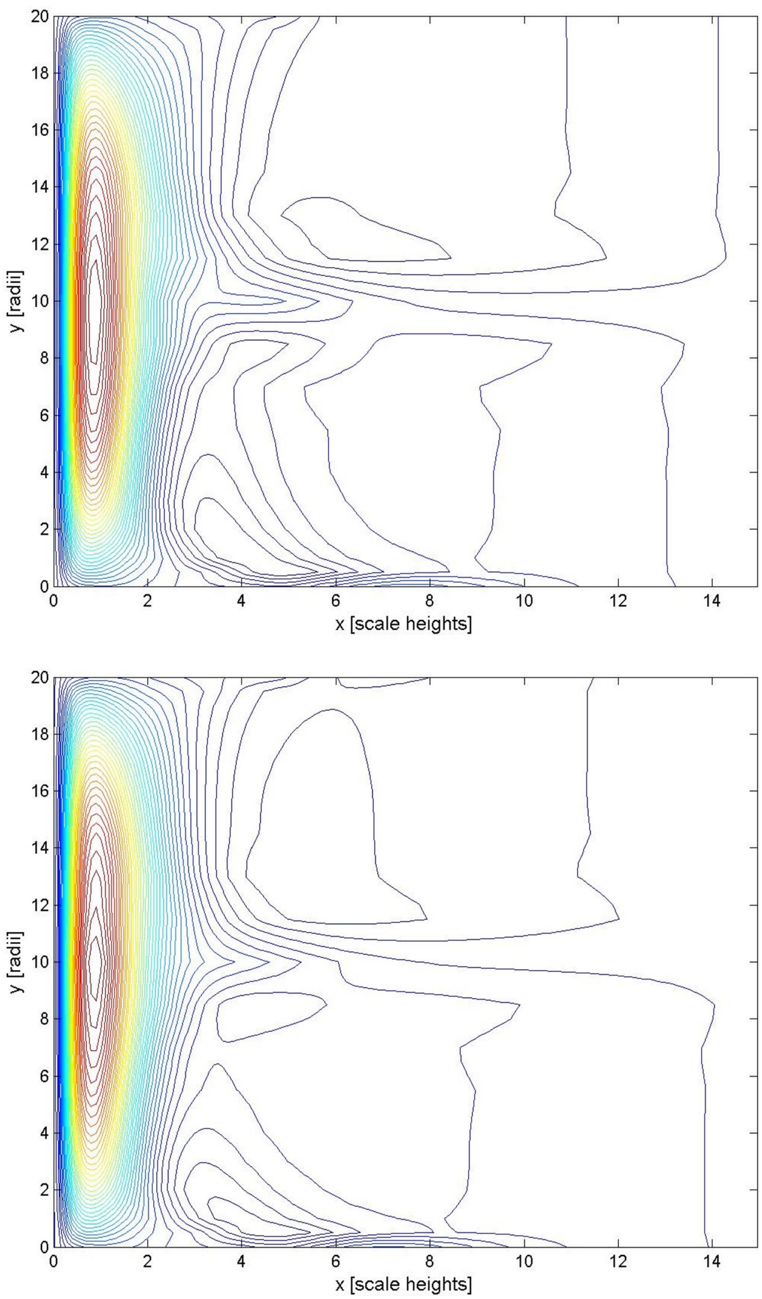

Figure 21: Contour plot of the streamfunction derived from the solution of the *CurvSOL* code with the pancake approximation (top) and the *Pancake* code (bottom) for the Rome machine simulated with a wall speed of 700 m/s and a countercurrent flow created by a linear wall temperature gradient, a feed drive, and a scoop inserted into the flow field.

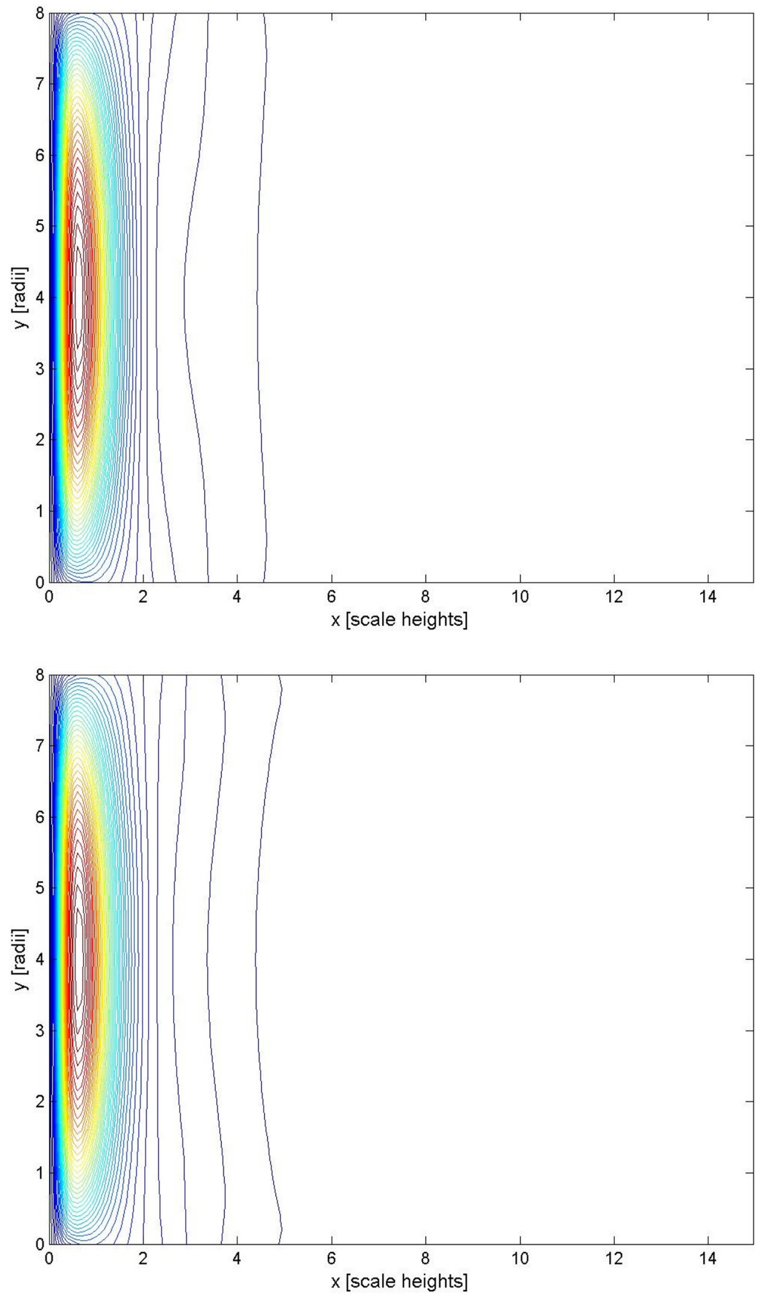

Figure 22: Contour plot of the streamfunction derived from the solution of the *CurvSOL* code with the pancake approximation (top) and the *Pancake* code (bottom) for the Iguaçu machine simulated with a wall speed of 500 m/s and a countercurrent flow created by a linear wall temperature gradient.

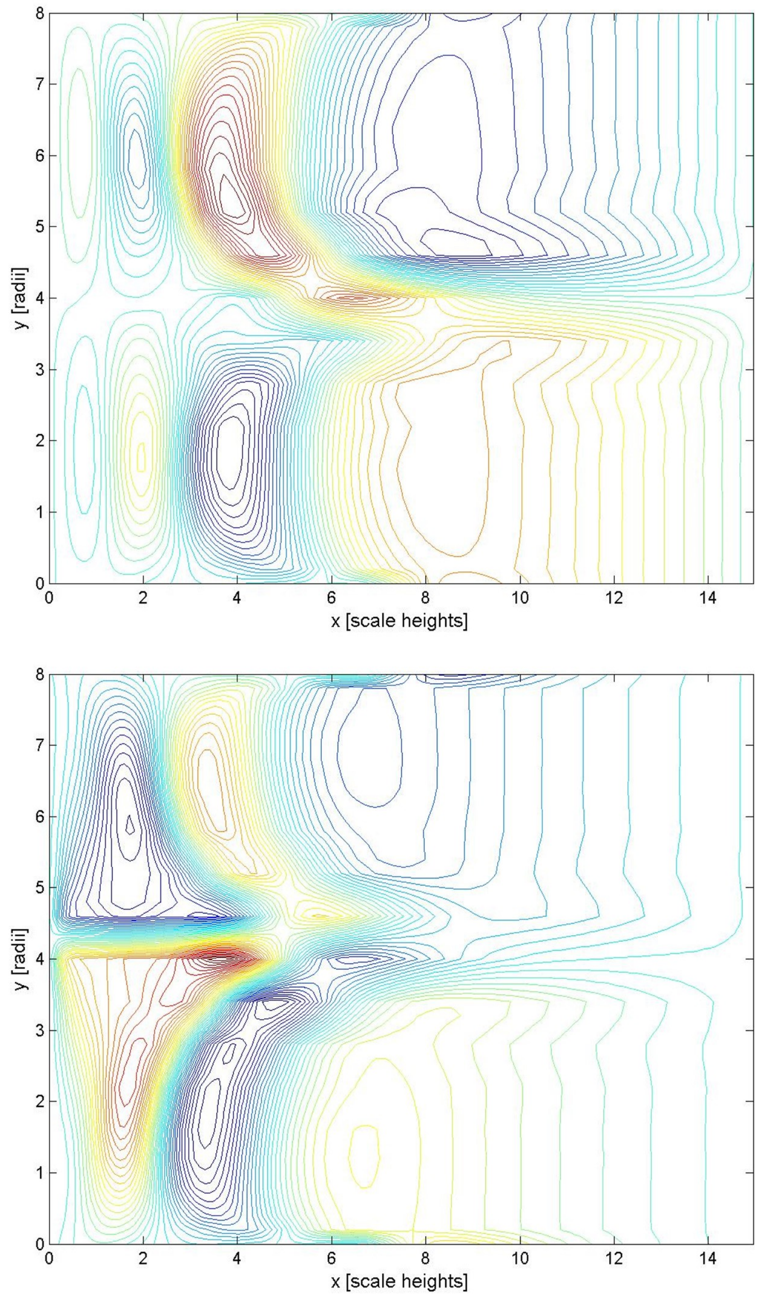

Figure 23: Contour plot of the streamfunction derived from the solution of the *CurvSOL* code with the pancake approximation (top) and the *Pancake* code (bottom) for the Iguaçu machine simulated with a wall speed of 500 m/s and a countercurrent flow created by a feed drive.

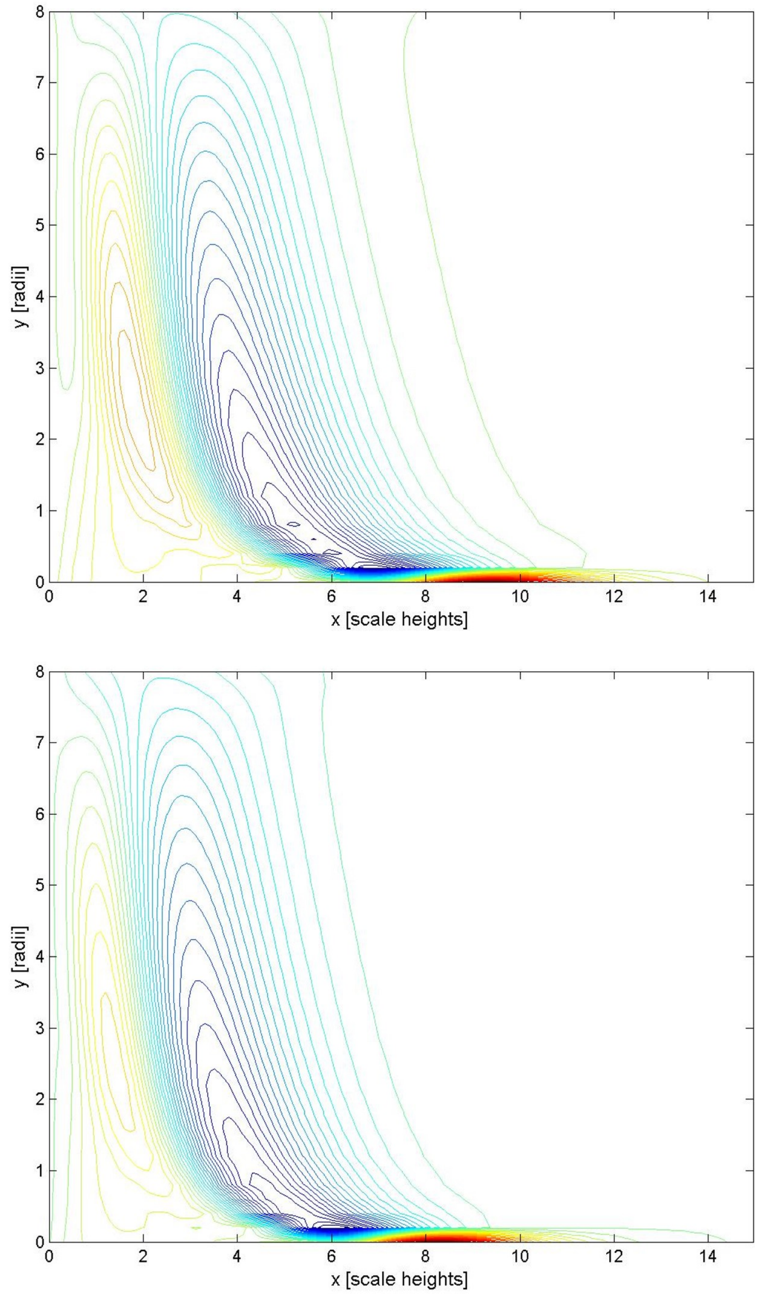

Figure 24: Contour plot of the streamfunction derived from the solution of the *CurvSOL* code with the pancake approximation (top) and the *Pancake* code (bottom) for the Iguaçu machine simulated with a wall speed of 500 m/s and a countercurrent flow created by a scoop inserted into the flow field.

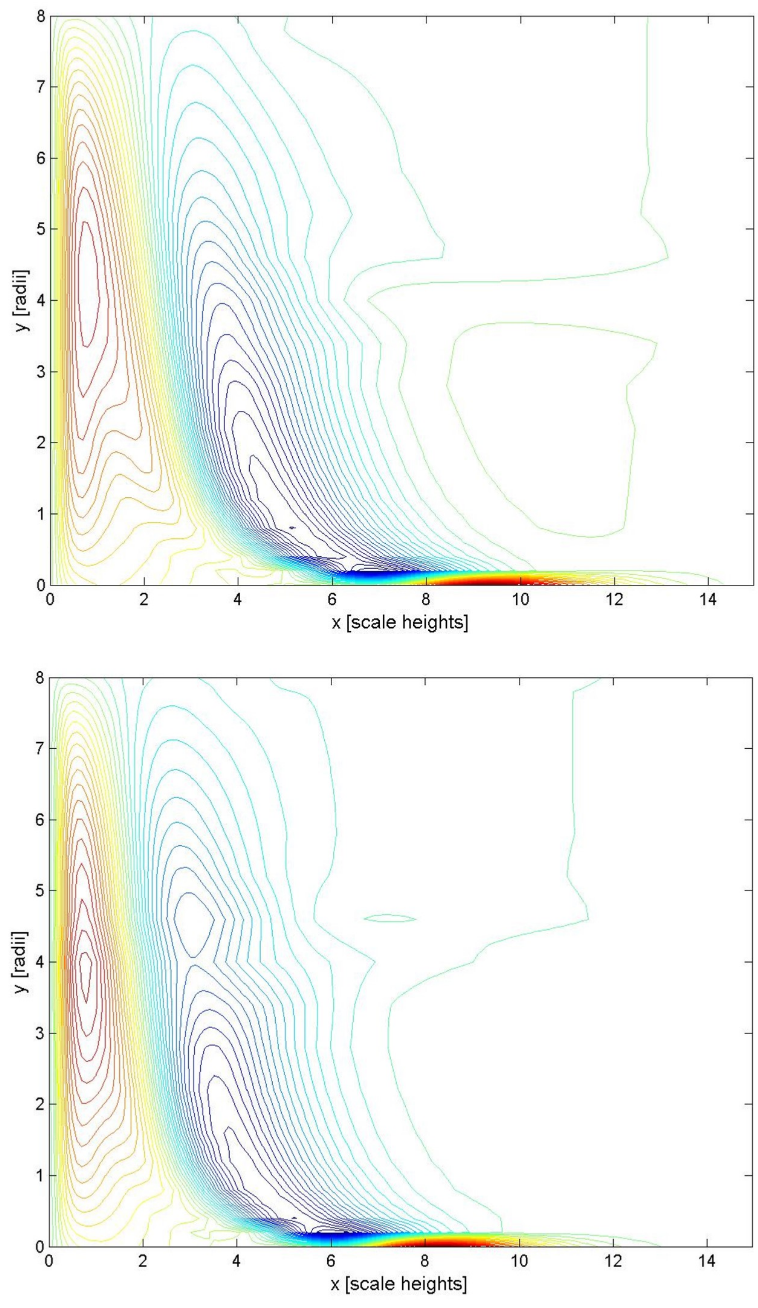

Figure 25: Contour plot of the streamfunction derived from the solution of the *CurvSOL* code with the pancake approximation (top) and the *Pancake* code (bottom) for the Iguaçu machine simulated with a wall speed of 500 m/s and a countercurrent flow created by a linear wall temperature gradient, a feed drive, and a scoop inserted into the flow field.

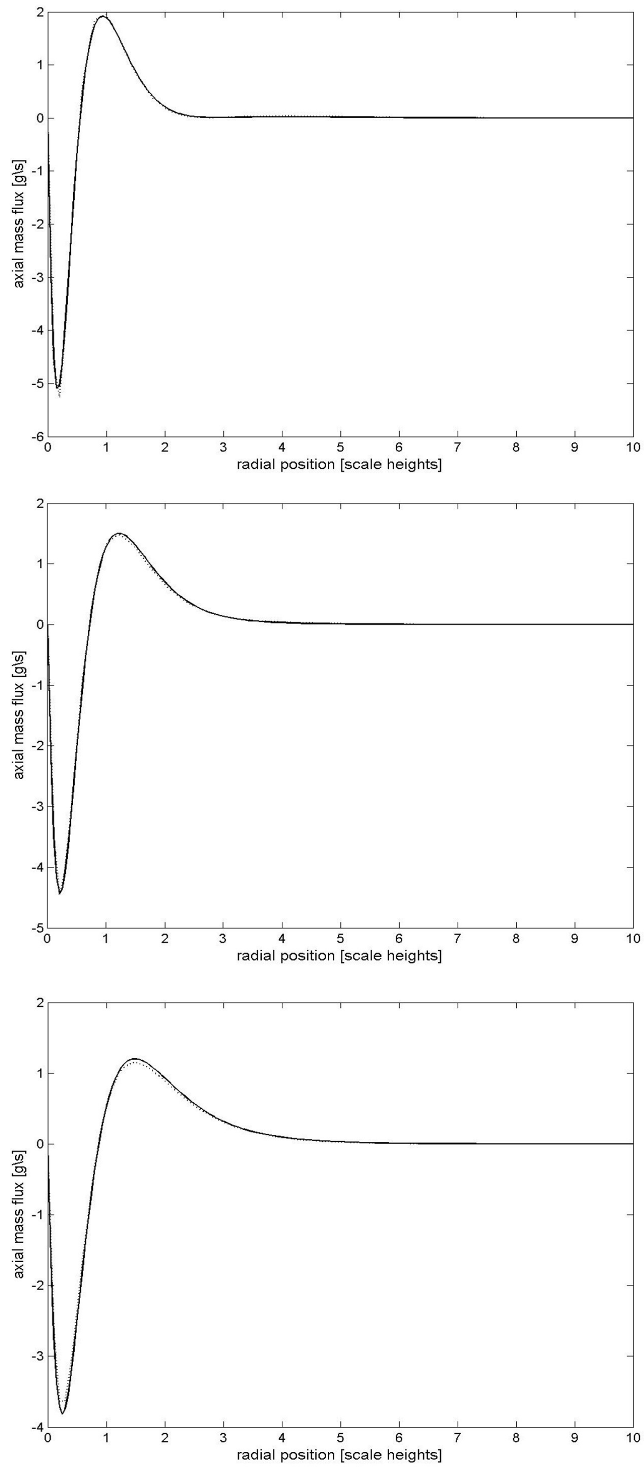

Figure 26: The axial mass flux is plotted from the quarter-plane of the Rome machine with a wall speed of 500 m/s (top), 600 m/s (middle), and 700 m/s (bottom) and the countercurrent flow created by a linear wall temperature gradient. The results from the *CurvSOL* code with the pancake approximation are shown by the dashed line and the those from *CurvSOL* considering the curvature of the rotor are represented by the dotted line.

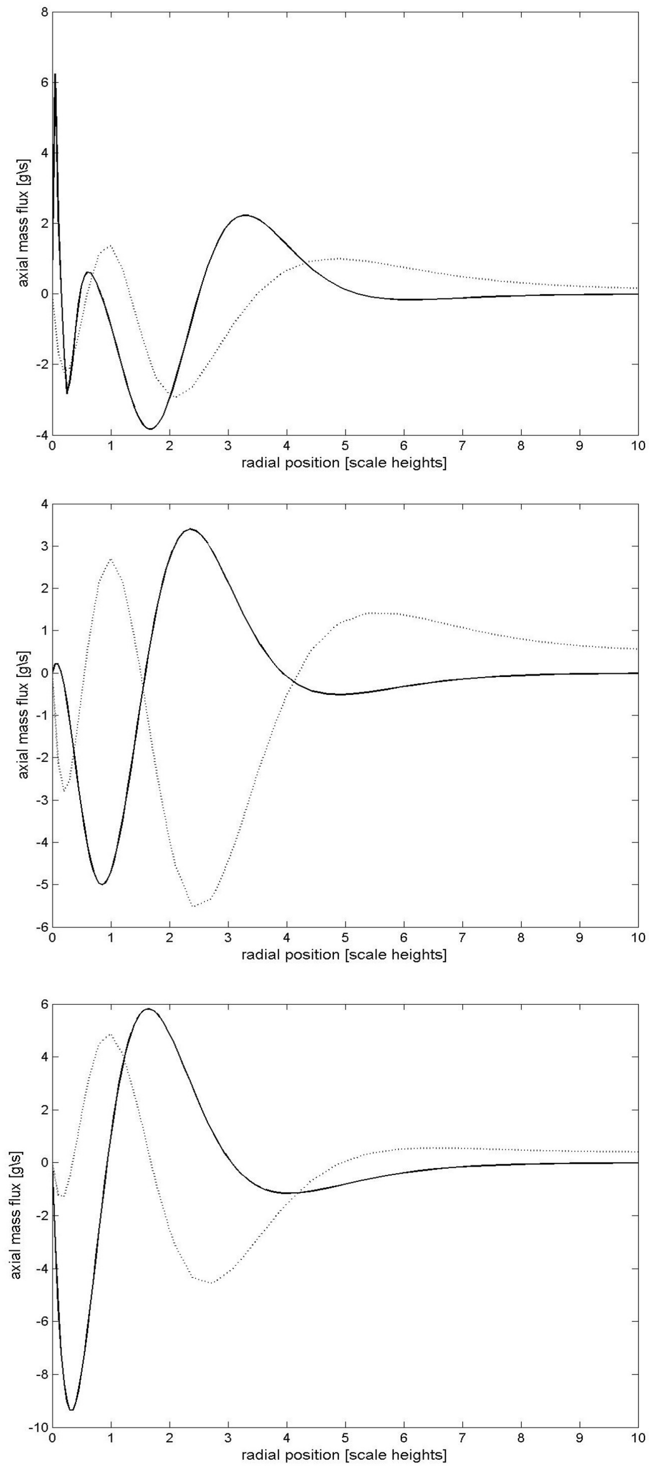

Figure 27: The axial mass flux is plotted from the quarter-plane of the Rome machine with a wall speed of 500 m/s (top), 600 m/s (middle), and 700 m/s (bottom) and the countercurrent flow created by a feed source. The results from the *CurvSOL* code with the pancake approximation are shown by the dashed line and the those from *CurvSOL* considering the curvature of the rotor are represented by the dotted line.

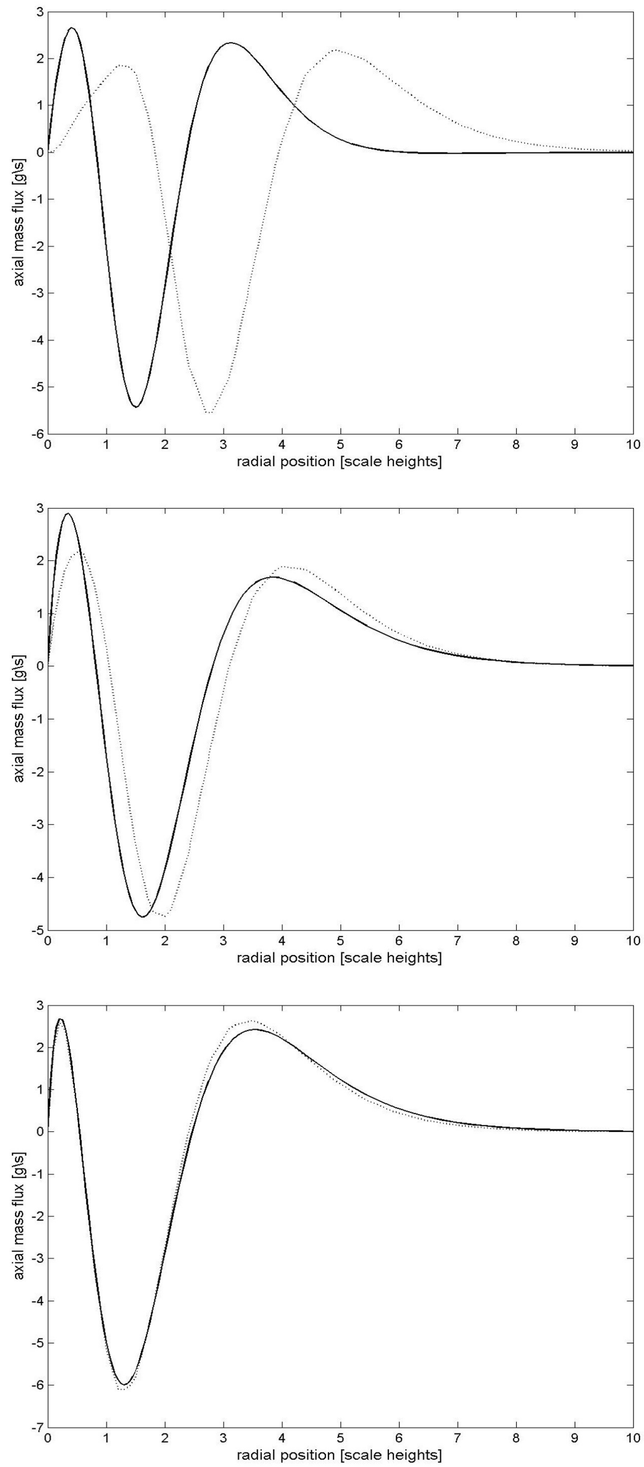

Figure 28: The axial mass flux is plotted from the quarter-plane of the Rome machine with a wall speed of 500 m/s (top), 600 m/s (middle), and 700 m/s (bottom) and the countercurrent flow created by a scoop inserted into the flow field. The results from the *CurvSOL* code with the pancake approximation are shown by the dashed line and the those from *CurvSOL* considering the curvature of the rotor are represented by the dotted line.

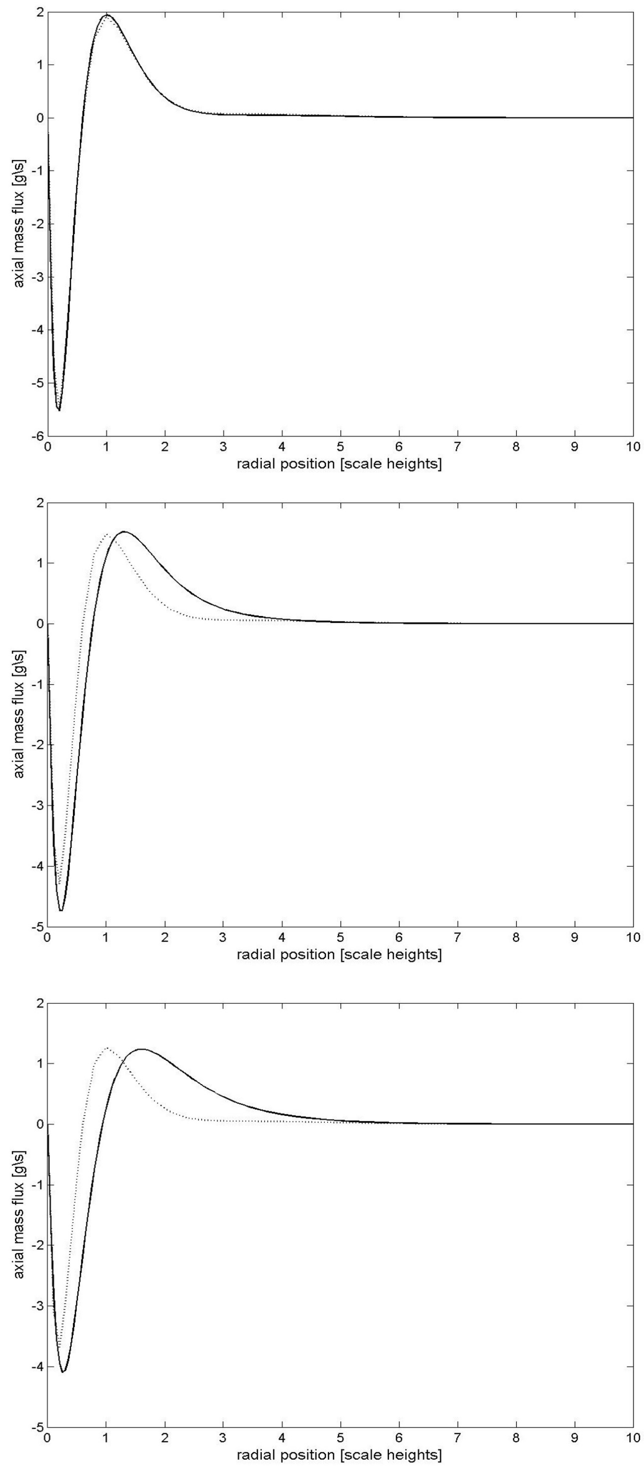

Figure 29: The axial mass flux is plotted from the quarter-plane of the Iguaçu machine with a wall speed of 500 m/s (top), 600 m/s (middle), and 700 m/s (bottom) and the countercurrent flow created by a linear wall temperature gradient. The results from the *CurvSOL* code with the pancake approximation are shown by the dashed line and the those from *CurvSOL* considering the curvature of the rotor are represented by the dotted line.

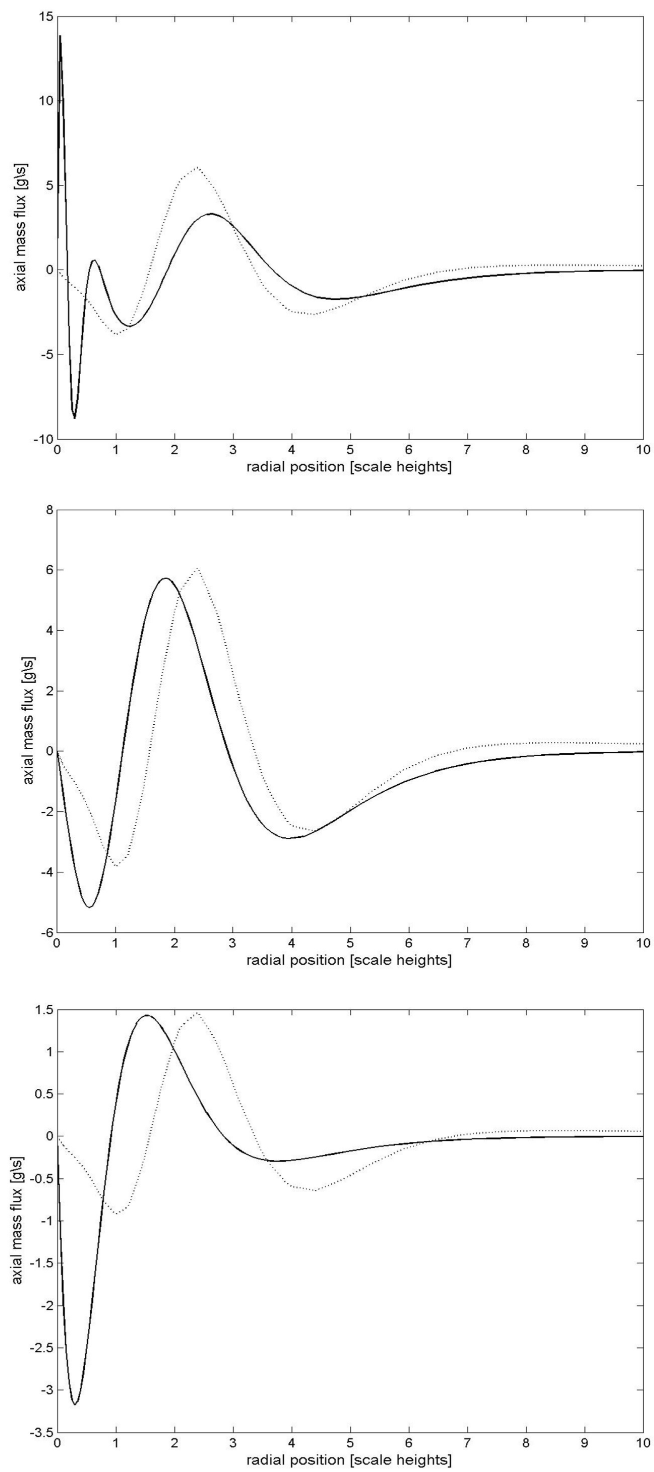

Figure 30: The axial mass flux is plotted from the quarter-plane of the Iguaçu machine with a wall speed of 500 m/s (top), 600 m/s (middle), and 700 m/s (bottom) and the countercurrent flow created by a feed source. The results from the *CurvSOL* code with the pancake approximation are shown by the dashed line and the those from *CurvSOL* considering the curvature of the rotor are represented by the dotted line.

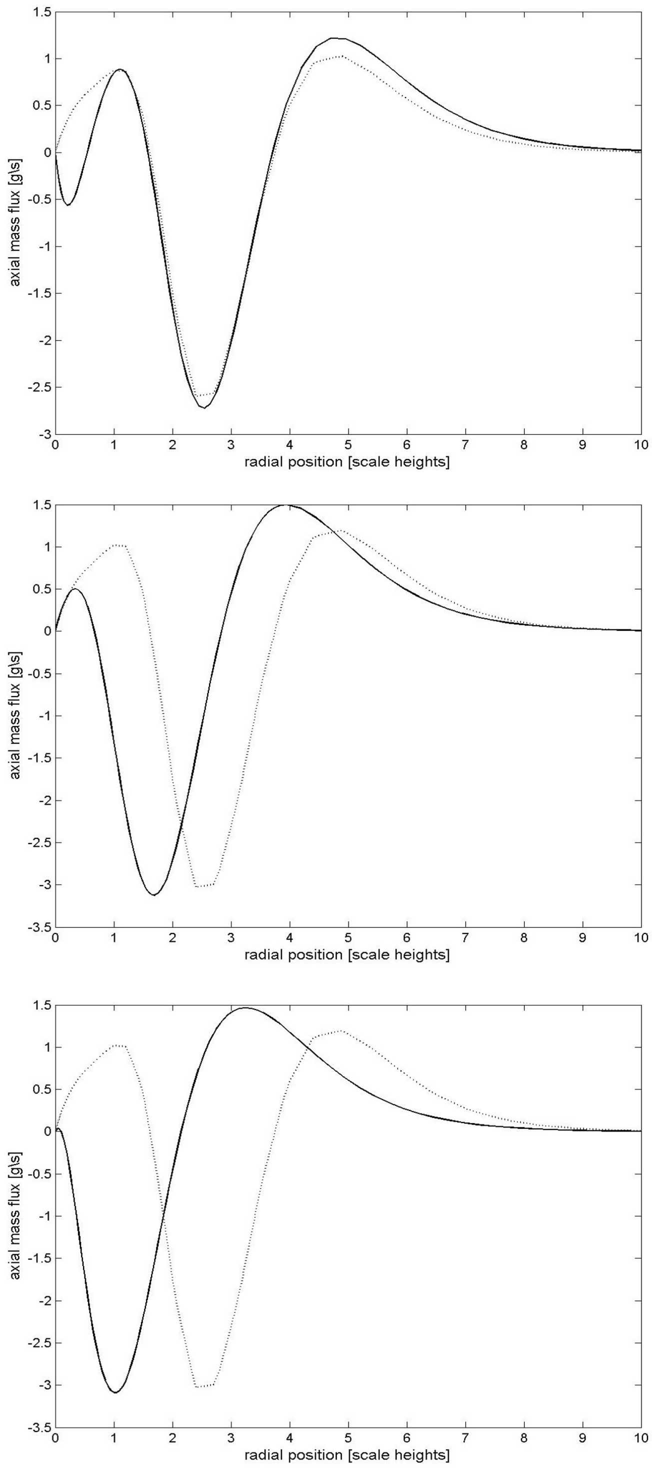

Figure 31: The axial mass flux is plotted from the quarter-plane of the Iguaçu machine with a wall speed of 500 m/s (top), 600 m/s (middle), and 700 m/s (bottom) and the countercurrent flow created by a scoop inserted into the flow field. The results from the *CurvSOL* code with the pancake approximation are shown by the dashed line and the those from *CurvSOL* considering the curvature of the rotor are represented by the dotted line.

5 Isotope Transport

The set of equations governing the transport of the isotopes in the process gas in a countercurrent centrifuge is not readily solvable using analytic means, and as mentioned in the introductory chapters of this work, a number of different methods have been developed to approximate both the axial concentration gradient and overall concentration profile. In this section, the governing equation for the concentration of the desired isotope is developed, the boundary conditions are defined, and Cohen's method of radial averaging is discussed. The derivation follows closely the work presented in [7][11][59][24][65].

5.1 Governing Equation

For a gas centrifuge with a single binary feed stream and product and waste extraction streams, the mass balance for the desired component (in this case the lighter isotope) across the machine may be expressed as

$$Nf = \theta Np + (1-\theta)Nw, \tag{5.1}$$

where Nf is the feed stream concentration, θ is the ratio of the product rate to the feed rate, termed the cut, Np is the product stream concentration, and Nw is the waste stream concentration.

As detailed by Wood, Mason, and Soubbarameyer [59], three basic transport phenomena affecting the molecules in a gas centrifuge: pressure diffusion $\vec{\phi}^P$, back diffusion $\vec{\phi}^B$, and convection $\vec{\phi}^C$. Figure 32 depicts these phenomena in a cross-sectional description of the interior of the centrifuge rotor. The net transport vector for the light isotope is then given as the sum of these three transport phenomena,

$$\vec{\phi} = \vec{\phi}^p + \vec{\phi}^B + \vec{\phi}^c. \tag{5.2}$$

Additionally, each of the three transport phenomena has a radial and axial component, given as

$$\vec{\phi}^p \left(\rho D \frac{\Omega^2 r}{RT} MN \ , \ 0 \right) \tag{5.3}$$

$$\vec{\phi}^B \left(-\rho D N_r - \rho D \frac{\Omega^2 r}{RT} N \sum_{j=1}^{n} M_j N_j \ , \ -\rho D N_z \right) \tag{5.4}$$

$$\vec{\phi}^c \left(\rho u N \ , \ \rho w N \right). \tag{5.5}$$

Defining

$$\Delta A = \frac{\Delta M \Omega^2}{2RT_0}, \tag{5.6}$$

and combining the components from each of the three transport phenomena, we have two components of net transport

$$\phi_r = -\rho D \left(N_r + 2\Delta A r N \right) + \rho u N \tag{5.7}$$

and

$$\phi_z = -\rho D N_z + \rho w N. \tag{5.8}$$

The radial and axial components may then be combined with the continuity equation to give the diffusion equation for the light isotope

$$-\rho D N_{zz} - \rho D \frac{1}{r} \left(r N_r + 2\Delta A r^2 N \right)_r + \rho w N_z = 0. \tag{5.9}$$

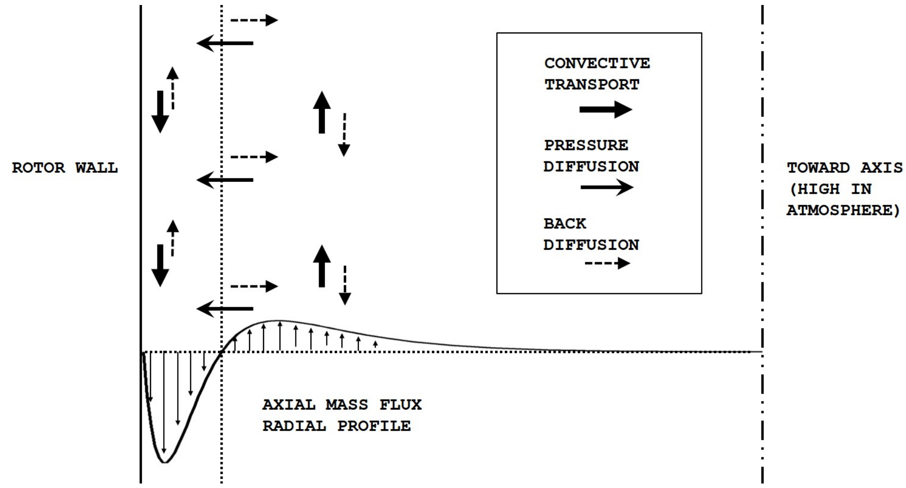

Figure 32: The three transport phenomena affecting the gas molcules in a simplified cross-sectional view of the centrifuge rotor [59]. In the two-dimensional cross section of the axisymmetric rotor volume, the net transport is made up of pressure diffusion, back diffusion and convection. These inputs are summed and the radial and axial components combined with the continuity to describe overall diffusion of the light isotope.

5.2 Boundary Conditions

There can be no radial transport of any component at the rotor wall or the axis. At the end caps, the axial transport must equal a constant, depending on the character of the source term corresponding to the end cap [59][90]. These conditions may be expressed high in the atmosphere as

$$N_r = 0, \qquad \text{for} \qquad r = 0, \tag{5.10}$$

and at the rotor wall as

$$N_r + 2\Delta A a N = 0, \qquad \text{for } r = a. \tag{5.11}$$

On the end caps, the flux through the surfaces of the caps is zero, so the sum across the radius is equal to the flux through the withdrawal ports [91][95]. This is given as

$$\int_0^a \phi_z 2\pi r dr = \int_0^a \left(-\rho D N_z + \rho w N\right) 2\pi r dr, \tag{5.12}$$

which, for $z = 0$ is written

$$\int_0^a \phi_z 2\pi r dr = -F(1-\theta)Nw, \tag{5.13}$$

and, for $z = z_H$

$$\int_0^a \phi_z 2\pi r dr = -F\theta Np. \tag{5.14}$$

These boundary conditions, combined with the diffusion equation (5.9) and the mass balance equation (5.1), form a set of partial differential equations that describe the transport of the desired component, which in this case are molecules of UF_6 composed of the lighter uranium isotope, uranium-235 [96][92].

5.3 Radial Averaging

The set of governing equations is not readily solvable using analytic means, and different solution methods have been developed to arrive at approximations for both the axial concentration gradient and overall concentration profile. Following a similar procedure as that used by Furry, Jones, and Onsager to simplify the diffusion equation for a distillation column, Cohen described the axial gradient of the radially averaged concentration of the isotope of interest [7][11][24][94]. He begins by noting that the density, axial velocity and desired concentration vary little in the radial direction in comparison to the variation in the axial variation [7]. Soubbaramayer points out that the maximum variation in r is less than the equilibrium case of elementary centrifugal separation without countercurrent flow inducing drive mechanism, as shown by

$$\frac{\Delta N}{N} < 2\Delta A a^2 = \frac{\Delta M}{M} A^2, \tag{5.15}$$

where ΔM is the difference in molecular weights of the two isotopic molecules that make up the binary mixture, and A is the previously defined stratification parameter

[11].

The radially averaged concentration, $\bar{N}$, is described as

$$\bar{N} = \frac{\int_0^a N 2\pi r dr}{\pi a^2}. \tag{5.16}$$

Inserting equation (5.9) into equation (5.16) and integrating over the radius gives

$$\int_0^a \phi_z 2\pi r dr = F\theta N p \qquad \text{for} \qquad z_F < z < z_T, \tag{5.17}$$

in the enriching section of the centrifuge, and

$$\int_0^a \phi_z 2\pi r dr = -F(1-\theta) N w \qquad \text{for} \qquad 0 < z < z_F, \tag{5.18}$$

in the lower stripping section of the centrifuge.

Considering equations (5.17) and (5.18) separately, we will begin in the enriching section. Inserting ϕ_z as defined in equation (5.8) into equation (5.17) gives

$$F\theta N p = \int_0^a \left(-\rho D N_z + \rho w N\right) 2\pi r dr. \tag{5.19}$$

Introducing a stream function defined such that

$$\psi = \int_0^a \rho w r' dr', \tag{5.20}$$

equation 5.19 becomes

$$F\theta N p = F\theta \bar{N} - 2\pi \int_0^a \psi N_r dr + \pi a^2 \rho D \bar{N}_z. \tag{5.21}$$

Assuming $\bar{N}$ as a good approximation for N, substituting $\bar{N}_z$ for N_z, and neglecting the axial diffusion terms in equation (5.9), the relationship between the radial and axial concentration gradients is

$$\rho w \bar{N}_z = \rho D \frac{1}{r} \left(r N_r + 2 \Delta A r^2 \bar{N} \right)_r . \tag{5.22}$$

Integrating with respect to r and solving for the radial concentration gradient gives

$$N_r = -2\Delta A r \bar{N} + \frac{\psi}{\rho D r} \bar{N}_z. \tag{5.23}$$

Plugging this result back into (5.21) gives

$$F\theta N p = F\theta \bar{N} + 4\pi \Delta A \bar{N} \int_0^a \psi r dr - \left(\frac{2\pi}{\rho D} \int_0^a \frac{\psi^2}{r} dr + \pi a^2 \rho D \right) \bar{N}_z. \tag{5.24}$$

This same procedure is repeated for the stripping section. Inserting equation (5.8) into equation (5.18) gives

$$-F(1-\theta) N w = \int_0^a \left(-\rho D N_z + \rho w N \right) 2\pi r dr, \tag{5.25}$$

which, with the introduction of the stream function from (5.20), becomes

$$-F(1-\theta) N w = -F(1-\theta)\bar{N} - 2\pi \int_0^a \psi N_r dr + \pi a^2 \rho D \bar{N}_z. \tag{5.26}$$

Once again, the radial concentration gradient is found through application of the same assumptions and approximations to equation (5.9) and integrating with respect to r. Similar to equation (5.24), substituting N_r back into equation (5.26) yields

$$\begin{aligned} -F(1-\theta) N p = -F(1-\theta)\bar{N} &+ 4\pi \Delta A \bar{N} \int_0^a \psi r dr \\ &- \left(\frac{2\pi}{\rho D} \int_0^a \frac{\psi^2}{r} dr + \pi a^2 \rho D \right) \bar{N}_z. \end{aligned} \tag{5.27}$$

For equation (5.24), we consider the boundary conditions

$$\bar{N}(z_T) = Np \qquad and \qquad \bar{N}(z_F) = Nf, \tag{5.28}$$

and for equation (5.27),

$$\bar{N}(z_F) = Nf \qquad and \qquad \bar{N}(0) = Nw. \tag{5.29}$$

Equations (5.28) and (5.29) along with equations (5.24) and (5.27) represent ordinary differential equations and boundary conditions that describe the axial gradient of the radial averaged concentration of the isotope of interest in the enriching section and stripping section, respectively, of the countercurrent centrifuge. Based primarily on the similarities to a distillation column, we can define a few quantities to help simplify these expressions [7][11]. If, in the enriching section, we let

$$\epsilon_s = 2\pi\Delta A \int_0^a \left(\frac{\psi}{L}\right) r dr, \tag{5.30}$$

$$K = a\left(\frac{\rho D\pi a}{L} + \frac{2\pi L}{\rho D a}\int_0^a \left(\frac{\psi}{L}\right)^2 \frac{1}{r} dr\right), \tag{5.31}$$

and

$$2L = \int_0^a |\rho w| \, 2\pi r dr, \tag{5.32}$$

equation (5.24) can now be written

$$F\theta(Np - \bar{N}) = L\left(2\epsilon_s \bar{N} - K\bar{N}_z\right), \tag{5.33}$$

where ϵ_s is the transfer coefficient, K is the transfer unit height, and L is the internal flow magnitude in each direction. Similarly, the stripping section differential equation becomes

$$-F(1-\theta)(Nw-\bar{N}) = L\left(2\epsilon_s\bar{N} - K\bar{N}_z\right). \tag{5.34}$$

It is important to note that, strictly speaking, the values of equations (5.30) through (5.32) are slightly different in the stripping section than in the enriching section due to the influence of the withdrawl streams in each section on the countercurrent flow [7][11]. However, this difference is assumed negligible in comparison with the magnitude of the internal flow. Additionally, this assumes that L, ϵ_S, and K are axially independent, or that the axial mass flux is only a function of the radial coordinate. Soubbaramayer [11] shows that through scaling each of the variables as

$$Z = a\eta, \quad \xi = A^2\left(1-\frac{r^2}{a^2}\right), \quad \eta_T = \frac{Z_T}{a}, \quad \eta_F = \frac{Z_F}{a},$$
$$\phi_P = \frac{F\theta}{\pi a\rho D}, \qquad \phi_W = \frac{F(1-\theta)}{\pi a\rho D}, \qquad \epsilon_0 = a^2\Delta A$$

equation (5.33) can be written

$$\phi_P Np = \bar{N}\left(\phi_P + 2\epsilon_0 J_1(\eta)\right) - \left(1+J_2(\eta)\right)\frac{d\bar{N}}{d\eta} \tag{5.35}$$

where the boundary conditions are now

$$\bar{N}(\eta_T) = Np \qquad \text{and} \qquad \bar{N}(\eta_F) = Nf, \tag{5.36}$$

and

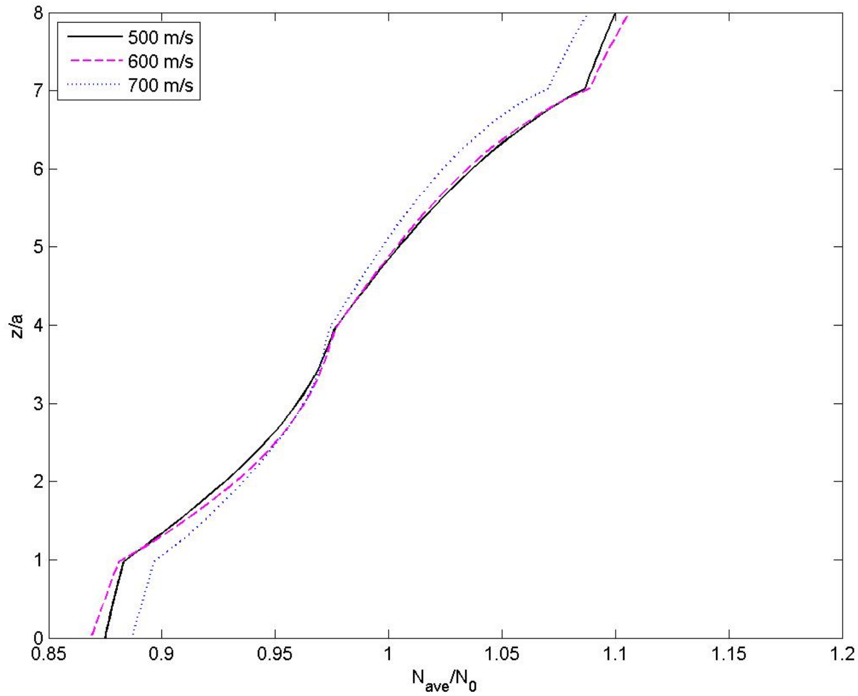

Figure 33: Results of the Radial Averaging Method for the Iguaçu machine. The average concentration N_{ave} of the light isotope U235 divided by the feed concentration N_0 is plotted for each axial plane in the Iguaçu machine with simulations run at three different wall speeds.

$$
\begin{aligned}
J_1(\eta) &= \frac{\pi}{(\pi a\rho D)}\frac{1}{A^2}\int_0^{A^2}\psi d\xi \\
J_2(\eta) &= \frac{\pi^2}{(\pi a\rho D)^2}\frac{1}{A^2}\int_0^{A^2}\frac{\psi^2}{1-\frac{\xi}{A^2}}d\xi.
\end{aligned} \tag{5.37}
$$

For the stripping section, equation (5.34) then can similarly be written

$$
-\phi_W Nw = \bar{N}\left(-\phi_W + 2\epsilon_0 J_1(\eta)\right) - \left(1 + J_2(\eta)\right)\frac{d\bar{N}}{d\eta} \tag{5.38}
$$

with boundary conditions

$$
\bar{N}(0) = Nw \qquad \text{and} \qquad \bar{N}(\eta_F) = Nf. \tag{5.39}
$$

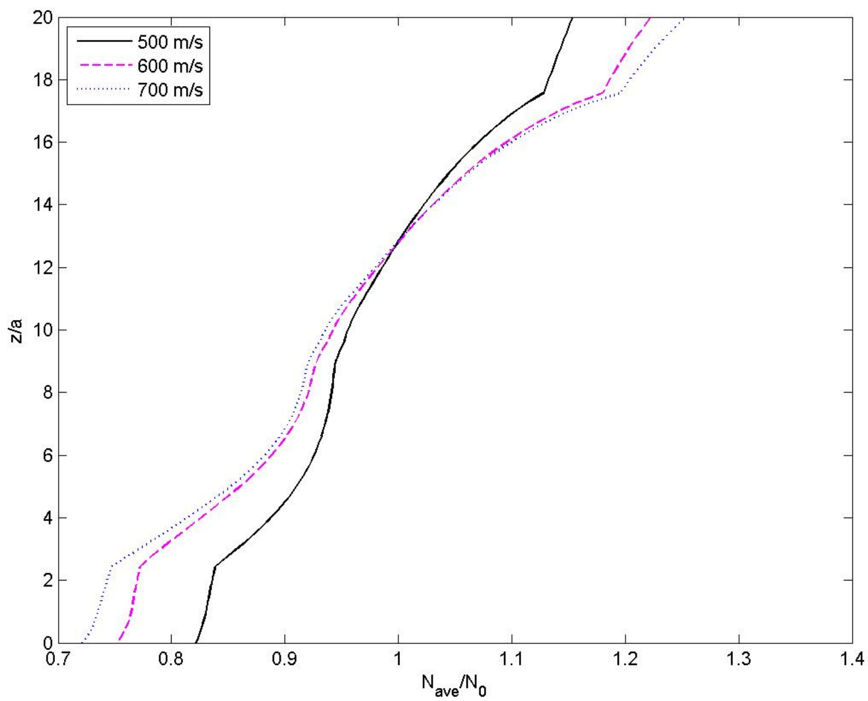

Figure 34: Results of the Radial Averaging Method for the Rome machine. The average concentration N_{ave} of the light isotope U235 divided by the feed concentration N_0 is plotted for each axial plane in the Rome machine with simulations run at three different wall speeds.

Figures 33 and 34 show the results of Cohen's radial averaging solution method for the Iguaçu and Rome machines with operating parameters listed in Table 1 and run at three different wall speeds: 500 m/s, 600 m/s, and 700 m/s. The normalized concentration of the light isotope is plotted against the axial location, given in radii. Once again, this method of averaging the concentration at each axial location in the domain assumes that the concentration does not vary dramatically in the radial direction. This has been shown to be accurate for higher wall speeds and larger diameter machines [7][9][11][31]. However, as the wall speed slows, the material is no longer confined to such a narrow region along the wall. The potential for significant radial variation increases as the wall speed slows and the rotor diameter decreases. The next chapter introduces a computational method designed to approximate the solution of equation (5.9) over the entire domain in order to illustrate any effects of wall speeds and rotor diameter in the radial concentration variation.

6 Finite Difference Approximation

As detailed in the previous chapter, no analytical solution exists for the diffusion equation with boundary conditions presented in the previous chapter. This chapter details the construction of a numerical model to approximate the solution. The results obtained using the axial mass flux profile from the *Pancake* flow solution are compared to those based on the *CurvSOL* solution. Additionally, the resulting concentration field is averaged at each axial division in the computational mesh and compared to the results of Cohen's radial averaging technique.

6.1 Finite Difference Scheme for Isotope Transport

When applying a central differencing technique to approximate partial differential equations, the space is often discretized using a sub-scripted $\{i, j\}$ indexing convention where i denotes the row and j denotes the column of the indexed value. Therefore, $N_{3,7}$ would refer to the N value in the 3^{rd} row and 7^{th} column of the array of values for N over the domain. This often gets confusing when mistaken for the traditional Cartesian space reference of $\{x, y\}$. Care must be taken to ensure the correct referencing when developing a scheme for numerical approximation of the equation.

Dividing equation (5.9) through by $-\rho D$ and expanding the radial derivative shown in parentheses gives,

$$\frac{\partial^2 N}{\partial r^2} + \frac{\partial^2 N}{\partial z^2} + \left(\frac{1}{r} + 2\Delta A r\right)\frac{\partial N}{\partial r} - \frac{\rho V_z}{\rho D}\frac{\partial N}{\partial z} + 4\Delta A N = 0. \tag{6.1}$$

Assuming a uniform grid size for the discretization, the first derivatives of N at the ith row and jth column can be approximated with central differencing as

$$\frac{\partial N_{i,j}}{\partial r} = \frac{1}{2\Delta r}\left(N_{i,j+1} - N_{i,j-1}\right), \tag{6.2}$$

and

$$\frac{\partial N_{i,j}}{\partial z} = \frac{1}{2\Delta z}\left(N_{i+1,j} - N_{i-1,j}\right). \tag{6.3}$$

Similarly, the second derivatives may be approximated as

$$\frac{\partial^2 N_{i,j}}{\partial r^2} = \frac{1}{\Delta r^2}\left(N_{i,j+1} - 2N_{i,j} + N_{i,j-1}\right), \tag{6.4}$$

and

$$\frac{\partial^2 N_{i,j}}{\partial z^2} = \frac{1}{\Delta z^2}\left(N_{i+1,j} - 2N_{i,j} + N_{i-1,j}\right). \tag{6.5}$$

Inserting these approximations into our expanded governing equation gives

$$\begin{aligned}
&\frac{1}{\Delta r^2}\left(N_{i,j+1} - 2N_{i,j} + N_{i,j-1}\right) \\
&\quad + \frac{1}{\Delta z^2}\left(N_{i+1,j} - 2N_{i,j} + N_{i-1,j}\right) \\
&\quad + \frac{1}{r}\frac{1}{2\Delta r}\left(N_{i,j+1} - N_{i,j-1}\right) \\
&\quad + 2\Delta A r\frac{1}{2\Delta r}\left(N_{i,j+1} - N_{i,j-1}\right) \\
&\quad - \frac{\rho V_z}{\rho D}\frac{1}{2\Delta z}\left(N_{i+1,j} - N_{i-1,j}\right) + 4\Delta A N_{i,j} = 0.
\end{aligned} \tag{6.6}$$

After collecting like concentration values, the above equation can be written

$$
\begin{aligned}
N_{i,j} & \left(4\Delta A - 2\left(\frac{1}{\Delta r^2} + \frac{1}{\Delta z^2}\right)\right) \\
& + N_{i,j+1}\left(\frac{1}{\Delta r^2} + \frac{1}{2\Delta r}\left(\frac{1}{r} + 2\Delta A r\right)\right) \\
& + N_{i,j-1}\left(\frac{1}{\Delta r^2} - \frac{1}{2\Delta r}\left(\frac{1}{r} - 2\Delta A r\right)\right) \\
& + N_{i+1,j}\left(\frac{1}{\Delta z^2} - \frac{\rho V_z}{\rho D}\frac{1}{2\Delta z}\right) \\
& + N_{i-1,j}\left(\frac{1}{\Delta z^2} + \frac{\rho V_z}{\rho D}\frac{1}{2\Delta z}\right) = 0.
\end{aligned} \tag{6.7}
$$

If we let

$$\alpha = 4\Delta A - 2\left(\frac{1}{\Delta r^2} + \frac{1}{\Delta z^2}\right), \tag{6.8}$$

$$\beta = \frac{1}{\Delta r^2} + \frac{1}{2\Delta r}\left(\frac{1}{r} + 2\Delta A r\right), \tag{6.9}$$

$$\delta = \frac{1}{\Delta r^2} - \frac{1}{2\Delta r}\left(\frac{1}{r} - 2\Delta A r\right), \tag{6.10}$$

$$\epsilon = \frac{1}{\Delta z^2} - \frac{\rho V_z}{\rho D}\frac{1}{2\Delta z}, \tag{6.11}$$

and

$$\gamma = \frac{1}{\Delta z^2} + \frac{\rho V_z}{\rho D}\frac{1}{2\Delta z}, \tag{6.12}$$

the preceding equation can be written more compactly as

$$\alpha N_{i,j} + \beta N_{i,j+1} + \delta N_{i,j-1} + \epsilon N_{i+1,j} + \gamma N_{i-1,j} = 0. \tag{6.13}$$

Solving for $N_{i,j}$, we have

$$N_{i,j} = -\frac{1}{\alpha}\left(\beta N_{i,j+1} + \delta N_{i,j-1} + \epsilon N_{i+1,j} + \gamma N_{i-1,j}\right). \tag{6.14}$$

The scaled radial coordinate described in previous chapters represents a non-uniform discretization. In the event that the computational domain is non-uniform, the varying intervals between points necessitates modification of the approximation for each derivative. For a non-uniform grid, we let

$$\alpha = 4\Delta A - 2\left(\frac{1}{\Delta r_1 \Delta r_2} + \frac{1}{\Delta z_1 \Delta z_2}\right), \tag{6.15}$$

$$\beta = \frac{1}{\Delta r_1 \Delta r_2} + \frac{1}{\Delta r_1 + \Delta r_2}\left(\frac{1}{r} + 2\Delta A r\right), \tag{6.16}$$

$$\delta = \frac{1}{\Delta r_1 \Delta r_2} - \frac{1}{\Delta r_1 + \Delta r_2}\left(\frac{1}{r} - 2\Delta A r\right), \tag{6.17}$$

$$\epsilon = \frac{1}{\Delta z_1 \Delta z_2} - \frac{1}{\Delta z_1 + \Delta z_2}\left(\frac{\rho V_z}{\rho D}\right), \tag{6.18}$$

and

$$\gamma = \frac{1}{\Delta z_1 \Delta z_2} + \frac{1}{\Delta z_1 + \Delta z_2}\left(\frac{\rho V_z}{\rho D}\right). \tag{6.19}$$

Equation (6.14) is implemented in *xPort*, a Matlab code employing the Jacobi line method, alternating the sweep direction after each complete sweep. Bi-harmonic smoothing is employed to dampen edge effects. The numerical derivatives used to create the finite difference scheme given in equation (6.14) are central differences based on the Taylor series expansion about the node. As these numerical first derivatives are known to be first order accurate, the error in the approximation linearly approaches zero as the discretization size approaches zero, establishing the consistency of the scheme [88][89]. Additionally, a relaxation parameter, ω, is defined to speed convergence such that

$$N_{i,j}^{n+1} = \omega N_{i,j}^{*} + (1-\omega) N_{i,j}^{n}. \tag{6.20}$$

With a relaxation factor chosen such that $0 < \omega \leq 1$, the convergence is slowed but ensured. Figure 35 depicts the process flow of the isotope transport finite differencing code.

Based on the analysis of the flow solutions presented in Chapter 4, two cases are selected for comparison of separation simulation results. A complete catalog of isotope transport simulation results and comparison figures appears in Appendix B. Figures 36 and 37 depict the comparison between the axial variation of the light isotope concentration in the results of Cohen's one dimensional radial averaging method and the two-dimensional finite differencing method. The results of *xPort* have been averaged at each axial sampling location for better comparison. The averaged results display strong agreement at the endcaps and diverge by as much as 6% at select axial locations.

Additionally, figures 38 and 39 compare the results of the one-dimensional radial averaging method and the averaged two-dimensional solution based on the flow field from the *Pancake* and *CurvSOL* codes for both the Rome and Iguaçu machines. The averaged two-dimensional *Pancake* and *CurvSOL* based Rome results at the higher wall speed of 700 m/s are nearly identical while those from the Iguaçu machine run with the smaller radius and lower wall speed of 500 m/s diverge slightly in the top half of the rotor. Figure 96 depicted in Appendix B shows that as the Rome wall speed is slowed from 700 m/s to 500 m/s, the averaged *Pancake* and *CurvSOL* results

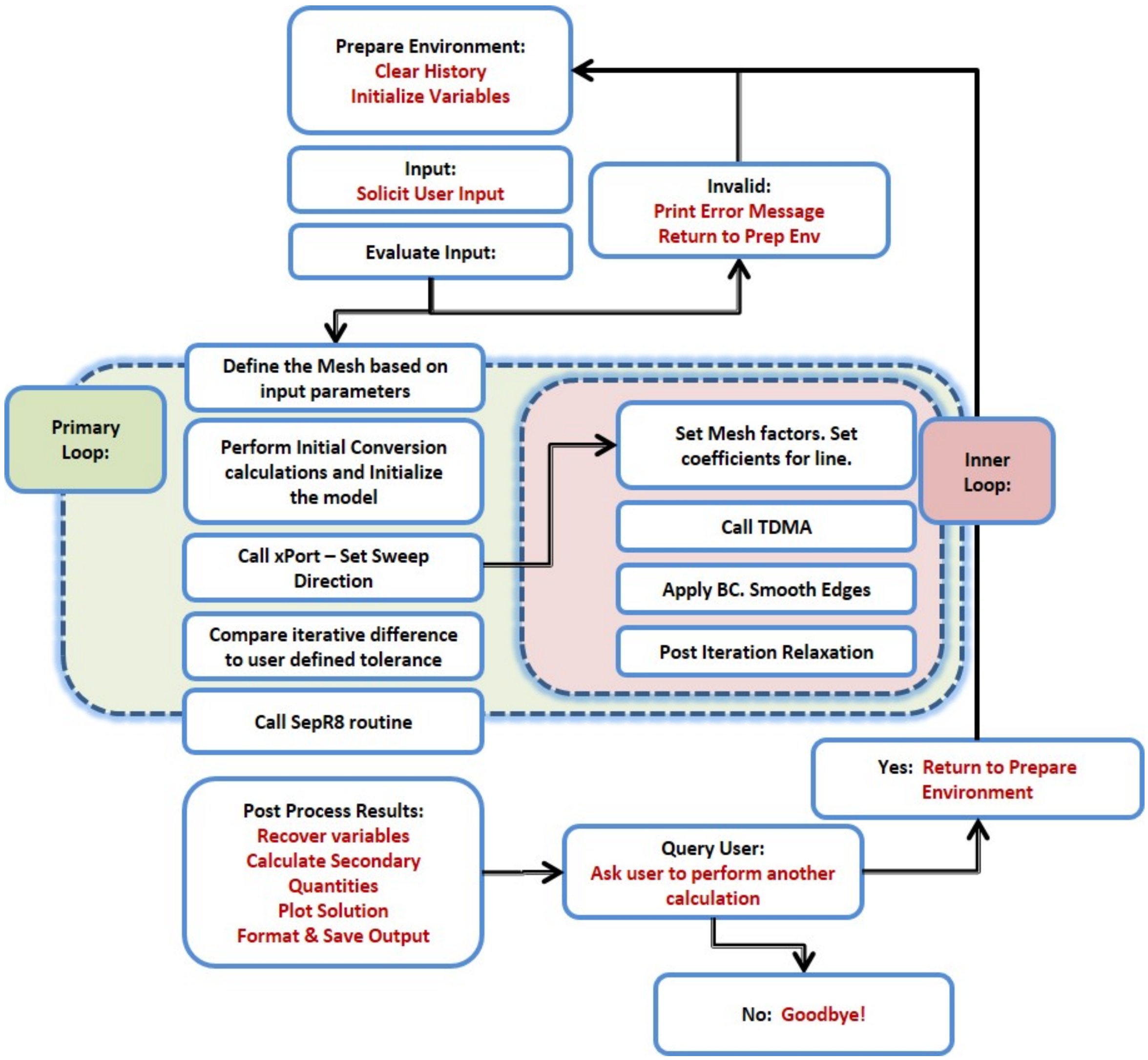

Figure 35: *xPort* Finite Differencing scheme model architecture. The user defines the computational mesh and the operating parameters for the centrifuge. After performing unit conversions, base calculations and variable initialization, the mesh is solved using the Jacobi line method with post-iteration relaxation, alternating sweep direction and employing bi-harmonic smoothing to dampen edge effects. Once the tolerance is achieved, the code calls the SepR8 post-processing routine, where the radial averaging occurs along with calculation of the separation factor, separation efficiency, and separative work.

diverge. Interestingly, as the Iguaçu wall speed is increased to 600 m/s the results align closely. But as the wall speed is further increased to 700 m/s, the results once again diverge.

Figures 40 through 43 display the results of *xPort* employing the flow solutions from the *Pancake* and *CurvSOL* code solutions for the Rome and Iguaçu centrifuges using the operating parameters listed in Table 1 and run at 700 m/s (Rome) and 500 m/s (Iguaçu). The two-dimensional contour plots are shown for each flow solution as well as three-dimensional continuous surface plots. In line with the findings of other previous efforts, the concentration of the light isotope increases from the wall to the axis (elementary centrifugal separation) and from the bottom to the top (axial separation induced by countercurrent flow) [93].

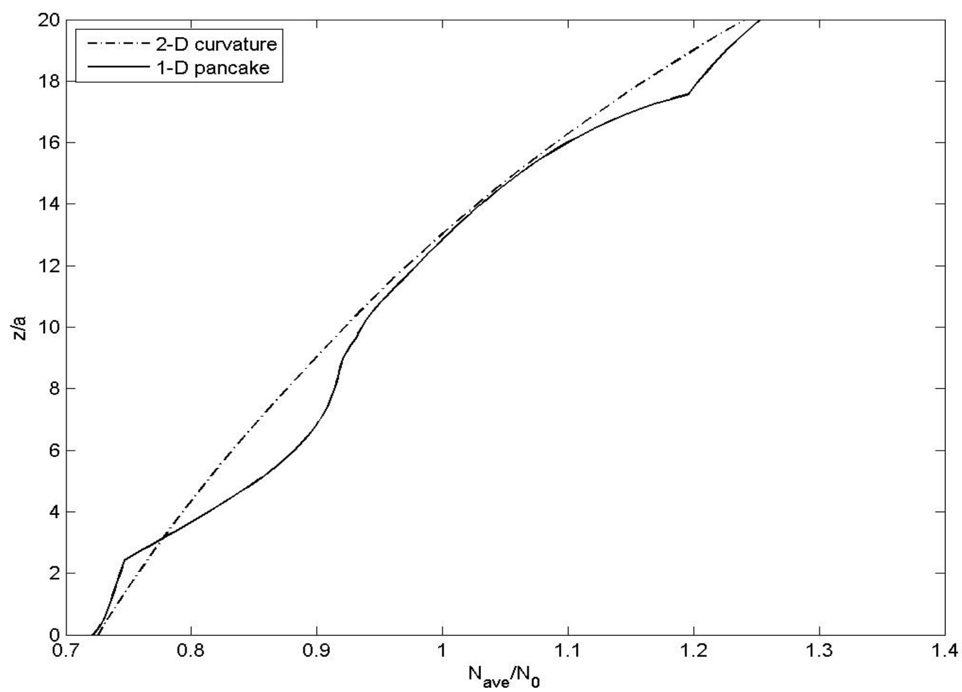

Figure 36: Comparison of the solutions of the diffusion equation for the Rome machine run at a 700 m/s wall speed. The axial variation of the light isotope concentration is shown using the results of both the finite differencing scheme (dashed line labeled "2-D curvature") and Cohen's radially averaging technique (solid line labeled "1-D pancake"). The results of *xPort* have been averaged at each axial sampling location for better comparison to the Cohen technique.

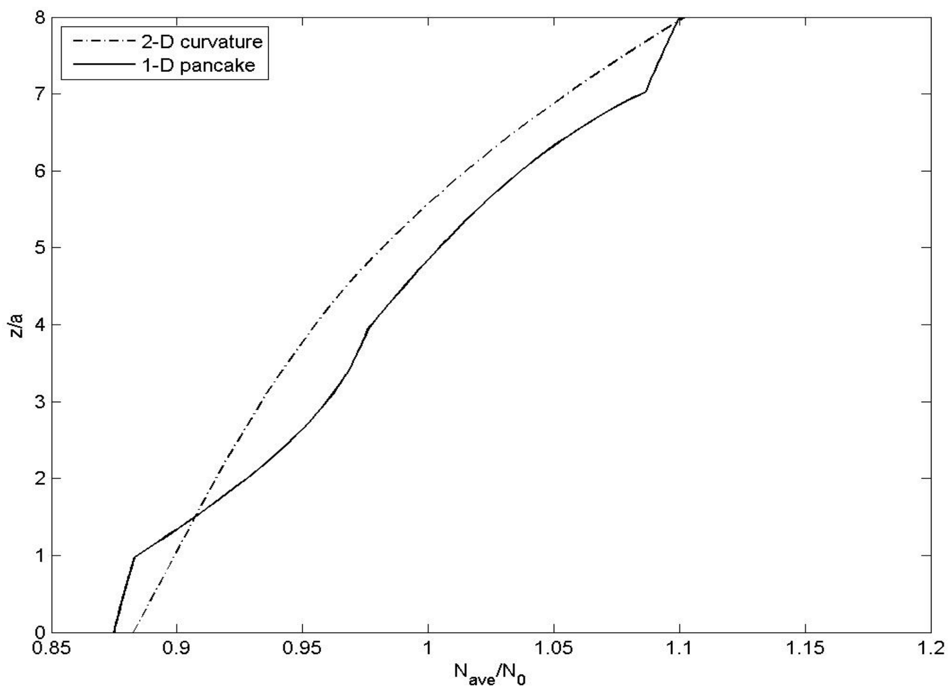

Figure 37: Comparison of the solutions of the diffusion equation for the Iguaçu machine run at a 500 m/s wall speed. The axial variation of the light isotope concentration is shown using the results of both the finite differencing scheme (dashed line labeled "2-D curvature") and Cohen's radially averaging technique (solid line labeled "1-D pancake"). The results of *xPort* have been averaged at each axial sampling location for better comparison to the Cohen technique.

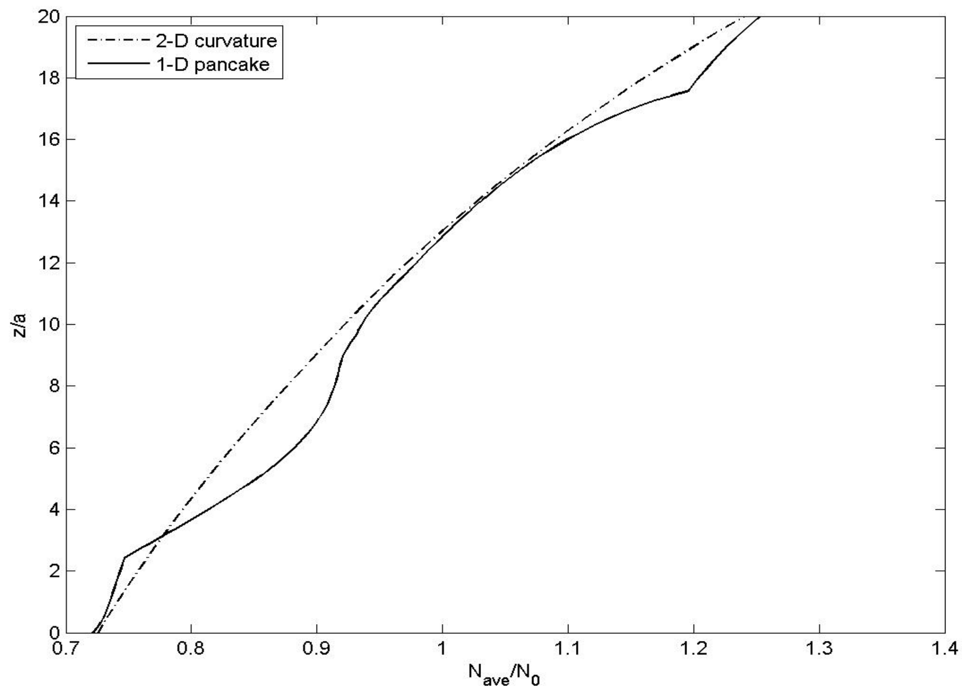

Figure 38: Comparison of the solutions of the diffusion equation for the Rome machine run at a 700 m/s wall speed. The axial variation of the light isotope concentration is shown using the results of the finite differencing scheme using the flow field from CurvSOL with curvature effects (dashed and dotted line labeled "2-D curvature"), the flow field from CurvSOL with the pancake approximation (dashed line labeled "2-D pancake"), and Cohen's radial averaging technique using the flow field from the Pancake code (solid line labeled "1-D pancake"). The results of *xPort* have been averaged at each axial sampling location for better comparison to the Cohen technique.

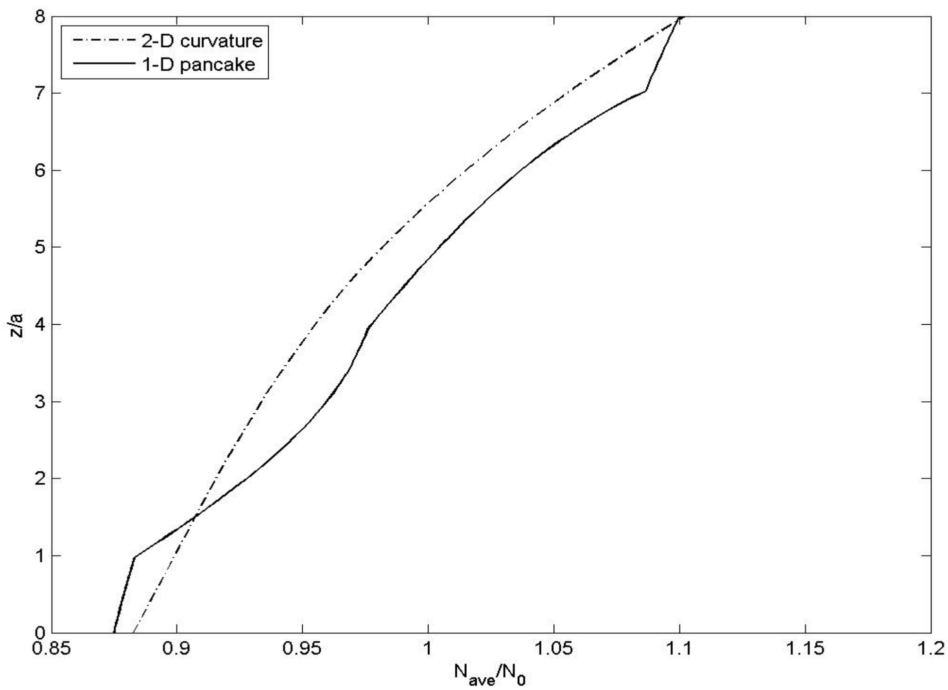

Figure 39: Comparison of the solutions of the diffusion equation for the Iguaçu machine run at a 500 m/s wall speed. The axial variation of the light isotope concentration is shown using the results of the finite differencing scheme using the flow field from CurvSOL with curvature effects (dashed and dotted line labeled "2-D curvature"), the flow field from CurvSOL with the pancake approximation (dashed line labeled "2-D pancake"), and Cohen's radial averaging technique using the flow field from the Pancake code (solid line labeled "1-D pancake"). The results of *xPort* have been averaged at each axial sampling location for better comparison to the Cohen technique.

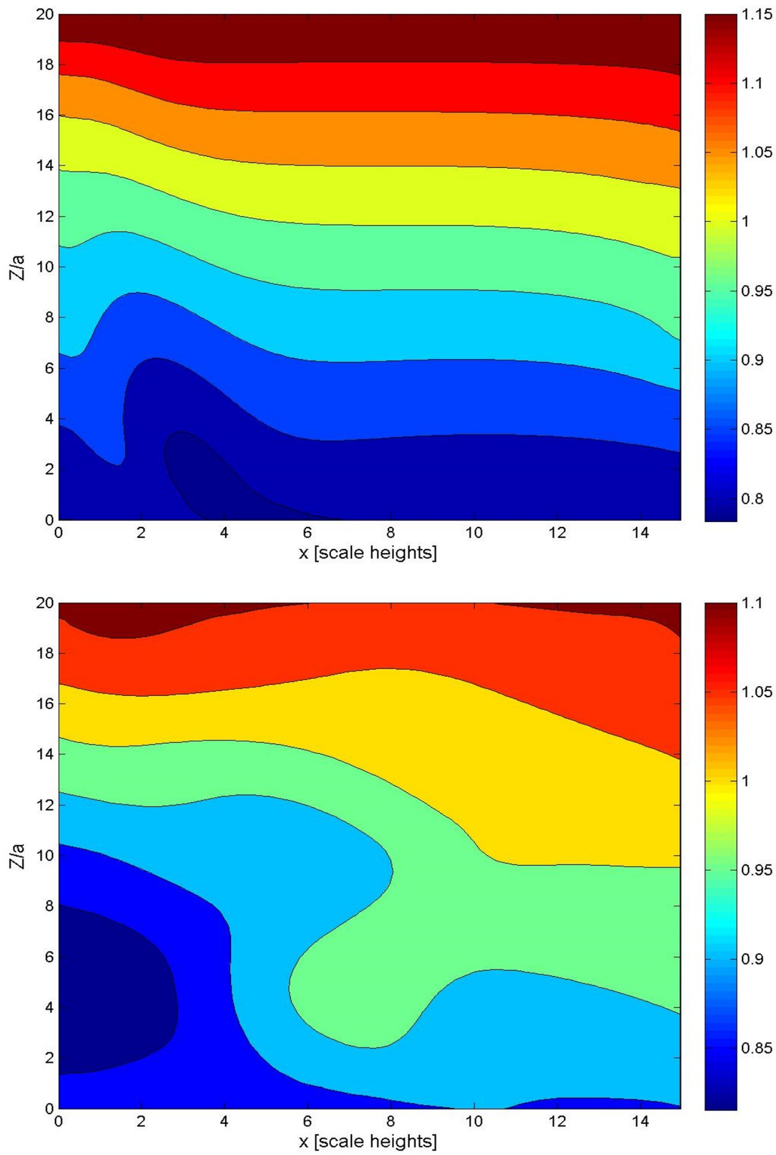

Figure 40: Two dimensional contour plot of the results of the finite difference code approximating the solution to the diffusion equation in the Rome machine with simulations run at 700 m/s wall speed. Two axial mass flux fields for each wall speed were used to run the simulations: the mass flow derived from the solution generated by the *CurvSOL* code (top) and the *Pancake* code (bottom).

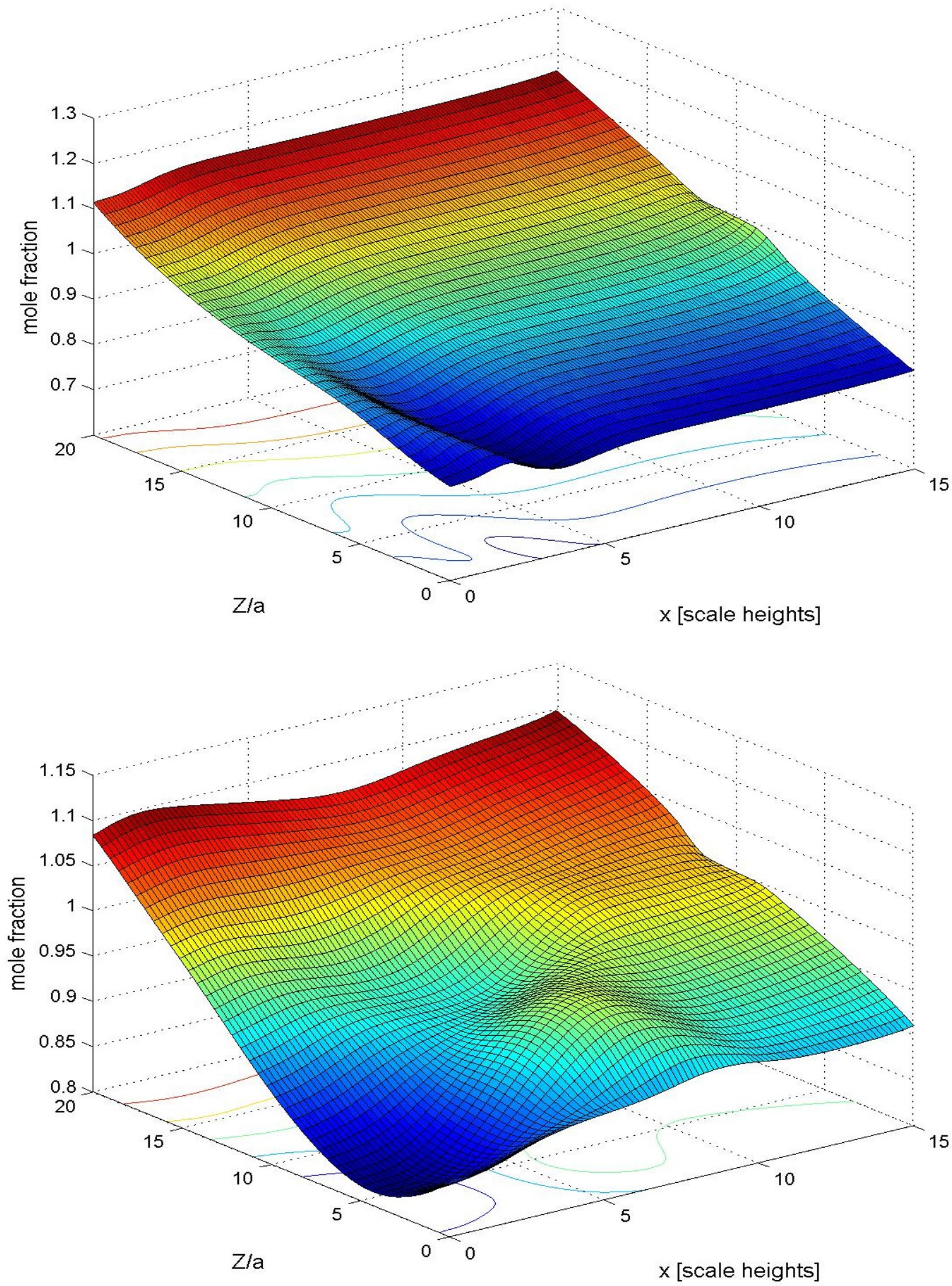

Figure 41: Continuous surface plot of the results of the finite difference code approximating the solution to the diffusion equation in the Rome machine with simulations run at 700 m/s wall speed. Two axial mass flux fields for each wall speed were used to run the simulations: the mass flow derived from the solution generated by the *CurvSOL* code (top) and the *Pancake* code (bottom).

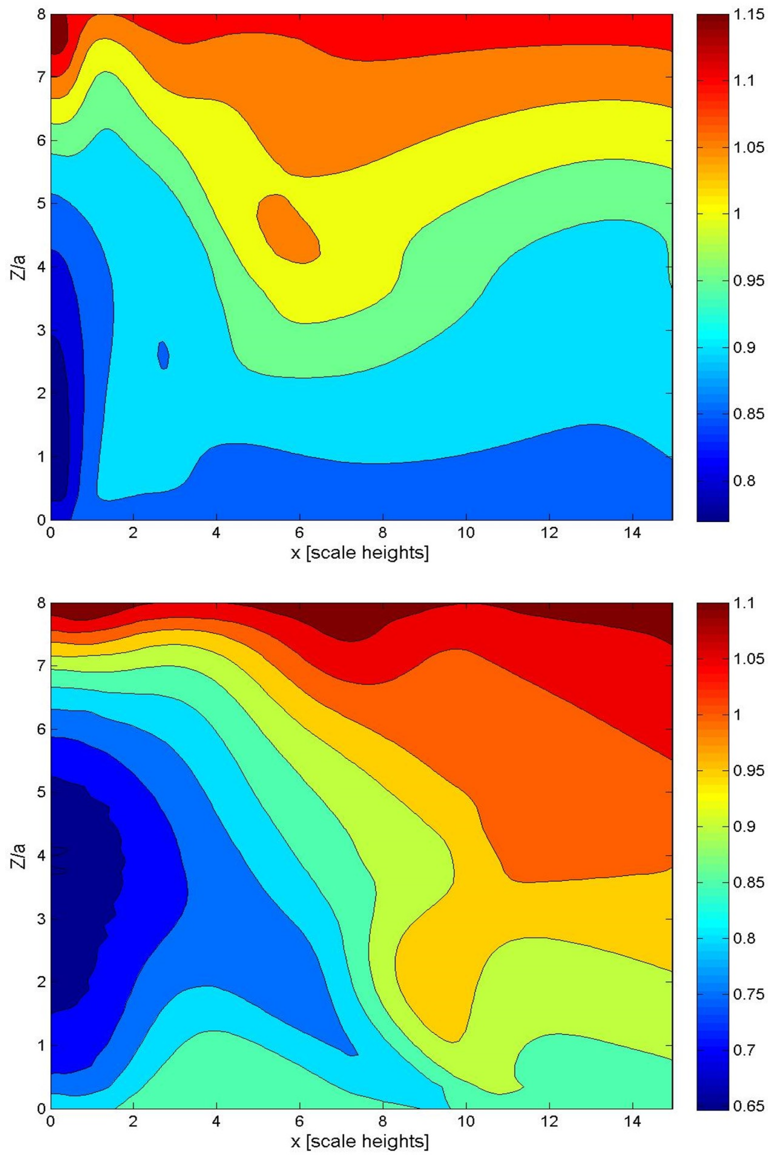

Figure 42: Two dimensional contour plot of the results of the finite difference code approximating the solution to the diffusion equation in the Iguaçu machine with simulations run at 500 m/s wall speed. Two axial mass flux fields for each wall speed were used to run the simulations: the mass flow derived from the solution generated by the *CurvSOL* code (top) and the *Pancake* code (bottom).

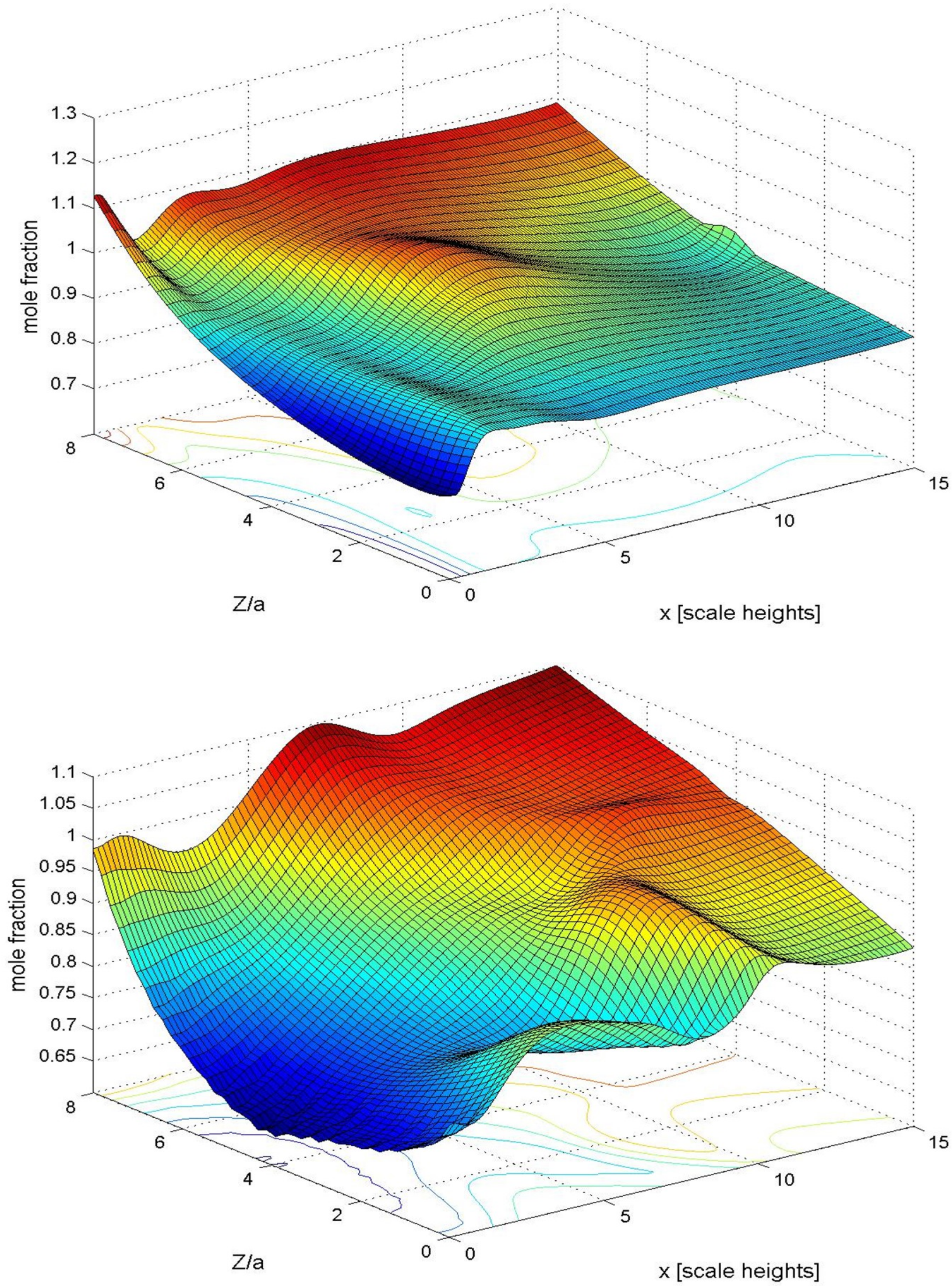

Figure 43: Continuous surface plot of the results of the finite difference code approximating the solution to the diffusion equation in the Iguaçu machine with simulations run at 500 m/s wall speed. Two axial mass flux fields for each wall speed were used to run the simulations: the mass flow derived from the solution generated by the *CurvSOL* code (top) and the *Pancake* code (bottom).

7 Separation

The separation of isotopes is governed by the transport described earlier in the Diffusion chapter. The results of the approximation detailed in the previous chapter give an estimate of the separative effect based on the operating parameters and centrifuge design. In this chapter, the results from the separation simulations are used as a means to characterize the performance of an individual centrifuge design. Ranging the cut value and the feed rate, centrifuge performance maps are generated for subsequent use in modeling routines for predictive analysis of enrichment cascades.

7.1 Quantifying Performance

The individual separation unit performance in an enrichment facility is generally measured by two quantities, the separation factor and the separative capacity. The overall separation factor is given as

$$\gamma = \frac{N_P}{1 - N_P} \cdot \frac{1 - N_W}{N_W}. \tag{7.1}$$

Practically, any commercial tool is characterized by the amount of useful work it can perform over a given period. In the case of the separation unit, this is the separative capacity, or separative work, and is defined as

$$\delta U = LV(N_P) + DV(N_W) - GV(N_F) \tag{7.2}$$

where L is the upflow, D is the downflow, G is the feed, N_P, N_W, and N_F are the product, waste, and feed concentrations, and $V(N)$ is the value function [65] and is given by

$$V(N) = (2N - 1)\ln\left(\frac{N}{1 - N}\right). \tag{7.3}$$

7.2 Centrifuge Performance Mapping

The overall separative performance of a centrifuge is estimated based on the isotopic diffusion predicted by the transport model. The input parameters of the transport model are then adjusted and a new separative performance estimate obtained. A systematic variation of parameters allows an effective mapping of centrifuge performance to determine an optimal performance estimate for that particular set of centrifuge design parameters [50]. A two-dimensional centrifuge performance map is obtained by varying the feed and cut over a specified range.

Figures 45 and 44 show performance maps of the separation factor and separative work of the fictional Rome and Iguaçu centrifuges created using the Pancake code developed by Wood [24][63]. Figures 46 through 48 depict performance maps for the Rome machine run with wall speeds of 500, 600, and 700 m/s. Figures 49 through 51 depict maps generated for the Iguaçu centrifuge operated at the same speeds. Figures 48 and 51 show a three dimensional view of the separative for the Rome and Iguaçu machines, respectively. In each of the figures from 46 to 51, the surfaces on the left were generated using the radial averaging method based on the results from the Pancake model. The surfaces on the right resulted from the finite differencing model based on the flow solution generated by the CurvSOL FEA code. Once again, three wall speeds were simulated: 500 m/s (top), 600 m/s (middle), and 700 m/s (bottom). The Iguaçu maps generated at the lower wall speeds agree closely, while the Rome maps have greater agreement at the higher wall speed. All of the performance mapping results for each centrifuge design and each wall speed simulated are found in Appendix C.

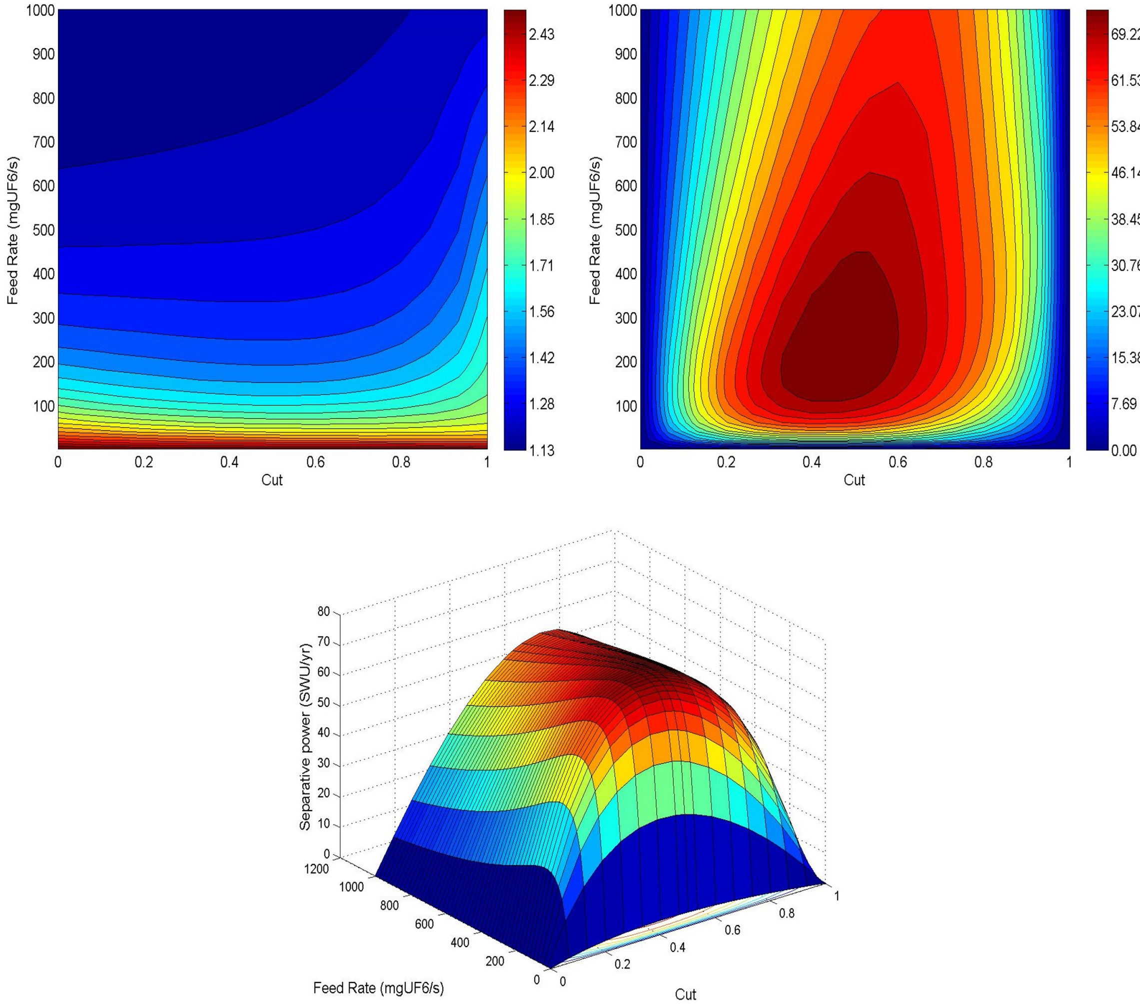

Figure 44: Performance maps for the Rome machine with simulations run at 700 m/s. The diffusion of the light isotope was modeled using Cohen's radial averaging technique based on the flow solution from the *Pancake* code. Three maps are shown: the Separation factor contour map (top left), the Separative power contour map (top right), and the Separative power continuous surface plot (bottom).

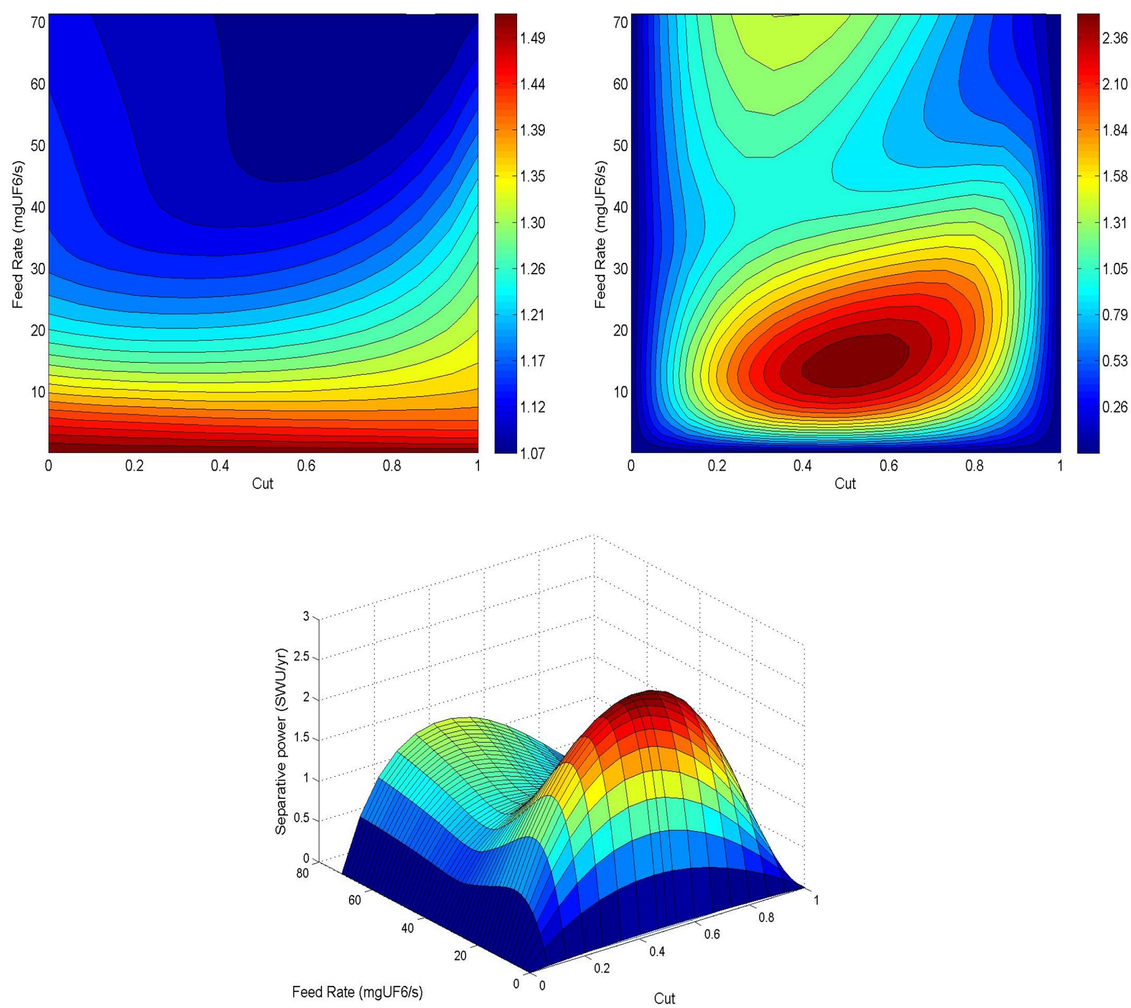

Figure 45: Performance maps for the Iguaçu machine with simulations run at 500 m/s. The diffusion of the light isotope was modeled using Cohen's radial averaging technique based on the flow solution from the *Pancake* code. Three maps are shown: the Separation factor contour map (top left), the Separative power contour map (top right), and the Separative power continuous surface plot (bottom).

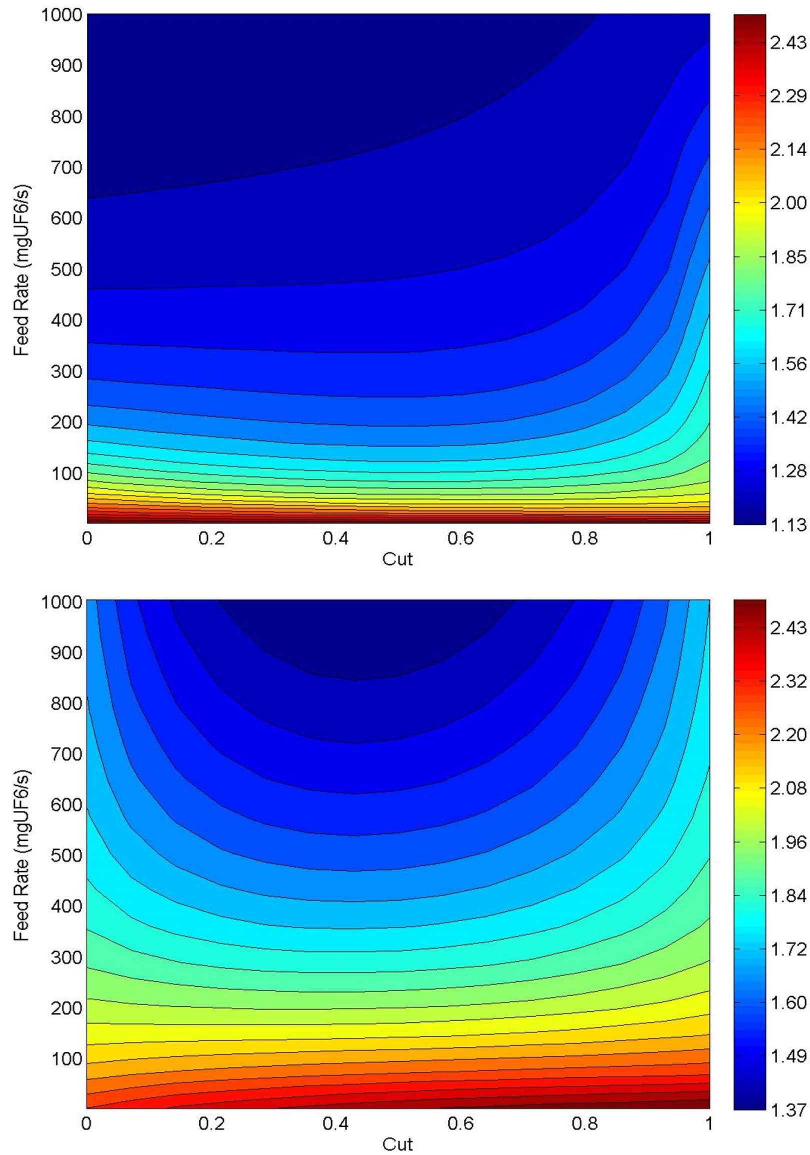

Figure 46: Two dimensional contour plots of the separation factor for the Rome machine run at 700 m/s wall speed. The diffusion of the light isotope was modeled using two methods: Cohen's radial averaging technique based on the flow solution from the *Pancake* code (top) and finite differencing utilizing the flow solution from the *CurvSOL* code (bottom).

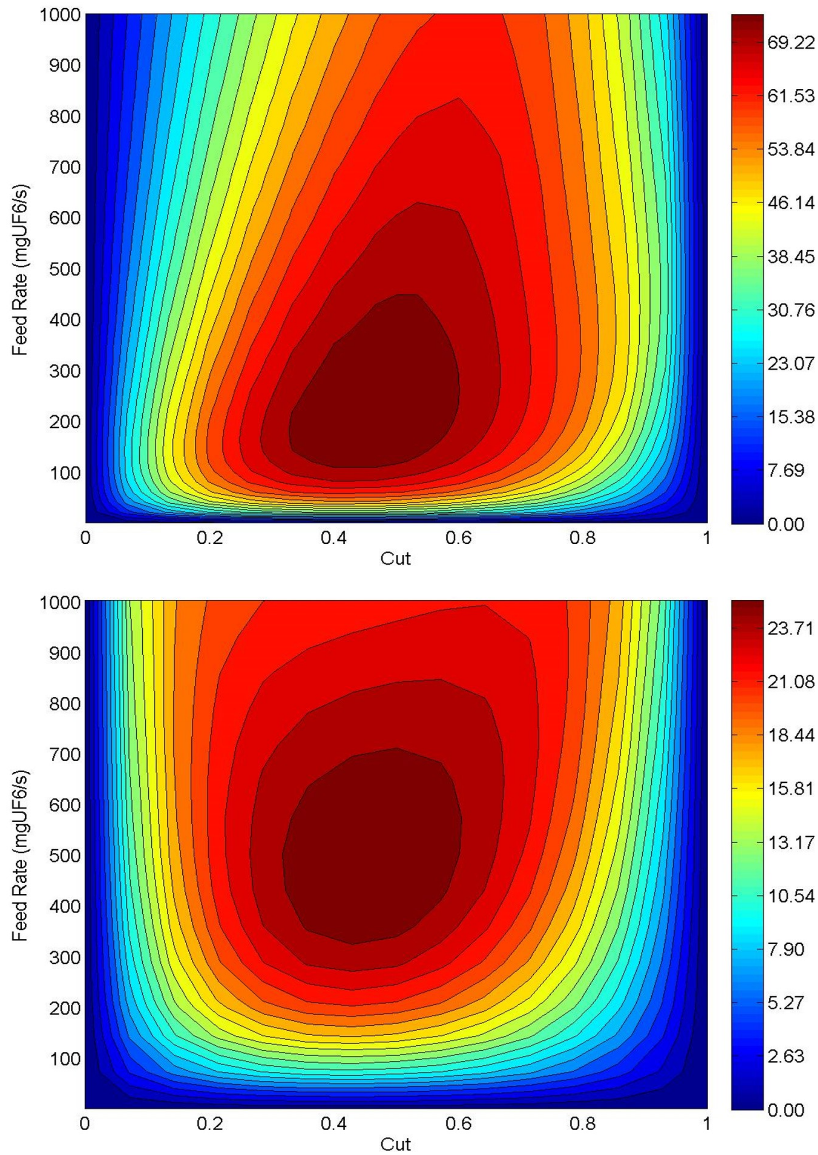

Figure 47: Two dimensional contour plots of the separative power for the Rome machine run at 700 m/s wall speed. The diffusion of the light isotope was modeled using two methods: Cohen's radial averaging technique based on the flow solution from the *Pancake* code (top) and finite differencing utilizing the flow solution from the *CurvSOL* code (bottom).

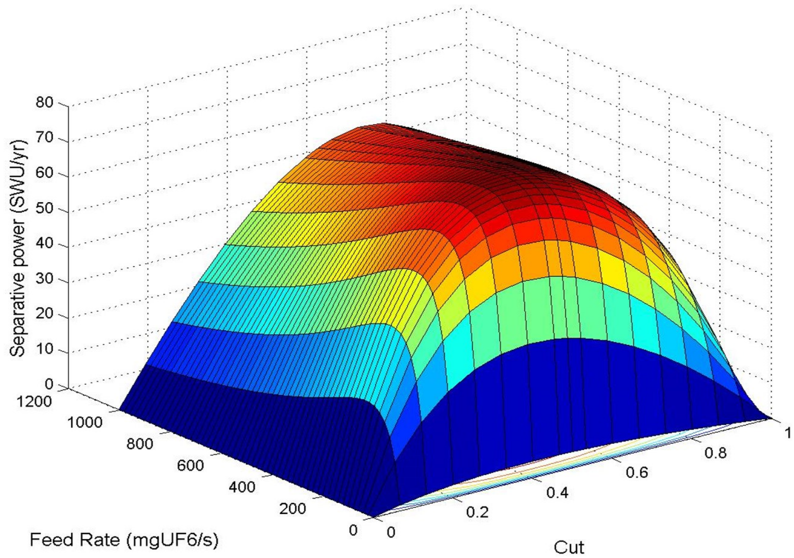

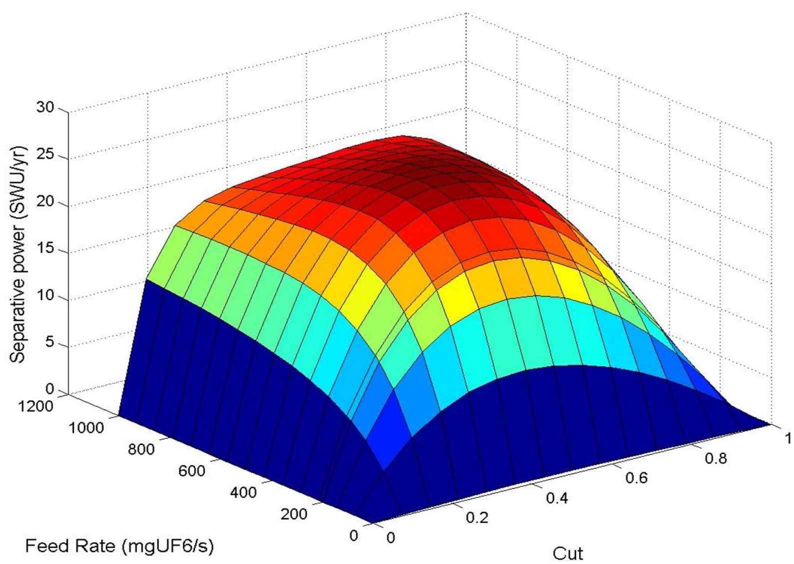

Figure 48: Three dimensional continuous surface plots of the separative power for the Rome machine run at 700 m/s wall speed. The diffusion of the light isotope was modeled using two methods: Cohen's radial averaging technique based on the flow solution from the *Pancake* code (top) and finite differencing utilizing the flow solution from the *CurvSOL* code (bottom).

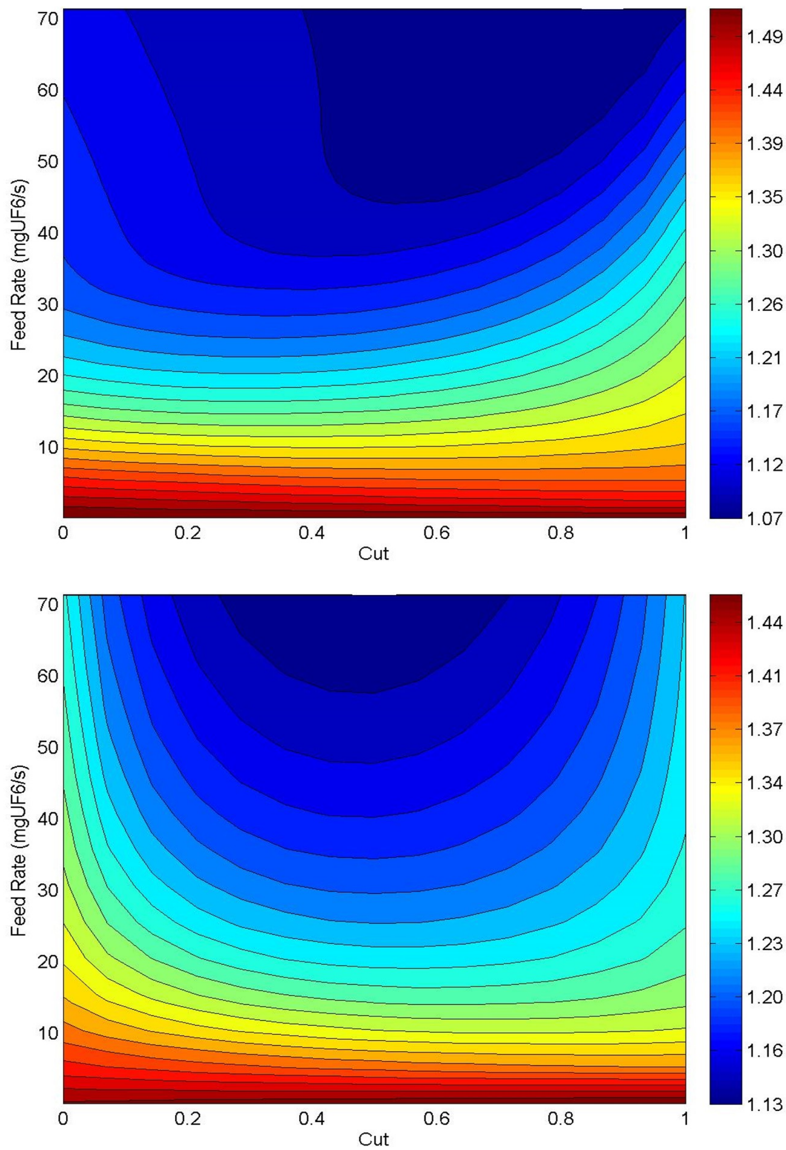

Figure 49: Two dimensional contour plots of the separation factor for the Iguaçu machine run at 500 m/s wall speed. The diffusion of the light isotope was modeled using two methods: Cohen's radial averaging technique based on the flow solution from the *Pancake* code (top) and finite differencing utilizing the flow solution from the *CurvSOL* code (bottom).

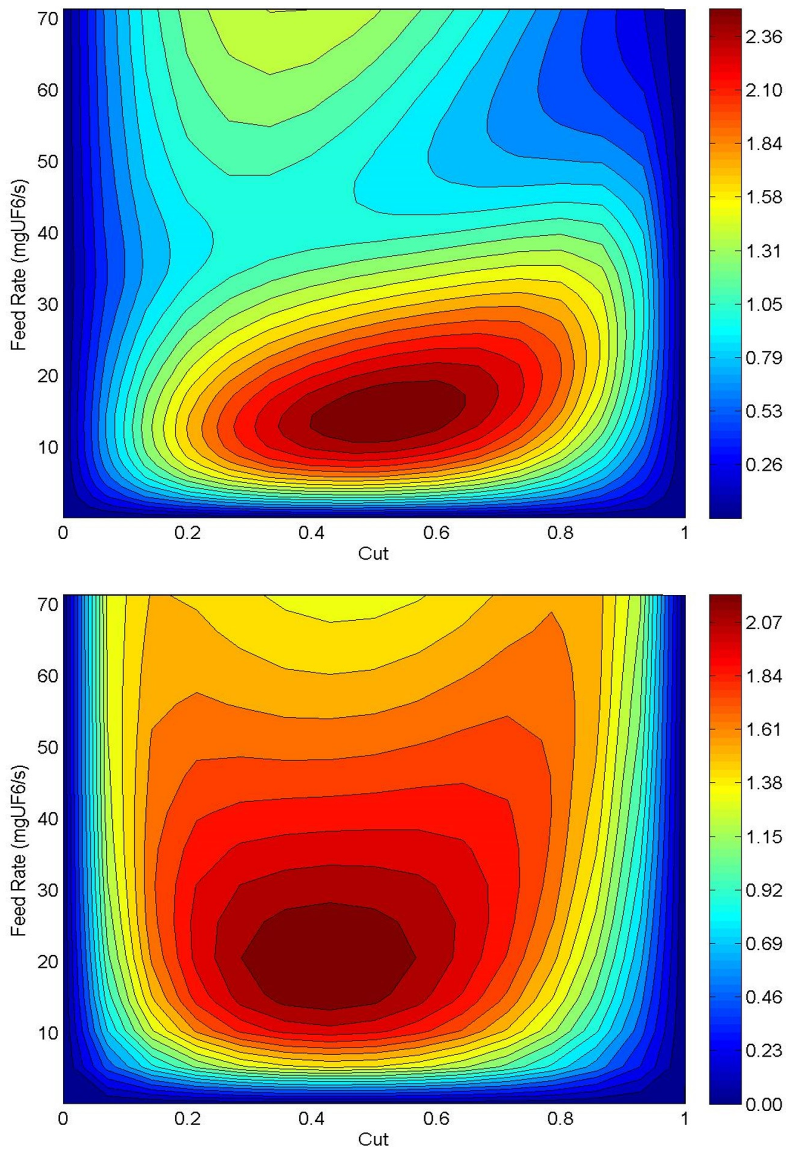

Figure 50: Two dimensional contour plots of the separative power for the Iguaçu machine run at 500 m/s wall speed. The diffusion of the light isotope was modeled using two methods: Cohen's radial averaging technique based on the flow solution from the *Pancake* code (top) and finite differencing utilizing the flow solution from the *CurvSOL* code (bottom).

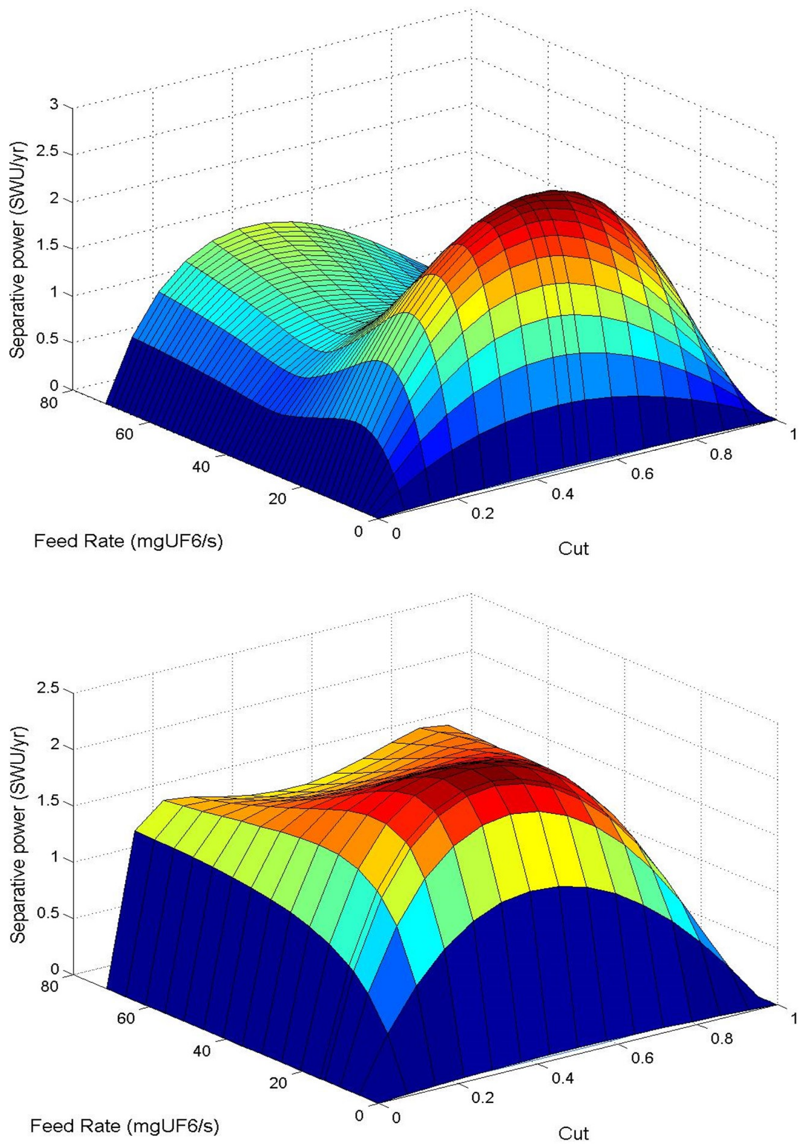

Figure 51: Three dimensional continuous surface plots of the separative power for the Iguaçu machine run at 500 m/s wall speed. The diffusion of the light isotope was modeled using two methods: Cohen's radial averaging technique based on the flow solution from the *Pancake* code (top) and finite differencing utilizing the flow solution from the *CurvSOL* code (bottom).

8 Applications

As described in the introduction, numerous applications exist for higher fidelity flow and transport models of gas centrifuges, ranging from optimization of commercial enrichment machines to nonproliferation monitoring. The overarching motivation for this project is improved nonproliferation focused modeling of existing and emerging state enrichment capabilities. In the same vein as the work presented in [84][85][86][87], this project is designed to provide another tool for the academic, political, and international safeguards communities to assess a State's ability to leverage their enrichment capability for other than declared purposes. This chapter begins with an introduction to cascade theory, continues with a fixed-plant proliferation analysis and breakout timeline estimation, and concludes with an isotopic ratio comparison method to characterize cascade enrichment history. Much of the material from this chapter is taken from *Fixed Plant Analysis of Iran's Post-JCPOA Breakout Potential* presented to the American Nuclear Society's Advances in Nuclear Nonproliferation Technology and Policy Conference (ANNTPC) and *Minor Isotope Safeguards Techniques(MIST): Analysis and Visualization of Gas Centrifuge Enrichment Plant Process Data Using the MSTAR Model* accepted for publication in *Nuclear Instruments and Methods in Physics Research Section A: Accelerators, Spectrometers, Detectors and Associated Equipment.*

8.1 Cascade Modeling

The separation achieved by a single separator unit can vary significantly between the types of separators. Additionally, the operational throughput of a single unit is so small that accumulation of appreciable quantities of enriched material requires a large number of separators connected in parallel banks, or stages, and a number of stages then connected in series. This arrangement of enrichment units is known as a cascade.

The study of cascade theory begins with a balance of the mass entering and leaving the entire system, or the cascade as a whole, as described by

$$F = P + W, \tag{8.1}$$

where F is the feed, P is the product withdrawn, also called the heads, and W is the waste, or tails. Theses figures are typically given as rates. Multiplying these rates by the concentration of the desired isotope in each stream gives the isotopic material balance,

$$FN_F = PN_P + WN_W, \tag{8.2}$$

with N_F, N_P, and N_W representing the concnetration of uranium-235 in the feed, heads, and tails, respectively. Applying this to each stage in the cascade gives

$$G_n = L_n + D_n, \tag{8.3}$$

and

$$G_n N_n = L_n N'_n + D_n N''_n, \tag{8.4}$$

where G_n is the n^{th} stage feed, L_n is the stage upflow, D_n is the stage downflow, and N_n, N'_n, and N''_n, are the isotope concentrations in the n^{th} stage feed, upflow, and downflow.

The ratio of the upflow and feed in a stage defines the stage cut,

$$\theta_n = \frac{L_n}{G_n}. \tag{8.5}$$

Incorporating equation (8.3) gives

$$\theta_n = \frac{L_n}{G_n} = 1 - \frac{D_n}{G_n}, \tag{8.6}$$

and further application of equation (8.4) gives

$$\theta_n = \frac{N_n - N_n''}{N_n' - N_n''}. \tag{8.7}$$

To achieve perfect efficiency, no losses must occur between stages, or

$$N_n = N_{n-1}' = N_{n+1}''. \tag{8.8}$$

This represents an ideal cascade. There are no losses due to mixing of concentration or losses of separative power. The ideal cascade does not contain a finite number of machines arranged in series parallel, rather a continuous variation. In practice, the ideal cascade is approximated with the 'squared-off' cascade of banks and stages. While impossible to achieve physically, the analysis of the ideal cascade helps in the design of the efficient physical system.

Continuing the n^{th} stage analysis, three different separation factors are derived from the abundance ratio, R, where

$$R(x) = \frac{x}{1-x}. \tag{8.9}$$

These are the overall stage separation factor

$$\gamma_n = \frac{R(N_n')}{R(N_n'')} = \frac{N_n'}{1-N_n'} \cdot \frac{1-N_n''}{N_n''}, \tag{8.10}$$

the stage heads separation factor

$$\alpha_n = \frac{R(N_n')}{R(N_n)} = \frac{N_n'}{1-N_n'} \cdot \frac{1-N_n}{N_n}, \tag{8.11}$$

and the stage tails separation factor

$$\beta_n = \frac{R(N_n)}{R(N''_n)} = \frac{N_n}{1 - N_n} \cdot \frac{1 - N''_n}{N''_n}. \tag{8.12}$$

Combining equations (8.10) through (8.12) gives

$$\gamma_n = \alpha_n \cdot \beta_n, \tag{8.13}$$

which, for the ideal cascade is

$$\sqrt{\gamma_n} = \alpha_n = \beta_n. \tag{8.14}$$

Letting $\psi = \gamma_n - 1$, equation (8.10) may be rearranged to give the n^{th} stage equilibrium line equation [24][65],

$$N'_n - N''_n == \frac{\psi_n N''_n (1 - N''_n)}{1 + \psi_n N''_n}. \tag{8.15}$$

Applying equations (8.3) and (8.4) to just the n^{th} stage gives

$$L_{E,n} = D_{E,n+1} + P, \tag{8.16}$$

and

$$L_{E,n} N'_{E,n} = D_{E,n+1} N''_{E,n+1} + P N_P. \tag{8.17}$$

Combining these two equations gives the n^{th} stage operating line equation

$$L_{E,n} N'_{E,n} = (L_n - P) N''_{E,n+1} + P N_P. \tag{8.18}$$

Applying the same analysis to the stripping section of the cascade yields the m^{th} stage equilibrium equation

$$N'_n - N''_n == \frac{\psi_m N''_m(1 - N''_m)}{1 + \psi_m N''_m}, \tag{8.19}$$

the stripping section operating line equations, represented for the m^{th} stage as

$$(W + L_{S,m-1})N''_{S,m} = WN_W + L_{S,m-1}N'_{S,m-1}. \tag{8.20}$$

Equations (8.15), (8.18), (8.19), and (8.20) may be combined to give the gradient equations for the enriching section

$$N''_{E,n+1} - N''_{E,n} = \frac{L_{E,n}}{L_{E,n} - P}\left(\frac{\psi_{E,n}N''_{E,n}(1 - N''_{E,n})}{1 + \psi_{E,n}N''_{E,n}} - \frac{P}{L_{E,n}}(N_P - N''_{E,n})\right), \tag{8.21}$$

and the stripping section

$$N''_{S,m+1} - N''_{S,m} = \frac{L_{S,m}}{L_{S,m} + W}\left(\frac{\psi_{S,m}N''_{S,m}(1 - N''_{S,m})}{1 + \psi_{S,m}N''_{S,m}} - \frac{W}{L_{S,m}}(N''_{S,m} - N_W)\right). \tag{8.22}$$

These gradient equations represent a finite differencing scheme that, along with the design and operating parameters of the cascade, describes the concentration gradient of the desired isotope throughout the cascade. Ideal cascade analysis proves useful in determining these design and operating parameters. Considering equations (8.8) and (8.14), expressions for the stage feed concentration in the enriching section are given as

$$N_n = \frac{R(N_F)\alpha_0^{n-1}}{1 + R(N_F)\alpha_0^{n-1}}, \tag{8.23}$$

and in the stripping section

$$N_m = \frac{R(N_F)\alpha_0^{m-1}}{1 + R(N_F)\alpha_0^{m-1}}. \tag{8.24}$$

Letting $m = n - n_s$, where n_s is the total number of stripping stages, the previous equation may be written

$$N_m = \frac{R(N_F)\alpha_0^{n-n_s-1}}{1 + R(N_F)\alpha_0^{n-n_s-1}}. \tag{8.25}$$

Further, equations (8.23) and (8.25) may be rearranged as

$$n_e = \ln\left(\frac{R(N_P)}{R(N_F)}\right) \cdot \frac{1}{\ln(\alpha_0)} + 1, \tag{8.26}$$

to describe the number of stages required in the enriching section, and

$$n_s = \ln\left(\frac{R(N_F)}{R(N_W)}\right) \cdot \frac{1}{\ln(\alpha_0)}, \tag{8.27}$$

for the number of required stages for the stripping section. Equations (8.7) and (8.11) may be combined to find an expression for the relationship between the stage cut and stage heads separation factor, given by

$$\theta_n = \frac{1 + (\alpha_0 - 1)N_n}{\alpha_0 + 1}. \tag{8.28}$$

Additionally, mass balance between the cascade product stream and the n^{th} enriching stage may be written

$$L_n N_n' = (L_n - P)N_n + PN_P. \tag{8.29}$$

Expressions for the cut and the separation factor given in equations (8.7) and (8.28) may be similarly drawn between the overall product stream and n^{th} stage to describe the stage feed rate

Table 2: Basic Cascade Design Information for the Performance Map Comparison Study [24]

Parameter	units	Iguaçu	Rome
Feed Rate	kgU/yr	20990	18630
Feed Conc.	at. frac.	0.0072	0.0072
Product Conc.	at. frac.	0.0350	0.0350
Tails Conc.	at. frac.	0.0035	0.0035
Enriching Stages	-	14	13
Stripping Stages	-	5	5
Stages Total	-	19	18
Nominal Separative Power	SWU/yr	10000	10000
Total Centrifuges	-	2268	186

$$G_n = P \cdot \frac{\alpha_0 + 1}{\alpha_0 - 1} \cdot \frac{N_P - N_n}{N_n(1 - N_n)}. \tag{8.30}$$

A similar expression for the stage feed in the stripping section is made by comparison between the overall tails stream and the m^{th} stripping stage and given

$$G_m = W \cdot \frac{\alpha_0 + 1}{\alpha_0 - 1} \cdot \frac{N_m - N_W}{N_m(1 - N_m)}. \tag{8.31}$$

Considering G_0 is the total cascade feed rate, the total number of centrifuges for the n^{th} stage, M_n, may then be found

$$M_n = G_n/G_0. \tag{8.32}$$

This is valid for the n^{th} stage in the enriching section as well as the m^{th} stage in the stripping section.

Equations (8.23) through (8.32) may be used to determine the ideal cascade based on defined parameters. These parameters along with the 'squared-off' approximation to the ideal cascade may then be used in the finite differencing scheme described in equations (8.21) and (8.22) to determine the desired isotope concentration gradient

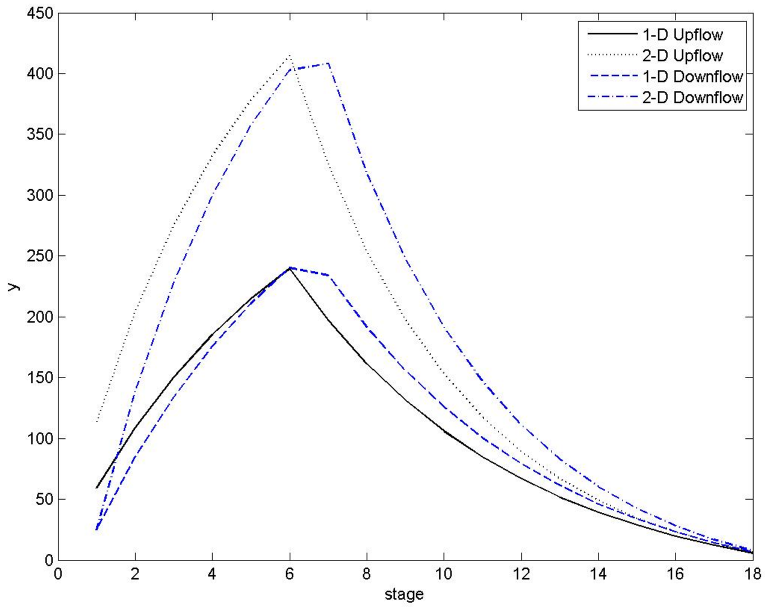

Figure 52: Comparison of upflow and downflow for the Rome machine simulation run with a wall speed of 700 m/s. The results of the cascade solver using the performance maps generated based on the one dimensional radial averaging technique and the two dimensional *xPort* code are compared by stage.

throughout the cascade. The matlab code *FixedCascBin* is software developed by Migliorini to solve these gradient equations for a user defined cascade of separators defined by two dimensional performance maps, assuming the uranium hexafluoride feed gas is a binary mixture of uranium-235 and uranium-238 [24][63].

Figures 52 and 53 depict comparisons of the upflow and downflow by stage in the cascades described in Table 2 for the Rome and Iguaçu centrifuge one dimensional and two dimensional separation code derived performance maps, respectively. In both cases, the estimated upflow and downflow are greater in the enriching section for the two dimensional code. However, in the stripping section, the one dimensional code solution estimate is greater in both cases. Similarly, figures 54 and 55 depict the upflow and downflow enrichment. In both cases the curves display strong agreement, but the enrichment in both flows is less at every stage for the two dimensional based performance map simulation.

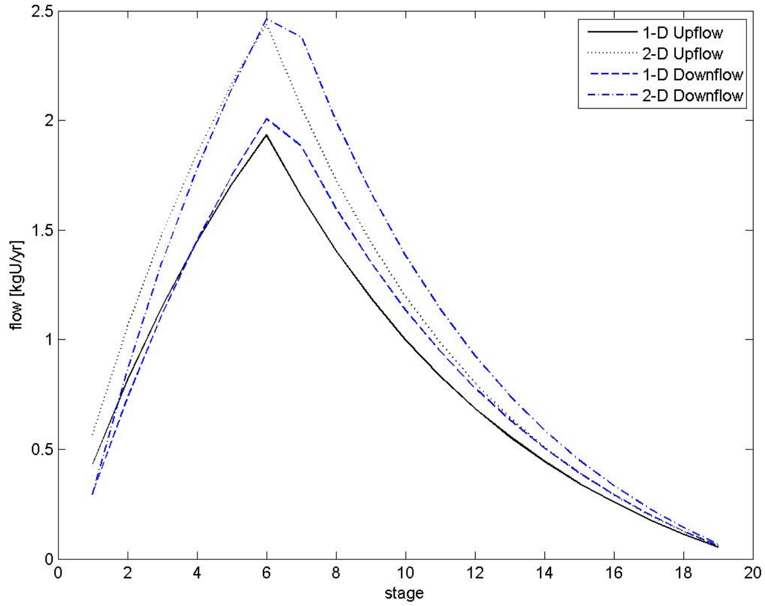

Figure 53: Comparison of upflow and downflow for the Iguaçu machine simulation run with a wall speed of 500 m/s. The results of the cascade solver using the performance maps generated based on the one dimensional radial averaging technique and the two dimensional *xPort* code are compared by stage.

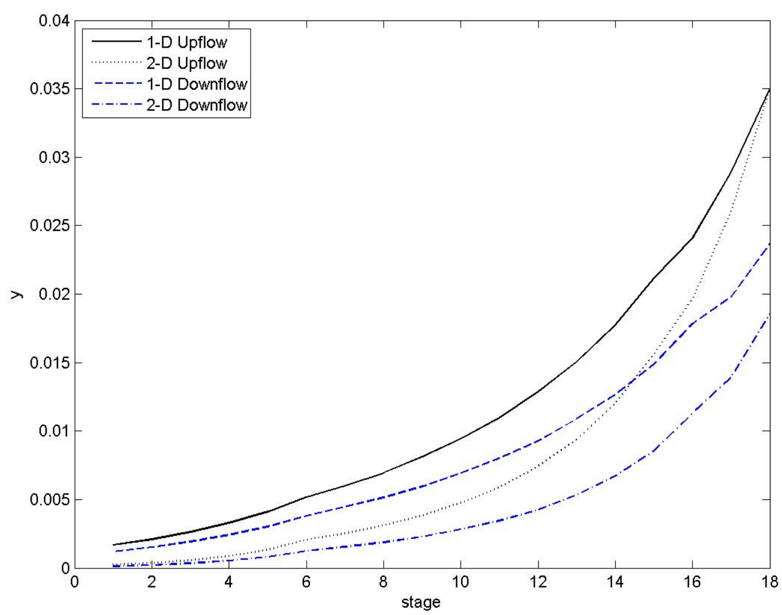

Figure 54: Comparison of upflow and downflow enrichment level for the Rome machine simulation run with a wall speed of 700 m/s. The results of the cascade solver using the performance maps generated based on the one dimensional radial averaging technique and the two dimensional *xPort* code are compared by stage.

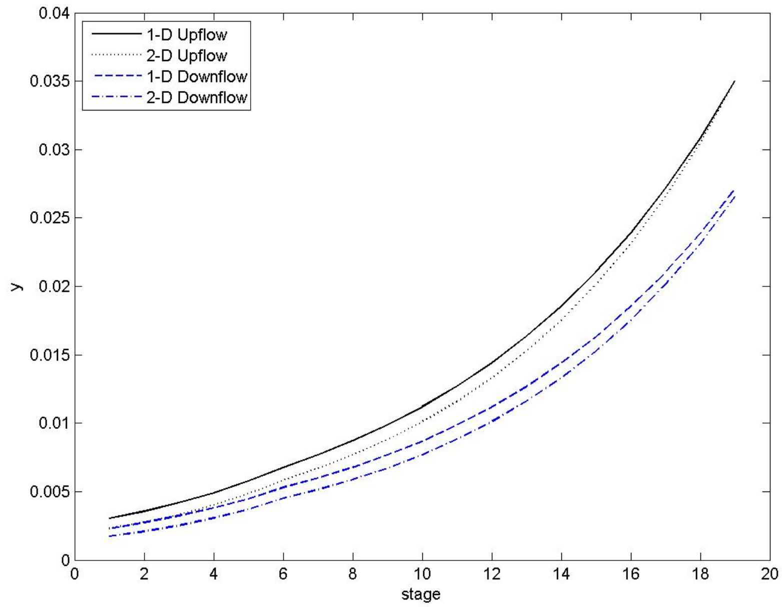

Figure 55: Comparison of upflow and downflow enrichment level for the Iguaçu machine simulation run with a wall speed of 500 m/s. The results of the cascade solver using the performance maps generated based on the one dimensional radial averaging technique and the two dimensional *xPort* code are compared by stage.

8.2 Breakout Scenarios

The enrichment capacity of a centrifuge cascade facility is often estimated based on the achievable amount of Separative Work Units of the aggregate number of machines in the facility rather than capacity of the actual cascades existing in the facility. While a cascade can be designed to approximate the necessary ideal cascade, SWU-based breakout timeline estimates do not take into consideration the time required to configure the equipment or the inherent error introduced when the ideal cascade is squared-off. A fixed-plant method produces a breakout timeline estimate based on existing cascades [97]. The *CascSCAN* code utilizes a modified version of Miglioirini's *FixedCascBin* cascade solver for binary separation, the information contained in the performance map, and cascade design parameters to scan over the range of possible cascade configurations to determine the time to necessary to achieve a significant quantity of weapons grade uranium [24]. Figure 56 depicts the architecture of the

CascSCAN code.

The number of cascades in each step of a 4-step batch enrichment process designed to enrich natural uranium to weapons grade may vary depending on the amount of feed material and desired product rate. Per the Joint Comprehensive Plan of Action (JCPOA) of 2015, the Islamic Republic of Iran is limited to 5,060 operational IR-1 centrifuges installed at the Natanz GCEP. Existing inventory of 3.5% low enriched uranium (LEU) is limited to 300 kg and no 20% in any form other than fabricated fuel is authorized. Additionally, the number of centrifuge cascades at the Natanz GCEP is limited to 30. Figures 57 amd 58 show the results of the *CascSCAN* code, scanning over all possible configurations of 5,060 centrifuges arranged in 173 machine cascades in either a full 4 step process or the modified 3 step process using an existing inventory of approximate 3.5% LEU. The tails of each step are recycled and included into the feed of the lower step. These simulations considered inclusion of existing inventories of 3.5% and near 20% (defined as 19.75% for analytic purposes when solving the cascade gradient equations) initially fed to the cascade at a rate that would exhaust the inventory in one year. Once the initial breakout estimate was obtained by exhausting the inventory in one year, the simulation process was repeated and the existing inventory fed at a rate to exhaust the supply in the amount time determined by the initial estimate.

The resulting data set was analyzed to determine a mean and minimum time to achieve one significant quantity of WGU. Though the simulations vary the amount of near 20% UF_6 introduced in step 3, the estimated breakout times do not include any time to convert near 20% fuel assemblies into UF_6. Figures 57 and 58 depict the minimum achievable breakout time for the 3 and 4 step batch processes for different levels of near 20% inventory. Figure 59 represents a comparison of the 3 and 4 step batch process for a particular amount of existing near 20% inventory and a range of 3.5% inventory. The 3 step process appears to offer no advantage over the 4 step

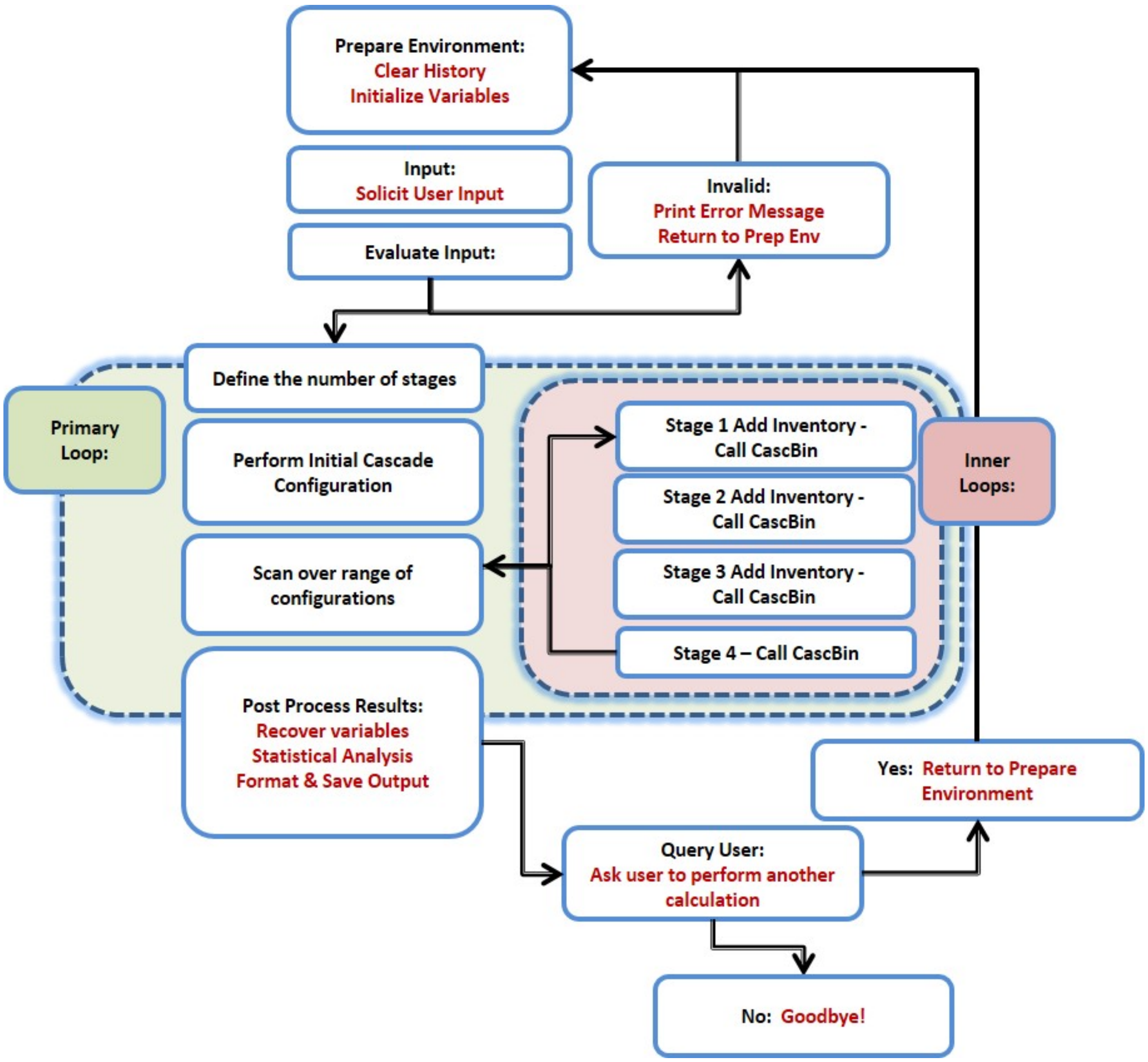

Figure 56: Cascade configuration scanning model architecture. The *CascSCAN* code sets an initial configuration of cascades based on the user defined total number of centrifuge tubes. Depending on the centrifuge design, the total number of machines is divided into a number of cascades that are then arranged in a "cascade of cascades" designed to enrich either natural uranium in 4 steps to weapons grade uranium or further enrich reactor grade uranium to weapons grade in 3 steps using existing stockpiles of reactor grade 3.5% and 19.75% enriched material. The code scans over the range of cascade configuration possibilities and determines the time required in each to obtain one significant quantity required to make a single nuclear weapon. All of the times are then collected and analyzed, and the mean and minimum breakout times reported for each configuration over the range of initial inventories of enriched material.

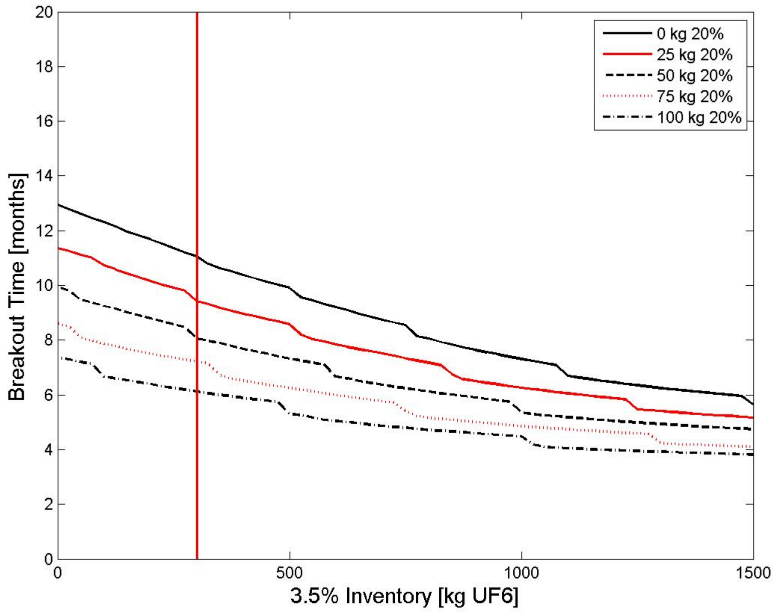

Figure 57: Four step breakout estimates. Results of 4-step batch process simulations with existing inventories of 3.5% ranging from 100-1500 kg and near 20% ranging from 0-100 kg. The vertical red line depicts the maximum inventory of 3.5% allowed by the JCPOA.

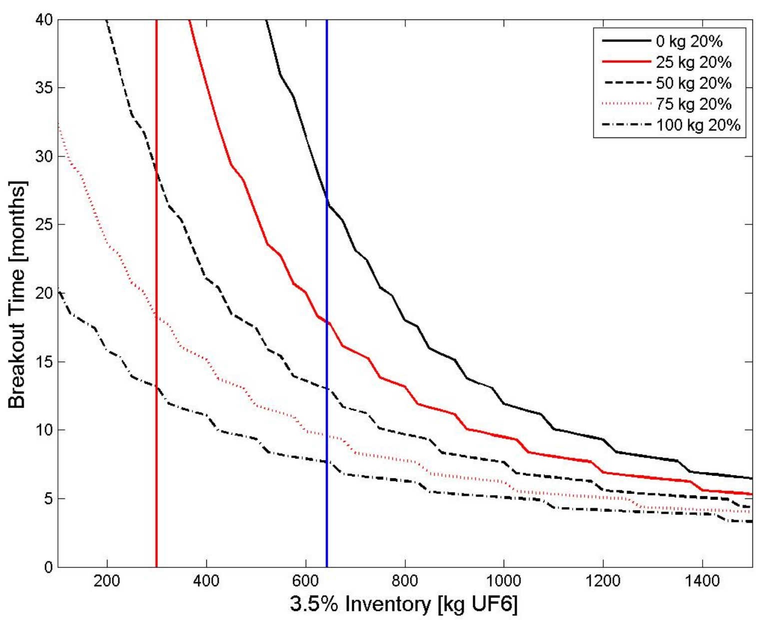

Figure 58: Three step breakout estimates. Results of 3-step batch process simulations with existing inventories of 3.5% ranging from 100-1500 kg and near 20% ranging from 0-100 kg. The vertical red line depicts the maximum inventory of 3.5% allowed by the JCPOA. The vertical blue line represents the minimum inventory of 3.5% necessary to use the 3-step process with no inventory of near 20%.

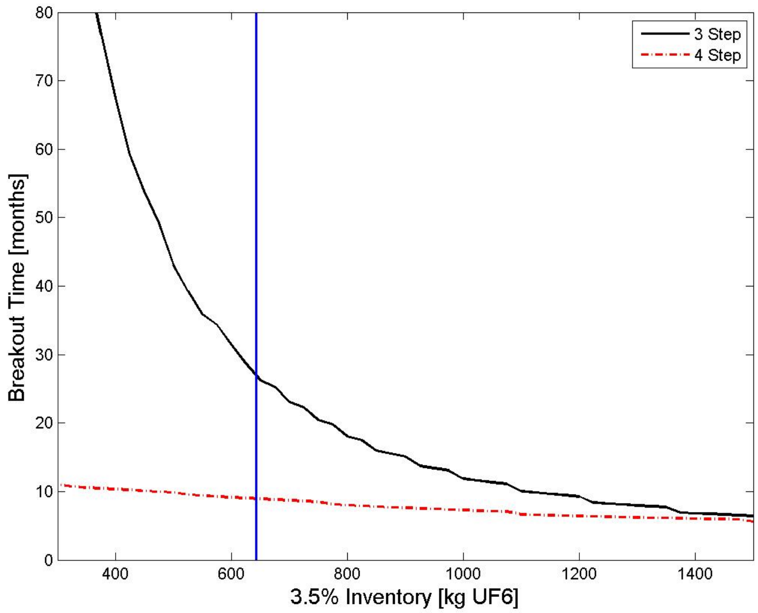

Figure 59: Comparison of the 3 and 4 step batch processes with no near 20% inventory added. No significant advantage is gained by using the 3-step process with inventories of 3.5% less than 1,500 kg. Again, the vertical blue line represents the minimum inventory of 3.5% necessary to use the 3-step process with no inventory of near 20%.

process with existing inventories of 3.5% LEU less than 1,500 kg. Improved centrifuge performance maps may contribute to more effective cascade modeling and increased confidence in breakout timeline estimates.

Figures 57 through 59 were created by the *CascSCAN* code using performance maps for the IR-1 centrifuge developed via the semi-empirical method developed by Migliorini, et al. [50][24]. Figures 60 and 61 depict the results of the Iguaçu machine employed in the cascade described in Table 3 and subject to the same constraints described in the JCPOA case study for the IR-1 centrifuge. Once again, two performance maps were used, one based on the one-dimensional radial averaging method of separation calculation and one based on the two dimensional numerical method. In all cases, the two dimensional numerical method based performance map predicts a lower breakout time, in some cases the difference is on the order of months.

Table 3: Iguaçu Cascade Design for the Performance Map Breakout Time Comparison [24]

Parameter	units	Iguaçu
Feed Rate	kgU/yr	2099
Feed Conc.	at. frac.	0.0072
Product Conc.	at. frac.	0.0350
Tails Conc.	at. frac.	0.0035
Enriching Stages	-	14
Stripping Stages	-	5
Stages Total	-	19
Nominal Separative Power	SWU/yr	1000
Total Centrifuges	-	228

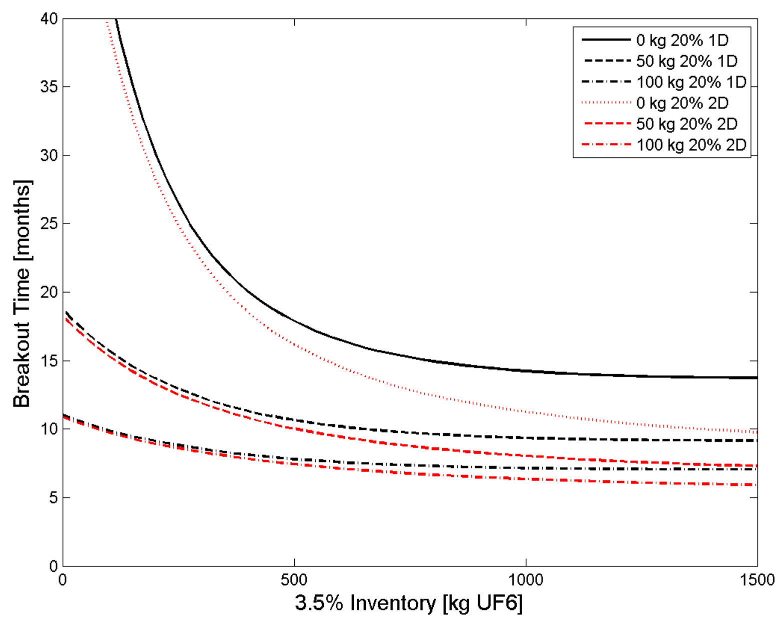

Figure 60: Comparison of the 4 step batch processes with performance maps derived from the one-dimensional radial averaging technique derived by Cohen (black curves) and the two-dimensional *xPort* code solution (blue curves).

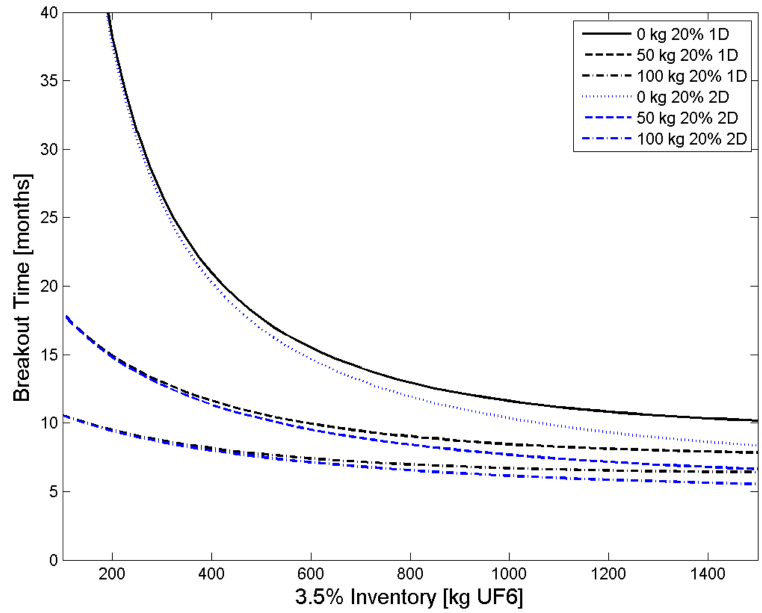

Figure 61: Comparison of the 3 step batch processes with performance maps derived from the one-dimensional radial averaging technique derived by Cohen (black curves) and the two-dimensional *xPort* code solution (blue curves).

8.3 Minor Isotope Safeguards Techniques (MIST)

Recently, Shephard, et al., proposed a new method for analysis and characterization of GCEPs utilizing the results of Minor Isotope Safeguards Techniques studies performed at Oak Ridge Gaseous Diffusion Enrichment Plant in the 1970-80's [98]-[108]. Based on the *MSTAR* model for cascade analysis, a universal and dimensionless surface is developed to describe all commercial cascades. *MSTAR* is a matched abundance ratio cascade code developed at Oak Ridge National Laboratory that may be used to calculate the uranium-235 to uranium-234 ratio of the heads and tails streams for a given feed stream in an enrichment cascade. The following derivation follows closely the work of de la Garza, Von Halle, and Shephard [109]-[111][112]-[114].

Considering equations (8.10) through (8.14), the effective stage separation factor for the i^{th} component may be given as

$$\gamma_i^* = \gamma_i/\beta_j = \gamma_i/\alpha_j, \tag{8.33}$$

where

$$\gamma_i = \gamma_0^{M_k - M_i}, \tag{8.34}$$

and the subscripts i, j, and k correspond to the target component uranium-234, the matched component uranium-235, and the key component uranium-238, respectively. From Von Halle and, subsequently, Shephard, et al., [98][110] defining

$$E_i = (\gamma_i^*)^{-1}/(1 - (\gamma_i^*)^{-N}), \tag{8.35}$$

$$S_i = (\gamma_i^*)^{-1}/((\gamma_i^*)^{M+1} - 1), \tag{8.36}$$

the mole fraction of the ith of j components for the feed, F, product, P, and tails, W, are given as

$$x_{i,P} = \frac{E_i x_{i,F}/(E_i + S_i)}{\sum_{i=1}^{j} E_i x_{i,F}/(E_i + S_i)}, \tag{8.37}$$

$$x_{i,W} = \frac{S_i x_{i,F}/(E_i + S_i)}{\sum_{i=1}^{j} S_i x_{i,F}/(E_i + S_i)}. \tag{8.38}$$

The atomic fraction of uranium-235 in the product and waste stream expressions are divided by the atomic fraction of uranium-234 to give

$$\frac{x_{5,P}/x_{4,P}}{x_{5,F}/x_{4,F}} = \frac{1 + S_4/E_4}{1 + S_5/E_5}, \tag{8.39}$$

$$\frac{x_{5,F}/x_{4,F}}{x_{5,W}/x_{4,W}} = \frac{1 + E_5/S_5}{1 + E_4/S_4}, \tag{8.40}$$

$$\frac{x_{5,P}/x_{4,P}}{x_{5,W}/x_{4,W}} = \frac{E_5/S_5}{E_4/S_4}. \tag{8.41}$$

Understanding that the molar mass of UF_6 varies depending on the isotope of uranium as $M_i = M_4 \approx 348$, $M_j = M_5 \approx 349$, and $M_k = M_8 \approx 352$. Therefore,

$$\gamma_4 = \gamma_0^{M_8 - M_4} \approx \gamma_0^{352-348} = \gamma_0^4, \tag{8.42}$$

$$\gamma_5 = \gamma_0^{M_8 - M_5} \approx \gamma_0^{352-349} = \gamma_0^3, \tag{8.43}$$

and

$$\gamma_4^* = \frac{\gamma_4}{\sqrt{\gamma_5}} \approx \frac{\gamma_0^4}{\sqrt{\gamma_0^3}} = \gamma_0^{5/2}, \tag{8.44}$$

$$\gamma_5^* = \frac{\gamma_5}{\sqrt{\gamma_5}} \approx \frac{\gamma_0^3}{\sqrt{\gamma_0^3}} = \gamma_0^{3/2}. \tag{8.45}$$

Substituting the results of equations (8.44) and (8.45) into equations (8.35) through (8.38) and (8.39) through (8.41) gives

$$\frac{x_{5,P}/x_{4,P}}{x_{5,F}/x_{4,F}} = \frac{1 + (1 - (\gamma_0^{-N})^{5/2})/((\gamma_0^{M+1})^{5/2} - 1)}{1 + (1 - (\gamma_0^{-N})^{3/2})/((\gamma_0^{M+1})^{3/2} - 1)}, \tag{8.46}$$

$$\frac{x_{5,F}/x_{4,F}}{x_{5,W}/x_{4,W}} = \frac{1 + ((\gamma_0^{M+1})^{3/2} - 1)/(1 - (\gamma_0^{-N})^{3/2})}{1 + ((\gamma_0^{M+1})^{5/2} - 1)/(1 - (\gamma_0^{-N})^{5/2})}, \tag{8.47}$$

$$\frac{x_{5,P}/x_{4,P}}{x_{5,W}/x_{4,W}} = \frac{((\gamma_0^{M+1})^{3/2} - 1)/(1 - (\gamma_0^{-N})^{3/2})}{((\gamma_0^{M+1})^{5/2} - 1)/(1 - (\gamma_0^{-N})^{5/2})}. \tag{8.48}$$

Finally, expressions for the x_5/x_8 ratio are developed.

$$\frac{x_{5,P}/x_{8,P}}{x_{5,F}/x_{8,F}} = \beta_5^N = \gamma_5^{N/2} = \gamma_0^{3N/2}, \tag{8.49}$$

and

$$\frac{x_{5,W}/x_{8,W}}{x_{5,F}/x_{8,F}} = \beta_5^{-(M+1)} = \gamma_5^{(M+1)/2} = \gamma_0^{-3(M+1)/2}, \tag{8.50}$$

both of which can be rearranged as

$$\left(\frac{x_{5,P}/x_{8,P}}{x_{5,F}/x_{8,F}}\right)^{-2/3} = \gamma_0^{-N}, \tag{8.51}$$

and

$$\left(\frac{x_{5,W}/x_{8,W}}{x_{5,F}/x_{8,F}}\right)^{-2/3} = \gamma_0^{M+1}. \tag{8.52}$$

Finally, plugging equations (8.51) through (8.52) back into equations (8.39) through (8.41) gives the ratio of x_5/x_4 ratios for product, feed, and waste as

$$\frac{x_{5,P}/x_{4,P}}{x_{5,F}/x_{4,F}} = \frac{1+\left(1-\left(\frac{x_{5,F}}{x_{8_F}}/\frac{x_{5,P}}{x_{8,P}}\right)^{5/3}\right)/\left(\left(\frac{x_{5,F}}{x_{8_F}}/\frac{x_{5,W}}{x_{8,W}}\right)^{5/3}-1\right)}{1+\left(1-\left(\frac{x_{5,F}}{x_{8_F}}/\frac{x_{5,P}}{x_{8,P}}\right)\right)/\left(\left(\frac{x_{5,F}}{x_{8_F}}/\frac{x_{5,W}}{x_{8,W}}\right)-1\right)} \tag{8.53}$$

$$\frac{x_{5,F}/x_{4,F}}{x_{5,W}/x_{4,W}} = \frac{1+\left(\left(\frac{x_{5,F}}{x_{8_f}}/\frac{x_{5,W}}{x_{8,W}}\right)-1\right)/\left(1-\left(\frac{x_{5,F}}{x_{8_F}}/\frac{x_{5,P}}{x_{8,P}}\right)\right)}{1+\left(\left(\frac{x_{5,F}}{x_{8_f}}/\frac{x_{5,W}}{x_{8,W}}\right)^{5/3}-1\right)/\left(1-\left(\frac{x_{5,F}}{x_{8_f}}/\frac{x_{5,P}}{x_{8,P}}\right)^{5/3}\right)} \tag{8.54}$$

$$\frac{x_{5,P}/x_{4,P}}{x_{5,W}/x_{4,W}} = \frac{\left(\left(\frac{x_{5,F}}{x_{8_f}}/\frac{x_{5,W}}{x_{8,W}}\right)-1\right)/\left(1-\left(\frac{x_{5,F}}{x_{8_F}}/\frac{x_{5,P}}{x_{8,P}}\right)\right)}{\left(\left(\frac{x_{5,F}}{x_{8_f}}/\frac{x_{5,W}}{x_{8,W}}\right)^{5/3}-1\right)/\left(1-\left(\frac{x_{5,F}}{x_{8_f}}/\frac{x_{5,P}}{x_{8,P}}\right)^{5/3}\right)} \tag{8.55}$$

If $x_4 + x_5 + x_8 = 1$, then

$$\frac{x_5}{x_8} = \left(\frac{1}{x_5} - \left(\frac{x_5}{x_4}\right)^{-1} - 1\right)^{-1} \tag{8.56}$$

Figure 62 represents the *MSTAR* model given by equations (8.53) through (8.55) plotted as a universal, dimensionless surface applicable to all ideal cascades regardless

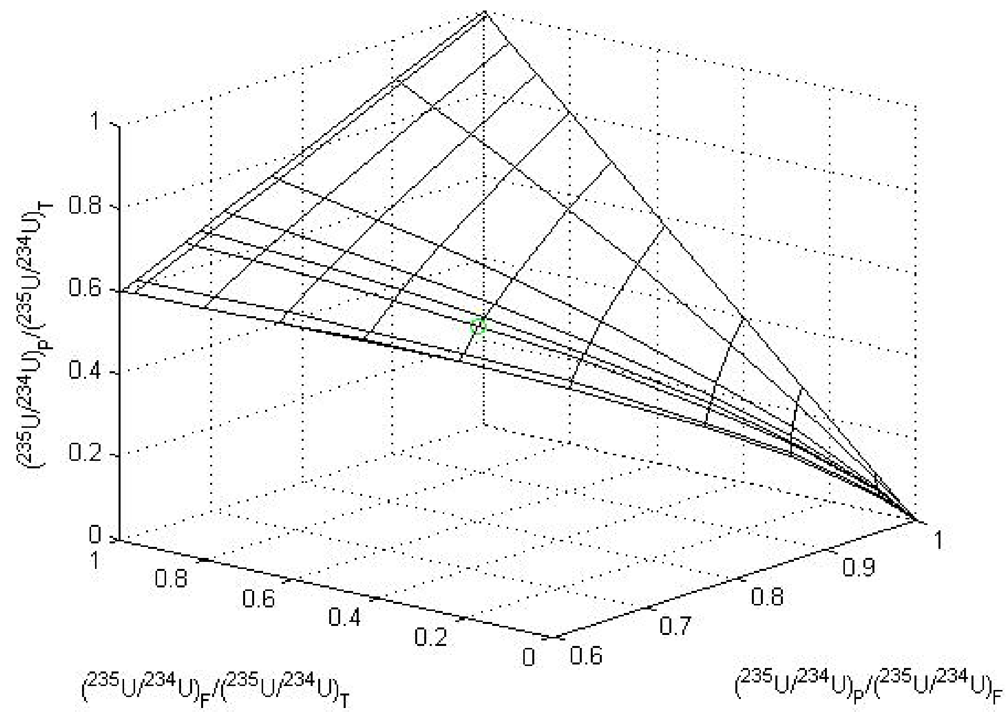

Figure 62: Surface created by the *MSTAR* model for all ideal cascades. The green circle represents a cascade fed with natural uranium that produces 5% heads and 0.3% tails.

of separator [109]. The gridlines represent specific product and tails enrichment levels corresponding to particular feed. However, the surface these gridlines describe represents all ideal cascades [110]. Analysis of simultaneous samples from heads, tails, and feed streams plotted on this surface characterize the usage of the cascade. The green circle represents natural uranium feed in an ideal cascade with 5% product and 0.3% tails assay.

Figure 63 shows this same cascade with off-normal operating results plotted on the surface. The blue stars represent a secondary feed stream. The magenta diamonds represent a secondary withdrawal stream. The red squares represent the same cascade with a secondary feed stream and a target product assay of 90%. Finally, the green x's represent the results of the *TransCasc* program run with the updated performance maps. *TransCasc* is a matlab code developed by Migliorini to simulate the concentration of the isotopes of uranium in a cascade during the transient phase

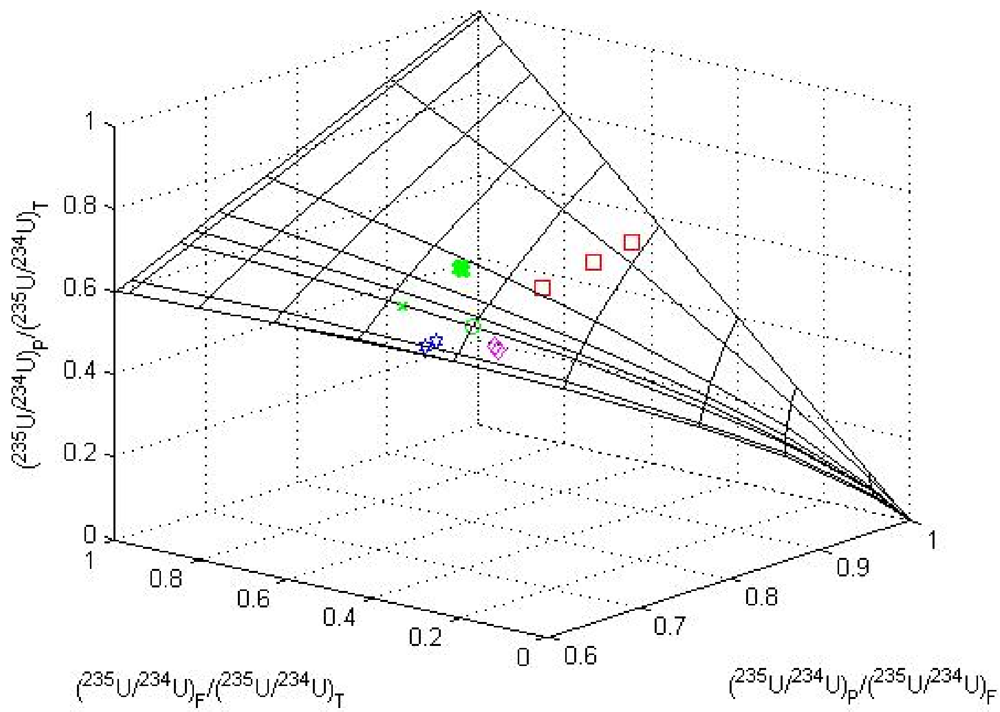

Figure 63: Surface created by the *MSTAR* model for all ideal cascades. The green circle represents a cascade fed with natural uranium that produces 5% heads and 0.3% tails. The blue stars represent that same cascade with a secondary feed stream. The magenta diamonds represent the same cascade with a secondary withdrawal stream. The red squares represent the same cascade with a secondary feed stream and a target product assay of 90%. The green x's represent the results of the TransCasc program run with the updated performance maps.

of off-normal operation returning to normal operating conditions. Figure 63 clearly demonstrates the utility of *MSTAR* in mapping and characterizing cascade operation and analysis of normal and off-normal cascade performance.

9 Summary and Recommendations

A variety of new techniques are presented which may prove useful to the separation phenomena and nonproliferation communities desiring to continue the conversation about enrichment capability and the time required to achieve significant quantities of highly enriched material. Based on the Onsager Equation with Carrier-Maslen end conditions, a linearized sixth-order partial differential equation describing the flow in the volume of the rotor of a gas centrifuge is solved using a finite element algorithm employed by the *CurvSOL* hydrodynamics code. The countercurrent flow in the centrifuge is generated as a result of gas feed and withdrawl, mechanical scoop interaction, and a rotor wall temperature gradient. These drive mechanisms are modeled by mass, momentum, and energy sources/sinks. The results are compared to results from the *Pancake* code, an existing code employing an eigenfunction expansion solution technique to solve the Onsager equation. Due to proprietary concerns and the potential sensitive nature of separation applications, two fictitious centrifuge designs, the Rome centrifuge and the Iguaçu centrifuge, have been accepted by the international community to enable collaboration and information sharing. Comparison of the axial mass flux, streamfunction, upflow ratio, and flow profile efficiency demonstrates excellent agreement between the *CurvSOL* and *Pancake* solutions for both the wall temperature gradient and scoop drive mechanisms, as well as the overall mass flux profile for both the Rome and Iguaçu designs. Results of *CurvSOL* simulations with and without the pancake approximation suggest that the radius of the rotor plays an important role in the effect of wall curvature on internal flow.

The axial mass flux profile derived from the hydrodynamic solution is used in a finite differencing scheme to obtain a numerical solution of the diffusion equation to predict the transport of uranium hexafluoride molecules in the *xPort* code. The set of equations governing the isotope transport is not readily solvable using analytic means, and different solution methods have been developed to arrive at approximations for both the axial concentration gradient and overall concentration profile. The generally accepted method of approximation describes the axial variation of the radially averaged concentration. As Dirac showed that separation is a function of velocity. Comparison of the radially averaged concentration for the Rome and Iguaçu machines show that as the wall speed increases, the difference in concentration between the top and the bottom of the machine increases for the Rome design but not for the Iguaçu. The newly developed two dimensional concentration field approximation allows for separative performance calculation at all points along the radial direction. Comparison of the two dimensional solution averaged at each axial plane and the one dimensional radial averaging solution shows that while the results from both methods differed by an atomic fraction of 6% at select axial plane near the middle of the rotor, the averages at the endcaps agree to within 2%. Plots of the two-dimensional solution show that the concentration of the Rome varies little radially while the radial variation for the Iguaçu is of the same order as the axial variation.

The separative performance and separation factor are mapped over ranging process gas feed rates and desired ratios of product to feed, and theses performance maps are typically employed in cascade analysis software packages. Using the existing *FixedCascBin*, a cascade gradient equation solver designed for a binary process gas, the stage flow rates and enrichments are calculated for cascades utilizing the Rome and Iguaçu machines. Comparison of the results from performance maps derived from the one dimensional radial averaging separation calculations and those from the *xPort* code show that while the magnitude of the flow in the stripping section is higher in the one dimensional case, both the upflow and downflow in the enriching section is higher in the two dimensional case. Overall, the two dimensional case upflow enrichment is lower at every stage until the top of the cascade, while the downflow enrichment is lower at every stage until the bottom of the cascade.

Two additional potential applications for the centrifuge performance maps are introduced. The *CascSCAN* code uses a modified version of the *FixedCascBin* to scan over the possible arrangement of centrifuges in cascades designed to enrich from natural uranium to weapons grade uranium in three or four step batch processes. *CascSCAN* is first used in a simulation of Iran's IR-1 centrifuge arranged in cascades in number and design conforming to the limitations detailed in the 2015 Joint Comprehensive Plan of Action (JCPOA). Using the same limitations on numbers of centrifuges and cascades, the case study is repeated for the Igucau centrifuge using both the performance maps based on the one dimensional radial averaging technique and the two dimensional *xPort* code results. Consistent with the results from the cascade flow and enrichment comparison study, the performance map based on the *xPort* results predicts a lower breakout time as additional inventory of enriched material is added to the feed stream. The results differ by as much as four months in the case of the four step batch process with 1500 kg of additional inventory enriched to 3.5% uranium-235.

Finally, a recently proposed method for enrichment plant monitoring and characterization offers a potential application for usage of the newly developed performance maps. Based on studies into the potential for minor isotope safeguards techniques (MIST) conducted at Oak Ridge National Laboratory in the 1970s and 1980s, the new MIST method uses the software code *TransCasc* to calculate the ratio of uranium-235 to uranium-234 in the heads and tails for a given feed. With the ability to calculate isotopic concentrations during transient periods, *TransCasc* was originally developed by Migliorini to characterize cascade transients during misuse or off normal operation scenarios. The potential utility of the *xPort* based performance maps is demonstrated by results of several scenarios simulated with *TransCasc* mapped on a surface that describes all commercial cascades and compared to results from *MSTAR*, a mixed abundance ratio cascade code.

Summary of Contributions

The goal of this project as stated in the introduction is an improved understanding of the isotope transport in low speed countercurrent centrifuges. Numerous modeling efforts exist in the literature to predict centrifuge performance, and each of these models has strengths and weaknesses based on the method or underlying assumptions. No previous model exists in the literature that utilizes the Onsager equation, relaxes the pancake approximation and incorporates isotope transport without radial averaging. The models developed in this effort allow the study of the effects of curvature on both the hydrodynamic flow profile and isotope transport, providing a better performance prediction for shorter, slower centrifuge designs. As a result of this research, three complete software codes have been developed and added to the inventory:

1. *CurvSOL* - This code uses a finite element algorithm to obtain a two-dimensional solution of the generalized Onsager equation, with gas feed and removal and including the effect of the rotor wall.

2. *xPort* - This code uses the results of *CurvSOL* in a finite difference scheme to estimate the isotope transport and the separative capacity of the centrifuge at the specified operating parameters.

3. CascSCAN - This code uses existing performance maps and a binary mixture fixed cascade gradient solving routine to scan over the possible cascade configurations needed to estimate the minimum time necessary to acquire a significant quantity of weapons grade uranium via 3 and 4 step batch process pathways.

A number of articles resulting from this research are prepared for submission in 2019. A comparison of the results of *CurvSOL* with previous efforts based on the pancake approximation is prepared for submission to *Separation Science and Technology*, as is a summary of the comparison of techniques for modeling the isotopic diffusion. These comparison results as well as the performance mapping and cascade modeling scenario products are planned for potential submission to the 60th Annual Meeting of the 2019 Institute of Nuclear Materials Management in 2019.

The underlying method serving as the basis for the proposed MIST application is detailed in "Minor Isotope Safeguards Techniques (MIST): Analysis and Visualization of Gas Centrifuge Enrichment Plant Process Data Using the *MSTAR* Model," appearing in volume 890 of *Nuclear Instruments and Methods in Physics Research Section A: Accelerators, Spectrometers, Detectors, and Associated Equipment* in 2018. This work was also presented at the 14th International Workshop on Separation Phenomena in Liquids and Gases in Stresa, Italy, in June of 2017.

Additionally, a portion of the nonproliferation breakout scenario modeling was accepted and presented at the 2016 American Nuclear Society's Advances in Nuclear Nonproliferation Technology and Policy Conference held September 25-30, 2016 in Santa Fe, New Mexico, winning second place in the student paper competition. This paper was also included in the 2017 ANS Winter Meeting held in Washington, DC, in October 2017. An overview of the modeling developed for this effort and a collection of breakout modeling using the previous and newly developed performance maps in a case study of breakout potential is prepared for submission to the United States Army Nuclear and Countering Weapons of Mass Destruction Agency's (USANCA) semi-annual *Countering Weapons of Mass Destruction Journal*.

Recommendations for Future Work

With the research presented here serving as a new basis, several areas are identified to serve as extensions of this effort.

1. Increased Local Fidelity. Perhaps higher fidelity analysis around the endcaps,

scoops, baffle could provide a more complete picture of the hydrodynamics in certain areas of interest. This solution could then easily be extended to the diffusion model.

2. MIST Misuse Scenarios. As described in the Applications chapter, the MIST based research has enormous potential for progress in the field of safeguards. Detailed study is recommended in the use of the newly created performance maps in conjunction with the *TransCasc* code for prediction of cascade characteristics resulting from off-normal operation or misuse.

3. Multi-Component Diffusion. The *xPort* code has potential for modification for multi-component analysis of the process gas. Once again, these results could be consolidated into performance maps over the feasible range of operating parameters and used in breakout scenario modeling or perhaps MIST analysis.

4. Incorporate Diffusion into *CurvSOL*. With the mechanics in place, the extension of the finite element framework to the isotope transport would allow for a more efficient transmission of operating parameters and would allow for greater flexibility when incorporating multi-component analysis.

References

[1] R. Rhodes, *The Making of the Atomic Bomb*. Simon and Schuster, 1988.

[2] Joint Committee on Atomic Energy. *Soviet Atomic Espionage*, Chapters 2–3, United States Government Printing Office, Washington, 1951.

[3] A. Jersild, *Sino-Soviet Alliance: An International History*. UNC Press Books, 2014.

[4] *IAEA Safeguards Glossary*, International Nuclear Verification Series No. 3, 2001 Edition, International Atomic energy Agency, Vienna, Austria, 2002.

[5] Environmental Protection Agency, *Paducah Gasaeous Diffusion Plant* https://cumulis.epa.gov/supercpad/cursites/csitinfo.cfm?id=0404794 accessed:May 2016.

[6] W. Fischer, G. Stein, "On-Site Inspections: Experiences from Nuclear Safeguarding," *Disarmament Forum*, Vol. 3, 1999.

[7] K. Cohen, *The Theory of Isotope Separation as Applied to the Large-Scale Production of U-235*. National Nuclear Energy Series Division III, Vol. 1B, McGraw-Hill, New York, 1951.

[8] G. Zippe, "Historical Review on the Decvelopment of Gas centrifuges for Uranium Enrichment," Proceedings of the Sixth International Workshop on Separation Phenomena in Liquids and Gases, Nagoya, 1998.

[9] D.R. Olander, *Technical Basis of the Gas Centrifuge*, University of California, Berkeley, 1972.

[10] D.R. Olander, "The Theory of Uranium Enrichment by the Gas Centrifuge," Progress in Nuclear Energy, 8: 1-33, 1981.

[11] Soubbaramayer, "Centrifugation," *Topics in Applied Physics: Uranium Enrichment*, Springer, 1979.

[12] M. Benedict, T.H. Pigford, H.W. Levi, *Nuclear Chemical Engineering*, 2nd Edition, McGraw-Hill, New York, 1981.

[13] A.S. Krass, P. Boksma, B. Elzen, W.A. Smit, *Uranium Enrichment and Nuclear Weapon Proliferation*, Taylor and Francis, London, England, 1983.

[14] S. Whitley, "Review of the gas Centrifuge until 1962 Part I Principles of Separation Physics," *Reviews of Modern Physics*, 56: 41, 1984.

[15] I.D. Heriot, "Uranium Enrichment by Gas Centrifuge," *Nuclear Science and Technology*, Commission of the European Communities, Luxembourg, 1988.

[16] V.D. Borisevich, H.G. Wood, "Gas Centrifugation," *Encyclopedia of Separation Sciences: Isotope Separations*, 3203-3207, Academic Press, 2000.

[17] H.G. Wood, "Effects of Separation Processes on Minor Uranium Isotopes in Enrichment Cascades," *Science and Global Security*, 16(1-2): 26-36, 2008.

[18] R.S. Kemp, "Gas Centrifuge Theory and Development: A Review of US Programs," *Science and Global Security*, 17(1): 1-19, 2009.

[19] J.F.A. Delbeke, G. Eklund, B.P.M. van Esch, G. Janssens-Maenhout, W. Janssens, "Verifying the Spin of Centrifuges," *Energy*, 35: 3123-3130, 2010.

[20] J.W. Beams, F.W. Linke, C. Skarstrom, "A Tubular Vacuum Type Centrifuge," *Science*, Vol. 86, No. 2230, 293-294, 1937.

[21] A. Bramley, "On the Theory of the Separation of Isotopes by Thermal or Centrifugal Methods," *Science*, Vol. 92, No. 2393, 427-428, 1940.

[22] K. Stewartson, "On Almost Rigid Rotations," *Journal of Fluid Mechanics*, 3(1): 17-26, 1957.

[23] www.harmjschoonhoven.com/Trinity/gfmr11-fig-ultracentrifuge-full.jpg (accessed 28 Sep 2018).

[24] P.J. Migliorini, *Modeling and Simulation of Gas Centrifuge Cascades for Enhancing the Efficiency of IAEA Safeguards*, Dissertation, the University of Virginia, 2013.

[25] V.W. Ekman, "On the Influence of the Earths Rotation on Ocean Currents," *Arkiv For Matematik, Astonomi Och Fysik*, Band 2, No. 10, 1905.

[26] J.W. Beams, L.B. Snoddy, A.R. Kuhlthau, "Tests of the Theory of Isotope Separation by Centrifuging," In *The Proceedings of the International Conference on the Peaceful Uses of Atomic Energy*, Geneva, Switzerland, 1958.

[27] G.F. Carrier, S.H. Maslen, "Flow Phenomena in Rapidly Rotating Systems," *USAEC Report* TID-188065, 1962.

[28] G.F. Carrier, "Phenomena in Rotating Fluids," *Proceedings of the 11th International Congress on Applied Mechanics*, Munich, Germany, 1964.

[29] L.Onsager, "Approximate Solutions of the Linearized Flow Equations," SQLO-001, UVA #OA-825B, University of Virginia, 1965.

[30] D.G. Avery, E. Davies, *Uranium Enrichment by Gas Centrifuge*, London: Mills and Boon, 1973.

[31] T. Matsuda, "Isotope Separation by Thermally Driven Countercurrent Gas Centrifuge," *Journal of Nuclear Science and Technology*, 12(8): 512-518, 1975.

[32] F.H. Bark, T.H. Bark, "On Vertical Boundary Layers in a Rapidly Rotating Gas," *Journal of Fluid Mechanics*, 78: 749-761, 1976.

[33] J.J.H. Brouwers, *On the Motion of a Compressible Fluid in a Rotating Cylinder*, Stichting Reactor Centrum Nederland, 1976.

[34] T. Matsuda, K. Hashimoto, "Thermally, Mechanically or Externaly Driven Flows in a Gas Centrifuge with Insulated Horizontal End Plates," *Journal of Fluid Mechanics*, 78(2): 337-354, 1976.

[35] W.G. May, "Separation parameters of gas centrifuges," *American Institute of Chemical Engineers Symposium Series*;(United States). Vol. 73. No. CONF-761109-P1. Exxox Nuclear Co., Inc., Ballston Spa, NY, 1977.

[36] T. Kai, "Basic Characteristics of Centrifuges (III) - Analysis of Fluid Flow in Centrifuges," *Journal of Nuclear Science and Technology*, 14(4): 267-281, 1977.

[37] J.J.H. Brouwers, "On Compressible Flow in a Gas Centrifuge and its Effect on the Maximum Separative Power," *Journal of Nuclear Technology*, 39: 311-322, 1978.

[38] D. Hanel, J. Humpert, "Numerical Solution of the Diffusion Equation," *Proceedings of the 3rd Workshop on Gases in Strong Rotations*, Rome, Italy, 323-338, 1979.

[39] S.H. Maslen, "The Basic Steady-State Flow Models for Computing Countercurrent Motions," GCTCG-3, UVA-ER-540-80U, University of Virginia, 1979.

[40] I. Harada, "A Numerical Study of Weakly Compressible Rotating Flows in a Gas Centrifuge, ' *Nuclear Science and Engineering*, 73: 225-241, 1980.

[41] I. Harada, "Computation of Strongly Compressible Rotating Flows," *Journal of Computational Physics*, 38: 335-356, 1980.

[42] L.D. Cloutman, R.A. Gentry, *Numerical Simulation of the Countercurrent Flow in a Gas Centrifuge*, Los Alamos National Lab, LA-8972-MS, 1983.

[43] E. Aoki, M. Suzuki, F. Yamamoto, "Numerical Studies on Gas Flow Around the Scoop of a Centrifuge," *Proceedings of the Sixth Workshop on Gases in Strong Rotation*, Tokyo (ed. Y. Takashima). pp 11-29.

[44] A.T. Conlisk, "The Effect of Aspect Ratio and Feed Flow Rate on Separative Power in a Gas Centrifuge," *Chemical Engineering Science*, 41(10): 2639-2650, 1986.

[45] M.H. Berger, "Finite Element Analysis of Flow in a Gas-Filled Rotating Annulus," *International Journal of Numerical Methods in Fluids*, 7: 215-231, 1987.

[46] C. Ying, Z. Guo, H.G. Wood, "Solution of the Diffusion Equations in a Gas Centrifuge for Separation of Multicomponent Mixtures," *Separation Science and Technology*, 31(18): 2455-2471, 1996.

[47] D.A. Andrade, J.L.F. Bastos, "A gas centrifuge thermal hydrodynamical model," *Proceedings of the Sixth International Workshop on Separation Phenomena in Liquids and Gases*, Nagoya, pp. 92-99, 1998.

[48] V.D. Borisevich, O.E. Morozov, O.N. Godisov, "Numerical Simulation of Bellows Effect on Flow and Separation of Uranium Isotopes in a Supercritical Gas Centrifuge," *Nuclear Instruments and Methods in Physics Research*, Sec. A, 455: 487-494, 2000.

[49] P. Omnes, "Numerical and Physical Comparisons of Two Models of a Gas Centrifuge," *Computers and Fluids*, 36(6): 1028-1039, 2007.

[50] P.J. Migliorini, W.C. Witt, H.G. Wood, "Semi-Empirical Method for Developing a centrifuge Performance Map," *Separation Science and Technology*, 48 (18): 2225-2233, 2013.

[51] S.V. Bogovalov, V.D. Borisevich, V.D. Borman, V.A. Kislov, I.V. Tronin, V.N. Tronin, "Verification of Numerical Codes for Modeling the Flow and Isotope Separation in gas Centrifuges," *Computers and Fluids*, 86: 177-184, 2013.

[52] H.G. Wood, J.B. Morton, "Onsager's Pancake Approximation for the Fluid Dynamics of a Gas Centrifuge," *Journal of Fluid Mechanics*, 101: 1-31, 1980.

[53] M.D. Gunzburger, H.G. Wood, "A Finite Element Method for the Onsager Pancake Equation," *Journal of Computer Methods in Applied Mechanics and Engineering*, 31: 43-59, 1982.

[54] J.A. Viecelli, "Exponential Difference Operator Approximation for the Sixth Order Onsager Equation," *Journal of Computational Physics*, 50(1): 162-170, 1983.

[55] M.D. Gunzburger, H.G. Wood, J.A. Jordan, "A Finite Element Method for Gas Centrifuge Flow Problems," *SIAM Journal on Scientific and Statistical Computing*, 5(1) 78-94, 1984.

[56] J.A. Viecelli, "Solution of the Onsager Equation in Doubly Connected Regions," *Journal of Computational Physics*, 56(3): 530-536, 1984.

[57] H.G. Wood, R. Babarsky, "Analysis of a Rapidly Rotating gas in a Pie Shaped Cylinder," *Journal of Fluid Mechanics*, 239: 249-271, 1992.

[58] R.J. Babarsky, H.G. Wood, "Approximate Eigensolutions for Non-Axisymmetric Rotating Compressible Flows," *Computational Methods in Applied Mechanical Engineering*, 81: 317-372, 1990.

[59] H.G. Wood, T.C. Mason, Soubbaramayer, "MultiIsotope Separation in a Gas Centrifuge Using Onsagers Pancake Model," *Separation Science and Technology*, 31(9): 1185-1213, 1996.

[60] R.J. Babarsky, W.I. Herbst, H.G. Wood, "A New Variational Approach to Gas Flow in a Rotating System," *Physics of Fluids* 14(10): 3624-3640, 2002.

[61] M. DeStadler, K. Chand, *A Finite Difference Numerical Method for Onsager's Pancake Approximation for Fluid Flow in a Gas Centrifuge*, Report UCRL-TR-236581, Lawrence Livermore National Laboratory, USA, 2007.

[62] S. Pradhan, V. Kumaran, "The Generalized Onsager Model for the Secondary Flow in a High-Speed Rotating Cylinder," *Journal of Fluid Mechanics*, 686:109-159, 2011.

[63] P.J. Migliorini, *Computational Tool for Analyzing Flows and Gradients in Gas Centrifuge Cascades*, Oak Ridge National Laboratory (ORNL), 2010.

[64] W.C. Witt, *The Onsager Equation with Curvature and Source Terms: A Finite Element Solution*, Thesis, University of Virginia, 2013.

[65] R.L. Hoglund, J. Shacter, and E. Von Halle, "Diffusion separation methods," *Encyclopedia of Chemical Technology*, 7: 639-723, 1979.

[66] Acheson, D. J., *Elementary Fluid Dynamics*, Oxford University Press, New York, 1990.

[67] P.K. Kundu, I.M. Cohen, D.R. Dowling, *Fluid Mechanics*, Fifth Edition, Academic Press, Boston, 2012.

[68] R. Bourn, T.D. Peterson, H.G. Wood, "Solution of the Pancake Model for Flow in a Gas Centrifuge by means of a Temperature Potential," *Computational Methods of Applied Mechanical Engineering*, 178: 183-197, 1999.

[69] T. Matsuda, K. Hashimoto, "The Structure of the Stewartson Layers in a Gas Centrifuge. Part 1. Insulated End Plates," *Journal of Fluid Mechanics*, 85: 433-442, 1978.

[70] T. Matsuda, K. Nakagawa, "A New Type of Boundary Layer in a Rapidly Rotating Gas," *Journal of Fluid Mechanics*, 126: 431-442, 1983.

[71] H. Mikami, "Thermally Induced Flow in a Gas Centrifuge," *Journal of Nuclear Science and Technology*, 10: 580-583, 1973.

[72] J.J.H. Brouwers, "On Compressible Flow in a Rotating Cylinder," *Journal of Engineering Mathematics*, 12(3): 265-285, 1978.

[73] O.C. Zienkiewicz, *The Finite Element Method.* London: McGraw-Hill, 1977.

[74] M. Asadzadeh, "An Introduction to the Finite Element Method (FEM) for Differential Equations," Draft Manuscript, 2014.

[75] F. Bassi, S. Rebay, "A High-Order Accurate Discontinuous Finite Element Method for the Numerical Soluaiton to the Compressible Navier-Stokes Equations," *Journal of Computational Physics*, 131: 267-279, 1997.

[76] M.E. Davis, "Boundary value Problems for Ordinary Differential Equations: Finite Element Methods," *Numerical Methods and Modeling for Chemical Engineers*, Courier Corporation, 2013.

[77] D. Liu, G. Xu, "General Sixth Order geometric Partial Differential Equation and its Application in Surface Modeling," *Journal of Information and Computational Science*, 4(1): 129-140, 2007.

[78] N. Mai-Duy, "Solving High Order Ordinary Differential Equations with Radial Basis Function Networks," *International Journal of Numerical Methods in Engineering*, 62(6): 824-852, 2005.

[79] R.J. Schnipke, *Finite Element Method for Fluid Flows*, Dissertation, the University of Virginia, 1986.

[80] L. Mu, J. Wang, G. Wei, X. Ye, S. Zhoa, “Weak Galerkin Methods for Second Order Elliptic Interface Problems,” *Journal of Computational Physics*, 250: 106-125, 2013.

[81] E. Suli, “Lecture Notes on Finite Element Methods for Partial Differential Equations,” *Mathematical Institute*, University of Oxford, 2012.

[82] K.N.S.K. Viswanadham, P.M. Krishna, R.S. Koneru, “Numerical Solutions of Fourth Order Boundary Value Problems by Galerkin Method with Quintic B-splines,” *International Journal of Nonlinear Science*, 10(2): 222-230, 2010.

[83] B. Zheng, *Finite Element Approximations of High Order Partial Differential Equations*, Dissertation, Pennsylvania State University, 2008.

[84] H.G. Wood, A. Glaser, “Computational Analysis of Signatures of Highly Enriched Uranium Produced by Centrifuge and Gaseous Diffusion,” *Proceedings of the INMM 49th Annual Meeting*, Nashville, TN, 2008.

[85] A. Glaser, “Characteristics of the Gas Centrifuge for Uranium Enrichment and Their Relevance for Nuclear Weapon Proliferation,” *Science and Global Security*, 16: 1-25, 2008.

[86] G. Mercurio, P. Peerani, P. Richir, W. Janssens, *Modeling of Interconnected UF6 Cascades for Non Proliferation Analysis*, 2012.

[87] W.C. Witt, P.J. Migliorini, D. Albright, H.G. Wood, “Modeling Iran’s Tandem Cascade Configuration for Uranium Enrichment by Gas Centrifuge,” *Proceedings of the INMM 54th Annual Meeting*, Palm Desert, CA, July 14-18, 2013.

[88] J.M. Hyman, “Numerical Methods for Nonlinear Differential Equations,” *Nonlinear Problems: Past and Future*, North Holland Publishing Company, 1982.

[89] D.N. Arnold, "Lecture Notes on Numerical Analysis of Partial Differential Equations," University of Minnesota, 2011.

[90] T. Kai, "Analysis of Separation Performance of Gas Centrifuge," In *The Proceedings of the Fifth Workshop on Gases in Strong Rotation, Charlottesville, Virginia*, (ed. H.G. Wood), 1-42, 1983.

[91] W. Nakayama, T. Torii, "Numerical Analysis of Separative Power of Isotope Centrifuges," *Journal of Nuclear Science and Technology*, 11: 495-504, 1974.

[92] R.J. Ribando, "A Finite Difference Solution of Onsager's Model for Flow in a Gas Centrifuge," *Computational Fluids*, 12(3): 235-252, 1984.

[93] P. Roblin, F. Doneddu, "Direct Monte Carlo Simulations in a Gas Centrifuge," In *22nd International Symposium on Rarefied Gas Dynamics* (ed. T.J. Bartel, M.C. Gallis), American Institute of Physics, 169-173, 2000.

[94] W.H. Furry, R.C. Jones, L. Onsager, "On the Theory of Isotope Separation by Thermal Diffusion," *Physics Review*, 55: 1083, 1939.

[95] T. Kai, "Basic Characteristics of Centrifuges (IV) - Analysis of Separative Performance," *Journal of Nuclear Science and Technology*, 14(7): 506-518, 1977.

[96] J.P. Lahargue, Soubbaramayer, "A Numerical Model for the Investigation of the Flow and Isotope Concentration Field in an Ultracentrifuge," *Computational Methods of Applied Mechanics in Engineering*, 15: 259, 1978.

[97] H.G. Wood, P.J. Migliorini, "Fixed Plant Proliferation Analysis of Iran's Natanz Plant," *Proceedings of the 52nd INMM Annual Meeting*, Orlando, FL, 2012.

[98] S. Blumpkin, E. Von Halle, "The Behavior of the Uranium Isotopes in Separation Cascades, Part I: Ideal Cascades," Oak Ridge Gaseous Diffusion Plant report K-1839, Part 1, 1972.

[99] S. Blumpkin, E. Von Halle, "Review of the Performance of Separation Cascades and the Behavior of the Minor Uranium Isotopes," (K-OA-2103), Union Carbide Corporation, Nuclear Division, Oak Ridge Gaseous Diffusion Plant, Oak Ridge, Tennessee, March 24, 1972.

[100] S. Blumpkin, E. Von Halle, "Minor Isotopic Measurements in a Gaseous Diffusion Cascade," (K-OA-2273), Union Carbide Corporation, Nuclear Division, Oak Ridge Gaseous Diffusion Plant, Oak Ridge, Tennessee, April 18, 1973.

[101] S. Blumpkin, E. Von Halle, "The Behavior of the Uranium Isotopes in Separation Cascades, Part II: A Short Cascade Designed for the Production of Power Reactor Fuel," Oak Ridge Gaseous Diffusion Plant report K-1839, Part 2, 1973.

[102] S. Blumpkin, E. Von Halle, "A Preliminary Report on the Minor Isotopic Measurements in a Gaseous Diffusion Cascade: MIST Test II," Oak Ridge Gaseous Diffusion Plant report K-OA-2388, 1973.

[103] S. Blumpkin, E. Von Halle, "The Behavior of the Uranium Isotopes in Separation Cascades, Part III: A Long Cascade Designed for the Production of a Small Quantity of Highly Enriched Uranium Simultaneously With a Much Larger Quantity of Power Reactor Fuel," Oak Ridge Gaseous Diffusion Plant report K-1839, Part 3, 1974.

[104] S. Blumpkin, E. Von Halle, "The Behavior of the Uranium Isotopes in Separation Cascades, Part IV: Special Topics," Oak Ridge Gaseous Diffusion Plant report K-1839, Part 4, 1974.

[105] S. Blumpkin, E. Von Halle, "The Behavior of the Uranium Isotopes in Separation Cascades, Part V: Review and Appraisal," Oak Ridge Gaseous Diffusion Plant report K-1839, Part 5, 1976.

[106] S. Blumpkin, E. Von Halle, "A Method for Estimating the Inventory of an Isotope Separation Cascade by the Use of Minor Isotope Transient Atom fraction Data," Oak Ridge Gaseous Diffusion Plant report K-1892, 1978.

[107] S. Blumpkin, S.A. Levin, E. Von Halle, "Minor Isotope Measurements for Safeguarding a Uranium Enrichment Plant," In *The Proceedings of ESARDA*, 185-191, 1979.

[108] S. Blumpkin, "Comparison of Measured and Calculated Uranium Isotopic Atom fractions in Cascade Streams at the Paducah Gaseous Diffusion Plant," Oak Ridge Gaseous Diffusion Plant report K-2034, 1982.

[109] A.M. Shephard, *Process Attribute Monitoring Approach to Gaseous Centrifuge Enrichment Plant Safeguards*, Dissertation, University of Tennessee, 2016.

[110] A.M. Shephard, B.R. Thomas, J.B. Coble, H.G. Wood, "Minor Isotope Safeguards Techniques (MIST): Analysis and Visualization of Gas Centrifuge Enrichment Plant Process Data Using the MSTAR Model," *Nuclear Instruments and Methods in Physics Research Section A: Accelerators, Spectrometers, Detectors, and Associated Equipment*, Vol 890, 2018, p 79-83, 2018.

[111] S. A. Levin, S. Blumpkin, E. Von Halle, "Use of Minor Uranium Isotope Measurements as an Aid in Safeguarding a Uranium Enrichment Cascade," International Atomic Energy Agency proceedings IAEA-SM-231-72, 1978.

[112] A. de la Garza, G.A. Garrett, J.E. Murphy, "Multicomponent isotope separation in cascades," *Chemical Engineering Science*, 15: 188-209, 1961.

[113] A. de la Garza, "A Generalization of the Matched Abundance Ratio Cascade for Multicomponent Isotope Separation," *Chemical Engineering Science*, 18: 73-82, 1963.

[114] A. de la Garza, "The Variable Key-Weight Cascade for Multicomponent Isotope Separation," K-1571, Union Carbide Corporation-Nuclear Division, ORGDP, Oak Ridge, TN, 1963

10 Appendix A - Flow Solutions

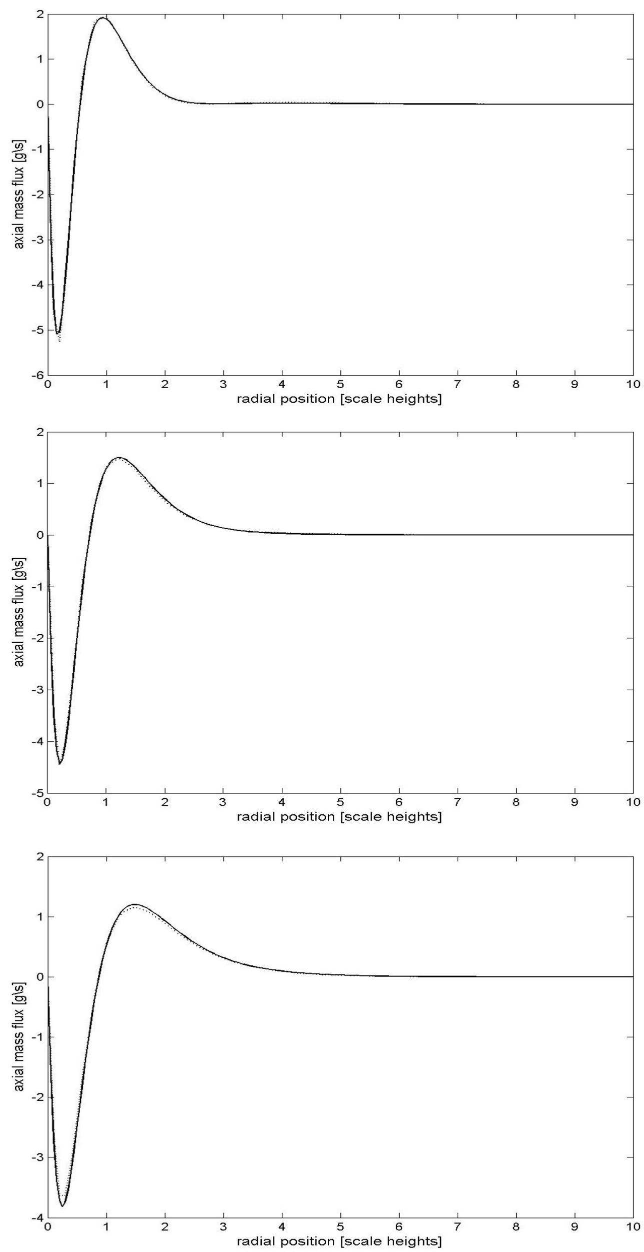

Figure 64: Axial Mass Flux plot from the quarter-plane of the Rome machine countercurrent flow create by a linear wall temperature gradient. Three wall speeds were simulated: 500 m/s (top), 600 m/s (middle), and 700 m/s (bottom). The results from the *CurvSOL* code with the pancake approximation are shown by the dashed line and the those from the *CurvSOL* code considering the curvature of the rotor wall are represented by the dotted line.

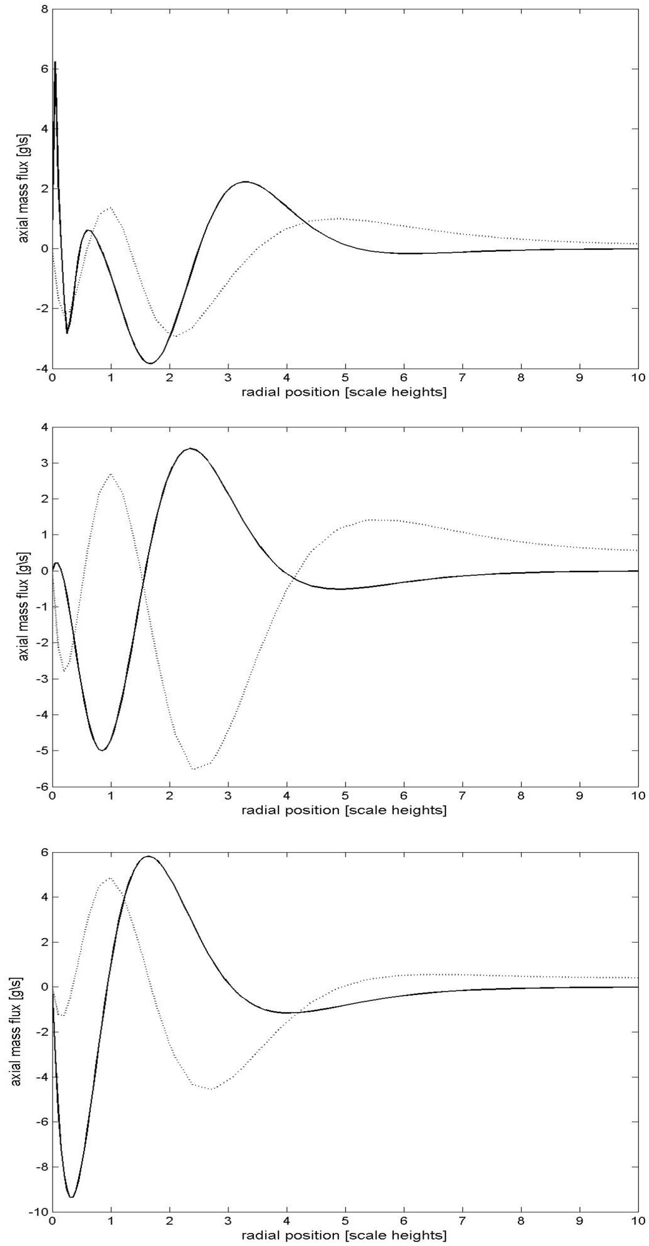

Figure 65: Axial Mass Flux plot from the quarter-plane of the Rome machine countercurrent flow create by a feed drive. Three wall speeds were simulated: 500 m/s (top), 600 m/s (middle), and 700 m/s (bottom). The results from the *CurvSOL* code with the pancake approximation are shown by the dashed line and the those from the *CurvSOL* code considering the curvature of the rotor wall are represented by the dotted line.

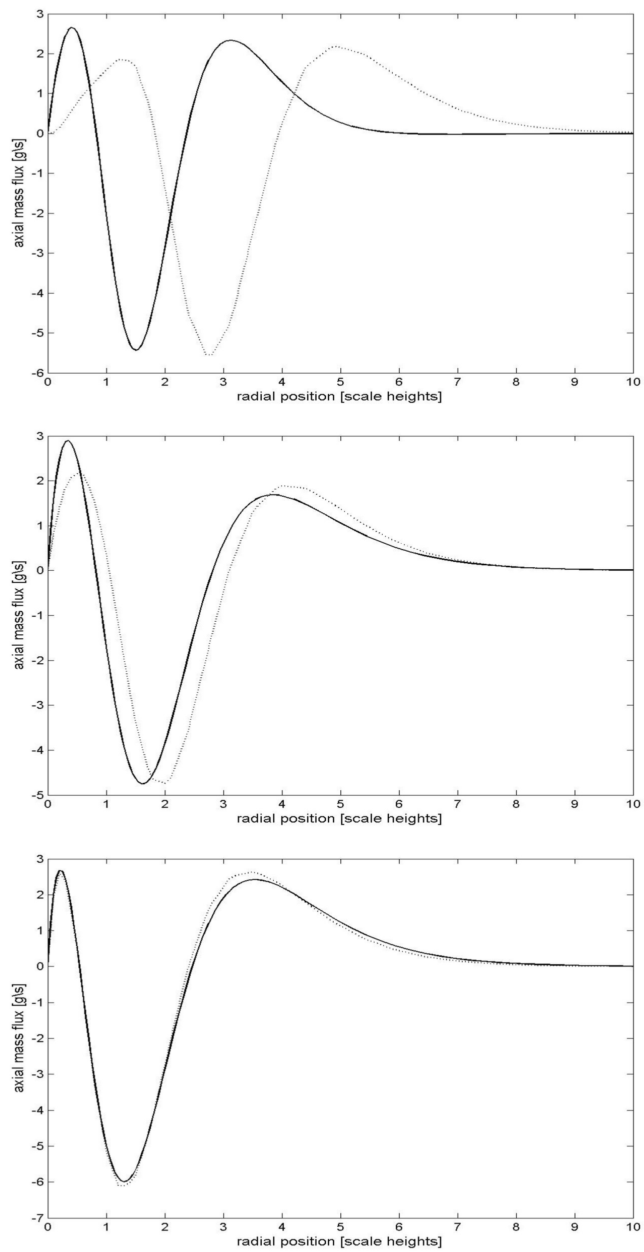

Figure 66: Axial Mass Flux plot from the quarter-plane of the Rome machine countercurrent flow create by a scoop drive. Three wall speeds were simulated: 500 m/s (top), 600 m/s (middle), and 700 m/s (bottom). The results from the *CurvSOL* code with the pancake approximation are shown by the dashed line and the those from the *CurvSOL* code considering the curvature of the rotor wall are represented by the dotted line.

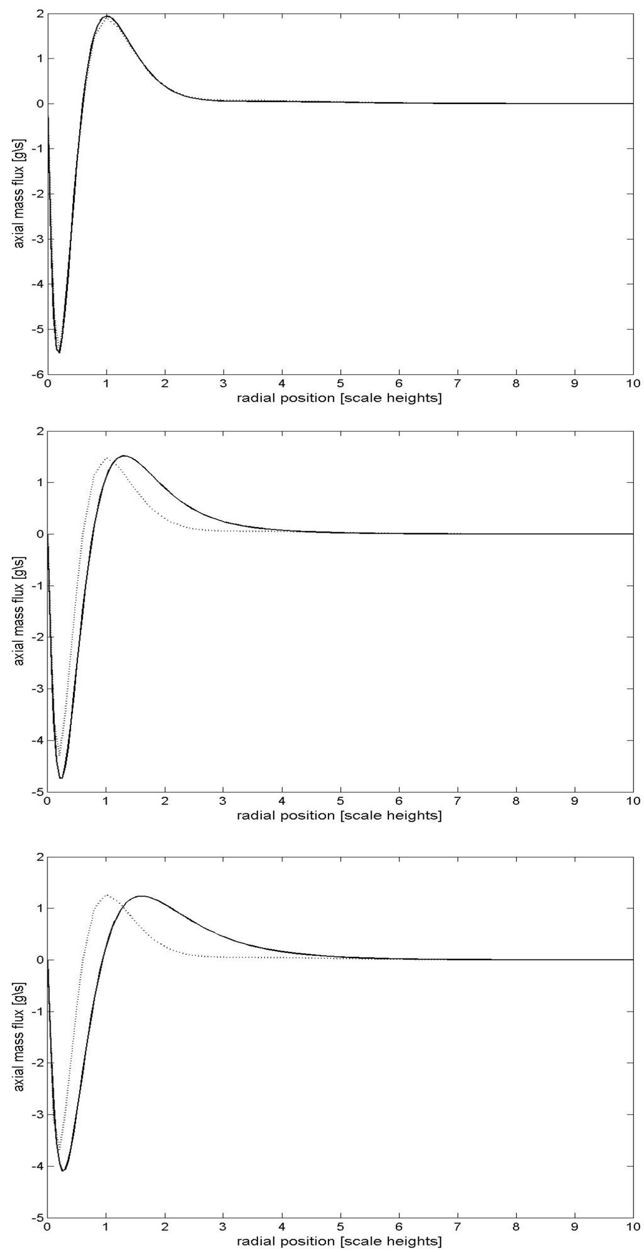

Figure 67: Axial Mass Flux plot from the quarter-plane of the Iguaçu machine countercurrent flow create by a linear wall temperature gradient. Three wall speeds were simulated: 500 m/s (top), 600 m/s (middle), and 700 m/s (bottom). The results from the *CurvSOL* code with the pancake approximation are shown by the dashed line and the those from the *CurvSOL* code considering the curvature of the rotor wall are represented by the dotted line.

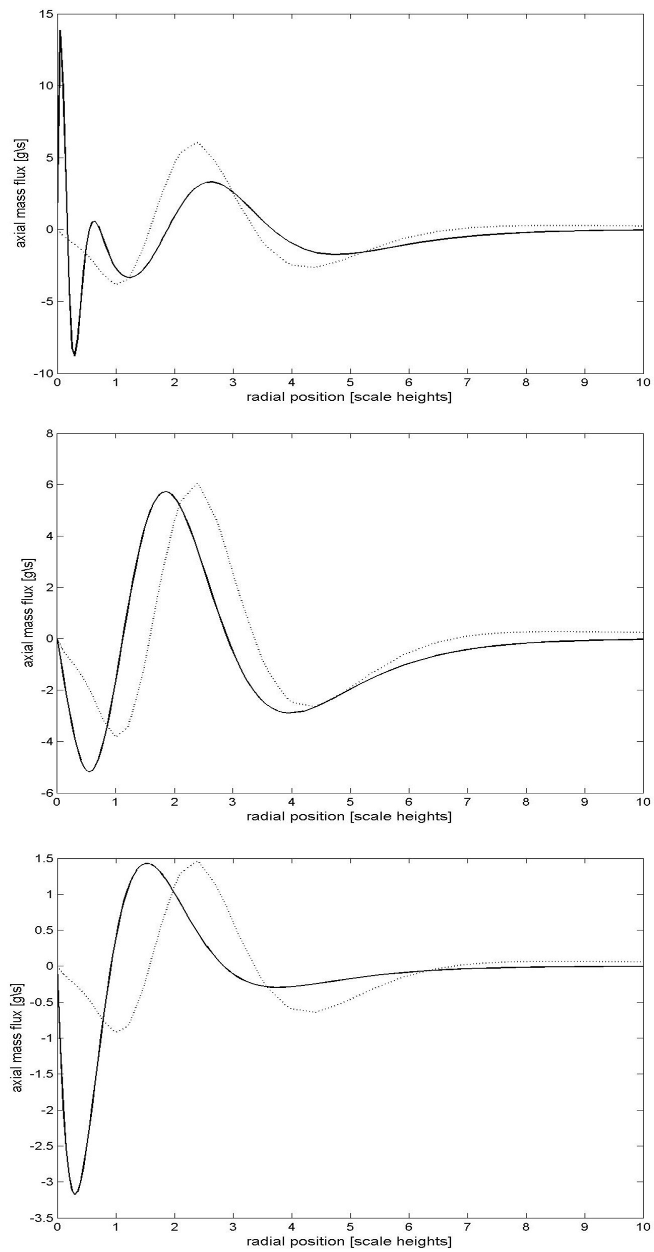

Figure 68: Axial Mass Flux plot from the quarter-plane of the Iguaçu machine countercurrent flow create by a feed drive. Three wall speeds were simulated: 500 m/s (top), 600 m/s (middle), and 700 m/s (bottom). The results from the *CurvSOL* code with the pancake approximation are shown by the dashed line and the those from the *CurvSOL* code considering the curvature of the rotor wall are represented by the dotted line.

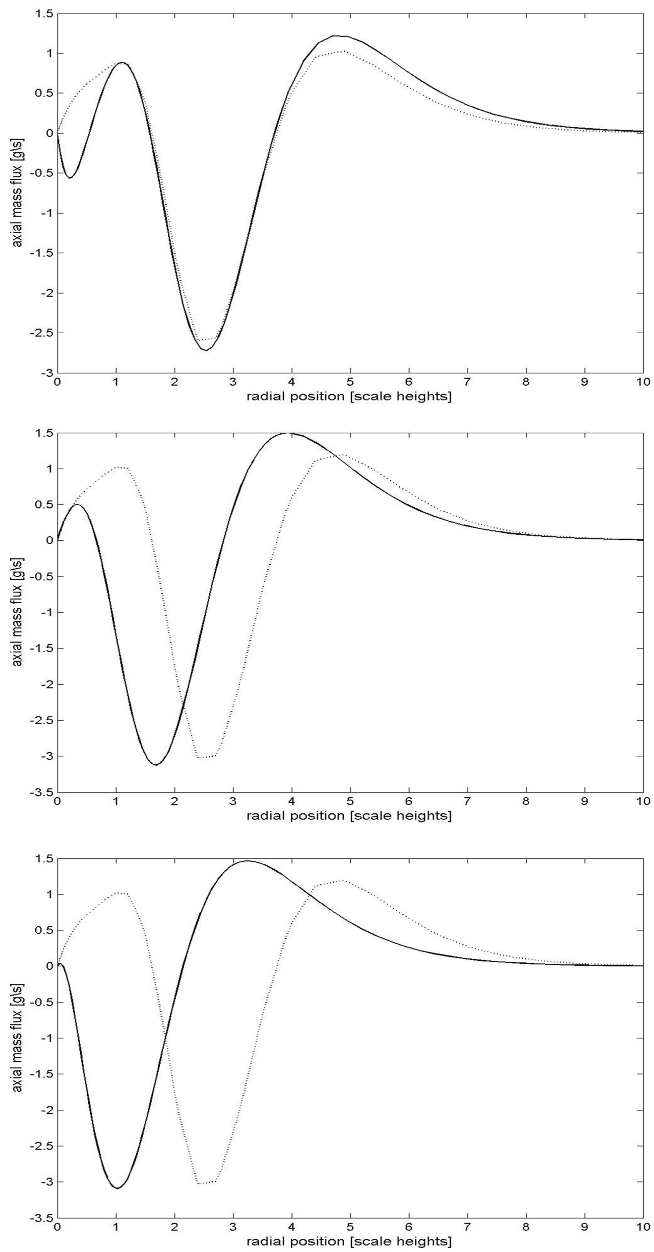

Figure 69: Axial Mass Flux plot from the quarter-plane of the Iguaçu machine countercurrent flow create by a scoop drive. Three wall speeds were simulated: 500 m/s (top), 600 m/s (middle), and 700 m/s (bottom). The results from the *CurvSOL* code with the pancake approximation are shown by the dashed line and the those from the *CurvSOL* code considering the curvature of the rotor wall are represented by the dotted line.

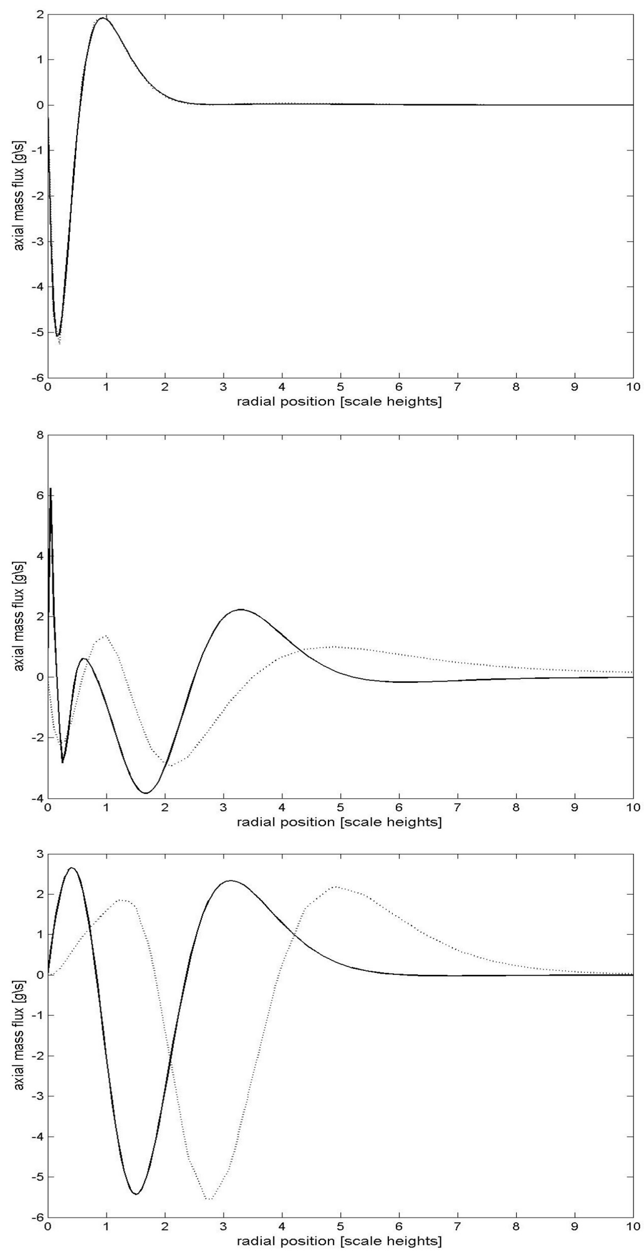

Figure 70: Axial Mass Flux plot from the quarter-plane of the Rome machine countercurrent flow with a wall speed of 500 m/s. The results from the linear wall temperature gradient (top), feed (middle), and scoop (bottom) drive mechanisms are shown. The results from the *CurvSOL* code with the pancake approximation are shown by the dashed line and the those from the *CurvSOL* code considering the curvature of the rotor wall are represented by the dotted line.

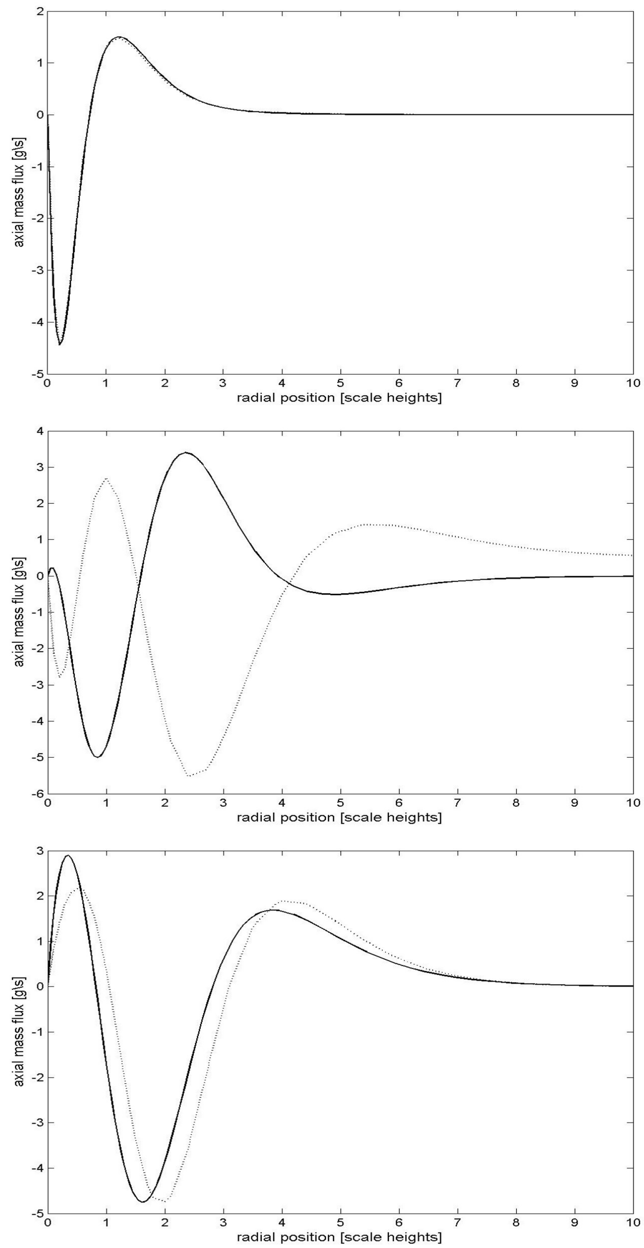

Figure 71: Axial Mass Flux plot from the quarter-plane of the Rome machine countercurrent flow with a wall speed of 600 m/s. The results from the linear wall temperature gradient (top), feed (middle), and scoop (bottom) drive mechanisms are shown. The results from the *CurvSOL* code with the pancake approximation are shown by the dashed line and the those from the *CurvSOL* code considering the curvature of the rotor wall are represented by the dotted line.

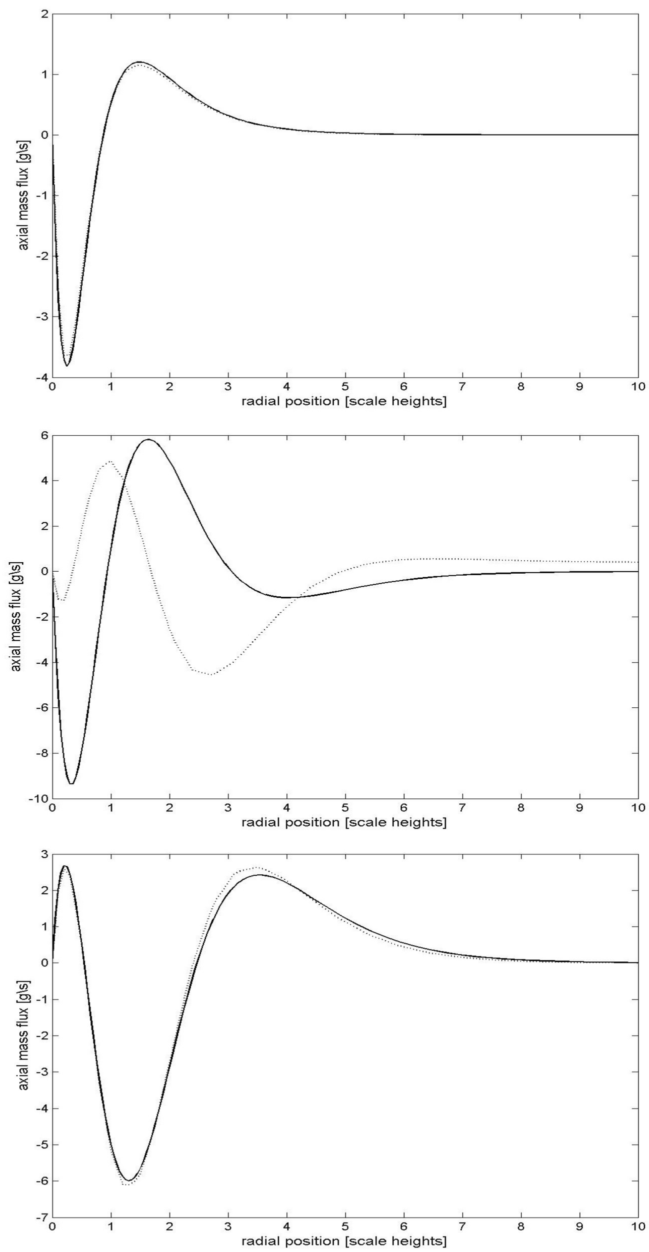

Figure 72: Axial Mass Flux plot from the quarter-plane of the Rome machine countercurrent flow with a wall speed of 700 m/s. The results from the linear wall temperature gradient (top), feed (middle), and scoop (bottom) drive mechanisms are shown. The results from the *CurvSOL* code with the pancake approximation are shown by the dashed line and the those from the *CurvSOL* code considering the curvature of the rotor wall are represented by the dotted line.

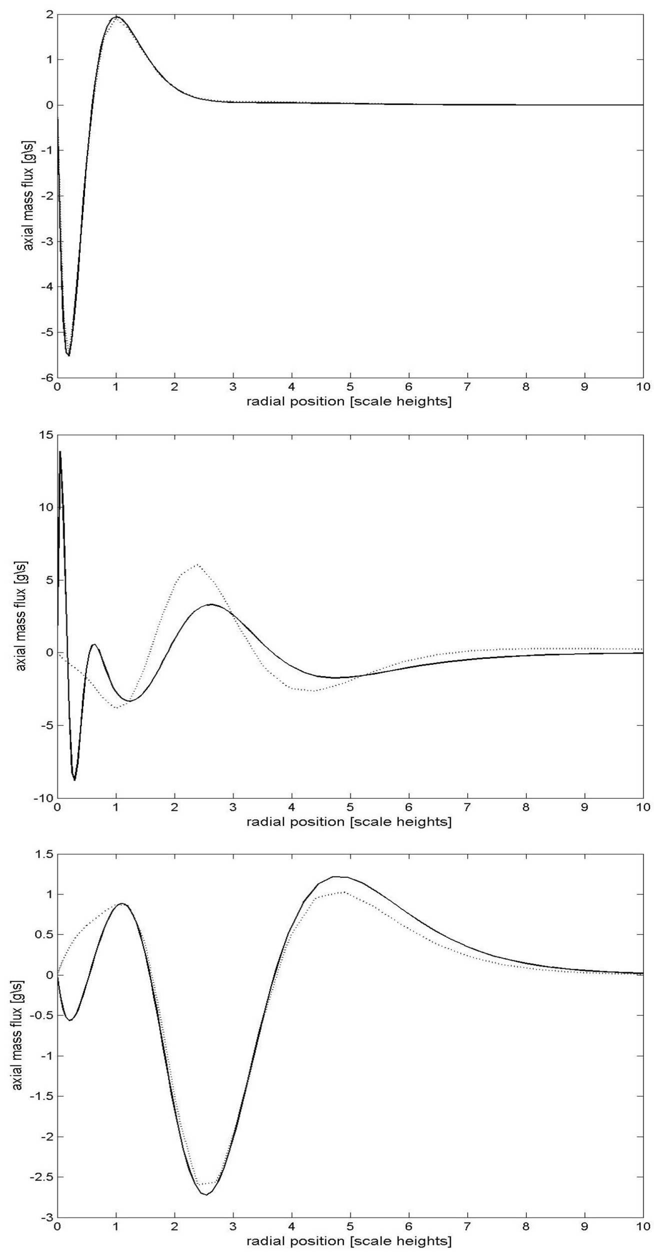

Figure 73: Axial Mass Flux plot from the quarter-plane of the Iguaçu machine countercurrent flow with a wall speed of 500 m/s. The results from the linear wall temperature gradient (top), feed (middle), and scoop (bottom) drive mechanisms are shown. The results from the *CurvSOL* code with the pancake approximation are shown by the dashed line and the those from the *CurvSOL* code considering the curvature of the rotor wall are represented by the dotted line.

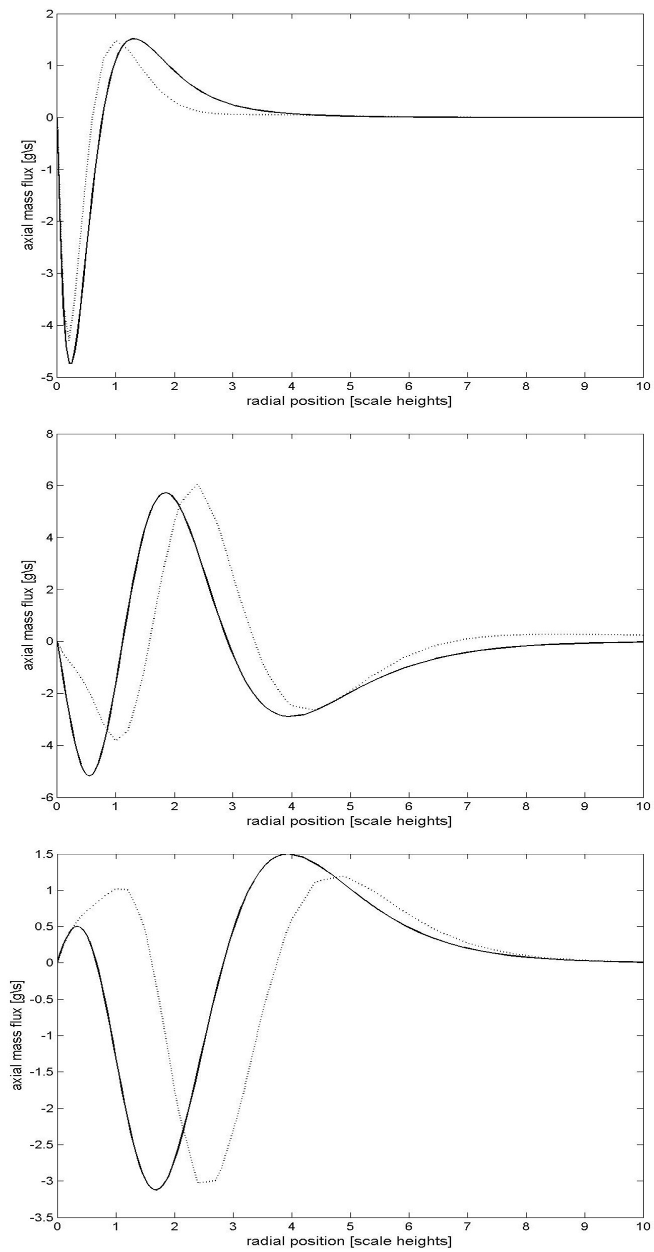

Figure 74: Axial Mass Flux plot from the quarter-plane of the Iguaçu machine countercurrent flow with a wall speed of 600 m/s. The results from the linear wall temperature gradient (top), feed (middle), and scoop (bottom) drive mechanisms are shown. The results from the *CurvSOL* code with the pancake approximation are shown by the dashed line and the those from the *CurvSOL* code considering the curvature of the rotor wall are represented by the dotted line.

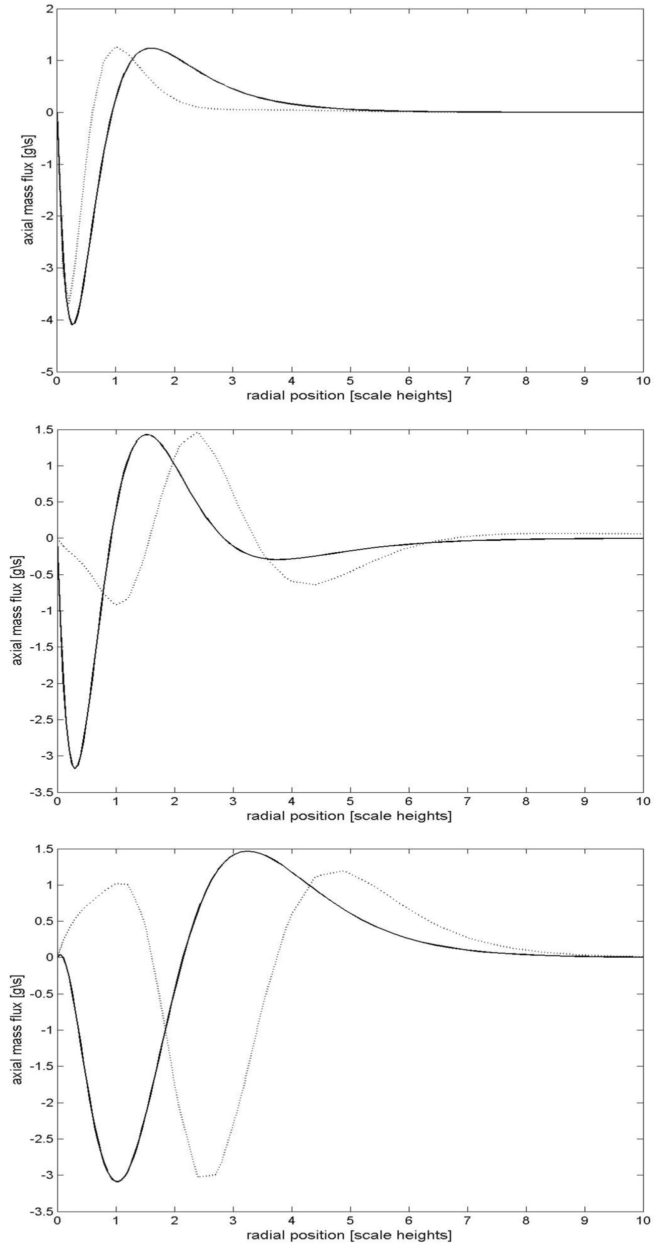

Figure 75: Axial Mass Flux plot from the quarter-plane of the Iguaçu machine countercurrent flow with a wall speed of 700 m/s. The results from the linear wall temperature gradient (top), feed (middle), and scoop (bottom) drive mechanisms are shown. The results from the *CurvSOL* code with the pancake approximation are shown by the dashed line and the those from the *CurvSOL* code considering the curvature of the rotor wall are represented by the dotted line.

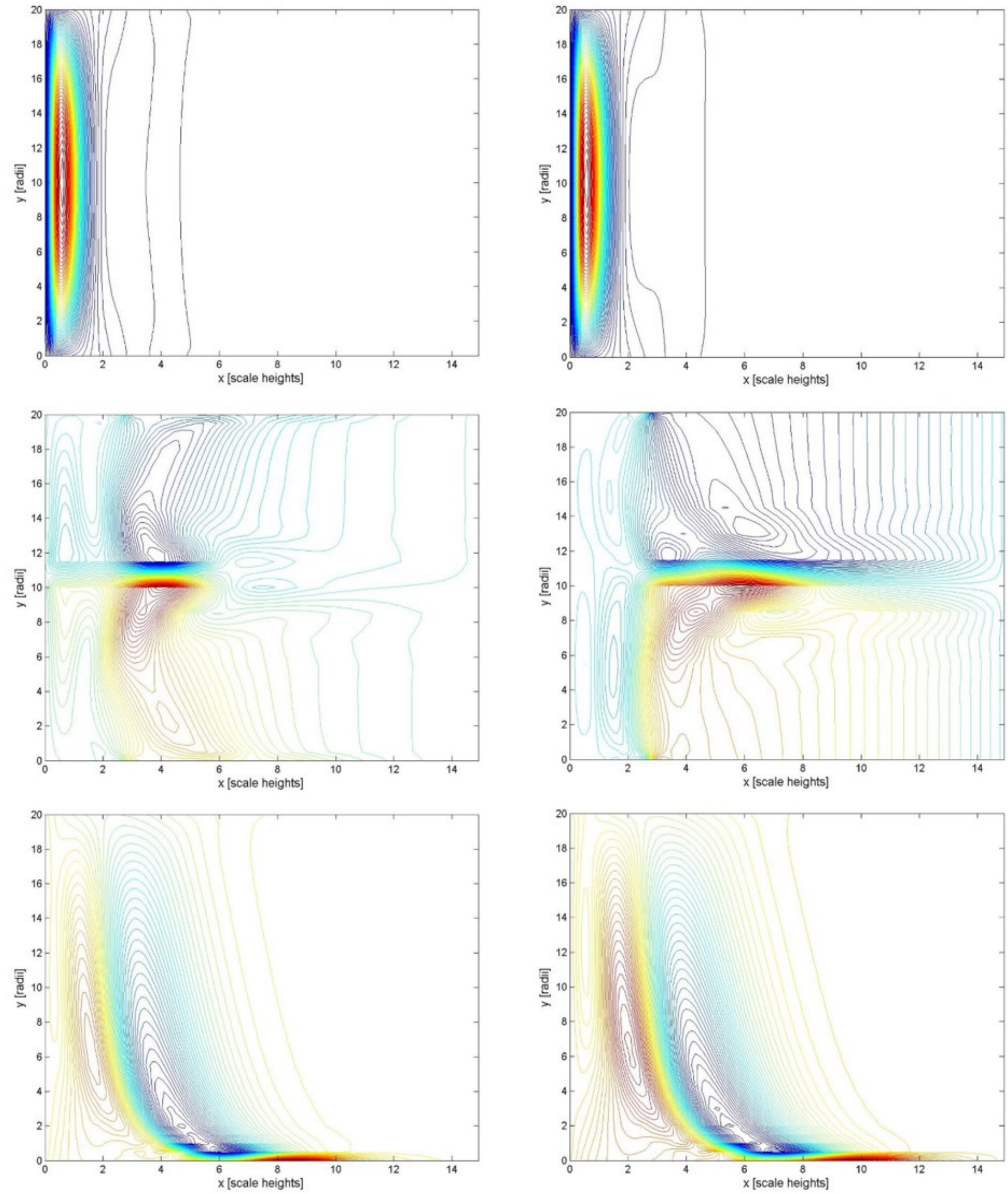

Figure 76: Streamfunction plots from the Rome machine with a wall speed of 500 m/s. The results of *Pancake* code are shown at left and the *CurvSOL* code with the pancake approximation in the right column. Three drive mechanism contributions are shown: linear wall temperature gradient (top), feed (center) and scoop drive (bottom).

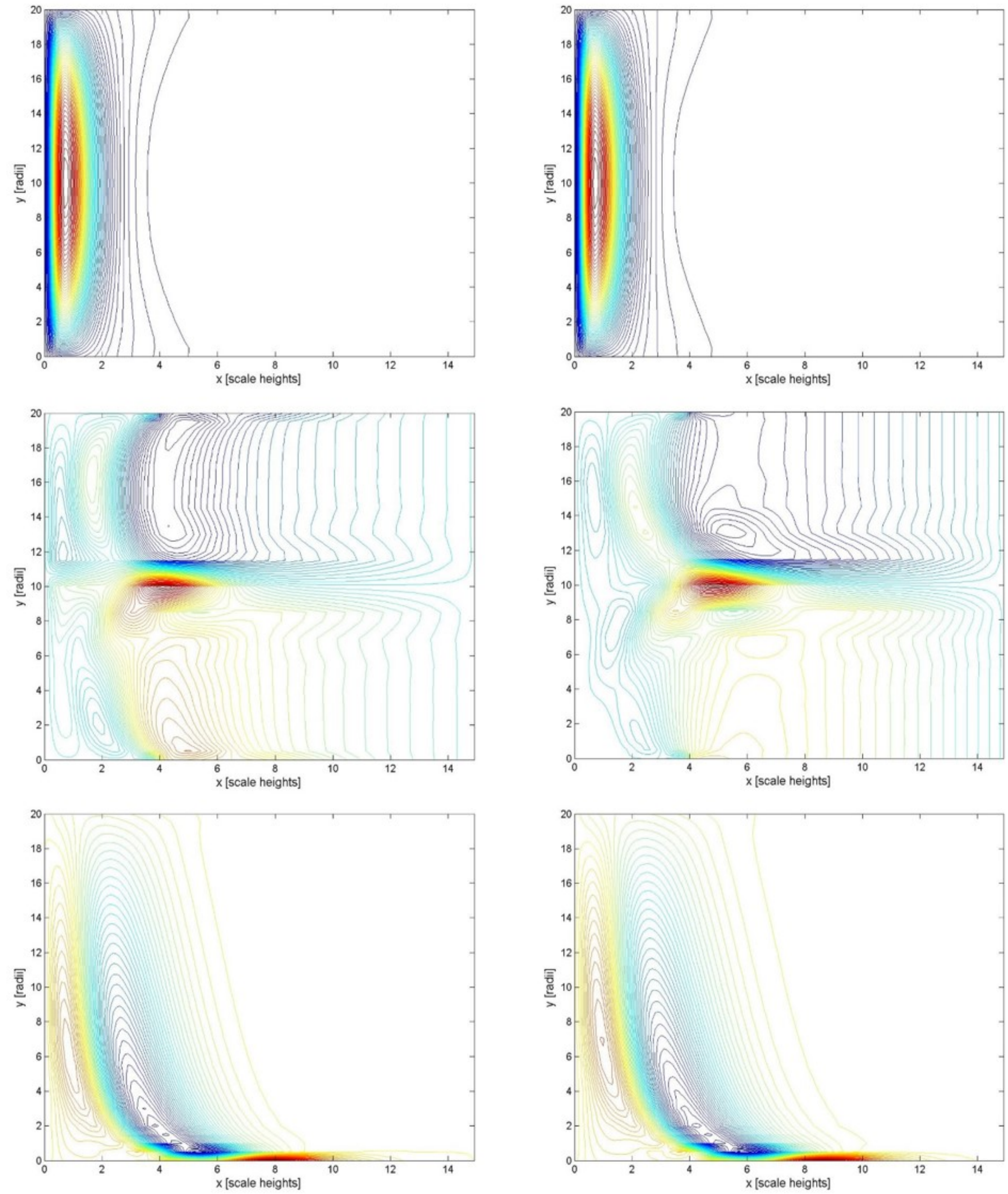

Figure 77: Streamfunction plots from the Rome machine with a wall speed of 600 m/s. The results of *Pancake* code are shown at left and the *CurvSOL* code with the pancake approximation in the right column. Three drive mechanism contributions are shown: linear wall temperature gradient (top), feed (center) and scoop drive (bottom).

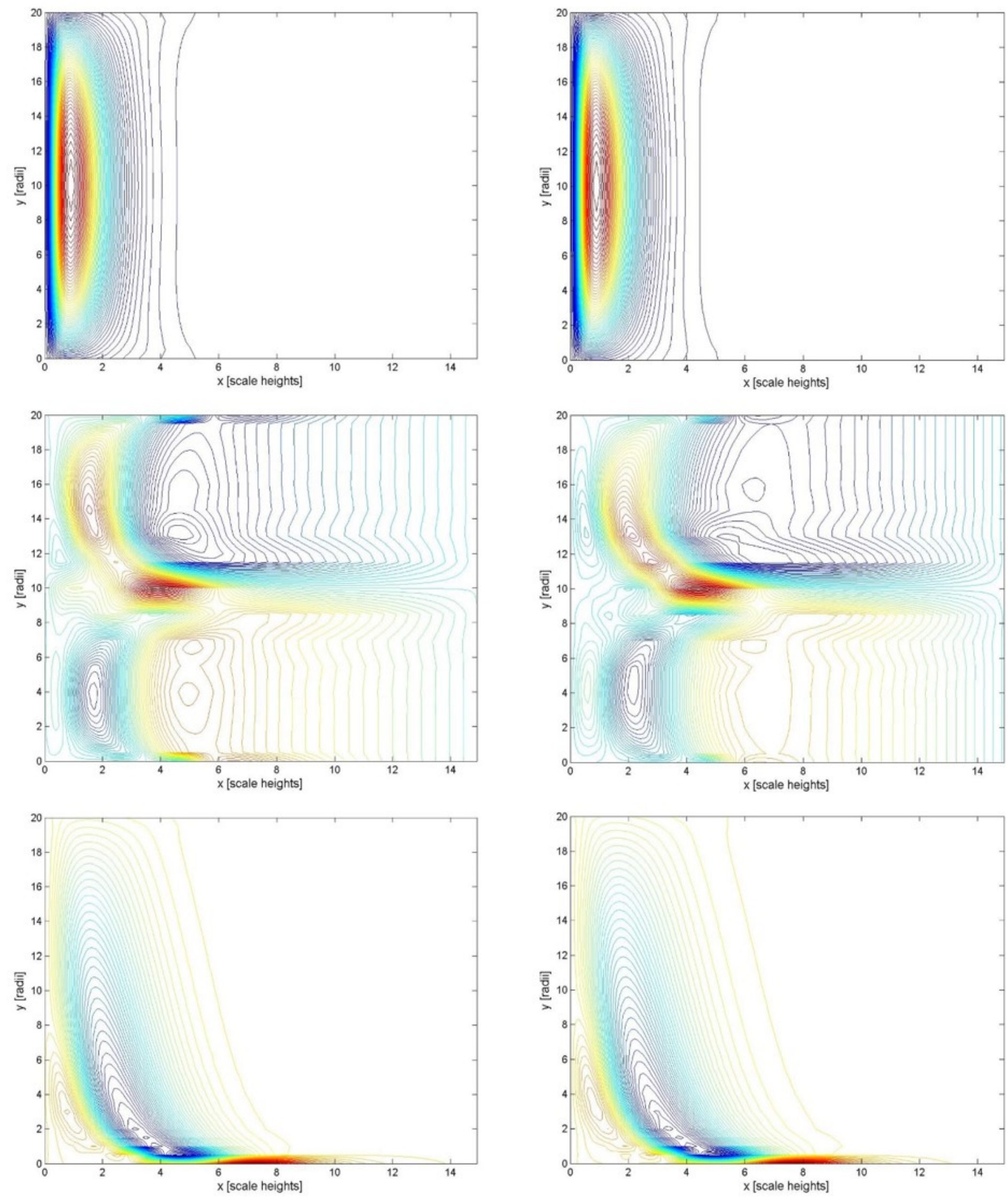

Figure 78: Streamfunction plots from the Rome machine with a wall speed of 700 m/s. The results of *Pancake* code are shown at left and the *CurvSOL* code with the pancake approximation in the right column. Three drive mechanism contributions are shown: linear wall temperature gradient (top), feed (center) and scoop drive (bottom).

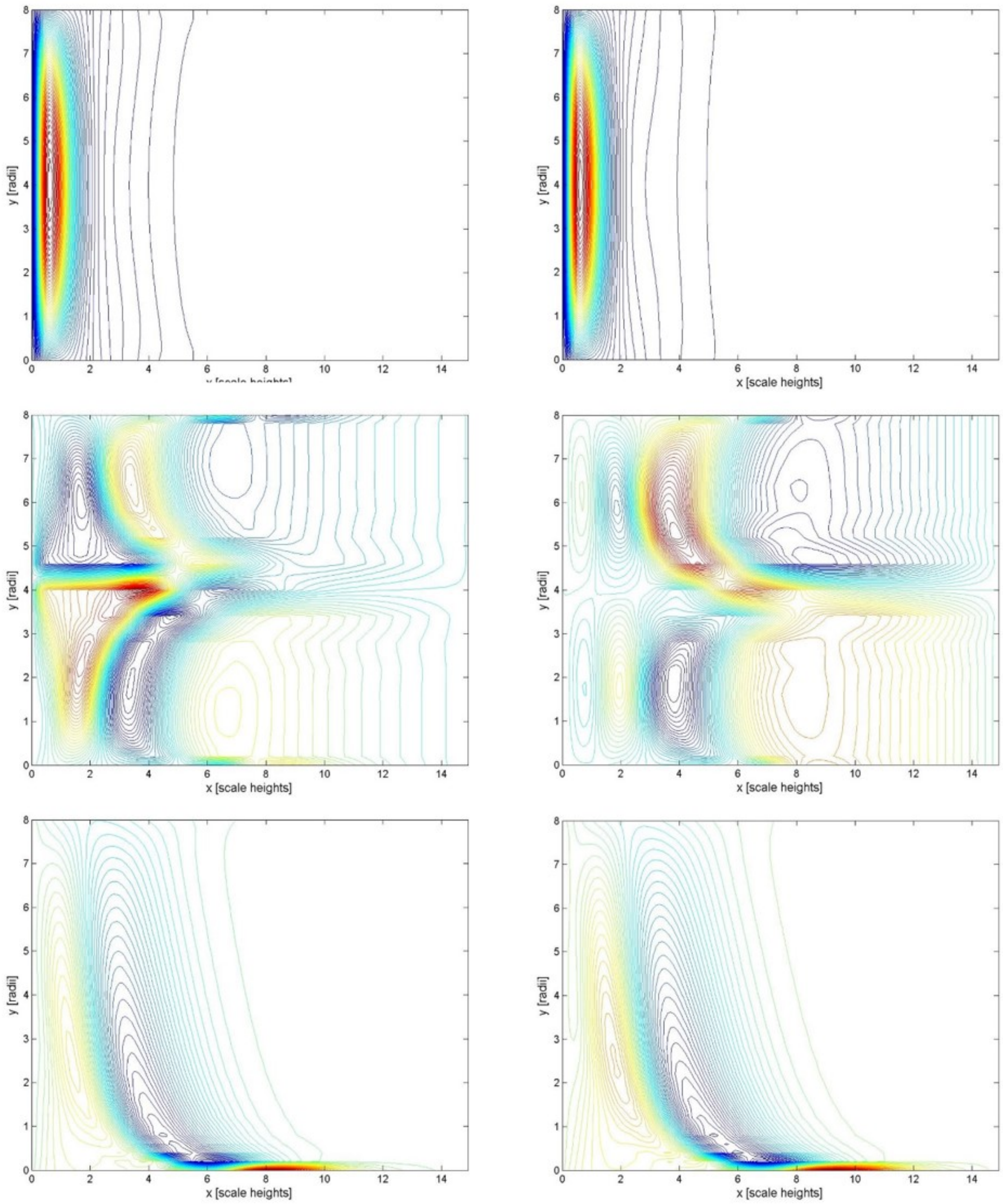

Figure 79: Streamfunction plots from the Iguaçu machine with a wall speed of 500 m/s. The results of *Pancake* code are shown at left and the *CurvSOL* code with the pancake approximation in the right column. Three drive mechanism contributions are shown: linear wall temperature gradient (top), feed (center) and scoop drive (bottom).

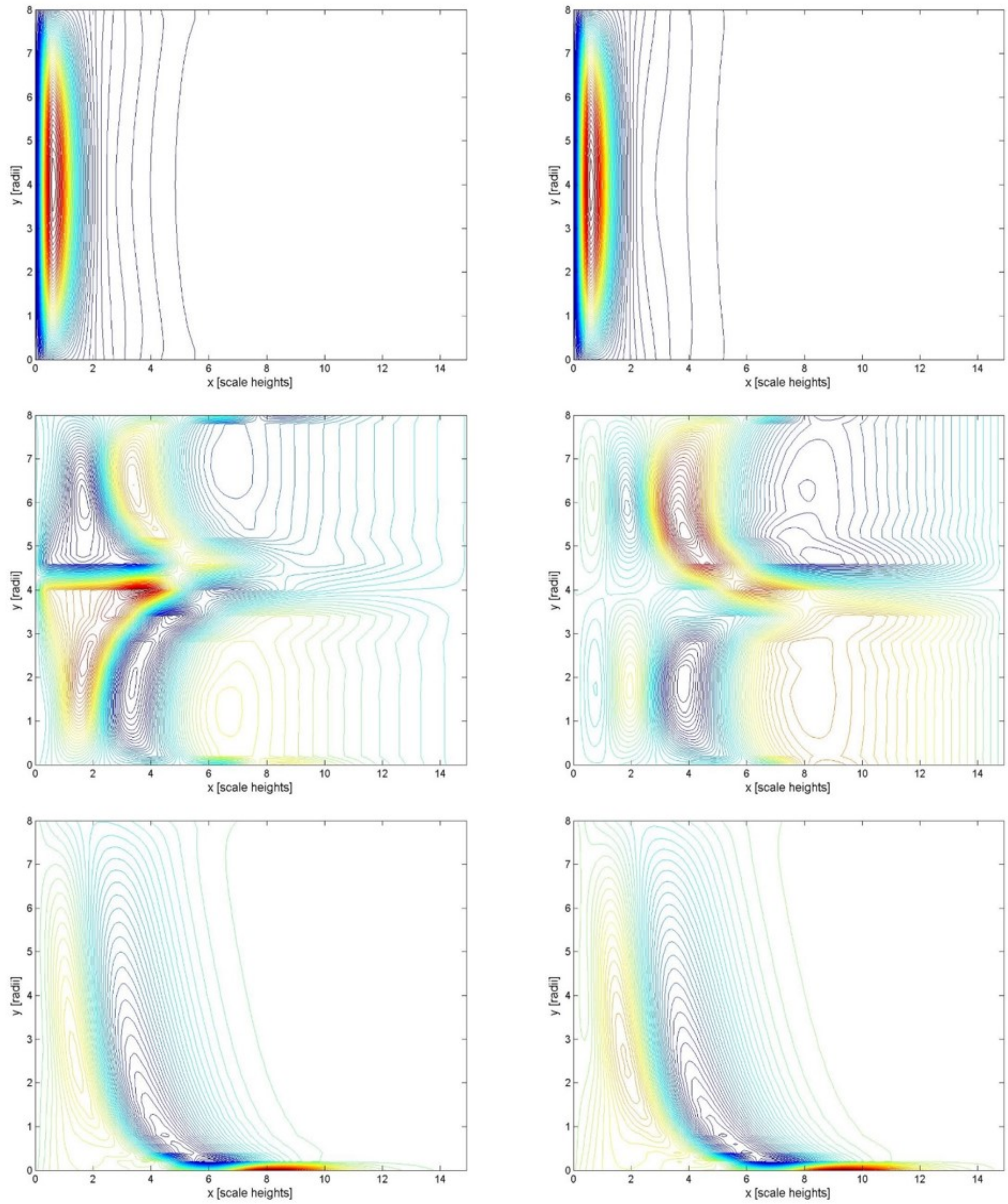

Figure 80: Streamfunction plots from the Iguaçu machine with a wall speed of 600 m/s. The results of *Pancake* code are shown at left and the *CurvSOL* code with the pancake approximation in the right column. Three drive mechanism contributions are shown: linear wall temperature gradient (top), feed (center) and scoop drive (bottom).

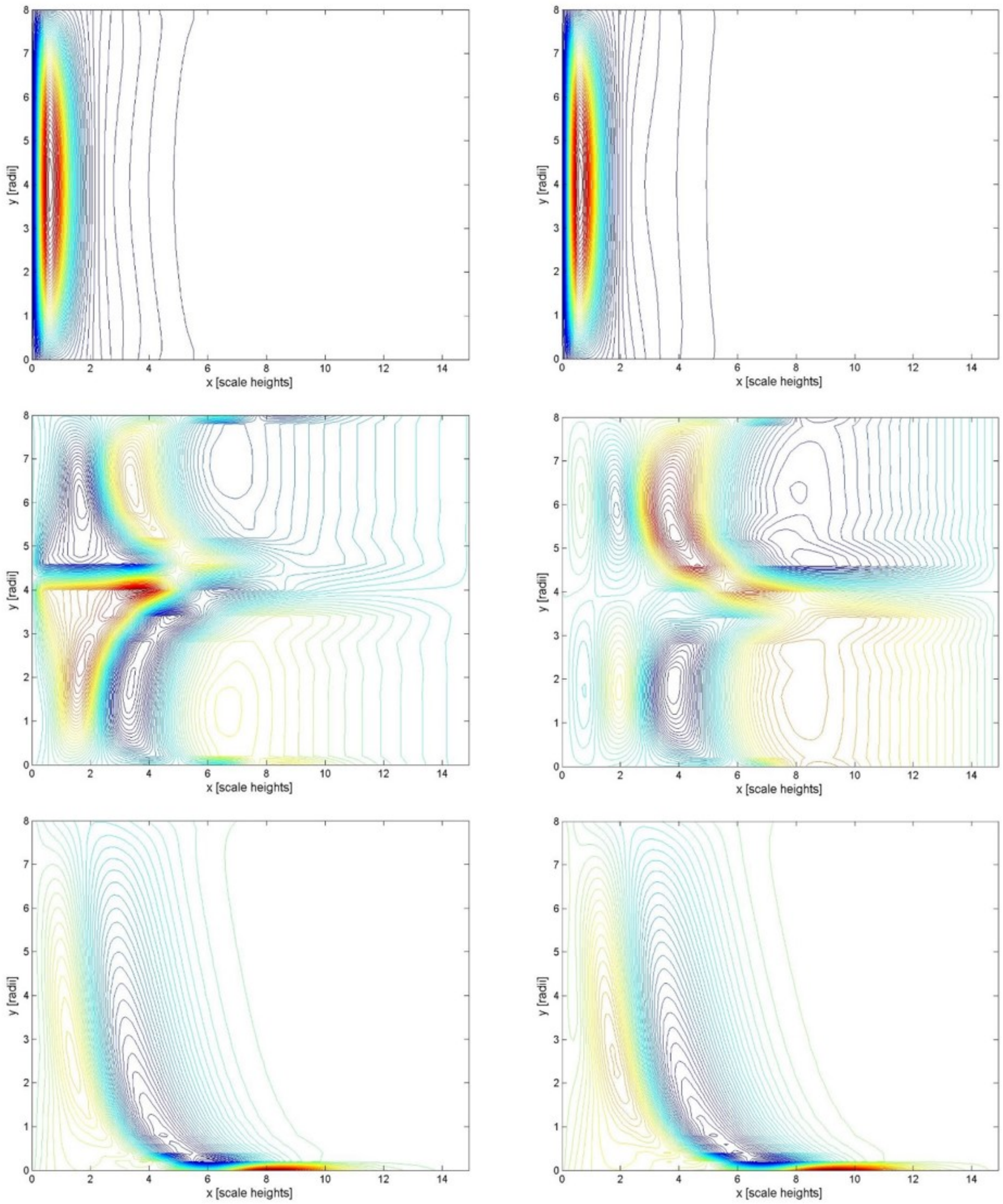

Figure 81: Streamfunction plots from the Iguaçu machine with a wall speed of 700 m/s. The results of *Pancake* code are shown at left and the *CurvSOL* code with the pancake approximation in the right column. Three drive mechanism contributions are shown: linear wall temperature gradient (top), feed (center) and scoop drive (bottom).

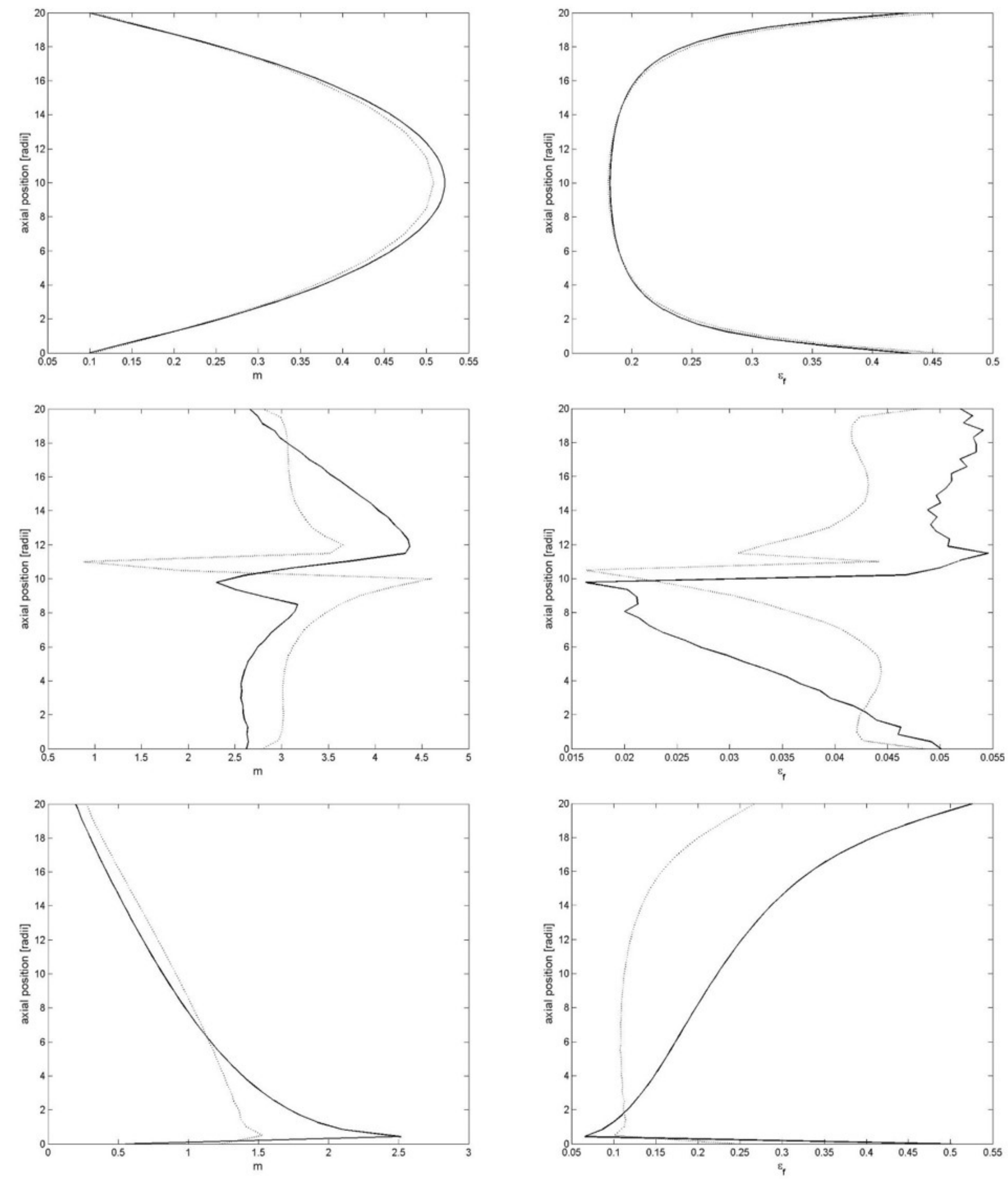

Figure 82: Simulation results from the Rome machine with a wall speed of 500 m/s. m values are shown in the column on the left and flow profile efficiency values shown to the right. Three drive mechanism contributions are shown: linear wall temperature gradient (top), feed (center) and scoop drive (bottom). The results of the *Pancake* code are depicted with the solid line while the results from the *CurvSOL* code with the pancake approximation are represented by the dotted line.

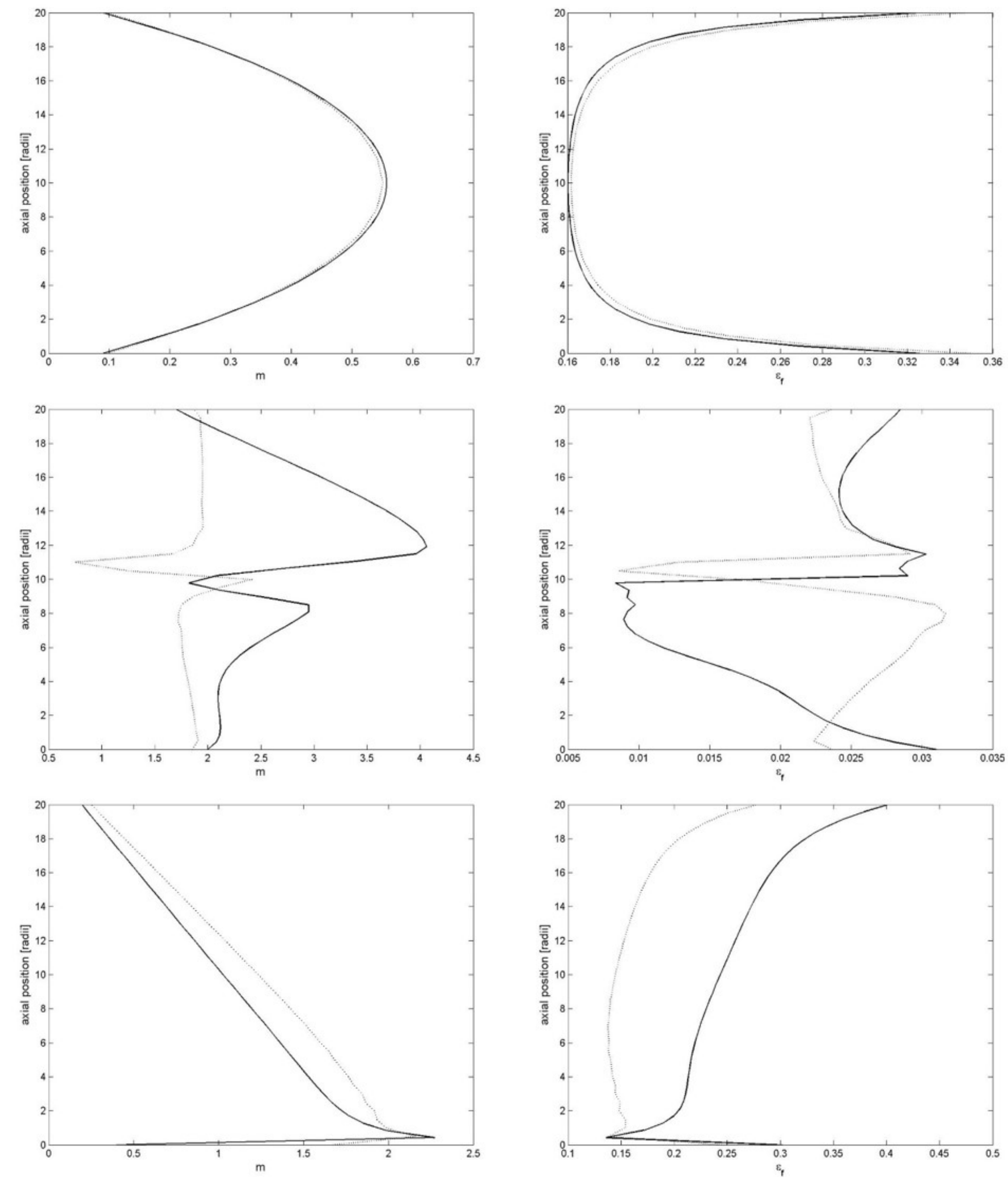

Figure 83: Simulation results from the Rome machine with a wall speed of 600 m/s. m values are shown in the column on the left and flow profile efficiency values shown to the right. Three drive mechanism contributions are shown: linear wall temperature gradient (top), feed (center) and scoop drive (bottom). The results of the *Pancake* code are depicted with the solid line while the results from the *CurvSOL* code with the pancake approximation are represented by the dotted line..

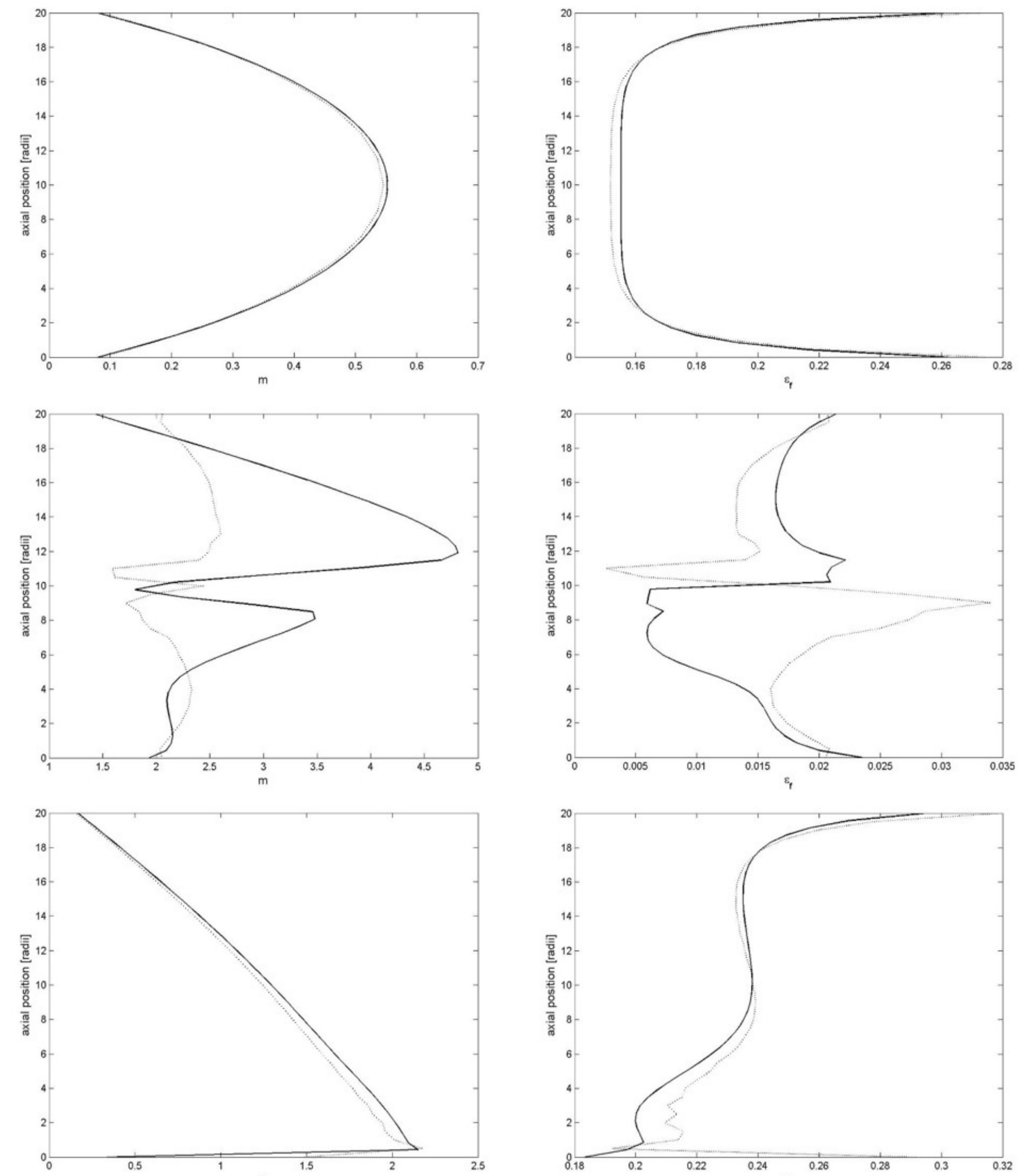

Figure 84: Simulation results from the Rome machine with a wall speed of 700 m/s. m values are shown in the column on the left and flow profile efficiency values shown to the right. Three drive mechanism contributions are shown: linear wall temperature gradient (top), feed (center) and scoop drive (bottom). The results of the *Pancake* code are depicted with the solid line while the results from the *CurvSOL* code with the pancake approximation are represented by the dotted line.

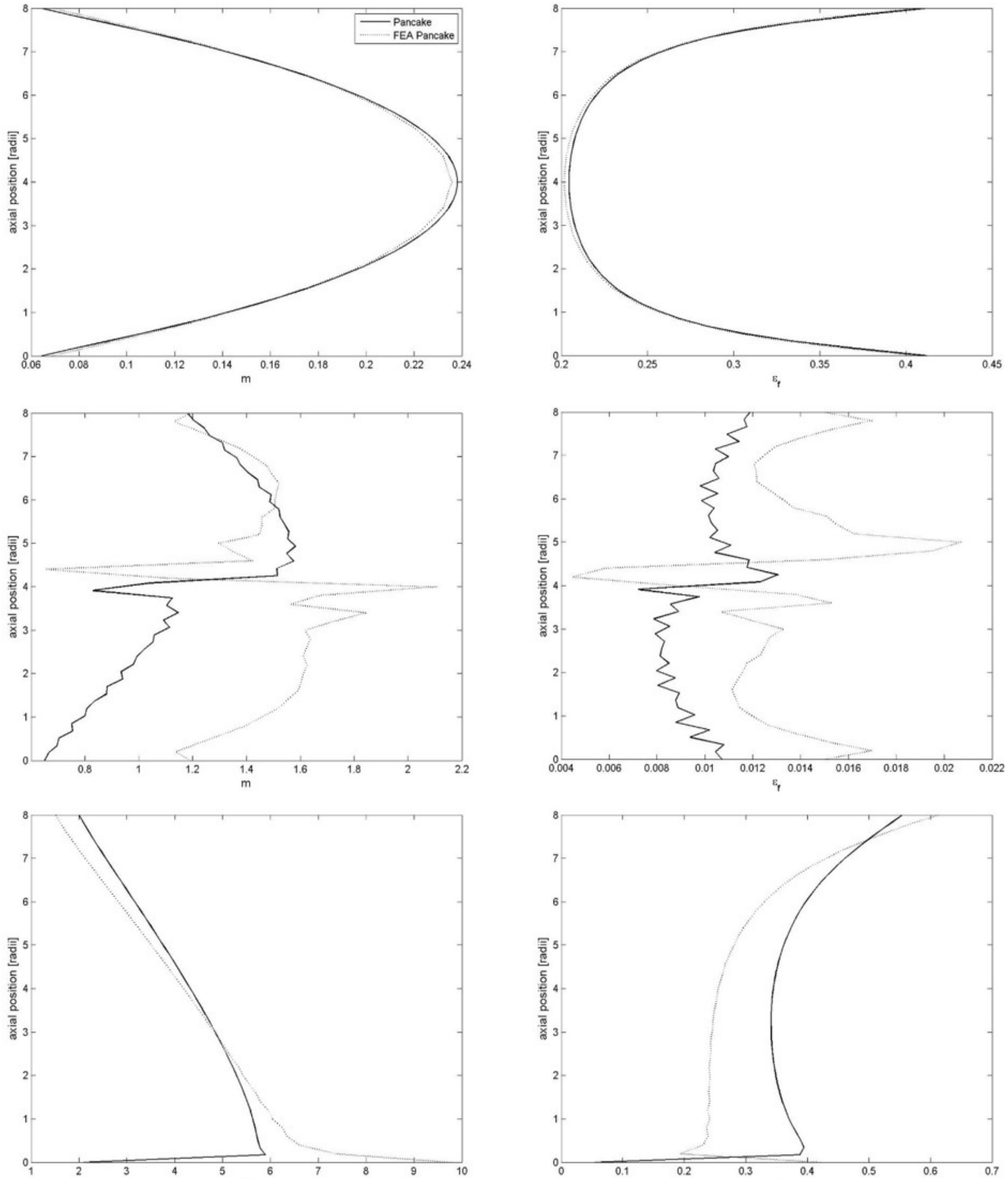

Figure 85: Simulation results from the Iguaçu machine with a wall speed of 500 m/s. m values are shown in the column on the left and flow profile efficiency values shown to the right. Three drive mechanism contributions are shown: linear wall temperature gradient (top), feed (center) and scoop drive (bottom). The results of the *Pancake* code are depicted with the solid line while the results from the *CurvSOL* code with the pancake approximation are represented by the dotted line.

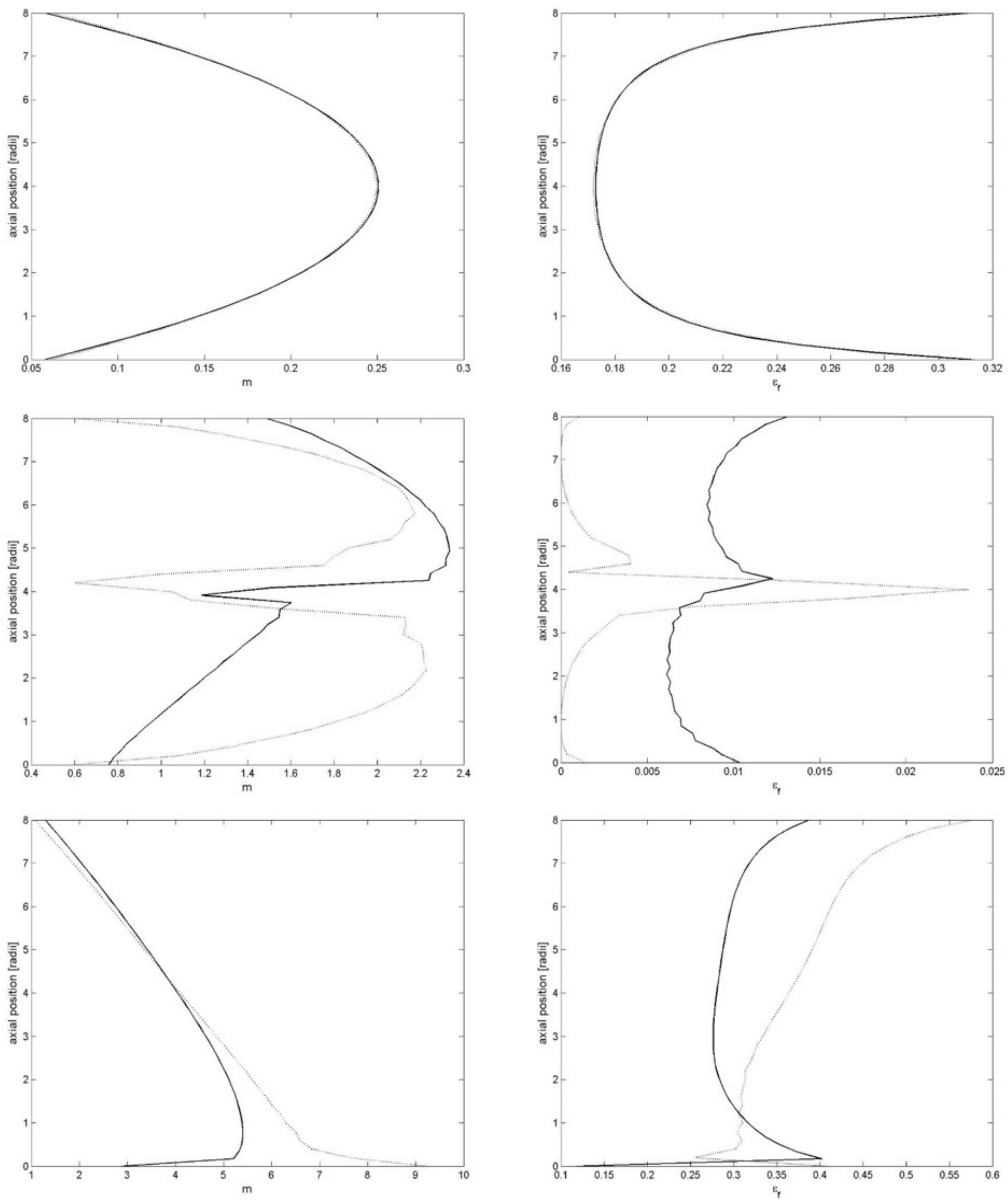

Figure 86: Simulation results from the Iguaçu machine with a wall speed of 600 m/s. m values are shown in the column on the left and flow profile efficiency values shown to the right. Three drive mechanism contributions are shown: linear wall temperature gradient (top), feed (center) and scoop drive (bottom). The results of the *Pancake* code are depicted with the solid line while the results from the *CurvSOL* code with the pancake approximation are represented by the dotted line.

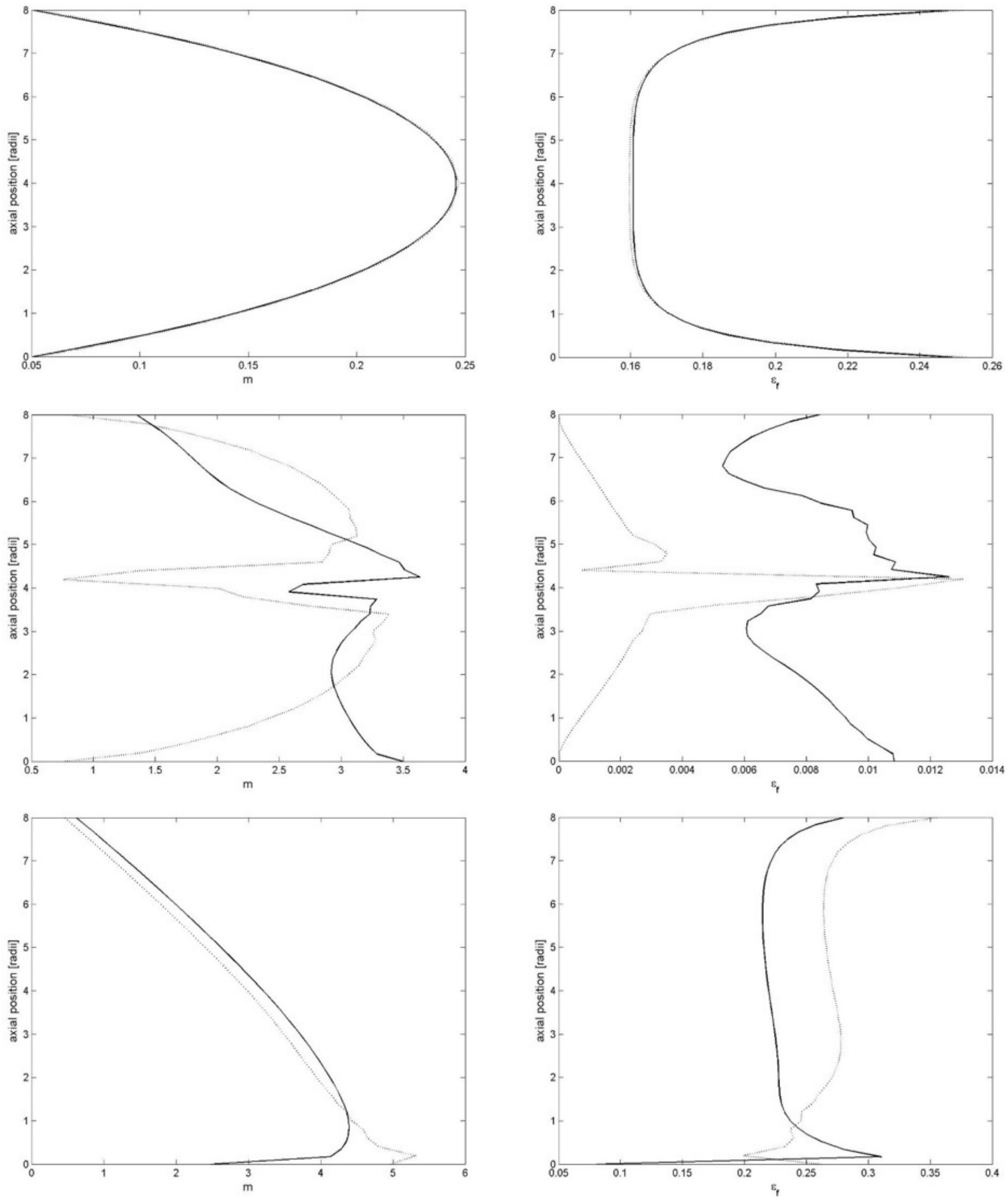

Figure 87: Simulation results from the Iguaçu machine with a wall speed of 700 m/s. m values are shown in the column on the left and flow profile efficiency values shown to the right. Three drive mechanism contributions are shown: linear wall temperature gradient (top), feed (center) and scoop drive (bottom). The results of the *Pancake* code are depicted with the solid line while the results from the *CurvSOL* code with the pancake approximation are represented by the dotted line.

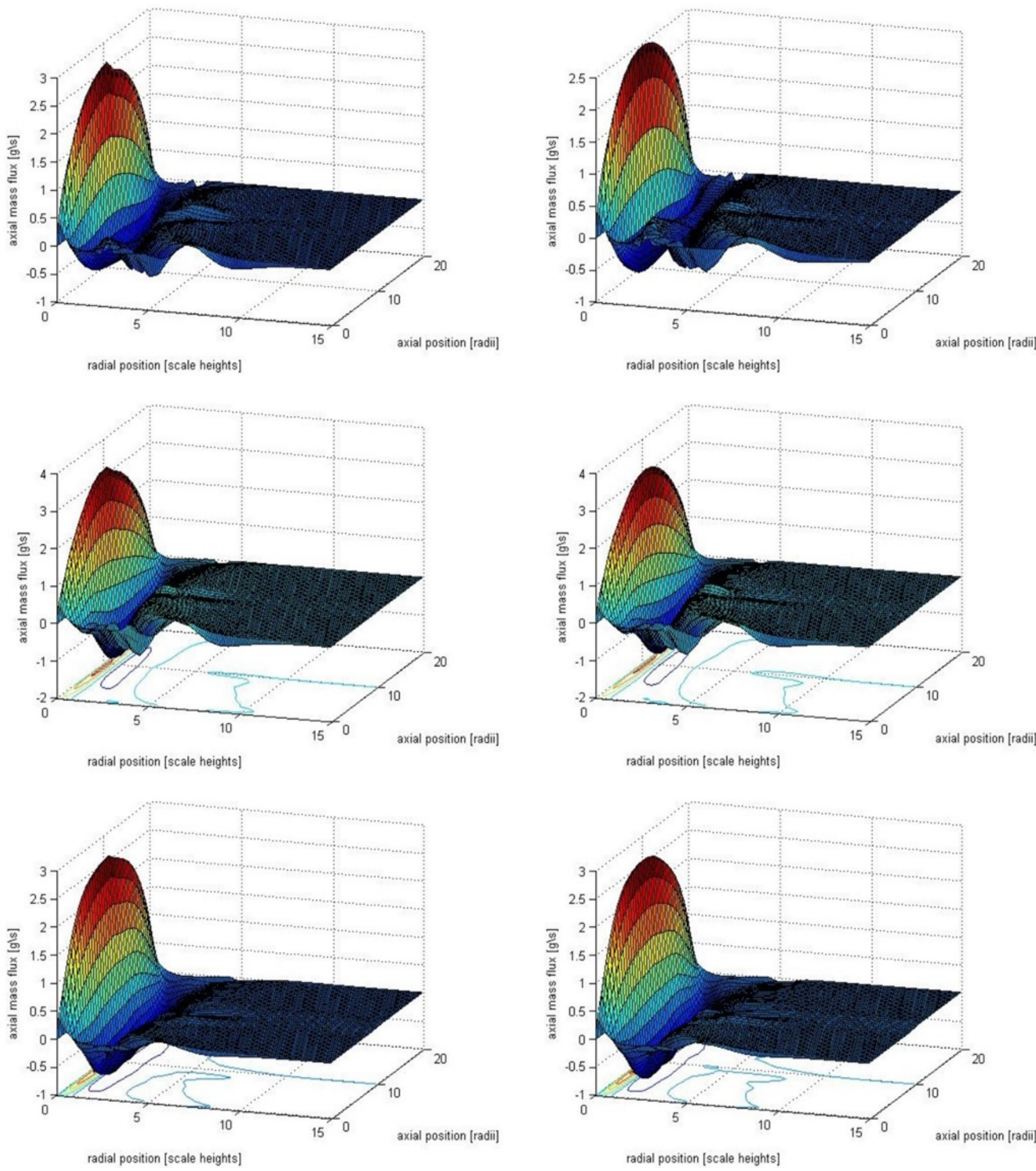

Figure 88: Total Axial Mass Flux continuous surface plots for the Rome machine. The results of *Pancake* code are shown at left and the *CurvSOL* code with the pancake approximation in the right column. The results from simulations at three wall speeds are shown: 500 m/s (top), 600 m/s (center), and 700 m/s (bottom).

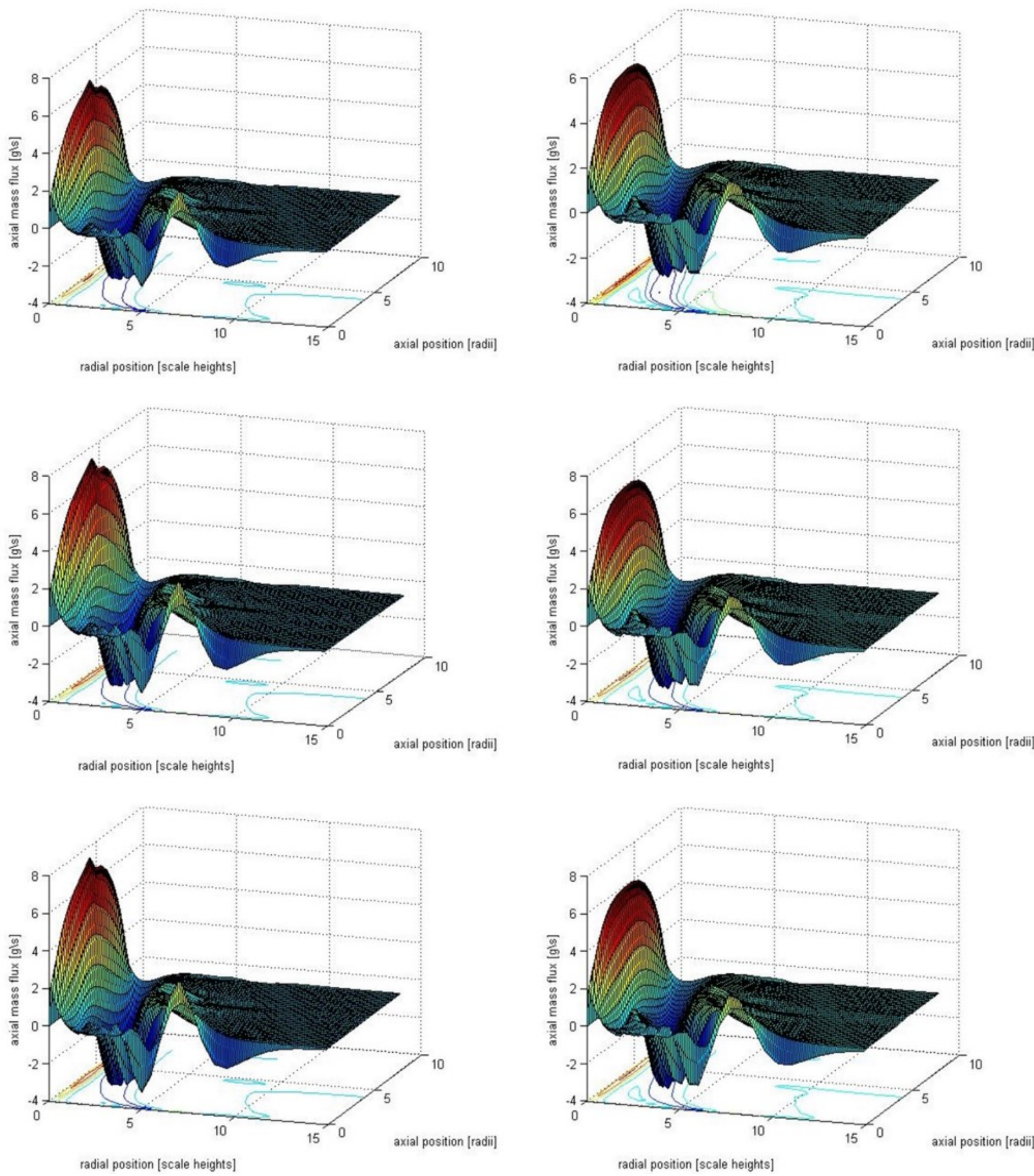

Figure 89: Total Axial Mass Flux continuous surface plots for the Iguaçu machine. The results of *Pancake* code are shown at left and the *CurvSOL* code with the pancake approximation in the right column. The results from simulations at three wall speeds are shown: 500 m/s (top), 600 m/s (center), and 700 m/s (bottom).

11 Appendix B - Isotope Transport Solutions

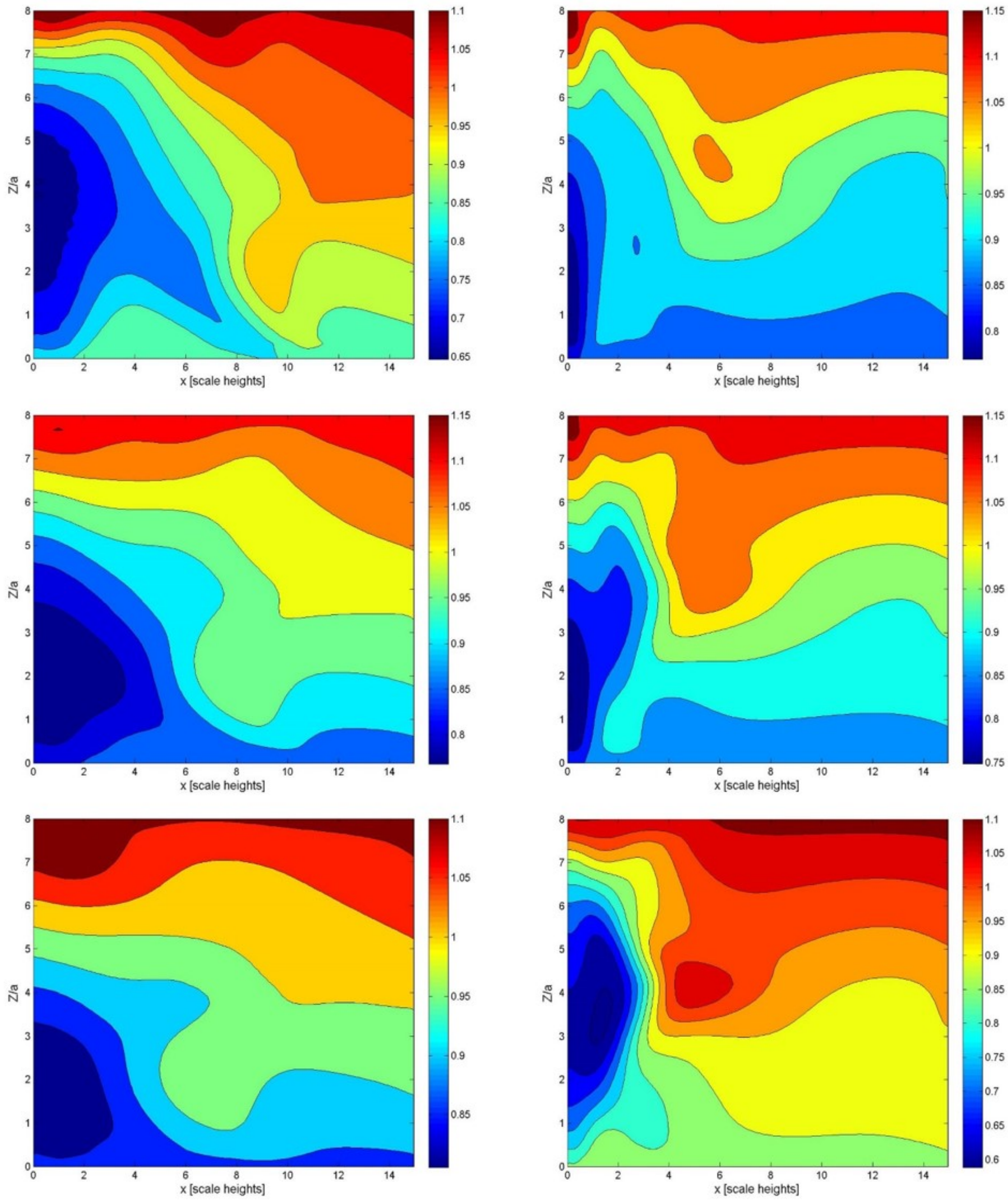

Figure 90: Two dimensional contour plots of the results of the finite difference code approximating the solution to the diffusion equation in the Iguaçu machine with simulations run at three different wall speeds:500 m/s (top), 600 m/s (middle), and 700 m's (bottom). Two axial mass flux fields for each wall speed were used to run the simulations: the mass flow from the *Pancake* code solution (left) and the mass flow field from the *CurvSOL* code (right).

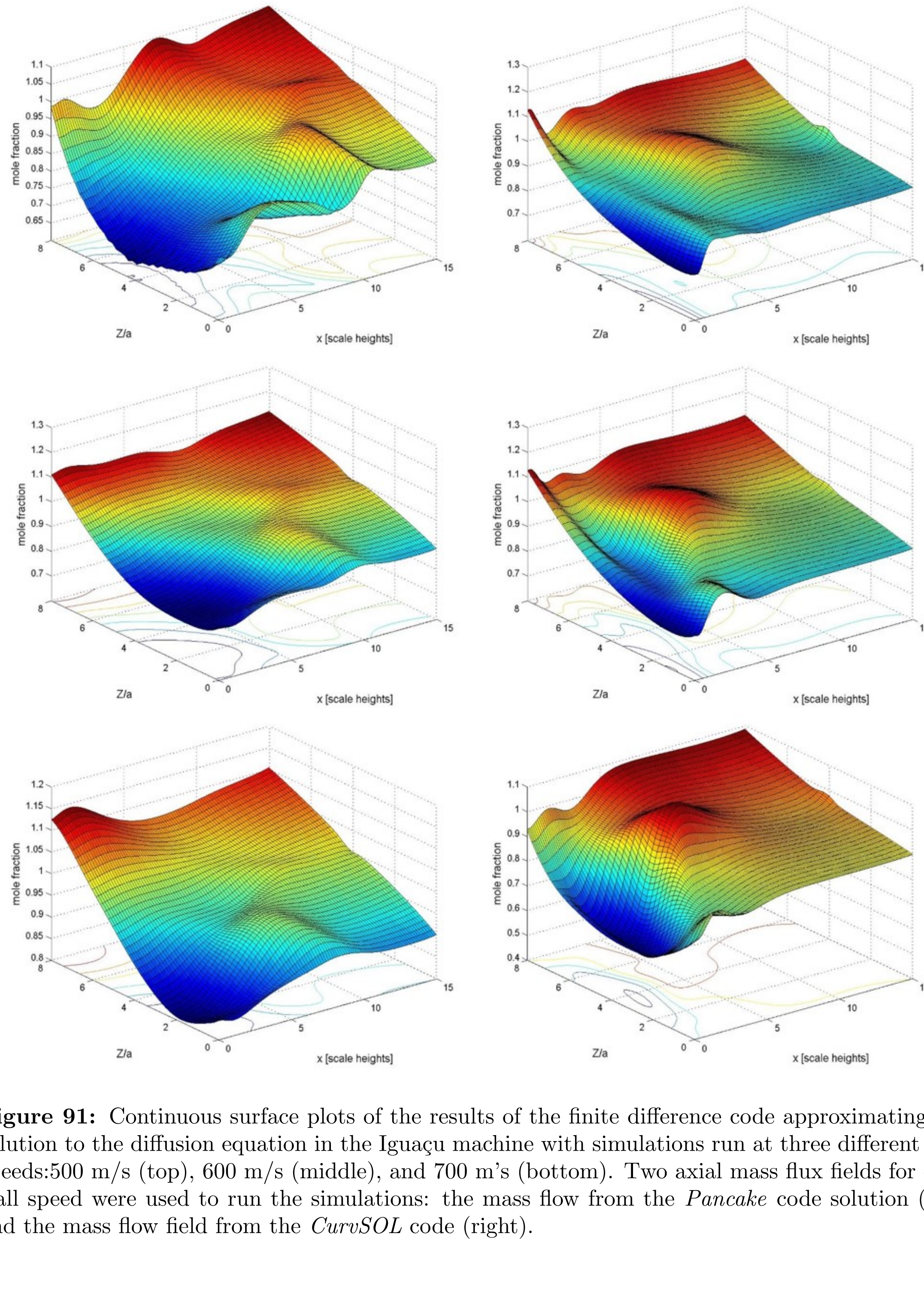

Figure 91: Continuous surface plots of the results of the finite difference code approximating the solution to the diffusion equation in the Iguaçu machine with simulations run at three different wall speeds:500 m/s (top), 600 m/s (middle), and 700 m's (bottom). Two axial mass flux fields for each wall speed were used to run the simulations: the mass flow from the *Pancake* code solution (left) and the mass flow field from the *CurvSOL* code (right).

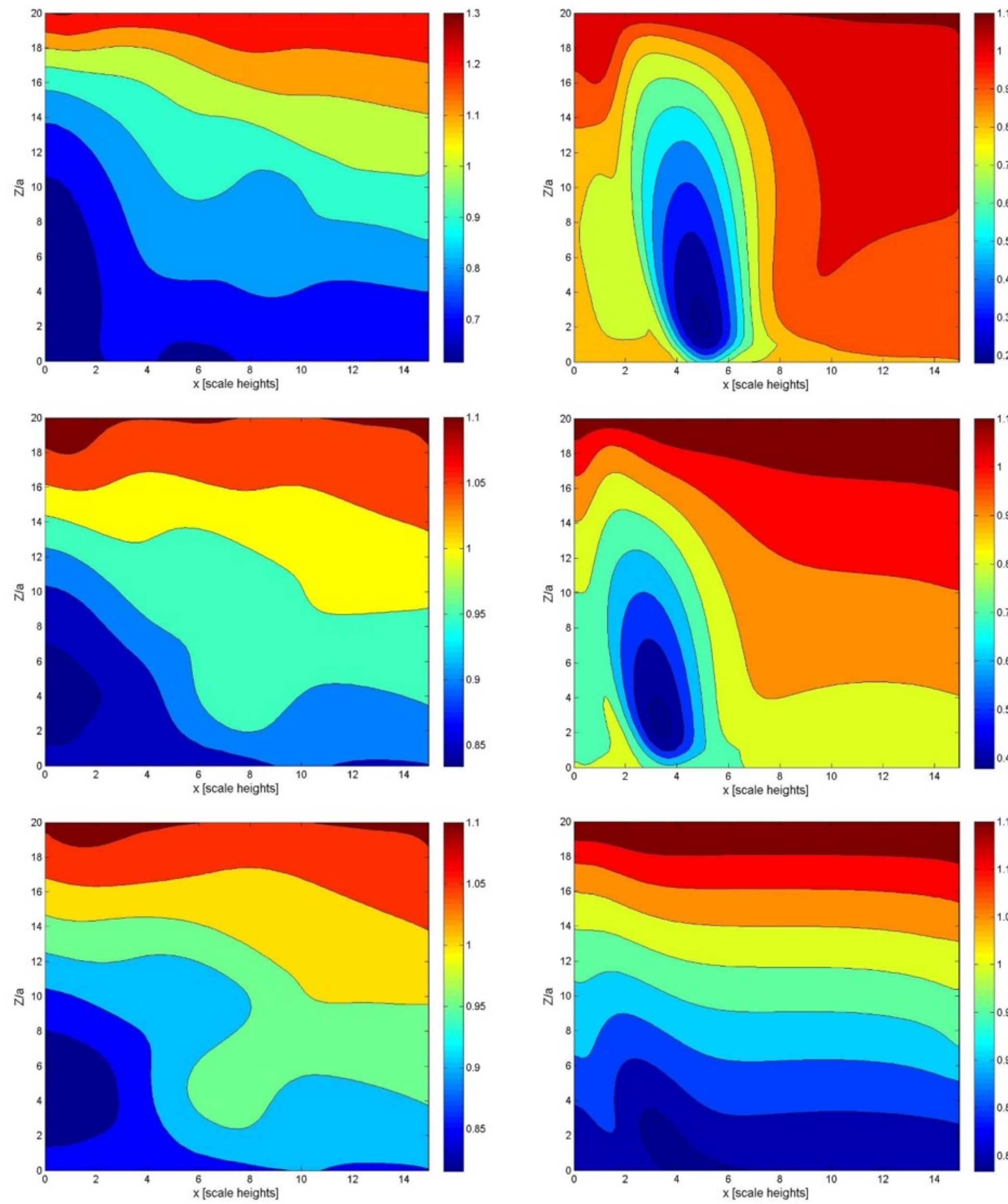

Figure 92: Two dimensional contour plots of the results of the finite difference code approximating the solution to the diffusion equation in the Rome machine with simulations run at three different wall speeds:500 m/s (top), 600 m/s (middle), and 700 m's (bottom). Two axial mass flux fields for each wall speed were used to run the simulations: the mass flow from the *Pancake* code solution (left) and the mass flow field from the *CurvSOL* code (right).

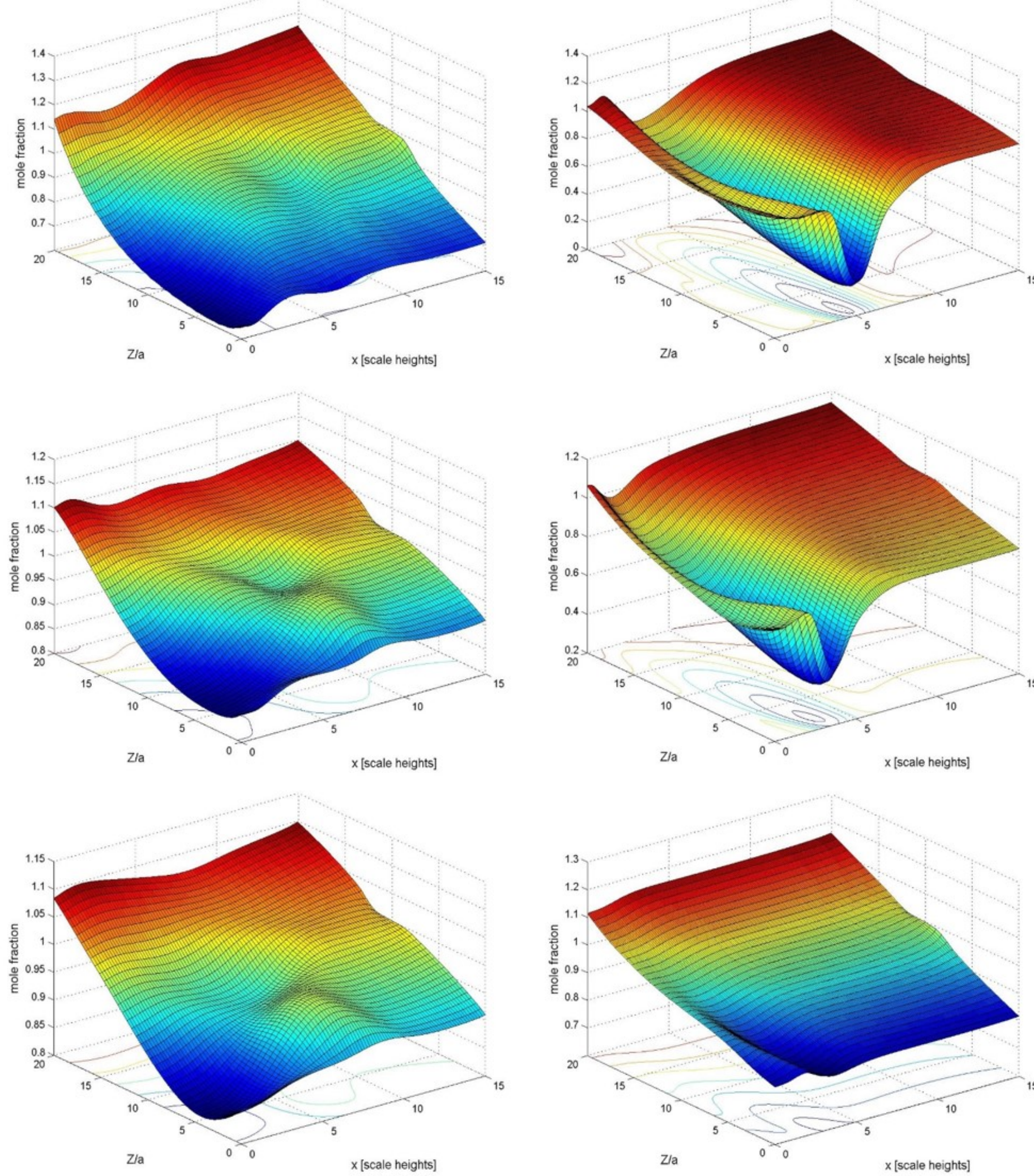

Figure 93: Continuous surface plots of the results of the finite difference code approximating the solution to the diffusion equation in the Rome machine with simulations run at three different wall speeds:500 m/s (top), 600 m/s (middle), and 700 m's (bottom). Two axial mass flux fields for each wall speed were used to run the simulations: the mass flow from the *Pancake* code solution (left) and the mass flow field from the *CurvSOL* code (right).

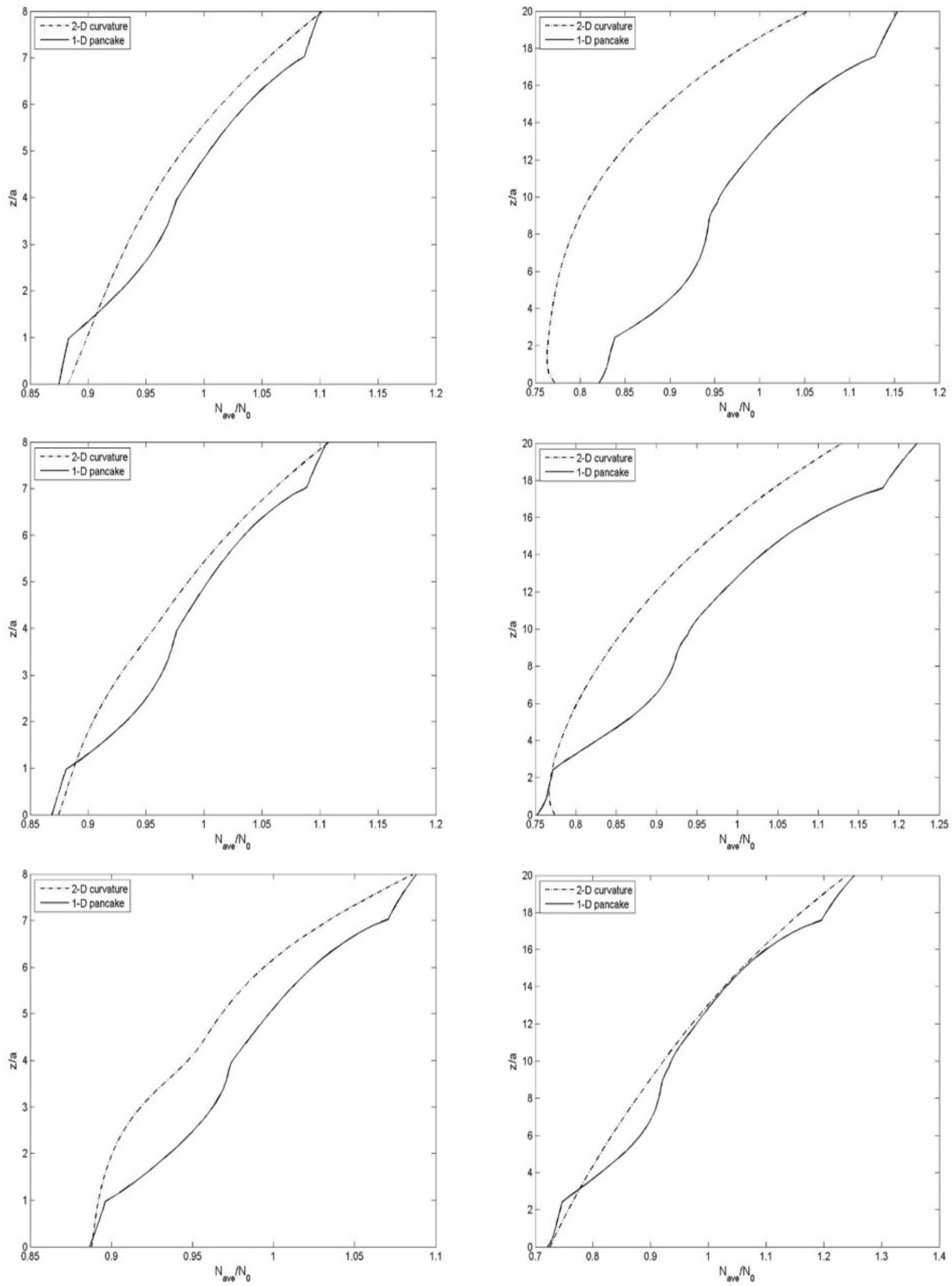

Figure 94: Comparison of the solutions of the diffusion equation for the Iguaçu (left) and the Rome (right) machines. The axial variation of the light isotope concentration is shown using the results of both the *xPort* finite differencing code (dashed line labeled "2-D curvature") and Cohen's radially averaging technique (solid line labeled "1-D pancake"). The results of the *xPort* code have been averaged at each axial sampling location for better comparison to the Cohen technique.

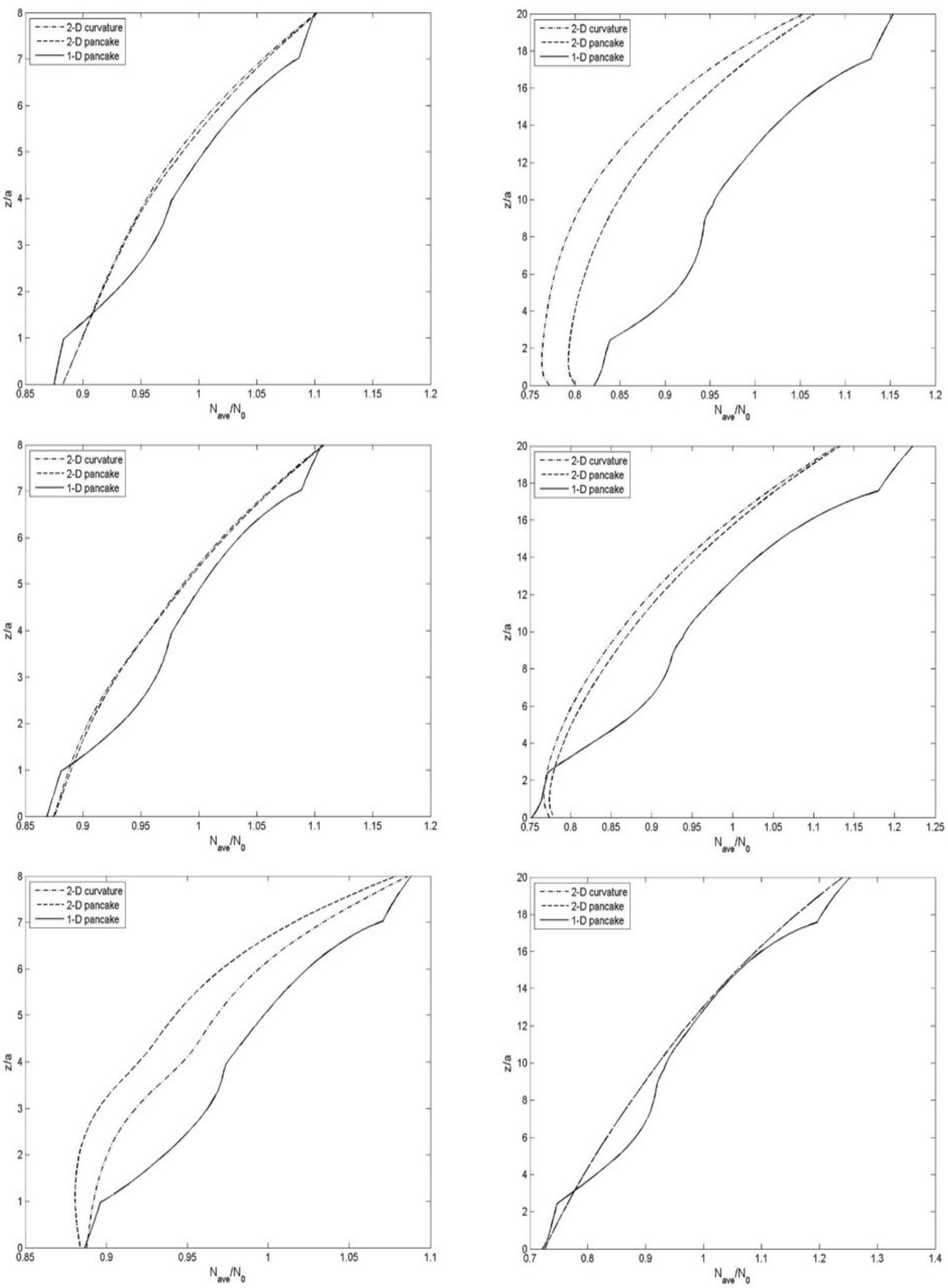

Figure 95: Comparison of the solutions of the diffusion equation for the Iguaçu (left) and the Rome (right) machines. The axial variation of the light isotope concentration is shown using the results of the *xPort* finite differencing code using the flow field from *CurvSOL* with curvature effects (dashed and dotted line labeled "2-D curvature"), the flow field from *CurvSOL* with the pancake approximation (dashed line labeled "2-D pancake"), and Cohen's radial averaging technique using the flow field from the *Pancake* code (solid line labeled "1-D pancake"). The results of *xPort* have been averaged at each axial sampling location for better comparison to the Cohen technique.

12 Appendix C - Performance Maps

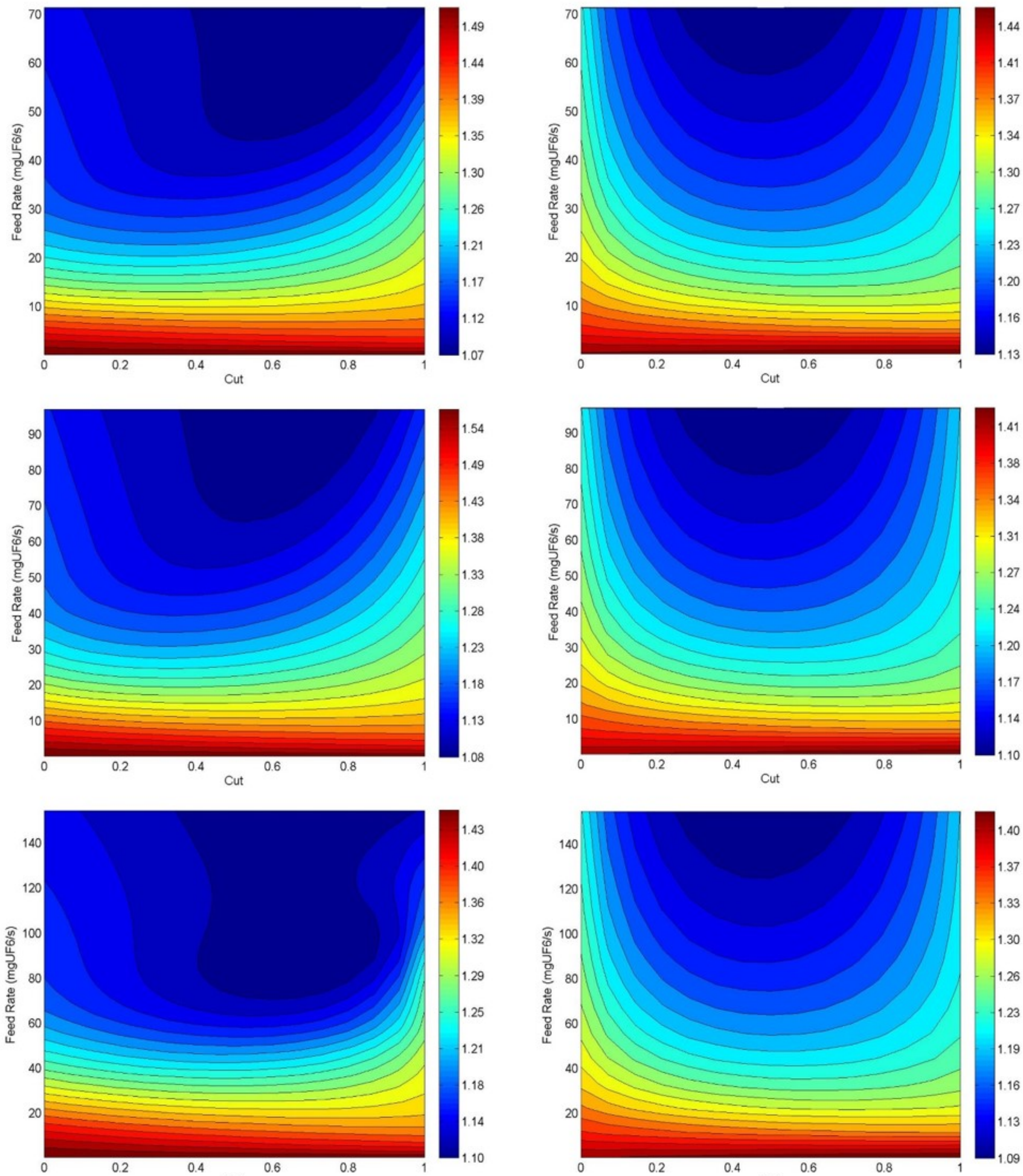

Figure 96: Two dimensional contour plots of the separation factor for the Iguaçu machine run at three different wall speeds: 500 m/s (top), 600 m/s (middle), and 700 m/s (bottom). The diffusion of the light isotope was modeled using two methods: Cohen's radial averaging technique based on the flow solution from the *Pancake* code (left) and finite differencing utilizing the flow solution from the *CurvSOL* code (right).

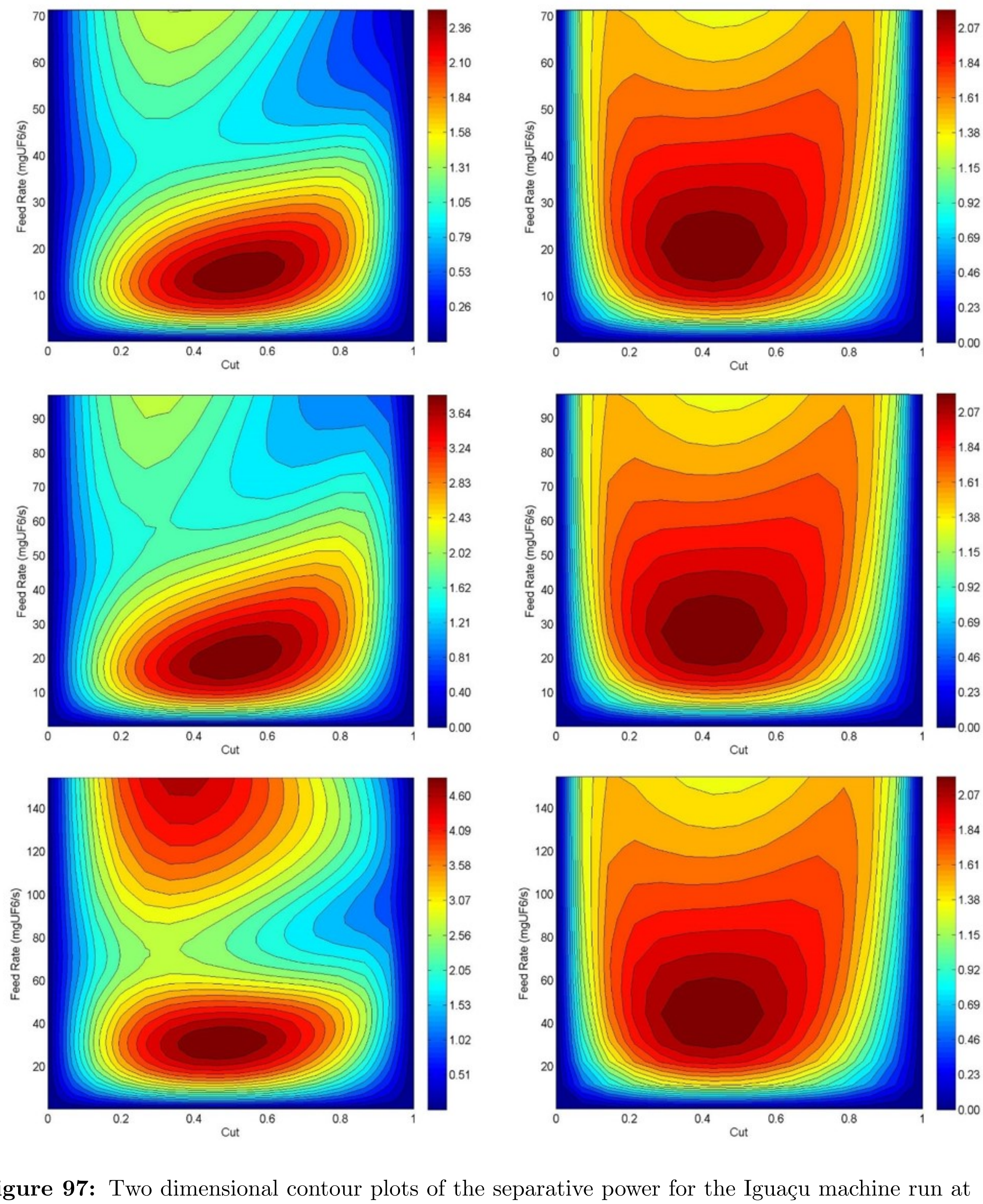

Figure 97: Two dimensional contour plots of the separative power for the Iguaçu machine run at three different wall speeds: 500 m/s (top), 600 m/s (middle), and 700 m/s (bottom). The diffusion of the light isotope was modeled using two methods: Cohen's radial averaging technique based on the flow solution from the *Pancake* code (left) and finite differencing utilizing the flow solution from the *CurvSOL* code (right).

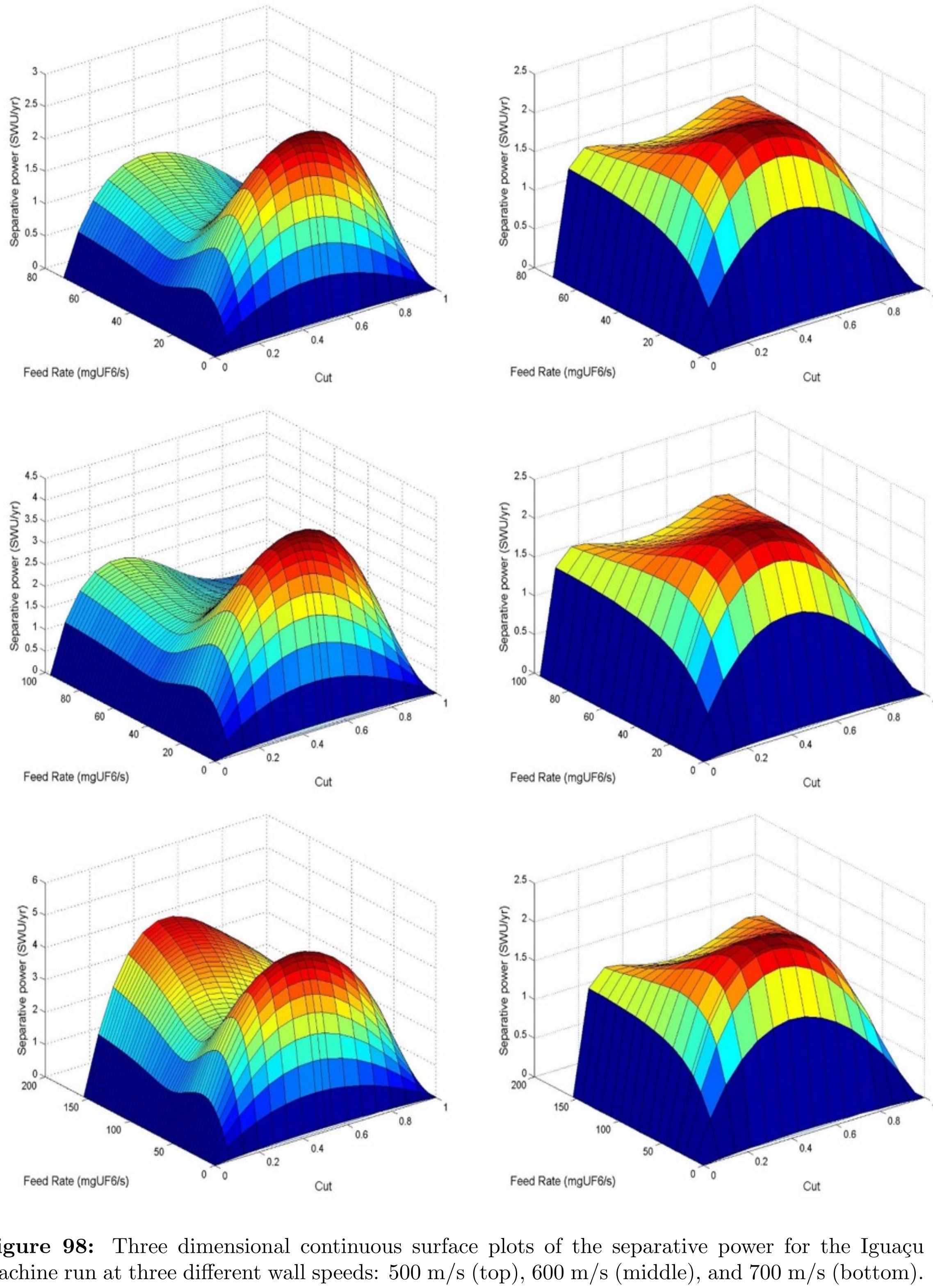

Figure 98: Three dimensional continuous surface plots of the separative power for the Iguaçu machine run at three different wall speeds: 500 m/s (top), 600 m/s (middle), and 700 m/s (bottom). The diffusion of the light isotope was modeled using two methods: Cohen's radial averaging technique based on the flow solution from the *Pancake* code (left) and finite differencing utilizing the flow solution from the *CurvSOL* code (right).

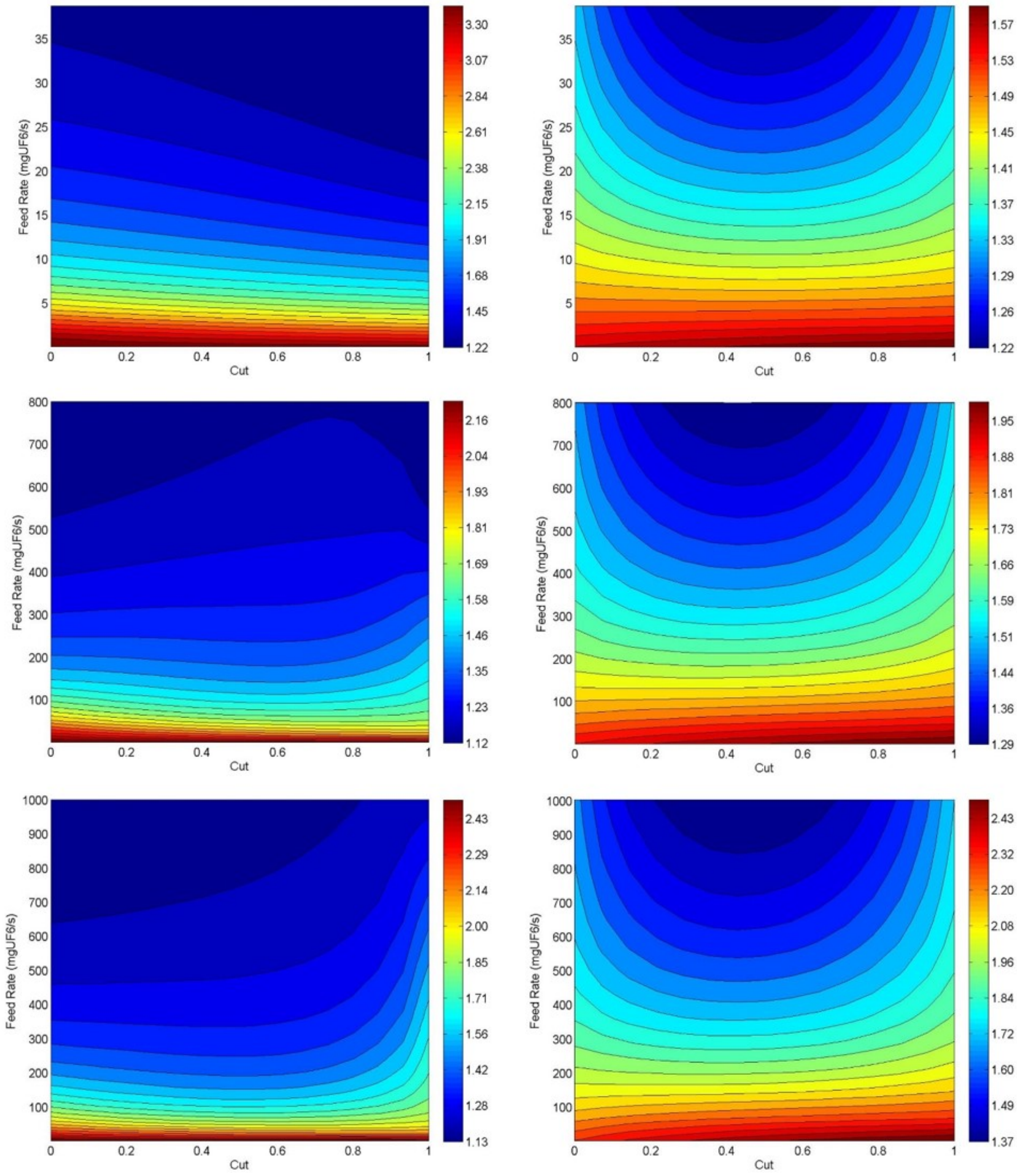

Figure 99: Two dimensional contour plots of the separation factor for the Rome machine run at three different wall speeds: 500 m/s (top), 600 m/s (middle), and 700 m/s (bottom). The diffusion of the light isotope was modeled using two methods: Cohen's radial averaging technique based on the flow solution from the *Pancake* code (left) and finite differencing utilizing the flow solution from the *CurvSOL* code (right).

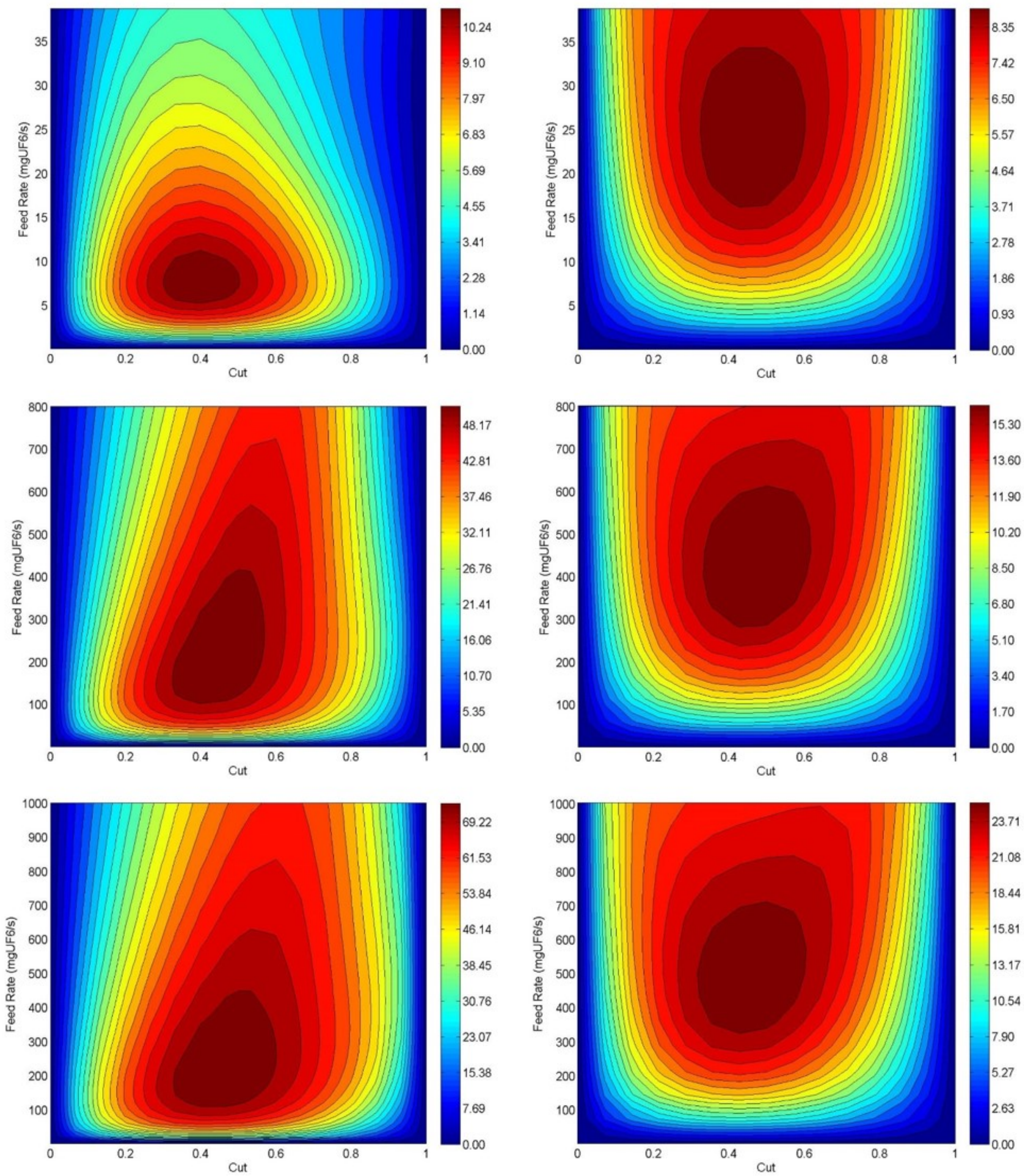

Figure 100: Two dimensional contour plots of the separative power for the Rome machine run at three different wall speeds: 500 m/s (top), 600 m/s (middle), and 700 m/s (bottom). The diffusion of the light isotope was modeled using two methods: Cohen's radial averaging technique based on the flow solution from the *Pancake* code (left) and finite differencing utilizing the flow solution from the *CurvSOL* code (right).

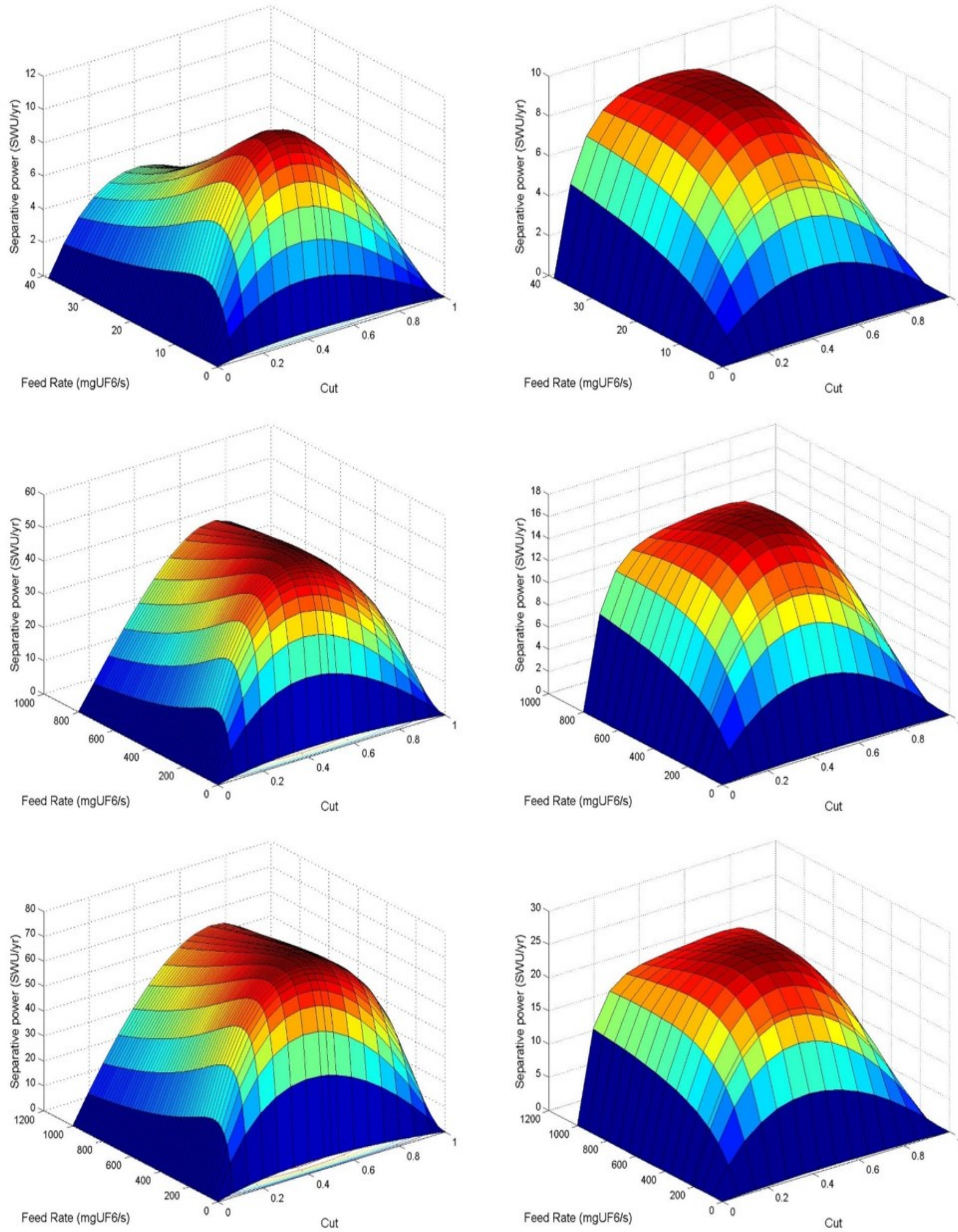

Figure 101: Three dimensional continuous surface plots of the separative power for the Rome machine run at three different wall speeds: 500 m/s (top), 600 m/s (middle), and 700 m/s (bottom). The diffusion of the light isotope was modeled using two methods: Cohen's radial averaging technique based on the flow solution from the *Pancake* code (left) and finite differencing utilizing the flow solution from the *CurvSOL* code (right).

13 Appendix D - Cascade Details

Table 4: Stage Details for the Iguaçu 19 Stage 228 Machine Cascade [24]

n	M	D	G	L	δU	γ_0
-	-	kgU/yr	kgU/yr	kgU/yr	SWU/yr	-
1	6	1874	3536	1662	258.20	1.276
2	11	3536	6671	3135	485.79	1.272
3	16	5009	9452	4443	687.06	1.276
4	20	6317	11921	5604	866.49	1.275
5	23	7478	14112	6634	1023.93	1.270
6	27	8508	16059	7550	1168.56	1.275
7	23	7325	13827	6502	1006.66	1.273
8	20	6277	11850	5573	862.22	1.276
9	17	5348	10097	4749	735.31	1.275
10	14	4524	8543	4019	621.51	1.271
11	12	3794	7166	3372	520.82	1.274
12	10	3147	5944	2797	433.33	1.275
13	8	2572	4860	2288	354.55	1.272
14	6	2063	3898	1836	284.52	1.261
15	5	1611	3045	1434	223.22	1.271
16	4	1209	2286	1077	166.35	1.281
17	3	852	1612	760	118.19	1.291
18	2	535	1012	477	74.41	1.300
19	1	252	477	225	35.02	1.309

Table 5: Stage Details for the Iguaçu 19 Stage 2268 Machine Cascade [24]

n	M	D	G	L	δU	γ_0
-	-	kgU/yr	kgU/yr	kgU/yr	SWU/yr	-
1	59	18739	35356	16617	258.20	1.274
2	111	35356	66710	31354	485.79	1.273
3	157	50094	94524	44430	687.06	1.273
4	198	63170	119207	56037	866.49	1.273
5	234	74776	141120	66344	1023.93	1.273
6	267	85083	160587	75504	1168.56	1.273
7	230	73253	138273	65020	1006.66	1.273
8	197	62769	118497	55728	862.22	1.273
9	168	53477	100969	47492	735.31	1.273
10	142	45241	85431	40190	621.51	1.273
11	119	37940	71655	33716	520.82	1.273
12	99	31465	59438	27973	433.33	1.273
13	81	25723	48601	22878	354.55	1.274
14	65	20628	38984	18356	284.52	1.274
15	51	16106	30446	14340	223.22	1.274
16	38	12090	22861	10771	166.35	1.273
17	27	8521	16117	7597	118.19	1.274
18	17	5346	10117	4770	74.41	1.275
19	8	2520	4770	2251	35.02	1.275

Table 6: Stage Details for the Rome 18 Stage 187 Machine Cascade [24]

n	M	D	G	L	δU	γ_0
-	-	kgU/yr	kgU/yr	kgU/yr	SWU/yr	-
1	5	16605	31144	14539	268.37	1.301
2	10	31144	58418	27274	537.54	1.312
3	14	43879	82311	38432	752.50	1.311
4	17	55037	103251	48214	913.35	1.305
5	20	64819	121613	56795	1074.48	1.305
6	23	73400	137728	64329	1235.99	1.308
7	19	62304	116922	54619	1020.27	1.303
8	16	52594	98714	46121	859.08	1.302
9	14	44096	82778	38682	752.42	1.310
10	11	36657	68827	32170	590.28	1.300
11	9	30145	56611	26467	482.85	1.299
12	8	24442	45912	21471	430.06	1.316
13	6	19446	36538	17092	322.30	1.305
14	5	15067	28319	13252	268.81	1.318
15	4	11227	21110	9883	214.94	1.331
16	2	7857	14780	6923	106.23	1.271
17	2	4897	9216	4319	106.92	1.357
18	1	2294	4319	2025	53.26	1.370